

Penetration of a Shaped Charge



Chris Poole

Corpus Christi College

University of Oxford

A thesis submitted for the degree of

Doctor of Philosophy

Trinity 2005

Acknowledgements

This research was funded by the EPSRC and *QinetiQ*, both of whom I would like to thank for funding the project.

I would also like to thank my supervisor, Jon Chapman, for his inspiration and guidance throughout this work. I am also indebted to John Curtis (*QinetiQ*) for his invaluable support on the project. I must also thank John Ockendon, who has been a fountain of enthusiasm and stimulation throughout the project. Sasha Korobkin must be thanked for his input and insight into the chapter on filling-flows. The metallurgical analysis would not have been possible without the help of Paula Topping and others in the Materials Department, whom I would like to acknowledge. Finally, on a Mathematical note, I would like to thank all those in OCIAM who have helped me throughout the project.

On a more personal level, I would like to thank all of those who have supported me and given me encouragement (and distractions!) since I have been in Oxford. In particular, I must mention the support of my family, the joviality of my friends in OCIAM (especially the DH9/DH10 folk, past and present), the conviviality of the OUSCR (and other ringers), and any other friends I haven't yet mentioned. It is the mixture of all these people that has kept me (relatively) sane and made my time in Oxford so enjoyable.

Abstract

A shaped charge is an explosive device used to penetrate thick targets using a high velocity jet. A typical shaped charge contains explosive material behind a conical hollow. The hollow is lined with a compliant material, such as copper. Extremely high stresses caused by the detonation of the explosive have a focusing effect on the liner, turning it into a long, slender, stretching jet with a tip speed of up to 12km s^{-1} .

A mathematical model for the penetration of this jet into a solid target is developed with the goal of accurately predicting the resulting crater depth and diameter. The model initially couples fluid dynamics in the jet with elastic-plastic solid mechanics in the target. Far away from the tip, the high aspect ratio is exploited to reduce the dimensionality of the problem by using slender body theory. In doing so, a novel system of partial differential equations for the free-boundaries between fluid, plastic and elastic regions and for the velocity potential of the jet is obtained.

In order to gain intuition, the paradigm expansion-contraction of a circular cavity under applied pressure is considered. This yields the interesting possibility of residual stresses and displacements. Using these ideas, a more realistic penetration model is developed. Plastic flow of the target near the tip of the jet is considered, using a squeeze-film analogy. Models for the flow of the jet in the tip are then proposed, based on simple geometric arguments in the slender region. One particular scaling in the tip leads to the consideration of a two-dimensional paradigm model of a “filling-flow” impacting on an obstacle, such as a membrane or beam.

Finally, metallurgical analysis and hydrocode runs are presented. Unresolved issues are discussed and suggestions for further work are presented.

Contents

1	Introduction	1
1.1	What is a shaped charge?	1
1.1.1	Mechanics of a shaped-charge jet	1
1.1.2	Applications of shaped charges	4
1.2	Background mathematics	5
1.2.1	Elasticity	5
1.2.2	Metal plasticity	11
1.2.3	Asymptotics	16
1.2.4	Slender body theory	17
1.3	Thesis outline	19
1.4	Statement of originality	20
2	Shaped-charge literature	22
2.1	Hydrodynamic models	22
2.1.1	Birkhoff jet impact	22
2.1.2	Water jets	25
2.2	Models from solid mechanics	27
2.2.1	Models of penetration	27
2.2.2	Plastic instability and jet particulation	29
2.2.3	Numerical models	30
2.3	Aims of thesis	31
3	An axisymmetric elastic-plastic model for penetration	32
3.1	Philosophy of the model	32
3.1.1	Parameter estimates	34
3.2	The jet	34
3.2.1	Boundary conditions	36
3.3	Plastic region	36
3.3.1	Boundary conditions	38

3.4	Elastic region	39
3.4.1	Boundary conditions	40
3.5	Different scalings	40
3.5.1	Geometric and other scaling ideas	41
4	Slender and outer analysis	44
4.1	Asymptotic analysis of nondimensional slender equations	44
4.1.1	Jet region	45
4.1.2	Plastic region	48
4.1.3	Inner elastic region	54
4.2	Outer region	56
4.2.1	Quasistatic outer region	56
4.2.2	Matching with a fully inertial outer region	62
4.2.3	Comments	65
4.3	Travelling-wave solution	65
4.4	Inertial effects	70
4.4.1	Modified inertial equations	70
4.5	Comments on elastic-plastic modelling	72
5	Gun-barrel mechanics	75
5.1	Linear elastic perfect-plastic cavity model	76
5.1.1	Elastic expansion	76
5.1.2	Elastic-plastic expansion	76
5.1.3	Simple plastic contraction with no residual stress	80
5.1.4	A possible model for cavity-contraction permitting a residual stress	80
5.1.5	“Elastic contraction”	83
5.1.6	Elastic-plastic contraction	85
5.1.7	Cyclic loading-unloading	89
5.2	A nonlinear problem	93
5.2.1	Elastic expansion	95
5.2.2	Elastic-plastic expansion	95
5.2.3	Contraction with no re-yielding	97
5.2.4	Contraction with further plastic flow	98
5.2.5	Comment	98
5.3	Application to shaped-charge penetration	99
5.3.1	Remarks	100
5.4	An asymmetric perturbation to the gun-barrel problem	101
5.4.1	Perturbation $\varepsilon Y(\theta, t) = \varepsilon(1 + \cos \theta)Q(t)$ to the cavity pressure	103

5.4.2	Perturbation $\varepsilon Y(\theta, t) = \varepsilon(1 + \cos N\theta)Q(t)$, $N \geq 2$ to the cavity pressure	107
5.4.3	Remarks	110
5.4.4	Effects of applying a non-radially-symmetric perturbation with varying sign as a function of θ to a plasticised annulus	111
5.4.5	Remarks	112
6	Ideas for a full elastic-plastic model	114
6.1	A full elastic-plastic model for the tip	114
6.1.1	Tip jet region	115
6.1.2	Plastic region	116
6.1.3	Elastic region	117
6.1.4	'Plasticised' elastic region	117
6.1.5	Remarks	118
6.2	Squeeze film analogy	120
6.2.1	Viscous squeeze film	120
6.2.2	Elasto-plastic squeeze film under horizontal tension	122
6.2.3	Elastic-plastic squeeze film under horizontal compression	129
6.2.4	Elasto-plastic squeeze film under compression, with known, varying base	130
6.2.5	Remarks	133
7	Paradigm tip models for the jet	135
7.1	Simple two-dimensional filling-flow models for the jet	136
7.1.1	A filling flow in a channel with constant height with various end-conditions	137
7.1.2	Comments	153
7.2	A model for a filling flow impacting a pre-stressed membrane	154
7.2.1	Inner and outer analysis	156
7.2.2	Global travelling wave solution	163
7.3	A model for a filling flow impacting a pre-stressed beam	168
7.3.1	Inner and outer analysis	169
7.3.2	Global travelling wave solution	171
7.4	A filling-flow impact model with general constitutive law $p = p(H)$	173
7.4.1	Similarity solution	175
7.5	Axisymmetric filling flows	177
7.5.1	General constitutive law $p = p(R)$	180
7.5.2	Similarity solution	181

7.6	Remarks	182
8	Metallurgical and hydrocode analysis	184
8.1	Shaped charge metallurgy literature	184
8.2	Metallurgical analysis	185
8.2.1	Microscopic analysis	189
8.3	Pictures of the microstructure	190
8.3.1	Images from ‘Face 1’	190
8.3.2	Images from ‘Face 2’, with penetration occurring ‘into’ the paper .	197
8.3.3	Observations	199
8.3.4	Remarks	201
8.4	Hardness	201
8.4.1	Hardness testing of the steel specimen	203
8.4.2	Remarks on hardness test results	204
8.5	Hydrocode analysis	204
8.5.1	Hydrocode plots	205
8.5.2	Analysis of hydrocode results	214
8.5.3	Comments	215
9	Conclusions	216
9.1	Summary of thesis	216
9.2	Conclusions and discussion	219
9.3	Future work	220
A	Stress and strain components in cylindrical polars for linear elasticity	223
B	Equations of small motion in cylindrical polars in an isotropic medium with no external body forces	225
C	Displacement and stress components in terms of the Love stress function $\chi(r, z, t)$ in cylindrical polars	226
D	The Navier-Stokes Equations	227
E	Metallurgical data for hardness testing	228
F	Inertial elastic-plastic gun-barrel expansion	230
F.1	Plastic region	230
F.2	Elastic region	231
F.3	Matching conditions	231

List of Figures

1.1	A sequence of events in shaped-charge jet formation.	2
1.2	Two diagrams showing well-bore perforation.	4
1.3	A diagram showing the deformation on a vector within an elastic medium caused by stressing the virgin elastic material.	6
1.4	An edge dislocation in a cylinder.	12
1.5	A diagram showing a pristine metal block and one with a dislocation introduced. The dislocation moves from right to left, the direction of the <i>Burgers vector</i>	12
1.6	Stress-strain relations for an elastic-plastic material.	14
1.7	A picture illustrating typical shear bands on the internal surface of a collapsed cylindrical cavity in stainless steel. We would like to acknowledge Professor Nesterenko <i>et al.</i> [102] for kindly allowing us to publish this image.	16
1.8	Slender body theory applied to a lightning conductor.	18
2.1	Hydrodynamic penetration.	23
3.1	A hardened steel block, penetrated by a silver shaped charge jet. The block has depth 80mm.	33
3.2	Axisymmetric elastic-plastic penetration of a shaped charge.	33
3.3	Output from a typical hydrocode run after penetration with a short jet has finished, showing some relative dimensions of the cavity depth and radius. The colouring represents σ_{rr} (top) and plastic strain rate (bottom); this will be discussed in detail later.	34
3.4	An elastic/plastic boundary $r = R(z, t)$	38
3.5	A schematic of the tip, slender and outer region.	41
3.6	A schematic showing geometric ideas.	41
3.7	A schematic showing the jet and plastic regions for four possible different scenarios for scalings of the tip and slender regions. These are based on geometrical arguments for an $\mathcal{O}(\varepsilon)$ cavity radius.	42

3.8	A schematic showing the jet and plastic regions for four possible different scenarios for scalings of the tip and slender regions. These are based on the r and z scales being identical in the tip region.	43
4.1	A figure showing a section of the slender region in which the magnitude of the plastic velocity is significantly lower than the magnitude of the jet velocity.	50
4.2	Elastic/plastic waves generated from the tip at finite angle are dissipated into the outer bulk.	52
4.3	A schematic phase-plane of possible trajectories from (X_0, Y_0)	70
4.4	Penetration with finite plastic region.	73
4.5	A photograph of a penetrated block, showing clear bowing of the edges. . .	74
5.1	Expansion of a gun-barrel under applied pressure $P(t)$	77
5.2	An $r - t$ graph showing elastic and plastic regions for expansion of a gun-barrel for some applied pressure $P(t)$. The inner surface of the gun-barrel yields at time $t = t_Y$	79
5.3	A schematic $r - t$ graph showing elastic and plastic regions for expansion and a possible idea for contraction of a gun-barrel for some applied pressure $P(t)$	81
5.4	An $r - t$ graph showing elastic and plastic regions for expansion and contraction of a gun-barrel for some applied pressure $P(t)$. The inner surface yields once on expansion, then again when the cavity pressure is being decreased.	86
5.5	An $r - t$ graph showing the stresses and displacements when cavity pressure is increased up to $P_* > \frac{\sigma_Y}{2}$, leading elastic expansion of the medium (①) and then elastic-plastic expansion (②). When the cavity pressure is decreased, the medium firstly contracts elastically (③). For $P_* > \sigma_Y$, there is elastic-plastic contraction until $\tilde{P} = 0$ (④). For any $P_* > \frac{\sigma_Y}{2}$, there are residual stresses and displacements.	90
5.6	A schematic of gun-barrel expansion/contraction. The two different paths depend on the relative sizes of P_* and σ_Y , thus allowing the possibility of the gun-barrel reyielding on contraction.	91
5.7	Four diagrams depicting different quantities during repeated expansion and contraction of a gun-barrel, produced from MATLAB. We take $\mu = 1$, $\sigma_Y = 1$ and $a = 1$. The colours correspond to the shaded regions in Fig. 5.6. Note that the maximum cavity pressure is greater than the yield stress, and so the material re-yields on contraction.	92

5.8	Two schematic diagrams for modelling the penetration as a series of two-dimensional gun-barrel problems.	100
5.9	Vector plots of the nondimensional velocity from MATLAB. The colouring represents the magnitude of the velocity. The nondimensional parameter values used were $\varepsilon = 0.2$, $\mu = 70$, $\lambda = 32$, $Q = 1 + 3t$ and $P = \frac{1}{2} + 3t$. The elastic-plastic boundary is denoted by the outer dotted black line.	108
5.10	A vector plot of nondimensional velocity at $t = 0.15$ s for $N = 2$. The colouring represents the magnitude of the velocity. The nondimensional parameter values used were $\varepsilon = 0.1$, $\mu = 70$, $\lambda = 32$, $Q = 1 + 3t$ and $P = \frac{1}{2} + 3t$. The elastic-plastic boundary is denoted by the outer dotted black line.	111
5.11	Von-Mises stress contours from FEMLAB modelling plasticised steel. . . .	112
5.12	A Von-Mises plot from FEMLAB on the same scale as Fig. 5.11. The outer boundary is stress-free, whereas the boundary conditions on the cavity are zero shear stress and $\sigma_{rr} = -3.78 \times 10^8 \text{kg m}^{-1} \text{s}^{-1}$ for $x > 0$, $\sigma_{rr} = -3 \times 10^8 \text{kg m}^{-1} \text{s}^{-1}$ for $x < 0$	113
5.13	A Von-Mises plot from FEMLAB on the same scale as Fig. 5.11, now illustrating the possibility of reverse yielding. The cavity boundary conditions are $\sigma_{r\theta} = 0$ and $\sigma_{rr} = -3.78 \times 10^8 \text{kg m}^{-1} \text{s}^{-1}$ for $x > 0$, $\sigma_{rr} = -3 \times 10^7 \text{kg m}^{-1} \text{s}^{-1}$ for $x < 0$, and the outer boundary remains stress-free.	113
6.1	The proposed elastic-plastic model showing jet, elastic, plastic and plasticised regions of the penetration.	115
6.2	A modification to the previous figure (Fig. 6.1), permitting residual stresses and including reyielding effects.	119
6.3	A viscous squeeze film.	121
6.4	Hill's squeeze film [36]. Observe that the plasticity spreads from the four sharp corners into the middle, and that the overhang is elastic.	123
6.5	A simple plastic squeeze film under tension.	123
6.6	Necking of the unstable plastic squeeze film. The curved part of the elastic region is determined by the height when it was last plastic.	124
6.7	A curved squeeze film parametrised with arc length, s and normal distance, n , from the lower surface.	132
6.8	A diagram illustrating a problem with mass conservation in incompressible plasticity and infinitesimal elasticity.	134
7.1	A schematic of a filling flow.	136
7.2	A filling flow in a frame moving with the turnaround point $X_0(t)$	137

7.3	Inner and outer regions for a filling flow moving with the turnaround point, $X_0(t)$	138
7.4	A numerical plot of the solution of (7.51) (from MAPLE). The parameters taken are $M = 20$, $k = 0.55$, $I = \frac{b_0}{L} \sim \frac{b_0}{b_e} = 1$, $C = 20$, $R = 1$, $b_0 = 0.7$ and $b_e = 0.7$	145
7.5	A numerical plot of the solution of 7.51 for small C (from MAPLE). The parameters taken are $M = 0.5$, $k = 0.55$, $I \sim 0$, $R = 1$, $C = 0.5$, $b_0 = 0.7$ and $b_e = 0.7$	146
7.6	Phase plane for the case $\gamma > 2$. The values taken are $\gamma = 3$ and $\beta = 2$ (from MATLAB).	147
7.7	Phase plane for the case $\gamma < 2$. The values taken are $\gamma = 1$ and $\beta = 2$ (from MATLAB).	148
7.8	A schematic phase plane plot for the system (7.67)-(7.68). The trajectories appropriate to our initial conditions are highlighted in red.	149
7.9	Four numerical plots (using MAPLE) showing $b(\tau)$, $V - \dot{X}_0$, $P_b(\tau)$ and $\dot{b}(\tau)$ all against time τ . We have taken $b_0 = 5$, $k = 0.76$, $\rho = 1$, $m = 1$, $H = 1$, $x_0 = 0$, $V = 5$ and $D = 1$	150
7.10	A schematic phase plane plot for the system (7.80)-(7.81). The trajectories appropriate to our initial conditions are again highlighted in red.	152
7.11	Two numerical plots (using MAPLE) showing $b(\tau)$ and $V - \dot{X}_0$ against time τ . We have taken $b_0 = 5$, $k = 0.76$, $\rho = 1$, $H = 1$, $x_0 = 0$, $V = 5$ and $\sigma_Y = 30$	153
7.12	A filling flow impacting on a membrane.	155
7.13	Initial conditions for the jet-membrane impact problem.	155
7.14	A schematic of the filling flow impacting a membrane, showing four separate asymptotic regions.	157
7.15	A subsonic travelling-wave profile, with $h_j = 2\text{mm}$, $\rho = 8920\text{kg m}^{-3}$, $c = 5000\text{ms}^{-1}$, $T = 1 \times 10^{11}\text{kgs}^{-2}$, $P = 2 \times 10^9\text{kg m}^{-1}\text{s}^{-2}$, $L = 0.5\text{m}$, $V = 2000\text{ms}^{-1}$ and $H_p = 20\text{mm}$. This leads to a solution $U = 2326\text{ms}^{-1}$ and $\xi_* = 0.91\text{m}$	167
7.16	The two supersonic travelling-wave profiles with $h_j = 2\text{mm}$, $\rho = 8920\text{kg m}^{-3}$, $c = 5000\text{ms}^{-1}$, $T = 1 \times 10^{11}\text{kgs}^{-2}$, $P = 2 \times 10^9\text{kg m}^{-1}\text{s}^{-2}$, $L = 1\text{m}$ and $V = 9000\text{ms}^{-1}$	168
7.17	An axisymmetric filling flow.	177
7.18	A schematic hysteresis diagram showing the displacement of the inner surface of a gun-barrel against applied cavity pressure, based on §5.1.6.	183

8.1	The set-up for a typical firing. The charge is fired down into stacked blocks of the target metal. The blocks are analysed afterwards.	186
8.2	The entry and exit points of a shaped charge after penetrating a hardened-steel block.	186
8.3	A cross-section of a target material showing penetration of a copper jet. . .	187
8.4	Another cross-section of a target showing a copper-lined cavity.	188
8.5	The large block is cut into a smaller, more manageable piece. The two marked faces will be polished.	189
8.6	Microstructure of an unpolished, sawn face.	189
8.7	A photo of the bulk microstructure of the target sufficiently far away (at least 1mm) from the edge of the cavity. Note that there is no evidence of cracking, shear bands or the silver jet.	190
8.8	A typical view of the microstructure within 1mm of the cavity edge after a very light etch. We consistently see that a band of width ~ 0.8 mm from the edge of the cavity has etched significantly more than the bulk.	191
8.9	Another view of the thin band local to the cavity after a light etch. We can see thin inclusions of silver. We also note from the brown markings that the thin band has etched significantly more than the outer bulk.	191
8.10	A view of the inner band after more etching. Note the darker colouring in the band and the silver inclusions.	192
8.11	A second view of the inner band after more etching. We observe silver tracking down the edge of the cavity and a crack partially-filled with silver in this particular image.	192
8.12	A clearer view of a silver inclusion after a total of 10 seconds of etching. The inner band now clearly shows cracks.	193
8.13	A picture showing cracks, silver inclusions, and a silver-lined cavity (with 10 seconds of etching).	193
8.14	This is another typical view of the microstructure local to the cavity after a 10 second etch. We can consistently observe that cracks and silver inclusions appear in the band ~ 0.8 mm from the cavity. The blue colouring shows where the specimen has been significantly etched.	194
8.15	A photo showing a closer view of one of the silver inclusions. Typically, they are at an angle of 30° to the direction of penetration, with a length of the order of 0.6mm.	194

8.16	A picture showing an inclusion of silver, larger than in Fig. 8.15. We can also see a network of cracks, mainly at an angle of between 20° and 40° to the direction of penetration. Note that the silver inclusion doesn't start from the edge of the cavity and that there is a crack at the bottom of the inclusion.	195
8.17	Another picture showing cracked regions. The wider black regions are also cracks, at a different altitude to the thinner cracks (and hence not in focus). There are also small damage voids, evident by altering the focus on the microscope.	195
8.18	A photograph within 0.8mm of the edge of the cavity, showing a silver inclusion and a network of cracks. Note, again, that the silver inclusion leads into several cracks.	196
8.19	A close-up of Fig. 8.18. From this, we observe that the width of a typical inclusion is $25\mu\text{m}$. We can see that several cracks emanate from the end of the inclusion.	196
8.20	A cross-sectional view of the target reveals cracking and silver inclusions around the cavity after a 10 second etch. This is seen consistently on other parts of the block, and the bulk is indistinguishable from Fig. 8.7.	197
8.21	A close-up of the silver inclusion uppermost in Fig. 8.20. The width is about $50\mu\text{m}$. This inclusion emanates from the edge of the cavity.	197
8.22	A picture showing a network of cracks around the cavity. Observe a silver inclusion amidst the cracks, which doesn't emanate from the edge.	198
8.23	A close-up of the inner silver inclusion from Fig. 8.22.	198
8.24	A schematic of a diamond indenter which is indenting a metal.	202
8.25	A typical indentation by a diamond indenter made into rolled hardened steel. The dimension of the indentation is of the order $1.6 \times 10^{-2} \text{ mm}$	202
8.26	A plan-view diagram showing indentations in the polished surface of our specimen.	203
8.27	Plots from Vickers Hardness tests.	203
8.28	A schematic of the initial conditions and the positions of the stations for the hydrocode runs. The edge of the domain $r = 35\text{cm}$ is not shown. . . .	205
8.29	A plot showing the distribution of σ_{rr} as a function of time for stations 1 to 10 in the target. The initial velocity of the jet is 7.5km s^{-1} , and its position can be tracked via Fig. 8.30.	206
8.30	Four plots showing the time-evolution plastic strain and total radial stress for transonic penetration. Observe the compressive stress-wave moving ahead of the penetration.	208

8.31	Two plots of plastic strain and total radial stress for a lower impact velocity. The white regions in the pressure plots represent negative pressure (compressive waves). Note that these waves propagate ahead of the tip even at the early stages of penetration.	209
8.32	Four plots showing plastic strain and material pressure during the early stages of penetration. These results were run on the finer grid.	211
8.33	Four plots showing the evolution of radial and axial velocity components. .	213

Chapter 1

Introduction

1.1 What is a shaped charge?

In the 1880s, the US navy performed experiments involving the detonation of gun-cotton blocks. The blocks had the initials “U.S.N.” hollowed into them. It was during these experiments that Charles Munroe, a navy scientist, made a serendipitous discovery. He observed that if the block was detonated with the marked surface in contact with a steel block, then there was a corresponding mark imprinted into the steel block afterwards. The importance of this observation, known as the *Munroe, Neumann, von Foerster* or *hollow-charge effect*, was recognised by Swiss scientists. They discovered that adding an inverted conical liner made from a compliant material, such as copper, would result in a slender, accelerating jet capable of significantly deep penetration into a steel target (a penetration depth of up to 1m is typical). This idea was then extensively developed by military scientists around the world in order to counter the large threat posed by tanks on the battlefield. Hence the first *shaped-charge* warhead was born. The first weapon based on the technology was trialled and used successfully in the second world war.

1.1.1 Mechanics of a shaped-charge jet

The formation of a shaped-charge jet is well-understood theoretically [95]. A typical shaped charge consists of an explosive with a liner material at one end and a detonator at the other. The liner is usually conical, although it can have other axisymmetric geometries such as a hemisphere, tulip or trumpet, to name but a few. Many liner materials have also been considered; examples include zirconium, steel and depleted uranium [9, 22, 34]. In view of the Munroe effect, the apex is the closest end of the conical liner to the detonator, as is shown in Fig. 1.1(a)¹. When the charge is detonated, a detonation wave races

¹Other parts of the warhead, such as guidance systems and computers are housed ahead of the liner.

from left to right in the charge with speeds from $6 - 7 \text{ km s}^{-1}$ and inducing pressures of around $3 \times 10^{10} \text{ Pa}$. This causes the surrounding casing to expand and ultimately leads to fragmentation [69].

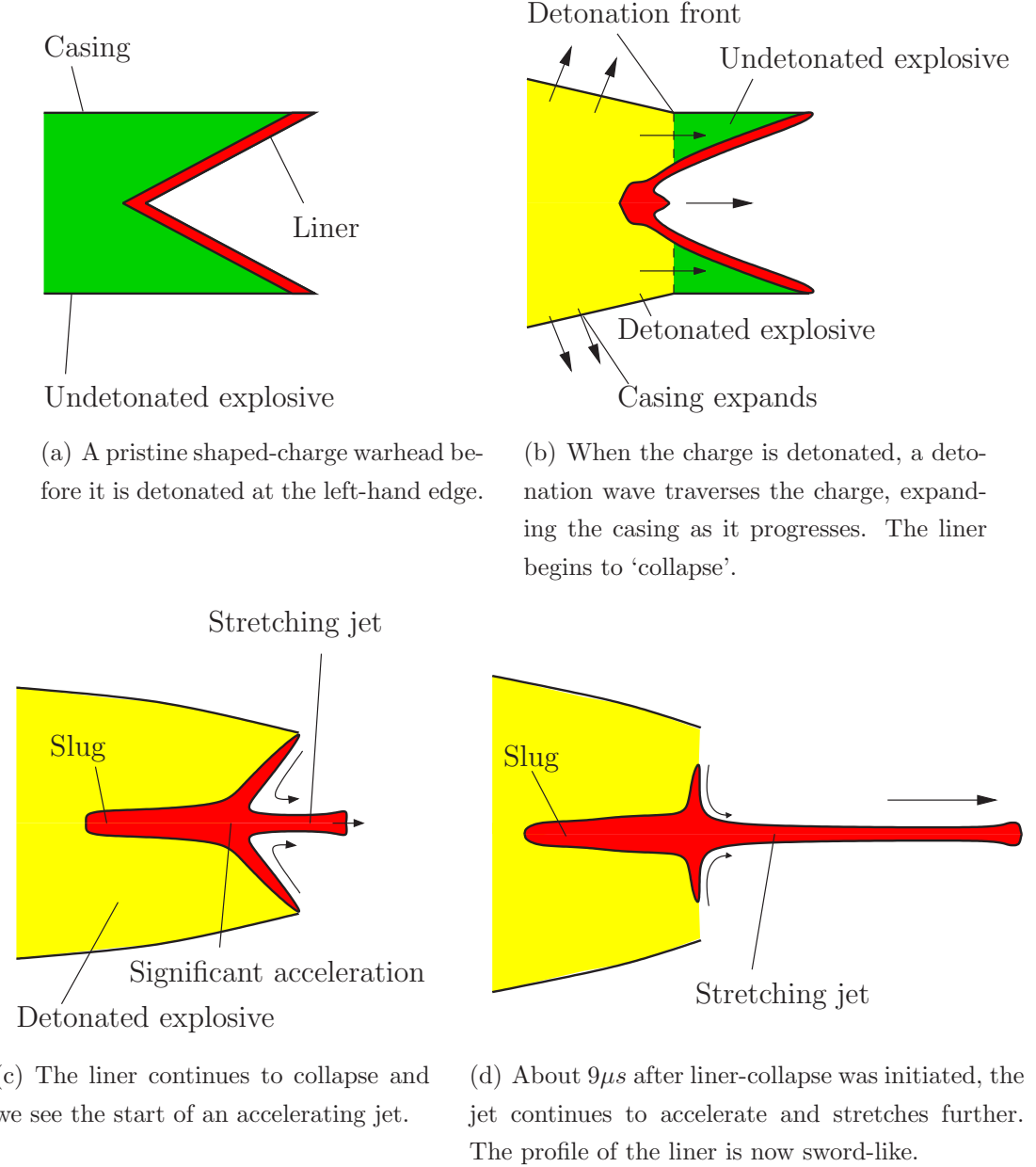


Figure 1.1: A sequence of events in shaped-charge jet formation.

Typically, the detonation wave takes only the order of $6 \mu\text{s}$ to reach the apex of the liner. The extreme pressure in the gaseous products of this detonation wave results in severe deformation of the liner towards its axis, a process known as 'collapsing'. The symmetry of the liner means that when opposite parts of the liner reach the axis, the only nonzero component of momentum is along the axis (although, in reality, perfect symmetry

is never realised). Thus, the initial geometry of the liner has the effect of focusing the momentum in the direction of the axis of the cone. The result of the liner-collapse is the classical Birkhoff-problem of impinging jets [7, 21]. Two new metal jets are consequently formed, both with net positive axial velocity (where we define positive z to be from left to right) and, courtesy of symmetry, no radial component of the velocity. One of the jets is a fast-moving, thin jet, typically with speeds of $6 - 12 \text{ km s}^{-1}$. The extreme pressure from the detonation wave greatly exceeds the yield stress of the liner material, and so the high-speed jet behaves like a plastic fluid. The other jet, known as the “slug”, trails behind, with a typical velocity of up to 1 km s^{-1} . For conical liners, the majority of the liner by mass goes into the slug. This is depicted in Figs. 1.1(b), 1.1(c).

The fast-moving jet continues to elongate owing to the initial tapering nature of the liner. This occurs until it impacts its target. The distance between the front of the liner and the target is termed the *stand-off*. The forming jet may either remain intact, or it may particulate into many small fragments, spreading out. The latter is undesirable because the cloud of fragments has little capability to penetrate [17, 19]. Off-axis drift may also occur with a coherent jet and is still a factor that reduces penetration depth, but the effects are far less pronounced than with incoherent jets [43] (that is, a jet in which the fast-moving particles in the jet do not form a cohesive mass of material, a consequence of ‘overdriving’ the jet). It is observed that a longer jet leads to deeper penetration, and so the appropriate stand-off must be estimated *a priori* so as to maximise the jet length.

About $50 \mu\text{s}$ after the detonator is ignited, the liner has a profile that resembles a sword (Fig. 1.1(d)). Typically, this is when the fast-moving, high-pressure jet strikes the target². The jet then creates a long, slender, almost perfectly-axisymmetric cavity in the target.

The main mechanism responsible for the penetration is well-documented to be plasticity of the target material, resulting from the extreme pressure at the tip of the jet. Although the exact temperature profile of the jet is not well understood, the average surface temperature of the jet is of the order 500°C (with some local hot-spots) and so the cavity is not a direct result of melting. The plastic flow leads to radial expansion of the target material about the axis of the jet, expanding the target and thus excavating a hole. Eventually, the plastic jet comes to a halt after having furrowed a deep cavity. This is, in reality, a combination of most of the jet’s energy being transferred to the target and growth of instabilities in the jet leading to off-axis penetration. After the penetration has terminated, it is observed experimentally [93] that the mass before penetration is equal to the mass afterwards (neglecting effects of spall), so that no material is ‘lost’ from the

²The jet, even if coherent, often breaks up at the ‘hilt’ of the sword. The part that is the slower moving slug is sometimes known as the “carrot”, and has little effect on the penetration.

target.

1.1.2 Applications of shaped charges

The purpose of a shaped charge is to make a slender hole in a material that is otherwise difficult to penetrate. This being so, much of its development has occurred because of the high demand from the military. However, there are many relatively peaceful applications to this remarkable technology, which we briefly outline in this section.

Firstly, we must mention an application in the oil industry, which uses more shaped charges per year than the military. This is the process of *well-bore perforation*. After a hole has been bored for an oil well, a process known as “cementing” occurs. Essentially, this is when the surface of the hole is coated in a layer of ‘cement’ along its entire length in order to strengthen it. Clearly, this has the detrimental effect of making it impossible to get any oil (or gas) from the surrounding rock. To remedy this, a “carrier-tube” containing many shaped charges is lowered down the hole. The charges are oriented such that, when detonated, they produce jets that move radially, thus penetrating the cement³. This is shown in Fig. 1.2.

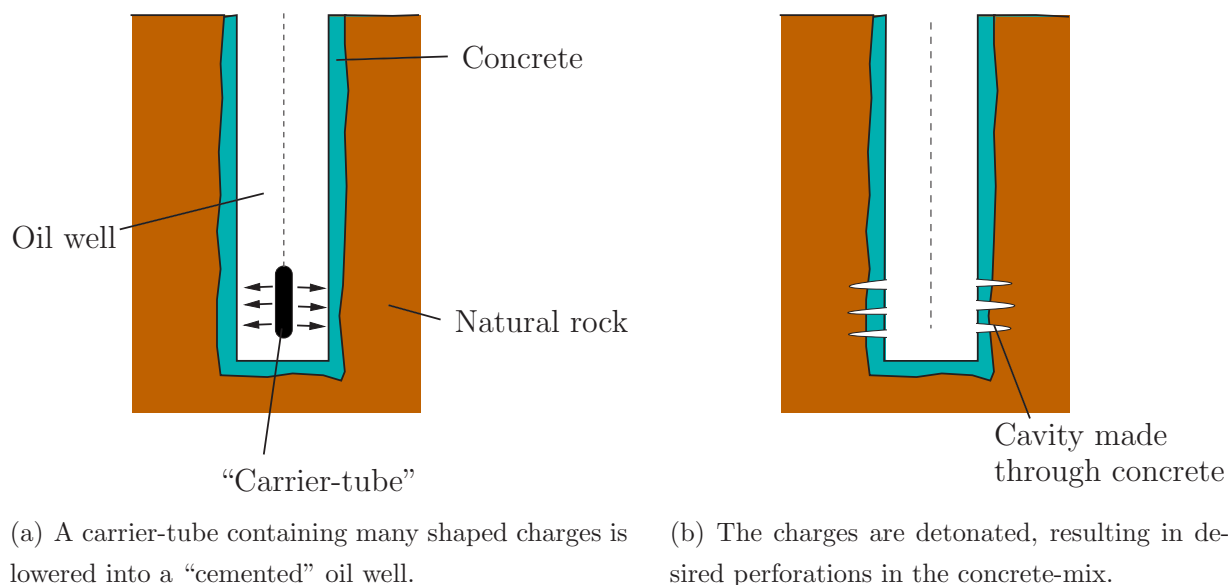


Figure 1.2: Two diagrams showing well-bore perforation.

Other major applications lie in industries in which a hole needs to be made. They include, among others, applications in the mining industry (drilling rock and tunnelling), demolition work (*e.g.* decommissioning unwanted structures), torpedoes, tree-felling,

³A problem with this process is that metal and other debris can block holes in the rock, decreasing its porosity. A more expensive alternative is to use lasers.

avalanche-control [70], jet-fighter ejector seats and safe-breaking. Although the underlying principles are the same, many of these applications have very specific demands on the use and accuracy of this technology.

1.2 Background mathematics

This section of the thesis outlines some of the theoretical fundamentals that will be of relevance to later models.

1.2.1 Elasticity

The theory of elasticity has been continuously developed since Galilei considered the now classic problem of bending a clamped beam in the first half of the 17th century [25]. Since then, the subject has flourished, giving rise to a rich vein of mathematics. Naively, the theory attempts to reconcile the deformations and stresses in a solid material with an applied force or displacement. We will now outline the building blocks of the theory, although must firstly point the reader towards the classic text on elasticity by Love [49].

1.2.1.1 Strain

When an elastic material is subjected to a stress, it will deform. In order to measure these deformations, one defines the *elastic strain* as the fractional change in the shape of the body. In one dimension, it is straightforward to visualise. Consider an elastic string of length L , which we stretch to a length \tilde{L} (at constant temperature). The stretching will move a small portion AB of the string of length δx , to $\tilde{A}\tilde{B}$, say, where \tilde{A} has been displaced by u and \tilde{B} has been displaced by $u + \delta u$. The strain in the x -direction is given by the ratio of the extension to the original length. As $\delta x \rightarrow 0$, it is written

$$\varepsilon_{xx} = \frac{\partial u}{\partial x}. \quad (1.1)$$

In order to generalise this result to three dimensions, we look at an arbitrary three-dimensional elastic body at constant temperature. Consider a vector with endpoints \mathbf{X} and $\mathbf{X} + \delta\mathbf{X}$ in an unstressed elastic medium. When the elastic medium is stressed, this vector will deform to a new vector, with endpoints \mathbf{x} and $\mathbf{x} + \delta\mathbf{x}$, say. These endpoints can also be posed in terms of a *displacement vector*, \mathbf{u} , with respect to the initial unstressed frame. Hence $\mathbf{x} = \mathbf{X} + \mathbf{u}(\mathbf{X})$ and $\mathbf{x} + \delta\mathbf{x} = \mathbf{X} + \delta\mathbf{X} + \mathbf{u}(\mathbf{X} + \delta\mathbf{X})$. This is shown in Fig. 1.3. We relate the components of the two line vectors via the chain rule, so $\delta x_i = \frac{\partial x_i}{\partial X_j} \delta X_j$, where δx_i is written for the i th component of $\delta\mathbf{x}$ and δX_j for the j th component of $\delta\mathbf{X}$.

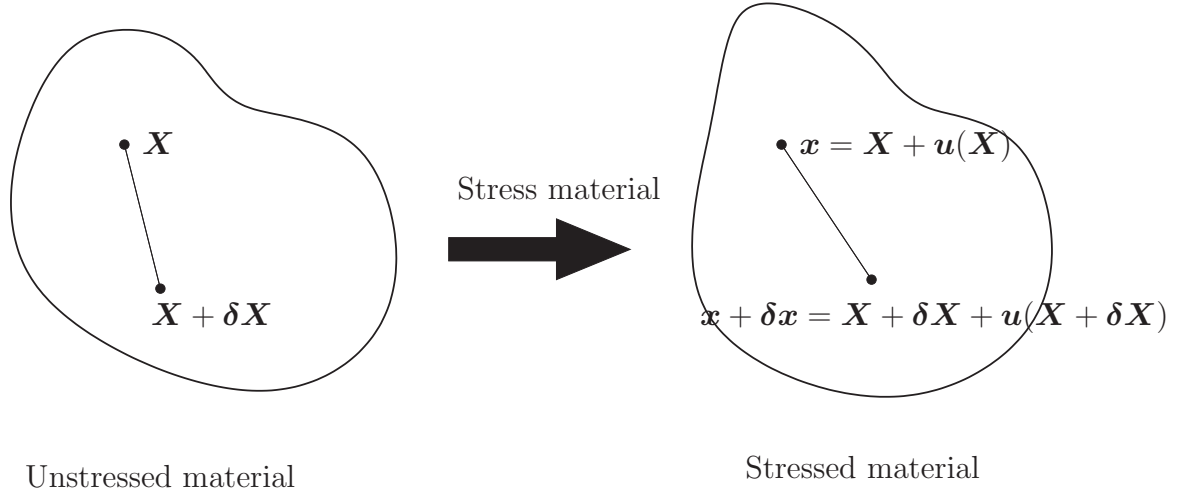


Figure 1.3: A diagram showing the deformation on a vector within an elastic medium caused by stressing the virgin elastic material.

The tensor $\frac{\partial x_i}{\partial X_j}$ is defined as the *deformation tensor*, written as \mathbf{F} . A measure of the deformation is thus given by

$$|\delta \mathbf{x}|^2 - |\delta \mathbf{X}|^2 = \delta x_i \delta x_i - \delta X_j \delta X_j \quad (1.2)$$

$$= \frac{\partial x_i}{\partial X_j} \delta X_j \frac{\partial x_i}{\partial X_k} \delta X_k - \delta X_j \delta X_j \quad (1.3)$$

$$= \left(\frac{\partial x_k}{\partial X_i} \frac{\partial x_k}{\partial X_j} - \delta_{ij} \right) \delta X_i \delta X_j \quad (1.4)$$

$$= \left(\delta_{ij} - \frac{\partial X_k}{\partial x_i} \frac{\partial X_k}{\partial x_j} \right) \delta x_i \delta x_j. \quad (1.5)$$

We define the *Green-Lagrange strain tensor* (relating to the reference frame) as

$$E_{ij} = \frac{1}{2} \left(\frac{\partial x_k}{\partial X_i} \frac{\partial x_k}{\partial X_j} - \delta_{ij} \right), \quad (1.6)$$

or

$$\mathbf{E} = \frac{1}{2} (\mathbf{F}^T \mathbf{F} - \mathbf{I}). \quad (1.7)$$

Similarly, the *Almansi strain tensor* (relating to the deformed frame) is written

$$e_{ij} = \frac{1}{2} \left(\delta_{ij} - \frac{\partial X_k}{\partial x_i} \frac{\partial X_k}{\partial x_j} \right), \quad (1.8)$$

or

$$\mathbf{e} = \frac{1}{2} (\mathbf{I} - (\mathbf{F}^{-1})^T \mathbf{F}^{-1}), \quad (1.9)$$

so that $|\delta \mathbf{x}|^2 - |\delta \mathbf{X}|^2 = 2E_{ij} \delta X_i \delta X_j = 2e_{ij} \delta x_i \delta x_j$. In terms of the displacements u_i , these strain tensors are

$$\begin{aligned} E_{ij} &= \frac{1}{2} \left(\left(\delta_{ki} + \frac{\partial u_k}{\partial X_i} \right) \left(\delta_{kj} + \frac{\partial u_k}{\partial X_j} \right) - \delta_{ij} \right) \\ &= \frac{1}{2} \left(\frac{\partial u_j}{\partial X_i} + \frac{\partial u_i}{\partial X_j} + \frac{\partial u_k}{\partial X_i} \frac{\partial u_k}{\partial X_j} \right), \end{aligned} \quad (1.10)$$

and

$$e_{ij} = \frac{1}{2} \left(\frac{\partial u_j}{\partial x_i} + \frac{\partial u_i}{\partial x_j} - \frac{\partial u_k}{\partial x_i} \frac{\partial u_k}{\partial x_j} \right). \quad (1.11)$$

When the shape of the deformed solid is close to the original reference shape, the terms $\frac{\partial u_k}{\partial x_i}$ are small and we may neglect the quadratic terms. This leads to the infinitesimal strain tensor for *linear elasticity*, termed the *Cauchy strain tensor*. We will write this as

$$\varepsilon_{ij} = \frac{1}{2} \left(\frac{\partial u_i}{\partial x_j} + \frac{\partial u_j}{\partial x_i} \right). \quad (1.12)$$

Clearly, this tensor is symmetric. The components of the strain tensor in cylindrical polars are given in (A.2)-(A.7).

1.2.1.2 Stress

We define the *stress tensor* as the three dimensional tensor σ_{ij} , where σ_{ij} is the force per unit area in the i th direction on a surface whose normal is in the j th direction with respect to the deformed frame. The *traction* vector T_i is defined as the force on a surface per unit area of deformed solid. By applying Newton's Law to a small tetrahedron, it is possible to shown that the traction on a boundary whose normal has components n_j is given by $T_i = \sigma_{ij}n_j$. It is also an easy exercise to show that the stress tensor is symmetric (by considering forces on different faces of a cuboid and taking moments), so that

$$\sigma_{ij} = \sigma_{ji}. \quad (1.13)$$

In order to write down equations for linear elasticity, we would like to relate the stress tensor σ to the Cauchy strain tensor ε . In 1670, Robert Hooke⁴ came up with such a law for a one-dimensional spring. Originally published in an anagrammatic form, his law stated that

“*ut tensio, sic vis*,”

which literally means that “as is the extension, so is the force”, more modernly translated as “force is proportional to extension”, or “stress is proportional to strain”. This is written more compactly as $\sigma = E\varepsilon$, where E is the *Young's modulus*.

The generalised Hooke law states that each of the components of stress can be written as a linear sum of the six components of strain at the point, hence

$$\sigma_{ij} = A_{ijkl}\varepsilon_{kl}, \quad (1.14)$$

⁴Poor old Robert Hooke is described historically as a “lean, bent and ugly man”, which may account for there being very few (if any) known portraits of him in existence!

where A_{ijkl} is a fourth rank tensor. For a homogeneous, isotropic material, this can be reduced to [78]

$$\sigma_{ij} = 2\mu\varepsilon_{ij} + \varepsilon_{kk}\lambda\delta_{ij}, \quad (1.15)$$

where μ and λ are *Lamé* constants. The parameter μ is often called the shear modulus, or modulus of rigidity (and is also denoted by G), and related to λ via the *bulk modulus* $K = \lambda + \frac{2}{3}\mu$. The bulk modulus is a measure of the material's resistance to volume change when subjected to a hydrostatic load (*i.e.* a load in which the only nonzero elements of the stress tensor are the diagonal entries, which are constant). The Young's modulus can be written in terms of λ and μ as $E = \frac{\mu(3\lambda+2\mu)}{\lambda+\mu}$. We also define *Poisson's ratio* as $\nu = \frac{\lambda}{2(\lambda+\mu)}$. This is equal to the ratio of the lateral strain to the longitudinal strain ($\nu = -\varepsilon_{yy}/\varepsilon_{xx}$ for a bar with axis parallel to the x -axis being stretched in the x -direction). It is usually positive, as when most materials are stretched, they tend to get thinner in cross-section. The 6×6 matrix relating stress to strain is called the *stiffness* matrix.

The equations of equilibrium for an elastic medium are derived from (1.15) by applying Newton's second law of motion to an arbitrary region in the body, Ω , say. Assuming that there are no external forces (*i.e.* body forces) on this region,

$$0 = \iint_{\partial\Omega} \sigma_{ij}n_j \, dS \quad (1.16)$$

$$= \iiint_{\Omega} \frac{\partial \sigma_{ij}}{\partial x_j} \, dV, \quad (1.17)$$

using Green's theorem. Since the region Ω is arbitrary, we finish with

$$\nabla \cdot \boldsymbol{\sigma} = 0, \quad (1.18)$$

or, in terms of the displacements,

$$(\lambda + \mu)\nabla(\nabla \cdot \mathbf{u}) + \mu\nabla^2 \mathbf{u} = 0. \quad (1.19)$$

These are *Navier's equations*⁵. The system of equations is elliptic, and so the boundary conditions are either the stress vector or displacement given on all boundaries, or some combination.

If the inertia of the elastic body is important, we can easily modify the equation to get

$$(\lambda + \mu)\nabla(\nabla \cdot \mathbf{u}) + \mu\nabla^2 \mathbf{u} = \rho \frac{\partial^2 \mathbf{u}}{\partial t^2}. \quad (1.20)$$

The system is now hyperbolic, and hence can generate elastic waves. There are, in fact, two wave speeds, namely the primary, or longitudinal wave speed ($c_p = \sqrt{\frac{\lambda+2\mu}{\rho}}$) and the shear, or secondary wave speed ($c_s = \sqrt{\frac{\mu}{\rho}}$). These waves are commonly observed in Earthquakes [44].

⁵These are also called the *Lamé equations*.

1.2.1.3 Compatibility

Recall the definition of the Cauchy strain tensor, (1.12). We could consider this as a system of equations in which the strains are prescribed, and hence we should be able to solve for the components u_i . In doing so, we see that there are six equations, but only three unknowns. Hence, there is no solution unless the strain tensor satisfies some compatibility conditions. To work out what the restrictions on the strain tensor are, we could argue by looking at small elements in a general elastic body [79]. Instead, we put the more concise argument as in Milne-Thomson [50]. If we write the strain matrix in terms of the spatial derivative of the displacements as

$$\boldsymbol{\varepsilon} = \frac{1}{2} \left(\begin{pmatrix} \cdots & \nabla u & \cdots \\ \cdots & \nabla v & \cdots \\ \cdots & \nabla w & \cdots \end{pmatrix} + \begin{pmatrix} \vdots & \vdots & \vdots \\ \nabla u & \nabla v & \nabla w \\ \vdots & \vdots & \vdots \end{pmatrix} \right), \quad (1.21)$$

we see that we should get zero if we take the curl of the rows and then the columns. The compatibility tensor is thus defined in terms of the alternating tensor ϵ_{ijk} by

$$\eta_{ij} = -\epsilon_{ikl}\epsilon_{jmn} \frac{\partial^2 \varepsilon_{ln}}{\partial x_k \partial x_m}. \quad (1.22)$$

When $\eta_{ij} = 0 \ \forall i, j$, there is a unique solution for the displacements up to rigid body motion⁶.

1.2.1.4 Stress functions

In two-dimensional or axisymmetric incompressible fluid dynamics, one often introduces a stream function ψ . This function is defined so that the incompressibility condition is automatically satisfied [2]. The key attribute of the stream function is that the two unknown components of the fluid velocity are simply derivatives of ψ , and so if we can solve one equation for ψ with appropriate boundary conditions, we can easily determine the two velocity components.

A similar notion exists in elasticity. A simple example to consider is the equations of equilibrium in plane strain,

$$\frac{\partial \sigma_{xx}}{\partial x} + \frac{\partial \sigma_{xy}}{\partial y} = 0, \quad (1.23)$$

$$\frac{\partial \sigma_{xy}}{\partial x} + \frac{\partial \sigma_{yy}}{\partial y} = 0. \quad (1.24)$$

⁶Essentially, by taking the curl, we have cross-differentiated the components of the strain and eliminated the different displacements. In plane strain, the compatibility condition can easily be worked out to be $\frac{\partial^2 \varepsilon_{xx}}{\partial y^2} + \frac{\partial^2 \varepsilon_{yy}}{\partial x^2} - 2 \frac{\partial^2 \varepsilon_{xy}}{\partial x \partial y} = 0$.

We introduce the *Airy Stress function*, $A(x, y)$, where the stress components are given as

$$\sigma_{xx} = \frac{\partial^2 A}{\partial y^2}, \quad \sigma_{yy} = \frac{\partial^2 A}{\partial x^2} \quad \text{and} \quad \sigma_{xy} = -\frac{\partial^2 A}{\partial x \partial y}, \quad (1.25)$$

so that (1.23)-(1.24) are automatically satisfied. We now use the vector identity

$$\nabla^2 \mathbf{u} = \nabla(\nabla \cdot \mathbf{u}) - \nabla \wedge (\nabla \wedge \mathbf{u}), \quad (1.26)$$

and take the divergence of Navier's equations (1.19). This yields

$$\nabla^2(\nabla \cdot \mathbf{u}) = 0, \quad (1.27)$$

and so $\nabla \cdot \mathbf{u}$, the *dilatation*, is harmonic. Finally, (1.15) gives the relationship

$$\sigma_{xx} + \sigma_{yy} = 2(\lambda + \mu)\nabla \cdot \mathbf{u}, \quad (1.28)$$

and so substituting for the stresses in terms of $A(x, y)$ leads to a very familiar equation in elasticity, namely the biharmonic equation:

$$\nabla^4 A(x, y) = 0. \quad (1.29)$$

Hence if we can solve the biharmonic equation with appropriate boundary conditions, we can solve for the state of stress. We can then solve for the displacements via the stress-strain relations (1.15) with suitable boundary conditions (substituting for the strains in terms of the displacements and checking the compatibility conditions).

The formulation above is simple to write down. A similar stress function exists for axisymmetric elasticity. Sadly, the derivation is neither intuitive nor simple. However, it is shown by Love [49] that there exists a stress function in axisymmetric coordinates, $\chi(r, z)$, that satisfies the (quasistatic) Navier equations. We term this function the *Love stress function*, and the equation that it satisfies is, remarkably,

$$\nabla^4 \chi(r, z) = 0. \quad (1.30)$$

The components of stress and displacement are given in terms of the Love stress function, $\chi(r, z)$, in (C.2)-(C.7).

1.2.1.5 Nonlinear elasticity

We have already described the theory of linear elasticity, valid for infinitesimal strain. If the strains are *finite*, we can no longer neglect the quadratic terms in (1.10), and so need a different theory. This theory is termed *finite hyperelasticity* (or just finite elasticity), and a material satisfying it is called a *Green-elastic* material. In order to write a relationship

analogous to Hooke's Law (1.15), we must firstly define the *first Piola-Kirchoff* stress tensor, \mathbf{S} . This is defined as⁷ the force per unit undeformed area acting on the deformed body and is related to the true stress, $\boldsymbol{\sigma}$, via the deformation tensor \mathbf{F} as [39]

$$\boldsymbol{\sigma} = \frac{1}{J} \mathbf{S} \mathbf{F}^T, \quad (1.31)$$

where $J = \det \mathbf{F}$. We now introduce the *strain-energy function* W . This is a scalar potential and is a measure of the energy stored in the material as a result of the deformation [36]. It is postulated to be a function of the eigenvalues of \mathbf{F} , known as the *principal stretches*. For an unconstrained hyperelastic material, it can be shown [39, 62] that

$$\mathbf{S} = \frac{\partial W}{\partial \mathbf{F}}. \quad (1.32)$$

Incompressible hyperelasticity

If the elastic material is incompressible, this equation is modified to

$$\mathbf{S} = -p(\mathbf{F}^{-1})^T + \frac{\partial W}{\partial \mathbf{F}}. \quad (1.33)$$

Here, p , the hydrostatic pressure, is the Lagrange multiplier for the constraint of incompressibility. To write this in terms of the true stress $\boldsymbol{\sigma}$, we use $\det J = 1$ to find that

$$\boldsymbol{\sigma} = -p\mathbf{I} + \frac{\partial W}{\partial \mathbf{F}} \mathbf{F}^T. \quad (1.34)$$

In order to determine the stresses for such a hyperelastic material, we need to write down an explicit law for the strain-energy function W . The simplest formulation is to assume a *Neo-Hookean* law. This is written as

$$W = \frac{\mu}{2}(I_1 - 3), \quad (1.35)$$

where I_1 is the first invariant of *Green's deformation tensor* $\mathbf{C} = \mathbf{F}^T \mathbf{F}$, written explicitly as

$$I_1 = \text{tr}(\mathbf{C}). \quad (1.36)$$

1.2.2 Metal plasticity

When applying a stress to an elastic metal, it is observed that Hooke's law (1.15) does not apply when the stress is over a certain threshold, and that, when the stress is released again, there is permanent deformation⁸. Plastic flow has occurred. Indeed, the theory of

⁷Similarly, the *second Piola-Kirchoff* stress tensor, \mathbf{T} , can be defined as the force per unit undeformed area acting on the undeformed body, and is related to the first Piola-Kirchoff stress tensor via $\mathbf{T} = \mathbf{F}^{-1} \mathbf{S}$.

⁸For example, this is seen when a stress is applied to a paper-clip: when the stress is low, it will behave elastically; when the stress is over a certain limit, the metal will behave plastically.

metal plasticity dates back to 1864, when Tresca published an account of punching and extrusion. He first postulated that a metal would yield plastically when the maximum shear stress was greater than some specified value. It has since been developed and refined over the centuries, the most comprehensive theory being given by Hill [36].

The flow occurs as the result of *dislocations* moving through the metal. Mathematically, a dislocation is represented as a singular solution to Navier's equations, (1.19). The solution may be a line singularity, or a point singularity. Suppose we take a cylinder of radius $r = a$, and somehow pull a line $r = a, \theta = 0$ out radially by an atom, say, 'sticking' it in its final configuration. This introduces what is called an *edge dislocation*, shown in Fig. 1.4. Clearly, we have introduced a stress field by creating the dislocation, even though there is no applied traction once the material is 'stuck' back together.

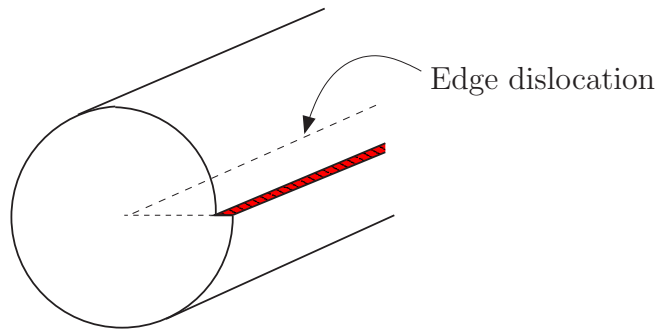


Figure 1.4: An edge dislocation in a cylinder.

If we look on an atomistic scale, we see that the lattice is no longer regular, but a discontinuity has been introduced in the atomistic spacing (Fig. 1.5). This can be observed experimentally, but only under an electron microscope as the lengthscale involved is 1nm. Further, applying stress to the lattice will cause the dislocation to propagate

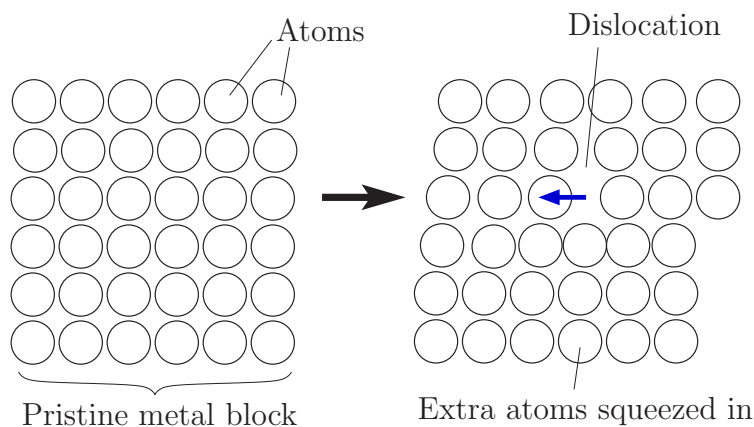


Figure 1.5: A diagram showing a pristine metal block and one with a dislocation introduced. The dislocation moves from right to left, the direction of the *Burgers vector*.

through the metal (as can be imagined by looking at Fig. 1.5). This is plastic flow. These

dislocations can often get ‘stuck’ at any material faults in the lattice, which goes some way to explain why plastic strain is irreversible.

An increasing amount of stress is often needed to maintain the movement of dislocations. This is because new dislocations are created during plastic flow (which requires energy). Further, the gradual agglomeration of dislocations getting ‘stuck’ in the material makes it increasingly harder for dislocations to move through the lattice. This concept is known as *work-hardening* (or strain-hardening), and leads to a stress-strain curve as in Fig. 1.6(a).

We need to make some further simplifications in order to write down tractable equations of plasticity and a ‘yield condition’. One such simplification we assume is based on another experimental observation, namely that the velocity field for the plastic flow is incompressible. As well as neglecting any thermal effects, we will also neglect any anisotropic loading/unloading effects such as the *Bauschinger effect*. This occurs as a result of the randomness of the crystalline grain-sizes and orientations in a metal; when a load is applied which causes plastic flow, the material can lean towards a favourable orientation for the metal’s crystal structure which, when the load is released and reapplied, results in the (now anisotropic) metal yielding at a much lower stress.

1.2.2.1 Yield

Armed with the aforementioned assumptions, we can now consider a *yield condition* for the plastic flow. This is some kind of law that defines the limit of elasticity under any applied stress. In order to interpret this condition geometrically, we introduce the three principal stresses σ_{11}, σ_{22} and σ_{33} . For an isotropic material, the yield condition only depends on the magnitude of these stresses. Using the principal directions as Cartesian coordinates, we see that the yield condition can be geometrically represented as a surface. This surface is known as the *yield surface*. For an isotropic material, the yield condition can be simplified by the key experimental observation that, to leading order, plastic yield is unaffected by any applied hydrostatic (isotropic) stress. This motivates splitting the stress tensor into a hydrostatic part, $p = \frac{1}{3}\sigma_{kk}$, and a *deviatoric* part, σ'_{ij} , defined by

$$\sigma_{ij} = -p\delta_{ij} + \sigma'_{ij}. \quad (1.37)$$

Note that the sum σ'_{kk} is automatically zero, and so, geometrically, the span of the three vectors $\{\sigma'_{11}\mathbf{e}_1, \sigma'_{22}\mathbf{e}_2, \sigma'_{33}\mathbf{e}_3\}$ represents a plane, where \mathbf{e}_j is the unit vector in the j -th principal direction. Since we have assumed that yield only depends on the hydrostatic part of the stress, adding any hydrostatic pressure p to the stress cannot affect the yield surface. Thus, the yield surface must be some kind of cylinder with axis $(1, 1, 1)$. By considering the projection of the cylinder onto the plane spanned by the deviatoric parts

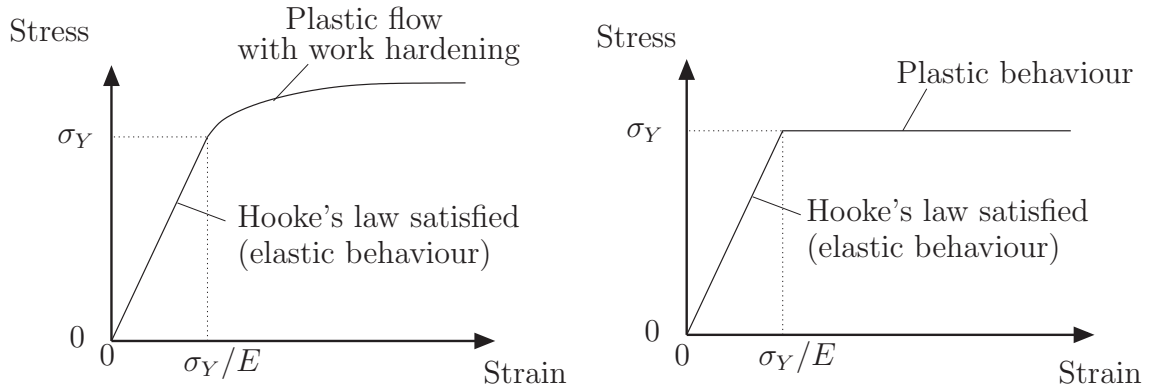
of the stress, one can consider further geometrical arguments involving symmetry of the principal parts of the stress to show that the cylinder must have six axes of symmetry [36]. This leads to two of the most famous yield conditions, namely those of *Tresca* and *Von-Mises*; the first assumes that the yield surface is hexagonal in cross-section, whereas Von-Mises' condition has a circular yield surface. In terms of the stresses, they are

$$\begin{aligned} \max(|\sigma'_{11} - \sigma'_{33}|, |\sigma'_{22} - \sigma'_{33}|, |\sigma'_{11} - \sigma'_{22}|) &= \sigma_Y \quad (\text{Tresca}), \\ \sigma'^2_{11} + \sigma'^2_{22} + \sigma'^2_{33} &= \frac{2}{3}\sigma_Y^2 \quad (\text{Von-Mises}), \end{aligned} \quad (1.38)$$

where the constant σ_Y is the *yield stress* of the material⁹. Tresca's condition is often preferred for analytical modelling as it is piecewise linear in the stresses and hence mathematically easier to manipulate algebraically. The Von-Mises condition is more common in numerical modelling as the relative sizes of the principal stresses do not need to be calculated at each stage.

1.2.2.2 Stress-strain relations and flow law

The assumption above of constant yield stress in (1.38) is termed *perfect plasticity*, with a stress-strain graph of Fig. 1.6(b). We need to relate the components of the stress tensor



(a) A stress-strain diagram for a material admitting plastic work-hardening.

(b) A stress-strain diagram for an elastic-perfectly-plastic material.

Figure 1.6: Stress-strain relations for an elastic-plastic material.

to those of the strain tensor whilst the material is plastic. Historically, many authors have put forward possible laws. The most physically realistic of these laws are the equations of *Reuss*. Reuss splits the total strain into an elastic part and a plastic part, where the elastic part is zero if there is no applied stress, and the plastic part represents permanent

⁹If we were to include work-hardening in this model, the right-hand side of the yield conditions would have an extra term $H(\epsilon)$. This function, initially zero, increases with the amount of plastic flow.

deformation. The plastic part of the strain is related to the deviatoric stress in perfect plasticity via

$$\sigma'_{ij} = \Lambda \dot{\varepsilon}_{ij}^{(p)}, \quad (1.39)$$

where $\Lambda > 0$ is a function of space and time, and $\dot{\varepsilon}_{ij}^{(p)} = \frac{1}{2}(\frac{\partial \dot{u}_i}{\partial x_j} + \frac{\partial \dot{u}_j}{\partial x_i})$ is the plastic part of the strain rate tensor. We note that Λ can be regarded as a Lagrange multiplier for the constraint that the material is at yield. This is seen using an Euler-Lagrange approach by minimizing the work-done by some state of stress, σ_{ij}^* , in the incremental plastic strain $d\varepsilon_{ij}$ (simply the product of the two) subject to the yield constraint. The flow law, since it is derived from the yield surface, is termed an *associative flow law*.

The Reuss flow-law assumes that the elastic strains in the material are non-trivial. In the case where $\dot{\varepsilon}_{ij}^{(p)} \gg \dot{\varepsilon}_{ij}^{(e)}$, the flow-law simplifies to the *Lévy-Mises* equations, which state that the deviatoric stress is related to the total strain rate via

$$\sigma'_{ij} = \Lambda \dot{\varepsilon}_{ij}. \quad (1.40)$$

These equations are easier to deal with mathematically, though are not applicable to all scenarios.

Other flow laws that we will not mention are given in [36]. The final constitutive law that we will give is the one used by the modern hydrocodes, namely the *Zerilli-Armstrong* law [105], which replaces Hooke's law and (1.39). It bases plastic slip on a thermally activated process, and can be written for a general body-centred-cubic metal as

$$\sigma = \sigma_0 + c_1 \exp(-c_2 T + c_3 T \log \dot{\varepsilon}) + c_4 \varepsilon^n + \frac{k}{\sqrt{l}}, \quad (1.41)$$

where σ_0 is some function of the initial inhomogeneity of the metal and the yield stress, T is temperature, l is an average grain diameter, k is some stress-intensity factor, and the constants c_i and n are properties of the particular metal.

1.2.2.3 Shear bands

Extreme plastic flow in a material can lead to *shear bands*. These are regions of very high strain in a material. They are thought to originate at small material defects or inhomogeneities (such as crack tips), and propagate in thin bands. The method behind their propagation is believed to be a result of a contest between two competing processes [100]. Firstly, we already know that the isothermal stress required to produce some strain increases with work hardening (Fig. 1.6(a)). However, plastic work causes the local temperature to increase, which in turn lowers the stress required to produce the same isothermal strain in the material. This process is known as *thermal softening*, and is a stronger effect than work hardening. Furthermore, it is unstable over a certain

threshold. Once this level of thermal softening is reached, any small instabilities (often caused by material defects) will grow, causing the plastic work and hence heat production to increase even more, which leads to further softening. This self-sustaining process, known as “localization”, results in a structure being formed. This is the shear band, an example of which is shown in Fig. 1.7. It is the instability and localization processes that

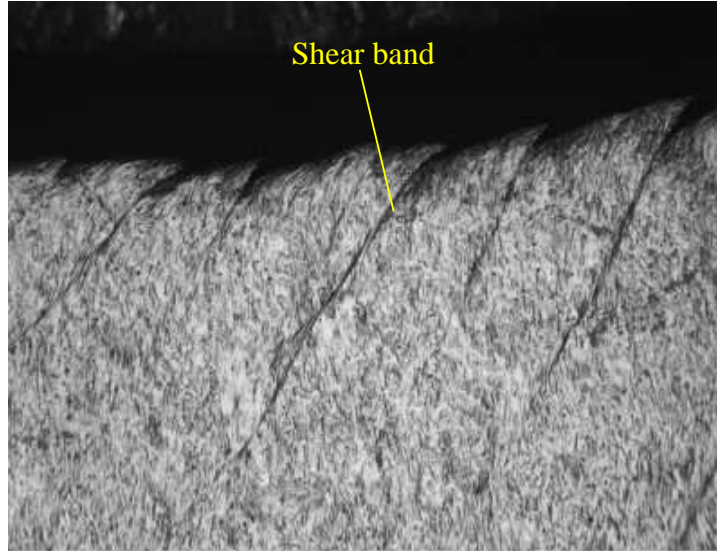


Figure 1.7: A picture illustrating typical shear bands on the internal surface of a collapsed cylindrical cavity in stainless steel. We would like to acknowledge Professor Nesterenko *et al.* [102] for kindly allowing us to publish this image.

account for the band being thin. The material surrounding the shear band then unloads because of the lower stress in the shear band, and all the shearing now occurs solely in the shear band. This shearing increases the local temperature in the band significantly, which, in turn, releases heat by conduction into the material either side of the band. The material on both sides of the shear band can now move as a rigid body (with respect to the band). Owing to the thinness, one can derive ‘boundary layer’ equations to model the shear band.

1.2.3 Asymptotics

Throughout this thesis, we will employ asymptotic techniques. This is a consequence of common occurrences of a small parameter, usually ε , in our equations. We give some common definitions. Formally, to define ‘order’ notation,

$$f(x) = \mathcal{O}(g(x)) \text{ as } x \rightarrow a \text{ if } \exists \text{ constants } K \text{ and } \delta \text{ such that} \\ 0 < |x - a| < \delta \Rightarrow |f(x)| \leq Kg(x). \quad (1.42)$$

Similarly,

$$f(x) = \mathcal{O}(g(x)) \text{ as } x \rightarrow a \text{ if } \frac{f(x)}{g(x)} \rightarrow 0 \text{ as } x \rightarrow a. \quad (1.43)$$

This enables us to define an *asymptotic expansion* for a function f . We will write

$$\begin{aligned} f(x; \varepsilon) &\sim \sum_{j=0}^{\infty} f_j(x) \phi_j(\varepsilon) \text{ as } \varepsilon \rightarrow 0 \\ &\text{if and only if} \\ \forall N, f(x; \varepsilon) - \sum_{j=0}^N f_j(x) \phi_j(\varepsilon) &= \mathcal{O}(\phi_{N+1}(\varepsilon)) \text{ as } \varepsilon \rightarrow 0. \end{aligned}$$

Usually, $\phi_n(\varepsilon) = \varepsilon^n$. We also note that the infinite sum $\sum_{j=0}^{\infty} f_j(x) \phi_j(\varepsilon)$ need not necessarily converge.

We also write down *matching conditions*, which are needed to match different asymptotic regions together. These are given by Van Dyke [92] and written as

$$(m\text{th term in inner})(n\text{th term in outer}) = (n\text{th term in outer})(m\text{th term in inner}),$$

or

$$“(mti)(nto)=(nto)(mti)” . \quad (1.44)$$

This rather cryptic condition is interpreted as follows. Take, for example, (1ti)(1to). This means “take the first term in the outer expansion, expand it in terms of the inner variables, and then take the first term of this”. The resulting expression must equal (1to)(1ti), with one of the expressions once more rewritten in terms of the other’s variables¹⁰.

1.2.4 Slender body theory

A *slender body* is an axisymmetric body with high aspect ratio¹¹, $r = \varepsilon f(z)$, say, where $0 < \varepsilon \ll 1$ [61]. The paradigm example of slender body theory in action is to consider a lightning conductor. Suppose it is described by $r = \varepsilon R(z)$, with $0 < \varepsilon \ll 1$, for $0 < z < 1$. Clearly, there are two lengthscales in the problem. If we are very close to the lightning conductor and sufficiently far from the endpoints, the body will appear to be infinitely long with a finite radius. Far away from the body, the body will appear infinitely thin, but now with finite length. From Maxwell’s equations, the field equation is simply

$$\nabla^2 \phi = 0, \quad (1.45)$$

for some potential, ϕ . The boundary conditions we impose are zero potential on $r = \varepsilon R(z)$ and a uniform field at infinity, so $\phi = Ez$ at infinity, where E is some constant. This is shown in Fig. 1.8.

¹⁰Expansions involving $\log \varepsilon$ have to be treated in a slightly different manner [38, 92].

¹¹The two-dimensional analogue of a slender body is termed a *thin body*, $y = \varepsilon f(x)$.

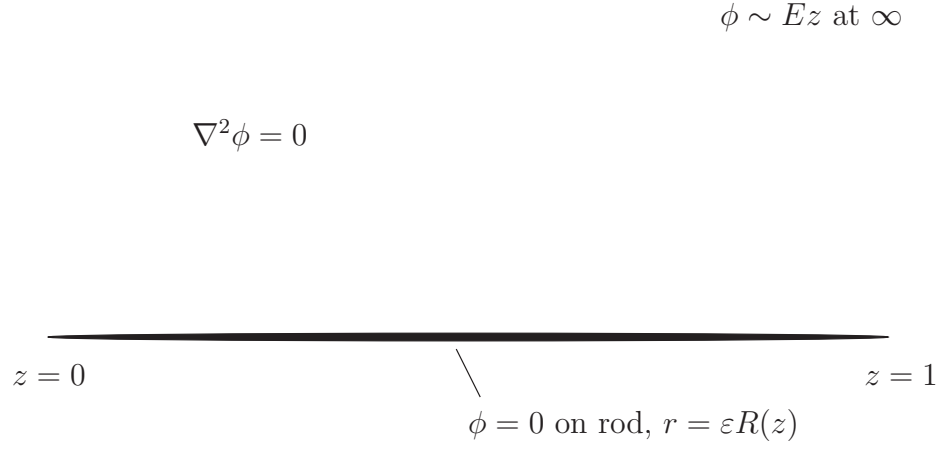


Figure 1.8: Slender body theory applied to a lightning conductor.

The key observation at this stage is that the problem is a fully three-dimensional one. Via potential theory, we can express the outer solution in terms of a Green's function for Laplace's equation, hence

$$\phi(r, z) = \int_0^1 \frac{Q(z')}{\sqrt{r^2 + (z - z')^2}} dz' + Ez, \quad (1.46)$$

where the unknown function $Q(z)$, which represents a series of point charges distributed along the rod, will be determined by imposing $\phi = 0$ on the rod.

Near the rod, $r \ll 1$ and so we rescale $r = \varepsilon r'$. This gives us an inner scaling. Expanding the outer solution for such r' gives

$$\int_0^1 \frac{Q(z')}{\sqrt{r^2 + (z - z')^2}} dz' \sim Q(z) \int_0^1 \frac{dz'}{\sqrt{\varepsilon^2 r'^2 + (z - z')^2}}, \quad (1.47)$$

as the dominant contribution to the integral is when $z - z' \ll 1$. Thus we find that [38], for some K ,

$$\phi(r, z) \sim Q(z) K \log(\varepsilon r') + Ez. \quad (1.48)$$

Applying $\phi = 0$ on $r' = R$ in the inner solution and matching this with (1.48) determines the strength of the point charges, $Q(z)$. More importantly, however, note that $\phi(r) =$

A $\log r$ is the two-dimensional solution to Laplace's equation, so by using slender body theory, we have reduced the dimensionality of the problem in the slender region by turning our axisymmetric body into a two-dimensional problem.

1.3 Thesis outline

Chapter 2 contains a conspectus of the shaped-charge literature. We start by discussing classical hydrodynamic models for penetration, paying special attention to the Birkhoff fluid-fluid impact. We briefly mention particulation and axisymmetric modelling, before discussing penetration with water jets. We then present existing models from solid mechanics and comment on the literature on plastic instabilities. After a brief outline of numerical formulations, we set out our aims for the thesis.

The classical Birkhoff jet-penetration model described in Chapter 2 motivates an elastic-plastic equivalent. In Chapter 3, we write down equations for such a model, with extra experimental evidence being an additional signpost for this route. Having set the scene for an axisymmetric elastic-plastic model, we give estimates for the different parameters involved, before subdividing the model into three different regions. Firstly, equations for an inviscid, irrotational fluid are considered in the jet region, with suitable boundary conditions. Moving out from the jet, we write down equations for plastic flow, briefly discussing supersonic versus subsonic plasticity and flow laws along with inertial effects. Finally, we consider the fully-inertial Navier equations in the elastic region. The chapter concludes with a discussion of different scalings, some based on geometrical ideas.

Chapter 4 contains the innards of the elastic-plastic model described in the previous chapter. We begin by nondimensionalising the governing equations, discussing two possible plastic velocity scales. We then exploit the slenderness of the system in developing a slender-body model, thus reducing its dimensionality. These equations are matched to the outer elastic solution, the latter obtained via the Love stress function. We attempt a travelling-wave formulation, before considering inertial effects and drawing conclusions about elastic-plastic modelling.

In Chapter 5, we draw analogies with the classic elastic-plastic expansion of a cylinder under internal pressure. By analysing this in more detail and considering literature on autofrettage (a process used to strengthen gun-barrels), we derive expressions for residual displacements and residual stresses based on linear elasticity with different pressure regimes. We move on to consider the problem with nonlinear elasticity and discuss the relevance to the cavity size in shaped-charge penetration, proposing a simple model in which the jet is treated as a known pressure-pulse. We close the chapter by considering non-radially-symmetric perturbations to the earlier solution in order to analyse the plastic

flow and resultant residual stresses.

We start Chapter 6 by writing down an elastic-plastic model for the tip, motivated by the gun-barrel analysis of Chapter 5. We move on to consider a plastic squeeze film as a simple analogy for the mechanism for removing target material around the tip. In doing so, we visualise the plastic flow and investigate the possibility of termination of the plastic region. We conclude this chapter with a brief discussion on plastic mass conservation.

Chapter 7 is devoted to paradigm tip models for the jet. These models are based on “filling-flows”. We begin with simplistic two-dimensional models to gain intuition into more representative models, which we write down by considering the fluid-plastic free-boundary as a membrane, beam, and then by using a general law between pressure and height. Using techniques in matched-asymptotics and scaling ideas motivated by earlier chapters, we can find travelling-wave solutions and similarity solutions to these models, giving us indications of the large-time behaviour. We conclude this chapter by writing down axisymmetric models; we motivate our final model by residual-displacement arguments from Chapter 5 and comment as to the solubility of all these models.

Chapter 8 is concerned with experimental and numerical results. We begin by discussing properties of the microstructure known via existing experimentation. We then present results of our own tests on a steel block penetrated by a silver jet, including a discussion of detailed microscopic pictures of the microstructure and hardness test results. We conclude the chapter with numerical results from *QinetiQ*’s hydrocode.

Finally, we close the thesis in Chapter 9. Here, we recapitulate the key points brought up in the previous chapters and list future work.

1.4 Statement of originality

The material in Chapter 2 is a review of existing literature and hence not original.

The following two chapters build on and improve the preliminary quasistatic model of Watkin [96]. This leads to a novel free-boundary problem and two possible plastic velocity scales. We match the inner and outer solutions and attempt a travelling-wave formulation as well as discussing the equivalent inertial problem. This is original work.

The bulk of Chapter 5 is original material. There exists some literature on residual stresses, although originality is claimed for the time-dependent modification and for consideration and clarification of the effect of cyclic loading-unloading on recoverable and non-recoverable parts of the stress tensor. Application of the ideas of residual stresses and displacements is novel for shaped-charge modelling. We also claim originality for the non-radially-symmetric perturbation to the simple cavity-expansion problem.

The elastic-plastic model for penetration in Chapter 6 is original work. Apart from

the outline of the viscous squeeze film and the work on the basic plastic squeeze film, the remainder of Chapter 6 is original (although there are some similarities with cold-rolling of metals).

The work we present in Chapter 7 builds upon Peregrine's filling-flow models [67, 68], and touches on classic similarity solutions of the shallow-water equations. The remainder of models in the Chapter are novel.

Finally, similar metallurgy analysis to that of Chapter 8 has been done before, although with differing results.

Chapter 2

Shaped-charge literature

The literature on the varied aspects of shaped-charge penetration is vast. We have already touched on the jet formation stage and some of its applications without going into detail such as, for example, liner geometry and composition. Much of this is at least outlined and referenced in the book by Walters and Zukas [95].

In this chapter, we give an account of existing ideas on the penetration of the target, discussing the classical hydrodynamic models before investigating more physical models based on solid mechanics. We also mention numerical “hydrocodes”, before motivating new models. A relatively recent detailed account on the penetration literature is given by Hebdon [32]. Metallurgical observations will be presented in a later chapter.

2.1 Hydrodynamic models

Early experiments on shaped-charge penetration indicated that the strength of the target did not play a major role in the depth of penetration. Hence, the first models that were developed neglected the strength of the target, treating both the jet and the target as fluids.

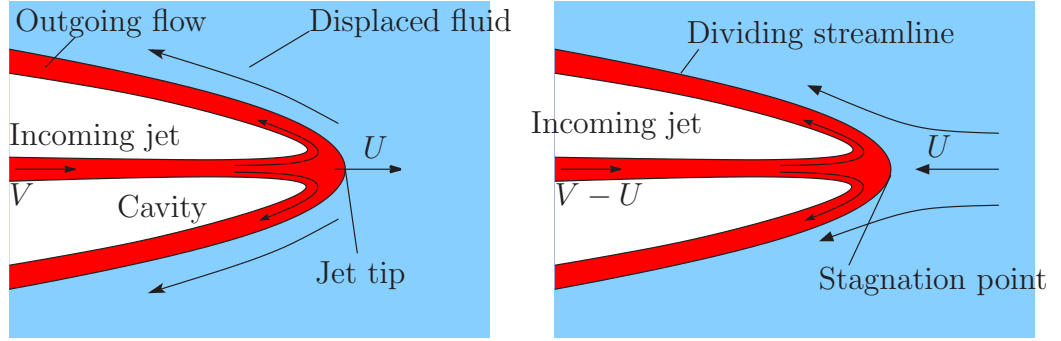
2.1.1 Birkhoff jet impact

The simplest inviscid model for penetration by an incompressible, continuous fluid jet of density ρ_j into a similar fluid of density ρ_t was developed by Birkhoff *et al.* [7, 11]¹. We briefly outline their model, which uses ideas from Helmholtz streamline theory.

Consider a jet of length L , density ρ_j and velocity V in two dimensions. When this fluid impacts a stationary fluid with density ρ_t , say, it displaces the stationary fluid, turning back on itself and thus creating a cavity whose boundary is a free-surface. The two fluids

¹Mott *et al.* [65] also discussed penetration by ‘Munroe’ jets at a similar time to Birkhoff.

are separated by a dividing streamline. We suppose that the velocity of penetration is U (Fig. 2.1(a)) and that the effects of gravity are negligible. With respect to a rest frame, the motion is unsteady. By changing to a frame moving with the penetration as shown in Fig. 2.1(b), we can write down a steady Bernoulli condition for both the jet and the target. Writing velocities as u , pressures as p and using the obvious subscripts for ‘jet’ and ‘target’ fluids, the conditions are:



(a) A liquid jet of velocity V impacting liquid at rest, penetrating with velocity U .

(b) Hydrodynamic penetration in a frame of reference moving with the stagnation point.

Figure 2.1: Hydrodynamic penetration.

$$\frac{p_j}{\rho_j} + \frac{1}{2}|u_j|^2 = \frac{1}{2}(V - U)^2, \quad (2.1)$$

$$\frac{p_t}{\rho_t} + \frac{1}{2}|u_t|^2 = \frac{1}{2}U^2, \quad (2.2)$$

where the Bernoulli constants have been calculated using zero flow (in the rest frame) at infinity and $p = 0$ on the free-surface. The pressures at the stagnation point must be equal, hence we obtain the penetration velocity U in terms of V and the densities as

$$U = \frac{V}{\left(1 + \sqrt{\frac{\rho_t}{\rho_j}}\right)}. \quad (2.3)$$

The depth of penetration is approximated by UT , where T is a typical timescale. We calculate this by arguing that the timescale over which the jet gets ‘used up’ is $L/(V - U)$, and so the penetration depth, d , is given by

$$d = L\sqrt{\frac{\rho_j}{\rho_t}}. \quad (2.4)$$

The shape of the free-streamline (and dividing streamline) can also be calculated in two dimensions using complex variable techniques [11, 51, 99]. To do this, four planes

are considered. Firstly, the complex potential plane Ω , where $\Omega = \phi + i\psi$. Here ϕ is the velocity potential and ψ is the stream function for the fluid. Hence streamlines are represented as the level sets of ψ in this plane. We also consider the Q -plane, where $Q = \log\left(\frac{dz}{d\Omega}\right)$. Writing the velocity as $u - iv = qe^{i\theta}$, we observe that the direction of flow is represented by the imaginary component in this plane. The fluid is now represented by an open-ended rectangle, which is mapped to the upper-half plane via a map $\xi = \cosh Q = \frac{1}{2}\left(\frac{d\Omega}{dz} + \frac{dz}{d\Omega}\right)$. Finally, a Schwarz-Christoffel map allows us to map this to the Ω -plane, allowing us to derive an expression for the velocity potential. By doing this analysis, the behaviour of the free-boundary is given via the relationship

$$x = 2 \log\left(\frac{y}{4} + 1\right) - \left(\frac{y}{4} + 1\right)^2. \quad (2.5)$$

For large x , this relationship shows that the boundary exhibits square-root behaviour, $y \sim \pm 4h\sqrt{-x}$, where h is the width of the incoming jet².

This simplified model for fluid-fluid penetration predicts the profile of the cavity, but has a solution that is unbounded for large negative x . This unphysical solution is not observed experimentally. An alternative model which takes the confinement of the cavity into consideration was derived by Hopkins *et al.* [40]. They depart from the Helmholtz theory by permitting the free-streamline to have non-constant velocity in the part of the flow that has just reversed direction. Hence, Bernoulli's equation does not hold in this region where the fluid slows down, a result of turbulence and viscous effects. The conformal mapping techniques now lead to a finite crater width for large negative x , given by

$$y \sim \pm h \left(\frac{2V\sqrt{\rho_j}\pi}{V\sqrt{\rho_j} - U\sqrt{\rho_t}} \right). \quad (2.6)$$

2.1.1.1 Penetration with particulated jets

Fluid jets can become particulated as the result of a classic Rayleigh instability [72]. Birkhoff *et al.* have developed similar models for analysing such jets [6]. The key difference is that each fluid particle is modelled as a solid particle with velocity V . Hence, the average pressure exerted by a particle on the fluid target is

$$p_j = \rho_j(V - U)^2. \quad (2.7)$$

Writing the equations in a frame moving with the penetration, the motion is locally steady and so Bernoulli's equation holds once more in the target. Thus, at the stagnation point, the velocities and pressures of the particles and target are in balance, yielding

$$\rho_j(V - U)^2 = \frac{1}{2}\rho_t U^2. \quad (2.8)$$

²Analysis of this kind arises frequently in "slamming" problems [63].

This results in a penetration velocity of

$$U = \frac{V}{\left(1 + \sqrt{\frac{\rho_t}{2\rho_j}}\right)}, \quad (2.9)$$

with depth of cavity given by

$$d = L\sqrt{\frac{2\rho_j}{\rho_t}}. \quad (2.10)$$

Comparing this with (2.4), a penetration depth of

$$d = L\sqrt{\frac{\lambda\rho_j}{\rho_t}}. \quad (2.11)$$

for $1 < \lambda < 2$ is proposed by Birkhoff *et al.* for intermediate phase jets.

2.1.1.2 Axisymmetric models

The Bernoulli analysis for the two-dimensional case trivially applies also to a continuous, incompressible, axisymmetric jet. The complex variable techniques previously used to establish the shape of the cavity sadly cannot be used. A good alternative is to use slender-body theory, outlined in §1.2.4. By considering a far-field solution as in Hebdon [32], one can derive a solution for the velocity potential and hence asymptotically show that the cavity shape for large negative z is

$$r \sim A\sqrt{-z}, \quad (2.12)$$

where A is some positive constant.

Watkin [96] discusses a similar formulation in which a solution for the velocity potential ϕ is given in terms of the Green's function for Laplace's equation, namely

$$\phi(r, z) = \int_{-\infty}^0 \frac{\varepsilon^2 R(\xi) R'(\xi)}{\sqrt{(z - \xi)^2 + r^2}} d\xi, \quad (2.13)$$

where $R(\xi)$ is the position of the outer free-boundary and $0 < \varepsilon \ll 1$ is the ratio of a typical radial lengthscale to a typical axial one. He then obtains an integro-differential equation for $R(z)$ which has to be solved numerically.

2.1.2 Water jets

The traditional method of mining rock is to break it up using a high-speed drill. A real danger in this process is that frictional heating can ignite methane and other flammable gases that were once trapped in the rock. This has motivated investigations into drilling with high-speed water jets.

The simplest form of a water jet is a continuous, high-speed, high-pressure jet. The jet impacts a designated target surface, excavating a hole. An experimental account of continuous water-jet penetration is described by various authors [10, 46]. Leach and Walker consider a high-speed jet with velocity 1km s^{-1} and pressure of up to 500MPa as well as a slower jet, with velocity 340m s^{-1} and pressure 60MPa . A jet with diameter 1mm and total volume 10cm^3 moving at the higher velocity produces a hole in sandstone which is 20mm deep and, irrespective of the depth of penetration, 5mm in diameter. Even faster jets with velocities of up to 9.5km s^{-1} can be produced by using a shaped charge with a water gel as the liner [97].

This penetration can be improved by adding abrasive particles such as grit or silicon carbide into the stream of the water jet. Hashish [31] reviews possible theories involving erosion mechanisms and deformation theories for penetration. The key idea is from Bitter [8], who considers impact via elastic-plastic deformation and introduces the “wear volume” (equivalent to our cavity volume). This is given by the ratio of plastic energy dissipation to energy required to remove unit volume. The effectiveness of this technique is discussed by Swanson *et al.* [81], who note that the mixing of the abrasive particles and the water jet is inefficient as it is difficult to get the particles near to the centre of the water jet.

A more interesting and relevant aspect of water jet penetration is the effect of *percussive jets*. This is similar to a particulated shaped-charge jet in that the separate particles impact the target, but crucially differs because it is beneficial for water jet penetration, and usually more efficient by up to an order of magnitude. These jets work by impacting the rock in a sequence of high-frequency, short duration bursts. The key feature of the jets is that they are produced by perturbing the discharge rate between just above and just below some average flow rate. Hence, some portions of the jet move faster than others, resulting in “bunching” of the jet and so the jet separates into discrete particles [55]. The main benefits of this technique over a pulsed, intermittent jet is that percussive jets are a lot easier to produce and do not suffer from ‘water hammer’ effects (*i.e.* pressure waves in the jet that result from stopping (and then restarting) the flow). Further, owing to the bunching effect, the momentum from the percussive jet is transferred to the target as a series of force peaks (and troughs); an intermittent jet would only produce a series of equal lower-force impacts. There are also advantages of percussive jets over continuous jets. Firstly, a percussive jet has a far higher ratio of impact area to volume of impacting water. This is found to be very beneficial for excavation by liquids. Also, it is observed experimentally that, for a continuous jet, it is the initial impact that has the greatest net effect on target penetration. This observation is clearly exploited by percussive jets. Finally, the cyclic loading/unloading promotes brittle fracture in the target.

An analytical model for the bunching of the jet is discussed by Sami and Ansari [77].

They develop a model using the axisymmetric, unsteady Navier-Stokes equations for a slender jet, allowing for surface tension effects. The modulation of the jet is modelled via the boundary condition

$$u(0, t) = U + (\delta U) \sin \lambda t, \quad (2.14)$$

where the jet is emitted at $z = 0$, λ is a constant (representing the frequency of the modulation), U is the constant flow velocity and δU is a small perturbation to the fluid velocity. They discuss three possible models for the jet radius as a function of position and time, with the following three separate frameworks:

- inertia effects \gg surface tension effects,
- jet radius $r \sim r_0 + \varepsilon r_1 + \mathcal{O}(\varepsilon^2)$,
- a Lagrangian model, where the velocity u of a particle is $u = U + \varepsilon u_1 + \mathcal{O}(\varepsilon^2)$.

These models give estimates for the jet radius, thus describing the bunching of the jet (which will eventually lead to jet break-up). They conclude that, although they have good analytical approximations, it is likely that drag (so far neglected) plays an important role in the break-up mechanism of the jet. This is confirmed by experimental observations, in which flat fluid discs are seen to deform as they move forward rapidly.

Eddingfield *et al.* [23] discuss models for turbulent *submerged* water jets (that is, a fluid penetrating inside a similar fluid). These models can be solved numerically by assuming a lengthscale over which turbulent viscous mixing occurs. They move on to discuss a multi-phase model for a water jet moving through air. The three separate phases are the core of the jet itself, the surrounding air flow, and droplet flow (from the jet) in the air, taking into account the drag.

2.2 Models from solid mechanics

The hydrodynamic model based on Bernoulli's equation gives a good estimate for penetration depth. However, it is not a true representation of the underlying physical processes and hence, at the cost of losing this extreme simplicity, many authors have considered models to take account of the solid mechanics. Although much of this literature is reviewed by Hebdon [32], we must outline some models.

2.2.1 Models of penetration

A full elastic-plastic model of penetration is extremely complex. Hence, the first models for penetration make the simplification of dividing the model into two processes, namely

an axial penetration and a radial crater expansion part [95]. These models perform well for high-velocity penetration where the inertia of the jet is much greater than the yield stress of the target, but can have marked differences with low-velocity (rod) penetration and particulated penetration.

One such model is developed by Szendrei [84, 85]. Among other authors, he borrows ideas from traditional fluid models by using a modified Bernoulli equation from classical high-velocity erosion literature. This is written as

$$\frac{1}{2}\rho_j(V - U)^2 + Y = \frac{1}{2}\rho_t U^2 + R, \quad (2.15)$$

where Y and R are empirical constants for the jet and target, respectively. These target strengths come into the penetration depth via a parameter K . Szendrei assumes a lower penetration velocity and models the jet as a rod. This is motivated by the fact that the jet slows down significantly after its ‘steady-state phase’ of penetration. Assuming cylindrical expansion, an expression similar to equation (2.4) is derived. The parameter K is also used to estimate the energy needed to create unit volume of crater, thus allowing an estimate of the stress field of the target to be given in terms of the material constants. The main flaw in this approach, apart from assuming cylindrical expansion and neglecting shear effects, is that the empirical strength constants Y and R are not related to the yield strength of the jet or target, and hence can’t be fully representative of the penetration.

Tate [86, 87] developed an elastic-plastic model for penetration. He assumes that the plastic flow field follows the magnetic field of a solenoid, motivated by ideas from Milne-Thomson [51]. He assumes the Levy-Mises flow law, incompressible plasticity and that temperature effects are negligible, ultimately leading to an expression for the rate of crater expansion in terms of the pressure from the jet.

Barnea and Sela [4] derive an elastic/plastic radial crater-expansion model with inertia. The Von-Mises yield condition is used in conjunction with an associated flow law to model the plasticity, assumed to be incompressible. They also assume that the penetration occurs with constant velocity U , and allow the possibility of nonzero shear stress. After changing to a frame moving with the penetration, they integrate the momentum equation across the plastic region, considering the target as a series of two-dimensional slices. They impose zero normal stress on the free-boundary $a(t)$ separating the cavity from the plastic region of the target, and eventually end up with a third-order ordinary differential equation for the $a(t)$. They also consider the large- U limit, obtaining an analytical estimate for the crater radius in terms of $a(0)$, $\dot{a}(0)$, the density of the target and its yield stress. A “cut-off velocity” (*i.e.* velocity below which no crater expansion occurs) is also estimated for large U . This is found to agree with the Szendrei estimate. The problem with their model, however, is that they are unable to provide any initial conditions for the crater position

or velocity, thus not reconciling the analysis with any of the tip mechanics. Furthermore, their model is a crater-expansion model, essentially considering radial cavity-expansion for penetration as a travelling-wave.

A recent study by Watkin [96] also develops an elastic-plastic model, assuming incompressibility and a perfect-plastic flow law. This model exploits the slenderness of the cavity and considers a local analysis of the flow sufficiently far from the tip. To simplify the equations, the jet is modelled as a constant pressure P . This results in an equation whose solution has the form of a travelling-wave. The equation contains undetermined parameters, which probably come from the tip or matching with the bulk elastic material.

2.2.2 Plastic instability and jet particulation

Particulation of a shaped-charge jet is detrimental to the overall depth of penetration, and so the nature of instabilities in such a jet has warranted study by many authors.

Robinson and Swegle [82, 83] discuss discrepancies between analytical and numerical models for a general elastic-plastic solid that is accelerated by surface tractions. They make a direct comparison with the classical Rayleigh-Taylor instability. A key difference is that wave propagation and the accelerating forces mean that the stress field is a now function of both the spatial variable and time. The authors use a Lagrangian numerical scheme and impose a small sinusoidal perturbation to the elastic-plastic boundary. They find that an important factor in the instability of the perturbation is the local stress gradient and comment that, for analytical modelling, both the elastic and plastic parts of the solid are important to determine when perturbations may become unstable.

Romero [74, 75] finds that the stability of a plastic sheet depends on a parameter Γ , defined by the ratio of inertial forces to plastic forces: if Γ is large, the sheet is stable. However, as the plastic sheet stretches, Γ decreases. His results are inconclusive for a more exact criterion of stability.

Particulation of the jet is considered by Yarin [103]. He develops the equations for a stretching jet in Lagrangian coordinates, firstly for a perfect-plastic jet, then using an elasto-viscoplastic model. He shows that the perfect-plastic regime is unstable, and ill-posed for short-wavelength perturbations. This occurs as the equation for small perturbations is an elliptic initial value problem (*c.f.* Laplace's equation). Conversely, the elasto-viscoplastic problem is well-posed. In the long-wavelength limit, the solution is in agreement with the perfect-plasticity model. The short-wavelength perturbations are now regularized by the elasticity. These perturbations are analysed using multiple-scales techniques. The conclusion is that there is a fastest growing disturbance at some intermediate wavelength owing to a trade-off between the destabilizing stress-dependent plasticity and the stabilizing effect of the elasticity of the metal.

A model for the necking of a rod is considered by Jeanclaude and Fressengeas [42]. They use a Lagrangian nonlinear visco-plastic formulation for the rod, and subject it to a linear perturbation. They conclude that the stabilizing mechanisms are inertial and visco-plastic effects, which compete against the geometrical effect of the necking of the rod; inertia slows down large-wavelength perturbations, whereas small-wavelength perturbations are damped by two-dimensional viscous effects. Hence, the most unstable wavelength varies with time.

Cowan and Bourne [19] use a Zerilli-Armstrong equation of state (1.41). They obtain their initial conditions from numerical codes (“hydrocodes”), and use a model based on minimizing the radius of curvature of the necked parts of an unstable jet. They discuss the “plastic particle velocity”, which is the average velocity between separate broken particles. They find that their predicted value for the plastic particle is in extremely good agreement with the mean experimental value. The experimental data, however, exhibits a significant amount of scatter, indicating that a stochastic model might be used. Indeed, Cowan [18] goes on to develop such a model. He uses a Monte Carlo process to simulate the random effects associated with jet break-up. From experimental data, he observes that the mean jet particle wavelength is 1.0, and notes the spread. Using this, he fits the experimental data to a normal distribution and samples using a Monte Carlo method. He finds good agreement between experimental data for plastic particle velocity and jet particle length with the results of the Monte Carlo simulation. He concludes that the random effects are caused by small manufacturing defects in the liner, inhomogeneity of the explosive and the non-trivial interaction of the deformation wave with the surface of the liner.

2.2.3 Numerical models

Numerical codes have been developed over the years to represent the penetration process. The aim of the code is to accurately represent the physical aspects of penetration whilst minimizing computational time. Models using both a Lagrangian framework (*e.g.* “DYNA”) and Eulerian formulation (*e.g.* “GRIM”) have been considered by various organisations. These codes are known as *hydrocodes*. The “GRIM” hydrocode was designed and is used extensively by *QinetiQ*. The code is based on equations for conservation of mass, momentum and energy. A general constitutive law to relate the stress to the strain needs to be specified by the user. The Zerilli-Armstrong law (1.41) is usually chosen. Often, the initial parameters immediately before impact are provided for “GRIM” by *QinetiQ*’s “JET-SUITE” [3, 14, 20, 41], an analytical jet-formation code. A Lax-Wendroff predictor-corrector scheme is then used by GRIM to solve the coupled nonlinear equations.

2.3 Aims of thesis

Our aim is to develop an elastic-plastic model that will model the physics of penetration. We endeavour to improve the introductory model by Watkin [96] and perform a tip analysis to resolve problems of initial conditions suffered by Barnea and Sela [4]. In doing so, we hope to describe an accurate method of penetration and expansion of the cavity that reflects the true nature of the intrinsic physical processes involved. Ultimately, we wish to predict the final crater geometry.

Although the hydrocode models produce very good results in most scenarios, analytical modelling is needed both to provide a check on the hydrocodes and so that more accurate numerical models can be developed in the future. Further, it is observed that the Eulerian hydrocodes are good at modelling all aspects of the penetration process, but are often very slow for large stand-off jets [41] and for fracture-dominated penetration [94]. An analytical model has the great advantage over the hydrocodes of its inherently quick evaluation time.

Despite the fact that two-dimensional models can be attacked with elegant complex variable methods, we will predominantly develop axisymmetric models. This is because the penetration is observed to be a primarily axisymmetric process (neglecting jet drift).

Chapter 3

An axisymmetric elastic-plastic model for penetration

3.1 Philosophy of the model

The classic hydrodynamic Birkhoff-type models (§2.1.1) provide a good first approximate solution for the penetration by virtue of Bernoulli's equation. They do not, however, model the true underlying physics of penetration. The fact that the radial and hoop stresses in the jet are up to two orders of magnitude greater than the yield stress of the target [4, 22, 86, 93, 95] strongly suggests that we should be modelling the target as an elastic-plastic material. Hence, we develop the obvious extension of the Birkhoff hydrodynamic model, namely to consider a jet impacting an elastic-plastic material.

By examining penetrated blocks of rolled-homogenous armour (RHA), we observe an almost perfectly-cylindrical cavity (Fig. 3.1). This motivates us to consider axisymmetric penetration. The model divides naturally into three different regions. The first region is the incoming *jet*, moving with velocity $V(t)$. The jet will impinge on the target and turn back on itself as in the hydrodynamic models, thus creating a cavity. The extremely high pressure in the jet impacting on the target leads to a *plastic* region in the target, and hence plastic flow. This is a possible mechanism to excavate the target material. Thirdly, when the stresses in the plastic region are not great enough to satisfy the yield condition, the material must revert to its *elastic* form again. These three regions are divided by free-boundaries, shown in Fig. 3.2. In drawing this figure, we have implicitly assumed that the plastic region extends far back from the tip of the jet. It is not obvious as to whether this is the case, or whether the plastic region terminates for some z nearer the tip. We will consider this when we analyse each of these regions individually, before simplifying the model further with a second trichotomy. We will eventually write nondimensional equations in a frame moving with the velocity of the stagnation point, $U(t)$. Since this

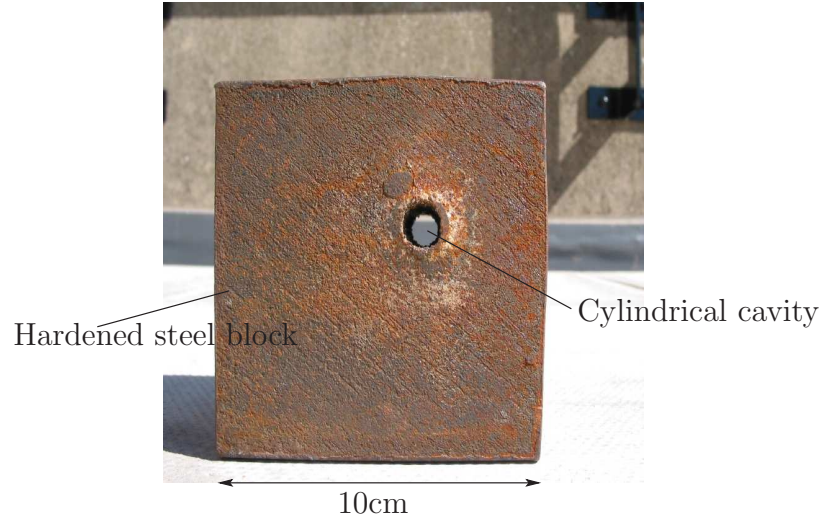


Figure 3.1: A hardened steel block, penetrated by a silver shaped charge jet. The block has depth 80mm.

frame is not inertial, we initially write all equations in a fixed frame of reference.

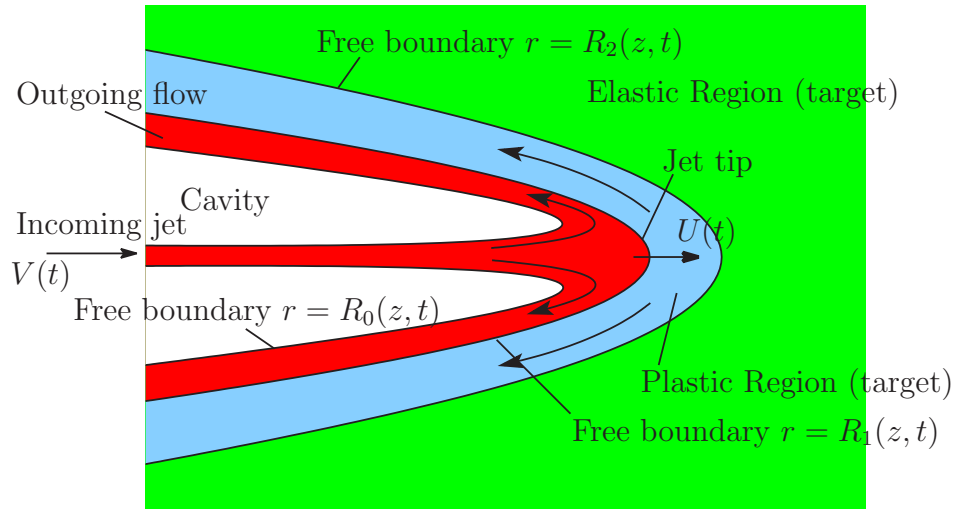


Figure 3.2: Axisymmetric elastic-plastic penetration of a shaped charge.

Concerning nomenclature, we will always write fluid velocities as the ordered triple $\mathbf{q} = (q_r, q_\theta, q_z)$, corresponding to the components in the (r, θ, z) directions respectively. The vector $\mathbf{u} = (u, v, w)$ will be reserved for displacements, with associated velocities $\dot{\mathbf{u}} = (\dot{u}, \dot{v}, \dot{w})$. In the following two chapters when in the moving frame, we will take the origin to be at the stagnation point, with the incoming jet coaxial with the negative z -axis. Further, when using colour in diagrams, we shall endeavour to consistently associate **green** with **elastic** behaviour, **red** with **jet** behaviour and **blue** with **plastic** behaviour (unless stated otherwise).

3.1.1 Parameter estimates

Before writing down the equations for the different regions, we present some typical values of the material parameters. We will consider a copper jet impacting a roll-hardened steel target, using data from [4, 15, 22, 93, 95]. We also give some *a posteriori* experimental estimates. The orders of magnitude for the dimensions are reinforced by looking at *QinetiQ* hydrocode runs (Fig. 3.3). Most, if not all of these parameters will be needed to nondimensionalise the model and are shown in Table 3.1.

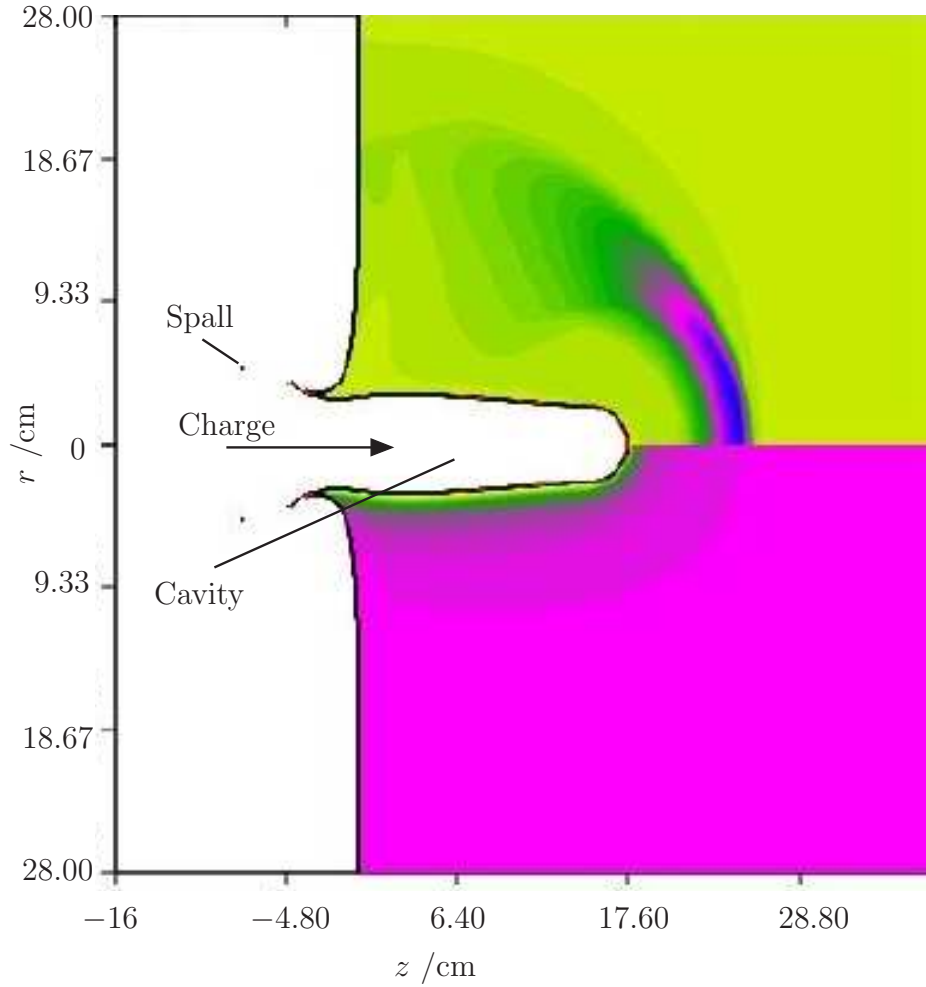


Figure 3.3: Output from a typical hydrocode run after penetration with a short jet has finished, showing some relative dimensions of the cavity depth and radius. The colouring represents σ_{rr} (top) and plastic strain rate (bottom); this will be discussed in detail later.

3.2 The jet

In writing down an analytical model for the jet, we need to make some sensible assumptions about it. The simplest approach is to model it as an inviscid, irrotational,

Quantity	Value
Incoming jet velocity	$2.5\text{km s}^{-1} \leq V(t) \leq 10\text{km s}^{-1}$
Typical penetration velocity	$U_0 \leq 5\text{km s}^{-1}$
Jet radius	$r_j \sim 3\text{mm}$
Density of copper jet	$\rho_j = 8920\text{kg m}^{-3}$
Reynolds number of copper jet	$\mathcal{R} \sim 10^4$
Yield stress of target	$10^7 \text{ (concrete)} \leq \sigma_Y \leq 2 \times 10^9\text{kg m}^{-1}\text{s}^{-2} \text{ (steel)}$
Shear modulus of the target	$\mu \sim 6.41 \times 10^{10}\text{kg m}^{-1}\text{s}^{-2}$
Bulk Modulus	$K \sim 1.4 \times 10^{11}\text{kg m}^{-1}\text{s}^{-2}$
Other Lamé constant for target	$\lambda = K - \frac{2}{3}\mu \sim 1 \times 10^{11}\text{kg m}^{-1}\text{s}^{-2}$
Density of the target	$7.86 \times 10^3\text{kg m}^{-3} \leq \rho_t \leq 9 \times 10^3\text{kg m}^{-3}$
Typical penetration depth	$L \sim 0.3 - 1\text{m}$
Typical final crater radius	$r_f \sim 7.5 - 15\text{mm}$
Elastic shear wave speed	$c_s = \sqrt{\frac{\mu}{\rho}} \sim 3\text{km s}^{-1}$
Elastic primary (transverse) wave speed	$c_p = \sqrt{\frac{\lambda+2\mu}{\rho}} \sim 5\text{km s}^{-1}$
Young's Modulus for target material	$E = \frac{\mu(3\lambda+2\mu)}{\lambda+\mu} \sim 2 \times 10^{11}\text{kg m}^{-1}\text{s}^{-2}$
Poisson's Ratio for target material	$\nu = \frac{\lambda}{2(\lambda+\mu)} \sim \frac{1}{3}$
Typical penetration timescale	$\tau \sim 10^{-4}\text{s}$

Table 3.1: Order of magnitude parameter estimates for shaped-charge data.

incompressible fluid with axisymmetry. In doing so, we implicitly neglect any effects of asymmetries in the jet formation process that can affect penetration. *i.e.* we assume that the jet is *coherent* [21, 43, 64]. We will also assume that the jet is stable and hence does not particulate [42, 74, 75, 103]. We thus neglect the possibility of any lateral drift of separate jet particles on the side walls of the crater [16]. Since the main mechanism for penetration is not by melting the target, we neglect any temperature effects in the jet.

Thus we can use equations from classical fluid dynamics and introduce the velocity potential, $\varphi(r, z, t)$, which satisfies Laplace's equation $\nabla^2\varphi = 0$, written in cylindrical polars as

$$\frac{1}{r} \frac{\partial}{\partial r} \left(r \frac{\partial \varphi}{\partial r} \right) + \frac{\partial^2 \varphi}{\partial z^2} = 0. \quad (3.1)$$

This is a statement of conservation of mass. Conservation of energy comes via Bernoulli's equation, which we write as

$$\frac{\partial \varphi}{\partial t} + \frac{p}{\rho} + \frac{1}{2} |\mathbf{q}|^2 = G(t), \quad (3.2)$$

where $G(t)$ is an unknown function of time t .

3.2.1 Boundary conditions

The jet has an inner free-boundary with the cavity, $r = R_0(z, t)$, and another with the plastic region, $r = R_1(z, t)$. The normal component of the stress must be continuous across both boundaries. Since the pressure of the jet is much greater than the pressure of the cavity, we can write the first boundary condition as

$$p = 0 \text{ on } r = R_0(z, t). \quad (3.3)$$

Continuity of normal stress across $r = R_1(z, t)$ gives

$$\mathbf{n} \cdot (\boldsymbol{\sigma} \cdot \mathbf{n}) = -p \text{ on } r = R_1(z, t), \quad (3.4)$$

where \mathbf{n} is the normal to $r = R_1(z, t)$, which we write as

$$\mathbf{n} = \left(1, 0, -\frac{\partial R_1(z, t)}{\partial z} \right). \quad (3.5)$$

The kinematic boundary conditions on $r = R_0(z, t)$ and $r = R_1(z, t)$ are

$$\mathbf{q} \cdot \mathbf{n} = \frac{\partial R_j}{\partial t} / |\nabla(r - R_0(z, t))| \text{ on } r = R_j(z, t), \quad j = 0, 1. \quad (3.6)$$

Reformulating the velocity of the inviscid fluid as $(\frac{\partial \varphi}{\partial r}, 0, \frac{\partial \varphi}{\partial z})$, we obtain

$$\frac{\partial R_j}{\partial t} = \frac{\partial \varphi}{\partial r} - \frac{\partial \varphi}{\partial z} \frac{\partial R_j}{\partial z} \text{ on } r = R_j(z, t), \quad j = 0, 1. \quad (3.7)$$

Note that the boundary condition on $r = R_1(z, t)$ may simplify depending on the plastic velocity scale.

3.3 Plastic region

When writing out the equations for a plastic medium, we need to write down a yield condition, force balance equations, a flow law and boundary conditions. We will assume that the plastic material has no temperature dependence and that we can neglect any work-hardening or thermal-softening effects. Thus the yield stress, σ_Y , is a constant. We also neglect any loading-unloading phenomena, such as the Bauschinger effect, which would otherwise lead to material anisotropy. Finally, we assume that the plastic material is incompressible.

The Birkhoff hydrodynamic model gives a rough estimate for the penetration velocity as half the incoming jet velocity. Depending on the jet velocity, we see from §3.1.1 that the penetration velocity can be subsonic, transonic (between the two sound speeds) or supersonic. Until recently, it was thought that the shear wave speed was the upper bound

for the movement of dislocations. Recent work involving atomistic simulations [30, 76] suggests that this is not the case, and that supersonic dislocations are possible. This can happen if the dislocations are “born” with transonic or supersonic velocity, and is attributed to nonlinear elasticity effects. Experimental evidence is still sketchy. In any case, since our primary concern is to determine when the jet will stop penetrating, we develop an axisymmetric plasticity model which holds when the penetration speed is below the shear sound speed.

We elect to use the Tresca yield condition as it is mathematically easier to implement for an analytical solution. By writing the deviatoric stresses in terms of the hydrostatic pressure and the total stress, the yield condition can be written

$$\max(|\sigma_{rr} - \sigma_{zz}|, |\sigma_{rr} - \sigma_{\theta\theta}|, |\sigma_{\theta\theta} - \sigma_{zz}|) = \sigma_Y, \quad (3.8)$$

where σ_Y is assumed to be constant.

Minimising the plastic work done subject to the stress vector remaining on the yield surface leads to an associated flow law relating the components of the plastic strain rate tensor to those of the deviatoric stress tensor. This requires a constitutive law. The most general constitutive law will include effects of temperature and many material parameters. Indeed, modern hydrocodes tend to use sophisticated laws, such as the *Johnson-Cook* model or, more commonly, a *Zerilli-Armstrong* model [100]. We will start with the simpler model of perfect plasticity, using the equations of Reuss [36]:

$$\Lambda \dot{\varepsilon}_{ij}^{(p)} = \sigma'_{ij}, \quad (3.9)$$

where Λ , an unknown Lagrange multiplier for the constraint (3.8), is a function of space and time and $\dot{\varepsilon}_{ij}^{(p)}$ is the plastic component of the total strain rate, $\dot{\varepsilon}_{ij}$, as in (1.40). We might try other flow laws that are also not dependent on temperature, such as the *Lévy-Mises* equations or *Hencky* stress-strain equations, which relate the total plastic behaviour of the target material to the stress. The high strain-rate rules out use of the latter [36], whereas the former, (1.40), may be applicable with good justification. We shall see that, in fact, this is the case. We note that the flow law automatically implies incompressibility, which could be rewritten in terms of the principal strain rates [71] as

$$\dot{\varepsilon}_{rr} + \dot{\varepsilon}_{\theta\theta} + \dot{\varepsilon}_{zz} = 0. \quad (3.10)$$

We also need to write down general momentum balance equations as well as the assumption of incompressibility. Assuming that there are no external body forces, the momentum equations are written in axisymmetric polars as

$$\frac{\partial \sigma_{rr}}{\partial r} + \frac{\partial \sigma_{rz}}{\partial z} + \frac{\sigma_{rr} - \sigma_{\theta\theta}}{r} = \rho \frac{\partial^2 u}{\partial t^2}, \quad (3.11)$$

$$\frac{\partial \sigma_{rz}}{\partial r} + \frac{\partial \sigma_{zz}}{\partial z} + \frac{\sigma_{rz}}{r} = \rho \frac{\partial^2 w}{\partial t^2}. \quad (3.12)$$

By symmetry, $\sigma_{z\theta} = \sigma_{r\theta} = 0$.

3.3.1 Boundary conditions

The plastic region is bounded by the free boundaries $r = R_1(z, t)$ and $r = R_2(z, t)$. On $r = R_1(z, t)$, we have continuity of traction (two stress components) and one kinematic boundary condition. Continuity of traction is given by (3.4) and by

$$\mathbf{t} \cdot (\boldsymbol{\sigma} \cdot \mathbf{n}) = 0. \quad (3.13)$$

Using axisymmetry, we know that the azimuthal velocity \dot{v} is zero. Thus the kinematic condition is written

$$(\dot{u}, 0, \dot{w}) \cdot \mathbf{n} = \frac{\partial R_1}{\partial t}. \quad (3.14)$$

i.e.

$$\dot{u} - \frac{\partial R_1}{\partial z} \dot{w} = \frac{\partial R_1}{\partial t} \quad \text{on } r = R_1. \quad (3.15)$$

Similarly, we have two equations involving normal and tangential components of the normal stress vector on $r = R_2(z, t)$, as well as continuity of normal displacement. The latter is easy to write down,

$$[\mathbf{u} \cdot \mathbf{n}]_{-}^{+} = 0, \quad (3.16)$$

whereas the stress balances need more attention because the boundary is not a material boundary. We adopt an approach analogous to that in deriving the Rankine-Hugoniot jump conditions in gasdynamics [47].

Consider an arbitrary closed volume V in an elastic-plastic medium, enclosing part of the elastic-plastic boundary $r = R(z, t)$, say (Fig. 3.4), and recall the useful *transport theorem* as in [60],

$$\frac{d}{dt} \int_V f(x, t) dV = \int_V \frac{\partial f}{\partial t} dV + \int_{\partial V} v_n f dS, \quad (3.17)$$

where f is an arbitrary function, ∂V is the boundary of V and v_n is the normal velocity of the free-boundary. By putting $f = \rho$ and splitting V into an elastic volume (V_+) and

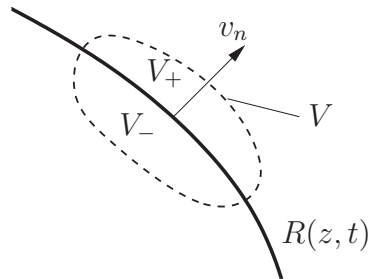


Figure 3.4: An elastic/plastic boundary $r = R(z, t)$.

a plastic part (V_-) we arrive at mass conservation [89]

$$[\rho(\dot{u}_n - v_n)]_-^+ = 0, \quad (3.18)$$

where \dot{u}_n is the normal component of the velocity, and the subscripts ‘+’ and ‘−’ denote the elastic and plastic sides of $r = R(z, t)$, respectively.

Another balance is obtained by putting $f = \rho \dot{u}_i$ (using summation convention) and by use of the equations of equilibrium,

$$[\sigma_{ij}n_j]_-^+ = \rho_-(\dot{u}_{n-} - v_n)[\dot{u}_i]_-^+. \quad (3.19)$$

Assuming that ρ is constant, we end up with the normal velocity being continuous and conditions on the normal and tangential stress,

$$[\dot{u}_n]_-^+ = 0, \quad (3.20)$$

$$[\sigma_{in} - \rho(\dot{u}_n - v_n)\dot{u}_i]_-^+ = 0. \quad (3.21)$$

In the case where inertia is negligible, the jump conditions simplify to continuity of both components of the normal stress (traction) and continuity of normal velocity, viz:

$$[\mathbf{n} \cdot (\boldsymbol{\sigma} \cdot \mathbf{n})]_-^+ = 0, \quad (3.22)$$

$$[\mathbf{t} \cdot (\boldsymbol{\sigma} \cdot \mathbf{n})]_-^+ = 0, \quad (3.23)$$

$$[\dot{\mathbf{u}} \cdot \mathbf{n}]_-^+ = 0. \quad (3.24)$$

We will also need to make some assumption about how the axial stress, σ_{zz} , behaves over the elastic-plastic boundary and on how it matches into the tip region. This will be discussed in more detail later.

3.4 Elastic region

The simplest elasticity model we can use is one of linear elasticity for an isotropic solid, assuming infinitesimal displacement, with suitable boundary conditions. Briefly, writing the stress in terms of the strain and hence displacement,

$$\sigma_{ij} = \mu \left(\frac{\partial u_i}{\partial x_j} + \frac{\partial u_j}{\partial x_i} \right) + \lambda \frac{\partial u_k}{\partial x_k} \delta_{ij}, \quad (3.25)$$

and by performing a force balance,

$$\nabla \cdot \boldsymbol{\sigma} = \rho \frac{\partial^2 \mathbf{u}}{\partial t^2}, \quad (3.26)$$

we arrive at *Navier’s equations* [49],

$$\mu \nabla^2 \mathbf{u} + (\lambda + \mu) \nabla (\nabla \cdot \mathbf{u}) = \rho \frac{\partial^2 \mathbf{u}}{\partial t^2}. \quad (3.27)$$

Since we are developing an axisymmetric model, the azimuthal displacement v must be zero. The r and z components of Navier's equations in axisymmetric cylindrical coordinates are

$$(\lambda + 2\mu) \left(\frac{\partial^2 u}{\partial r^2} + \frac{\partial}{\partial r} \left(\frac{u}{r} \right) \right) + (\lambda + \mu) \frac{\partial^2 w}{\partial r \partial z} + \mu \frac{\partial^2 u}{\partial z^2} = \rho \frac{\partial^2 u}{\partial t^2}, \quad (3.28)$$

$$\mu \left(\frac{\partial^2 w}{\partial r^2} + \frac{1}{r} \frac{\partial w}{\partial r} \right) + (\lambda + \mu) \frac{\partial}{\partial z} \left(\frac{\partial u}{\partial r} + \frac{u}{r} \right) + (\lambda + 2\mu) \frac{\partial^2 w}{\partial z^2} = \rho \frac{\partial^2 w}{\partial t^2}. \quad (3.29)$$

3.4.1 Boundary conditions

As mentioned in §3.3, the boundary conditions on $r = R_2(z, t)$ are continuity of the normal and tangential components of the normal stress vector, continuity of displacement, and a relationship between the velocities, (3.22)-(3.23). The boundary condition (3.24) now simplifies, as we are using an infinitesimal displacement elasticity model. Explicitly, the elastic component of the velocity on the boundary is effectively zero, and so we rewrite (3.24), contrasting it with the fluid-plastic kinematic boundary condition (3.15), as

$$\dot{u} - \frac{\partial R_2}{\partial z} \dot{w} = 0 \quad \text{on } r = R_2. \quad (3.30)$$

The boundary conditions at infinity are of decaying stress and zero displacement (to fix the body in space), so that

$$\sigma_{ij}(x_i) \rightarrow 0 \text{ and } u_i(x_i) \rightarrow 0 \text{ as } x_i \rightarrow \infty. \quad (3.31)$$

3.5 Different scalings

We have, so far, given dimensional equations for the three different regions. To attempt to solve these equations analytically we make a key observation, which is very apparent by looking at Fig. 3.1 and by looking at results from hydrocode simulations: **the cavity is slender**. This leads to dividing the model into three more regions, shown in Fig. 3.5.

Firstly, the *tip* region is where the incoming jet hits the target and is rapidly turned around by the impact. This is where the target material is excavated to create a cavity. A possible mechanism for removing the target material will be discussed later. The returning jet material flows into the *slender* region. Here, it is clear that when we nondimensionalise the model, there will be a small nondimensional parameter, ε , say, equal to the ratio of a typical radial lengthscale to a axial lengthscale. Hence, exploiting the slenderness of the hole by using asymptotic techniques, we will be able to reduce the dimensionality of the problem. When referring to the slender region, we only refer to the returning jet and not the incoming jet. Far away from the slender region in the elastic material, we have

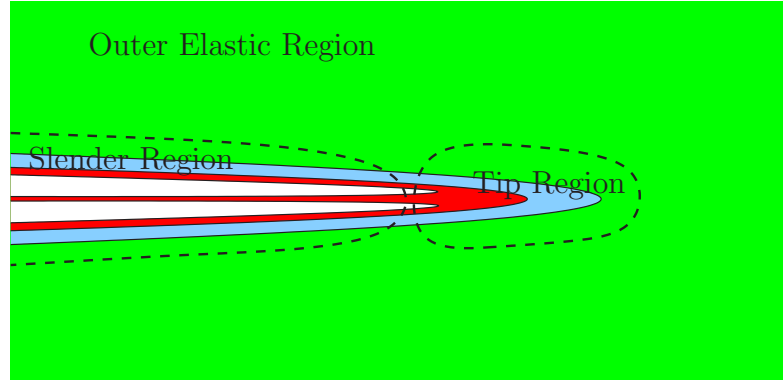


Figure 3.5: A schematic of the tip, slender and outer region.

the *outer* region. The penetration is regarded as some kind of line discontinuity in this region. We will solve the equations of elasticity here, then use matched asymptotics to match into the inner slender region.

3.5.1 Geometric and other scaling ideas

Before looking at each individual region more closely, we make some comments on the global effect of using certain scalings. We start by considering the slender region. Suppose the crater radius is $\mathcal{O}(\varepsilon)$. The simplest radial scalings for the size of the returning jet and the plastic region are both being $\mathcal{O}(\varepsilon)$. These scalings can affect the scalings for r and z in the tip region depending on how they match asymptotically into the tip and on how they come down to zero there. We propose tip scalings resulting from geometric ideas.

When matching the slender region into the tip region, we expect the free-boundaries to be locally parabolic. Hence, for the plastic region, say, to be $\mathcal{O}(\varepsilon)$ in the slender region, we must have the free-boundaries coming into the tip region looking like $R_1 \sim \varepsilon\sqrt{-z}$ and $R_2 \sim \varepsilon\sqrt{-z} + \varepsilon$. This tells us that the axial tip scaling for the plastic region is $z \sim \mathcal{O}(1)$. A similar argument holds for the jet region. The idea is perhaps best illustrated by considering two similar wedges with small angle, one sliding into the other as in Fig. 3.6.

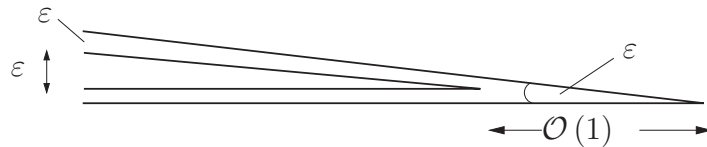


Figure 3.6: A schematic showing geometric ideas.

Another sensible scaling is to consider one, or indeed both, of the fluid and plastic region being $\mathcal{O}(\varepsilon^2)$. Thus when matching into the tip region from the slender region, the

jet region, for example, has free-boundaries matching into the tip region like $R_0 \sim \varepsilon\sqrt{-z}$ and $R_1 \sim \varepsilon\sqrt{-z} + \varepsilon^2$. Hence the appropriate axial tip scaling is $z \sim \mathcal{O}(\varepsilon^2)$ so that R_1 goes to zero. This motivates considering the four possible scalings in Fig. 3.7.

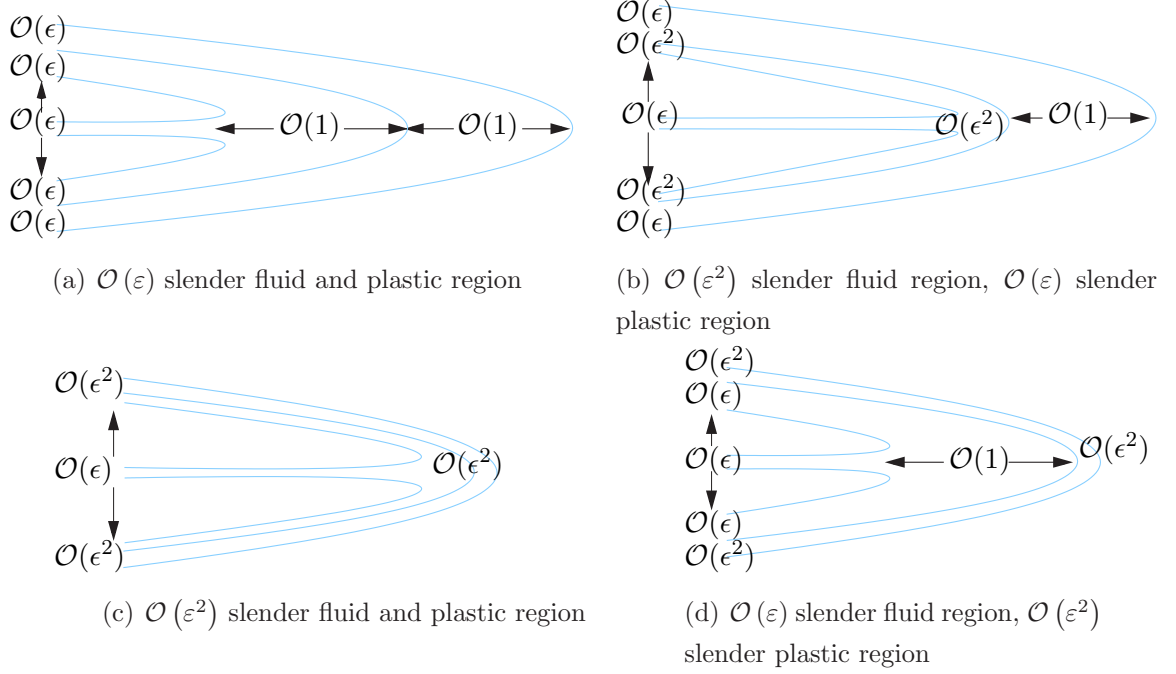


Figure 3.7: A schematic showing the jet and plastic regions for four possible different scenarios for scalings of the tip and slender regions. These are based on geometrical arguments for an $\mathcal{O}(\varepsilon)$ cavity radius.

We have briefly outlined four possible scalings motivated by geometrical arguments. With a little thought, it is clear that some of these scalings will lead to inner asymptotic regions in the tip, since we are considering scenarios in which r and z scale differently. This is because we will not be able to get a solution to Laplace's equation in which the jet flow turns back on itself unless we consider different asymptotic regions. This motivates writing down four more possible tip scalings with associated slender scalings based on an aspect ratio of unity in the tip regions. In doing so, the geometric-type arguments do not necessarily hold and we need to consider the possibility that the free-boundaries can leave the tip region tending to a constant value when matching into the slender region. Four possibilities with r and z scaling similarly in each region in the tip are shown in Fig. 3.8. Note that Fig. 3.7(c) and Fig. 3.8(c) are the same possible scalings.

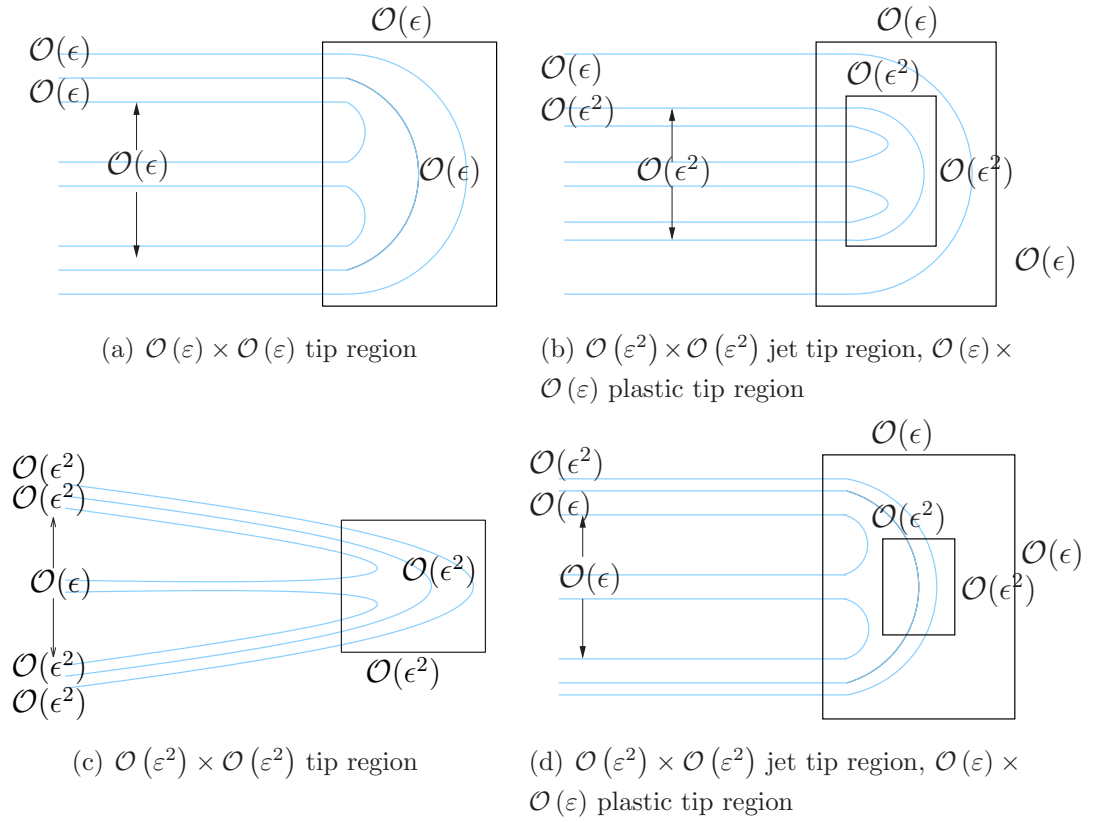


Figure 3.8: A schematic showing the jet and plastic regions for four possible different scenarios for scalings of the tip and slender regions. These are based on the r and z scales being identical in the tip region.

Chapter 4

Slender and outer analysis

We have briefly discussed possible slender scalings in the previous chapter. We start this chapter by considering the slender scalings in Fig. 3.7(a), before utilising asymptotic techniques to solve the equations. We will then pose the outer problem and match the solution into the slender region. We develop a model where the jet has penetrated sufficiently far away from the entry point of the target, so essentially we consider a jet penetrating into an infinite target.

We initially develop a model in which the axial plastic velocity scale is significantly smaller than the axial jet velocity U_0 . This simplifies the boundary condition (3.7) on $r = R_1(z, t)$ to $\mathbf{q} \cdot \mathbf{n} = 0$, and will be justified more fully in §4.1.2. We will then consider travelling-wave solutions to the coupled system of equations, before considering the effects of inertia when the plastic and fluid velocity scales are comparable. Eventually, we will see that these models do not yield sensible solutions to the problem, indicating that further modelling improvements are required.

4.1 Asymptotic analysis of nondimensional slender equations

We firstly change to coordinates moving with the stagnation point, $z = z_1(t)$, by introducing the new variables

$$z' = z - z_1(t), \tag{4.1}$$

$$t' = t. \tag{4.2}$$

Writing the velocity of the stagnation point as $U(t) = \frac{dz_1}{dt}$, the associated derivatives become

$$\frac{\partial}{\partial t} = -U(t) \frac{\partial}{\partial z'} + \frac{\partial}{\partial t'}, \quad (4.3)$$

$$\frac{\partial}{\partial z} = \frac{\partial}{\partial z'}. \quad (4.4)$$

We are now in a position to nondimensionalise the equations in the three separate regions, using data and the same notation as in §3.1.1.

4.1.1 Jet region

We can think of the slender jet region as flow through a slender annulus in the negative z direction. Changing to coordinates moving with the stagnation point, $z_1(t)$, and scaling $z' = L\bar{z}$, $r = r_j\bar{r}$ and $\varphi = U_0 L\bar{\varphi}$, where U_0 is the velocity scale given by half the initial velocity of the incoming jet (motivated by hydrodynamic models), (3.1) becomes

$$\frac{1}{\epsilon^2} \frac{1}{\bar{r}} \frac{\partial}{\partial \bar{r}} \left(\bar{r} \frac{\partial \bar{\varphi}}{\partial \bar{r}} \right) + \frac{\partial^2 \bar{\varphi}}{\partial \bar{z}^2} = 0, \quad (4.5)$$

where $\epsilon = \frac{r_j}{L} \ll 1$. Note that in performing this r scaling, we implicitly assume that $r = \mathcal{O}(\epsilon L)$.

In writing down the Bernoulli equation (3.2) in an accelerating frame, we need to remember that there will be a term concerned with the inertia of the frame. Thus, we recall the derivation of Bernoulli's equation and consider the momentum equation

$$\frac{\partial \mathbf{q}}{\partial t} + (\mathbf{q} \cdot \nabla) \mathbf{q} = -\frac{1}{\rho_j} \nabla p. \quad (4.6)$$

We scale time as $t' = \frac{L}{U_0} \bar{t}$ and let $\hat{\varphi} = \bar{\varphi} - \bar{U}(\bar{t})\bar{z}$ be a new potential, where $U(t) = U_0 \bar{U}(\bar{t})$. Using (4.4), the velocity in the new frame is given by

$$\hat{\mathbf{q}} = \bar{\mathbf{q}} - (0, 0, \bar{U}), \quad (4.7)$$

where the fluid velocity has been scaled $\mathbf{q} = U_0 \bar{\mathbf{q}}$. Nondimensionalising the pressure as $p = \rho_j U_0^2 \bar{p}$, the momentum equation becomes

$$\left(-\bar{U} \frac{\partial}{\partial \bar{z}} + \frac{\partial}{\partial \bar{t}} \right) (\hat{\mathbf{q}} + (0, 0, \bar{U})) + ((\hat{\mathbf{q}} + (0, 0, \bar{U})) \cdot \nabla) (\hat{\mathbf{q}} + (0, 0, \bar{U})) + \nabla \bar{p} = 0, \quad (4.8)$$

where ∇ is now the obvious nondimensional operator. Hence

$$\nabla \left(\frac{\partial \hat{\varphi}}{\partial \bar{t}} + \frac{d\bar{U}(\bar{t})}{d\bar{t}} \bar{z} + \frac{1}{2} |\hat{\mathbf{q}}|^2 + \bar{p} \right) = 0. \quad (4.9)$$

We integrate this to obtain a ‘modified’ Bernoulli equation involving an arbitrary function of nondimensional time $G(\bar{t})$,

$$\frac{\partial \hat{\phi}}{\partial \bar{t}} + \frac{d\bar{U}(\bar{t})}{d\bar{t}} \bar{z} + \frac{1}{2} |\hat{\mathbf{q}}|^2 + \bar{p} = G(\bar{t}). \quad (4.10)$$

A further simplification can be made by writing another new velocity potential

$$\phi = \hat{\phi} - \int_0^{\bar{t}} G(\xi) d\xi, \quad (4.11)$$

which gives, dropping the bars and hats,

$$\frac{\partial \phi}{\partial t} + \frac{dU(t)}{dt} z + \frac{1}{2} \left(\left(\frac{\partial \phi}{\partial z} \right)^2 + \frac{1}{\varepsilon^2} \left(\frac{\partial \phi}{\partial r} \right)^2 \right) + p = 0. \quad (4.12)$$

Note that since $\frac{\partial^2 \phi}{\partial z^2} = \frac{\partial^2 \bar{\phi}}{\partial \bar{z}^2}$, ϕ also satisfies Laplace’s equation, (4.5).

Nondimensional boundary conditions

Scaling the free boundary $R_0(z, t)$ with r_j , the zero pressure on the inner cavity condition (3.3) becomes

$$\bar{p} = 0 \text{ on } \bar{r} = R_0(\bar{z}, \bar{t}). \quad (4.13)$$

The normals to the free boundaries become

$$\mathbf{n} = \left(1, 0, -\varepsilon \frac{\partial R_j(\bar{z}, \bar{t})}{\partial \bar{z}} \right), \quad j = 0, 1, \quad (4.14)$$

whilst the velocity in the inviscid fluid is now $\left(\frac{U_0}{\varepsilon} \frac{\partial \bar{\phi}}{\partial \bar{r}}, 0, U_0 \frac{\partial \bar{\phi}}{\partial \bar{z}} \right)$. Hence, balancing the normal component of the fluid velocity on the boundary $\bar{r} = R_0(\bar{z}, \bar{t})$ with the velocity of the boundary, (3.7) becomes

$$\frac{1}{\varepsilon} \frac{\partial \bar{\phi}}{\partial \bar{r}} - \varepsilon \frac{\partial R_0}{\partial \bar{z}} \frac{\partial \bar{\phi}}{\partial \bar{z}} = \varepsilon \left(\frac{\partial}{\partial \bar{t}} - U(\bar{t}) \frac{\partial}{\partial \bar{z}} \right) R_0(\bar{z}, \bar{t}) \text{ on } \bar{r} = R_0(\bar{z}, \bar{t}). \quad (4.15)$$

Substituting ϕ for $\bar{\phi}$ so that the velocity potential is in the moving frame and dropping bars, we find that the boundary condition becomes

$$\frac{\partial \phi}{\partial r} - \varepsilon^2 \frac{\partial R_0}{\partial z} \frac{\partial \phi}{\partial z} = \varepsilon^2 \frac{\partial R_0}{\partial t} \text{ on } r = R_0(z, t). \quad (4.16)$$

Assuming that the plastic velocity scales are significantly smaller than the jet velocity, the boundary condition on $r = R_1(z, t)$ simplifies to $\mathbf{q} \cdot \mathbf{n} = 0$ in the rest frame. In the moving frame, it becomes

$$\frac{\partial \phi}{\partial r} - \varepsilon^2 \frac{\partial R_1}{\partial z} \left(\frac{\partial \phi}{\partial z} + U(t) \right) = 0 \text{ on } r = R_1(z, t). \quad (4.17)$$

Asymptotic expansion

We now take advantage of the small parameter in the equations and perform an expansion in ε . From the equations, the natural expansion for ϕ is in powers of ε^2 , hence

$$\phi(r, z, t) \sim \phi_0(r, z, t) + \varepsilon^2 \phi_2(r, z, t) + \mathcal{O}(\varepsilon^4). \quad (4.18)$$

Substituting this expansion into (4.5) and looking at $\mathcal{O}(1)$ and $\mathcal{O}(\varepsilon^2)$ leads to the following:

$$\mathcal{O}(1) : \frac{1}{r} \frac{\partial}{\partial r} \left(r \frac{\partial \phi_0}{\partial r} \right) = 0; \quad (4.19)$$

$$\mathcal{O}(\varepsilon^2) : \frac{1}{r} \frac{\partial}{\partial r} \left(r \frac{\partial \phi_2}{\partial r} \right) = -\frac{\partial^2 \phi_0}{\partial z^2}. \quad (4.20)$$

The boundary conditions become

$$\mathcal{O}(1) : \frac{\partial \phi_0}{\partial r} = 0 \text{ on } r = R_0(z, t) \text{ and } R_1(z, t); \quad (4.21)$$

$$\mathcal{O}(\varepsilon^2) : \frac{\partial R_0}{\partial t} = \frac{\partial \phi_2}{\partial r} - \frac{\partial R_0}{\partial z} \frac{\partial \phi_0}{\partial z} \text{ on } r = R_0(z, t), \quad (4.22)$$

$$\frac{\partial \phi_2}{\partial r} - \varepsilon^2 \frac{\partial R_1}{\partial z} \left(\frac{\partial \phi_0}{\partial z} + U(t) \right) = 0 \text{ on } r = R_1(z, t). \quad (4.23)$$

Integration of (4.19) gives

$$\phi_0(z, t) = A(z, t) \log r + B(z, t). \quad (4.24)$$

Applying the two boundary conditions (4.21), we find that $A(z, t) = 0$ and so

$$\phi_0 = \phi_0(z, t). \quad (4.25)$$

We now integrate the $\mathcal{O}(\varepsilon^2)$ equation, (4.20), to get an expression for $\phi_2(r, z, t)$:

$$\phi_2(r, z, t) = C(z, t) \log r + D(z, t) - \frac{\partial^2 \phi_0}{\partial z^2} \frac{r^2}{4}. \quad (4.26)$$

The $\mathcal{O}(\varepsilon^2)$ boundary conditions (4.22)-(4.23) thus give us

$$C(z, t) = \frac{1}{2} \frac{\partial}{\partial t} (R_0^2) + \frac{1}{2} \frac{\partial}{\partial z} \left(\frac{\partial \phi_0}{\partial z} R_0^2 \right) \quad (4.27)$$

$$= \frac{1}{2} \frac{\partial}{\partial z} \left(\left(\frac{\partial \phi_0}{\partial z} + U(t) \right) R_1^2 \right). \quad (4.28)$$

Eliminating $C(z, t)$, we arrive at a ‘conservation of mass’ equation

$$-\frac{\partial}{\partial t} (R_0^2) + \frac{\partial}{\partial z} \left(\left(\frac{\partial \phi_0}{\partial z} + U \right) R_1^2 - \frac{\partial \phi_0}{\partial z} R_0^2 \right) = 0. \quad (4.29)$$

We are left with Bernoulli's equation (4.12). Using the expansion (4.18) and expanding the velocity $U \sim U^{(0)} + \varepsilon^2 U^{(2)} + \dots$,

$$\begin{aligned} p = & - \left(\frac{\partial \phi_0}{\partial t} + \frac{1}{2} \left(\frac{\partial \phi_0}{\partial z} \right)^2 + \frac{dU^{(0)}}{dt} z \right) \\ & - \left(\frac{\partial \phi_2}{\partial t} + \frac{1}{2} \left(\frac{\partial \phi_2}{\partial r} \right)^2 + \left(\frac{\partial \phi_0}{\partial z} \right) \left(\frac{\partial \phi_2}{\partial z} \right) + \frac{dU^{(2)}}{dt} z \right) \varepsilon^2 + \dots \end{aligned} \quad (4.30)$$

Use of the boundary condition (4.13) tells us that

$$\frac{\partial \phi_0}{\partial t} + \frac{1}{2} \left(\frac{\partial \phi_0}{\partial z} \right)^2 + \frac{dU^{(0)}}{dt} z = 0 \text{ on } r = R_0. \quad (4.31)$$

This expression, however, is independent of r , so must be zero everywhere. To obtain the pressure on $r = R_1$, after some algebra, we get

$$\begin{aligned} p(R_1) - p(R_0) = & \left\{ \frac{\partial C}{\partial t} \left(\log \frac{R_0}{R_1} \right) - \frac{1}{4} \frac{\partial^3 \phi_0}{\partial z^2 \partial t} (R_0^2 - R_1^2) \right. \\ & + \frac{1}{2} \left(C(z, t)^2 \left(\frac{1}{R_0^2} - \frac{1}{R_1^2} \right) + \frac{1}{4} \left(\frac{\partial^2 \phi_0}{\partial z^2} \right)^2 (R_0^2 - R_1^2) \right) \\ & \left. + \frac{\partial \phi_0}{\partial z} \left(\frac{\partial C}{\partial z} \left(\log \frac{R_0}{R_1} \right) - \frac{1}{4} \frac{\partial^3 \phi_0}{\partial z^3} (R_0^2 - R_1^2) \right) \right\} \varepsilon^2, \end{aligned} \quad (4.32)$$

where $C(z, t)$ is as in (4.27). In the case where $U(t)$ is constant, we can differentiate the 'eikonal' equation (4.31) to simplify this expression as

$$\begin{aligned} p(R_1) - p(R_0) = & \left\{ \frac{\partial C}{\partial t} \left(\log \frac{R_0}{R_1} \right) - \frac{3}{8} \left(\frac{\partial^2 \phi_0}{\partial z^2} \right)^2 (R_1^2 - R_0^2) \right. \\ & \left. + \frac{1}{2} C(z, t)^2 \left(\frac{1}{R_0^2} - \frac{1}{R_1^2} \right) + \frac{\partial \phi_0}{\partial z} \left(\frac{\partial C}{\partial z} \left(\log \frac{R_0}{R_1} \right) \right) \right\} \varepsilon^2. \end{aligned} \quad (4.33)$$

To avoid confusion with the hydrostatic pressure in either plastic or elastic regions, we will write this 'inflation pressure' as P . We aim to match P into the plastic region, which we now consider.

4.1.2 Plastic region

Much akin to the jet region, we think of the plastic region as flow of target material through an annulus. This flow is driven by material from the tip region, plasticised by the very high pressure in the jet. A good comparison to make for both the plastic and the elastic region is to compare it to the expansion of a slowly-varying gun-barrel under applied pressure $P(z, t)$, where $P(z, t)$ is great enough to induce yield.

We start nondimensionalising the model by scaling all stresses with the yield stress, σ_Y . The yield condition becomes

$$\max(|\sigma_{rr} - \sigma_{zz}|, |\sigma_{rr} - \sigma_{\theta\theta}|, |\sigma_{\theta\theta} - \sigma_{zz}|) = 1, \quad (4.34)$$

where the stresses are now nondimensional. As in models for expansion of a cylinder under applied pressure, [36, 13], we assume that σ_{zz} is the intermediate stress. This can be shown to be correct *a posteriori* and also by numerical models [58]. Thus

$$|\sigma_{rr} - \sigma_{\theta\theta}| = 1. \quad (4.35)$$

We now turn our attention to the flow law. In the previous chapter, we wrote down Reuss's equations for plastic flow (3.9). These relate the components of the plastic part of the strain tensor in terms of the deviatoric stresses. As hinted at in the previous chapter, we make a simplification by neglecting the elastic part of the strain rate tensor so that the total stress is dominated by the plastic stress, $\dot{\varepsilon}_{ij} \approx \dot{\varepsilon}_{ij}^{(p)}$. In doing so, we recover the *Lèvy-Mises* equations for plastic flow,

$$\Lambda \dot{\varepsilon}_{ij} = \sigma'_{ij}. \quad (4.36)$$

This simplifies the equations significantly. However, we must give the caveat that in certain circumstances, neglecting the elastic part of the strain rate leads to significant errors and also to discontinuities in the stress over the elastic-plastic boundary [36, 37]. This is apparent when considering expansion of a thin cylinder under constant internal pressure when the elastic part of the stress can be important. Nevertheless, as we are looking at a semi-infinite elastic region with an $\mathcal{O}(\varepsilon)$ plastic region, this approximation is a good one [35].

We can now write down the deviatoric stresses in terms of the velocities, which are written down with respect to the inertial frame. To do so, we need an appropriate scale for the plastic velocities. At first glance, we might scale the velocities with the only velocity scales available to us in the slender region, *i.e.* the jet-velocity scalings. This would say that the plastic and jet velocities are comparable in the slender region. However, the scales for the plastic velocities should really be determined by the matching into the tip region, as the jet imposes no significant shear (whereas the confinement of the cavity leads the slender jet scale to be on a par with the velocity scale of the incoming jet). We anticipate that this velocity scale is significantly smaller than the jet velocity in the slender region, and so initially scale the axial plastic velocity $\dot{w} = \delta U_0 \bar{\bar{w}}$ where δ is a small nondimensional parameter. The radial plastic velocity is rescaled $\dot{u} = \varepsilon \delta U_0 \bar{\bar{u}}$. The extra factor of ε arises from the radial lengthscale being $\mathcal{O}(\varepsilon)$. A schematic of the relative velocities is shown in Fig. 4.1. In this formulation, we are viewing the jet in the slender region as plasticising the target to allow material to be excavated. It is possible, albeit more unlikely, that the plastic velocity scale is comparable to the jet velocity. This will be considered in §4.4

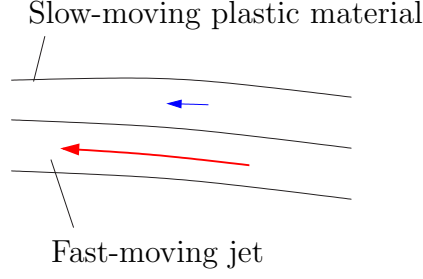


Figure 4.1: A figure showing a section of the slender region in which the magnitude of the plastic velocity is significantly lower than the magnitude of the jet velocity.

Scaling $\Lambda = \frac{\sigma_Y L}{\delta U_0} \bar{\Lambda}$, and dropping the bars, the leading-order deviatoric stresses are

$$\sigma'_{rr} = \Lambda \frac{\partial \dot{u}}{\partial r}, \quad (4.37)$$

$$\sigma'_{\theta\theta} = \Lambda \frac{\dot{u}}{r}, \quad (4.38)$$

$$\sigma'_{zz} = \Lambda \frac{\partial \dot{w}}{\partial z}, \quad (4.39)$$

$$\sigma'_{rz} = \frac{\Lambda}{2\varepsilon} \frac{\partial \dot{w}}{\partial r}. \quad (4.40)$$

As we are assuming axisymmetry, we know that the other stress and deviatoric stress components must satisfy

$$\sigma_{r\theta} = \sigma_{z\theta} = \sigma'_{r\theta} = \sigma'_{z\theta} = 0. \quad (4.41)$$

Further, since there can be no θ -dependence in the velocities,

$$\dot{v} = \dot{\varepsilon}_{r\theta} = \dot{\varepsilon}_{z\theta} = 0. \quad (4.42)$$

In view of the flow law, we now consider the incompressibility condition (3.10) in terms of the velocities to get

$$\frac{\partial \dot{u}}{\partial r} + \frac{\dot{u}}{r} + \frac{\partial \dot{w}}{\partial z} = 0. \quad (4.43)$$

A typical timescale for the plastic flow is $t \sim L/(\delta U_0)$. We can thus introduce the nondimensional ratio $\alpha = \rho_t U_0^2 / \sigma_Y$ and rescale time in such a manner as to obtain the nondimensional force-balance equations in the inertial frame:

$$\frac{\partial \sigma_{rr}}{\partial r} + \varepsilon \frac{\partial \sigma_{rz}}{\partial z} + \frac{\sigma_{rr} - \sigma_{\theta\theta}}{r} = \alpha \varepsilon^2 \delta^2 \frac{\partial \dot{u}}{\partial t}, \quad (4.44)$$

$$\frac{\partial \sigma_{rz}}{\partial r} + \varepsilon \frac{\partial \sigma_{zz}}{\partial z} + \frac{\sigma_{rz}}{r} = \alpha \varepsilon \delta^2 \frac{\partial \dot{w}}{\partial t}. \quad (4.45)$$

We will comment on the size of the nondimensional coefficients after consideration of the boundary conditions.

4.1.2.1 Nondimensional boundary conditions

The nondimensional unit normal and unit tangent to the elastic-plastic boundary $R_1(z, t)$ are

$$\mathbf{n} = \left(-1, 0, \varepsilon \frac{\partial R_1}{\partial z} \right), \quad (4.46)$$

$$\mathbf{t} = \left(\varepsilon \frac{\partial R_1}{\partial z}, 0, 1 \right), \quad (4.47)$$

which gives the traction vector

$$\boldsymbol{\sigma} \cdot \mathbf{n} = \left(-\sigma_{rr} + \sigma_{rz} \frac{\partial R_1}{\partial z} \varepsilon, 0, -\sigma_{rz} + \sigma_{zz} \frac{\partial R_1}{\partial z} \varepsilon \right). \quad (4.48)$$

Hence, the nondimensional leading-order stress balances (3.4) and (3.13) become

$$\sigma_{rr} = -\alpha P \text{ on } r = R_1(z, t), \quad (4.49)$$

$$\sigma_{rz} = 0 \text{ on } r = R_1(z, t), \quad (4.50)$$

where P is the nondimensional pressure from the fluid region given in (4.33). Recall that we are regarding the plastic region as being a result of (radial) stress from the jet. Ergo, for this model to be valid, the pressure P must be great enough to induce plastic yield (*i.e.* satisfy the yield condition). Hence, as $P \sim \mathcal{O}(\varepsilon^2)$, the model is only valid if $\alpha \varepsilon^2 \sim \mathcal{O}(1)$. From Table 3.1, we can estimate $\varepsilon \sim 5 \times 10^{-3}/0.5 \sim 10^{-2}$ and $\alpha \sim 9 \times 10^3 \times (4 \times 10^3)^2/\sigma_Y \sim 10^{11}/\sigma_Y$. The all-important coefficient thus has order of magnitude $10^7/\sigma_Y$, and so our proposed model is only valid for softer targets such as concrete or softer metals¹.

Such a parameter-regime has consequences for equations (4.44)-(4.45), in that we can neglect the inertial effects in the slender plastic region if δ is suitably small ($\delta^2 \ll \varepsilon$ is sufficient). Furthermore, it suggests a large plastic region in the tip, as the nondimensional jet pressure is order unity in the tip. This is consistent with the geometric ideas of Fig. 3.7. Inertial terms must hence play an important role in the plastic region in the tip, as the plastic velocity in the tip is comparable to the jet velocity. Tip equations will thus be hyperbolic in both plastic and inner elastic regions, resulting in waves. From Table 3.1, we can see that the penetration velocity and elastic wave speeds are, typically, comparable. Thus, we expect the waves generated in the tip region to leave the tip at finite angle and dissipate in the outer bulk (Fig. 4.2), not interfering with the motion in the slender region. This is another signpost for neglecting inertia in the plastic region and developing a quasistatic plasticity model.

¹The classical elastic-plastic analysis of a cylindrical cavity under applied pressure P [36] shows that the dimensional pressure needs to be greater than $\sigma_Y/2$ for plastic flow. This will be considered in more detail in a later chapter.

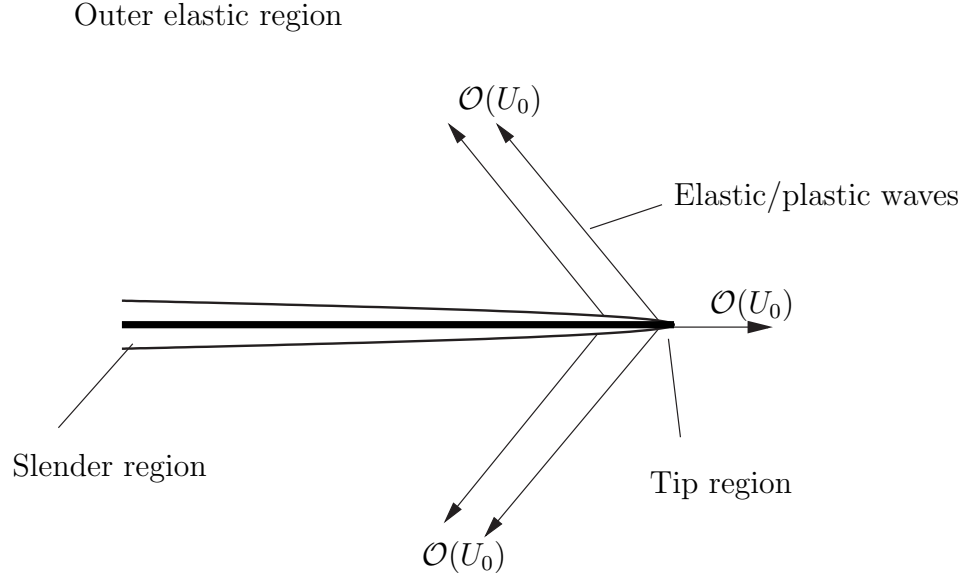


Figure 4.2: Elastic/plastic waves generated from the tip at finite angle are dissipated into the outer bulk.

Concerning the elastic-plastic boundary conditions in this model, nondimensionalisation of the normal force balances (3.22)-(3.23) gives us two jump conditions on the elastic-plastic boundary,

$$\left[\sigma_{rr} - 2\sigma_{rz} \frac{\partial R_2}{\partial z} \varepsilon + \sigma_{zz} \left(\frac{\partial R_2}{\partial z} \right)^2 \varepsilon^2 \right]_{-}^{+} = 0, \quad (4.51)$$

$$\left[-\sigma_{rr} \frac{\partial R_2}{\partial z} \varepsilon + \sigma_{rz} \frac{\partial R_2}{\partial z} \varepsilon^2 - \sigma_{rz} + \sigma_{zz} \frac{\partial R_2}{\partial z} \varepsilon \right]_{-}^{+} = 0. \quad (4.52)$$

Clearly, we write the nondimensional continuity of displacement as

$$[\mathbf{u}]_{-}^{+} = 0, \quad (4.53)$$

as in (3.16). The nondimensional version of the condition (3.30) on the velocities is

$$\dot{u} - \frac{\partial R_2}{\partial z} \dot{w} = 0 \text{ on } r = R_2, \quad (4.54)$$

whereas the nondimensional kinematic condition is

$$\dot{u} - \frac{\partial R_1}{\partial z} \dot{w} = \frac{\partial R_1}{\partial t} \text{ on } r = R_1. \quad (4.55)$$

Asymptotic expansion

We now expand the plastic velocities and stresses in powers of ε :

$$\dot{u} \sim \dot{u}^{(0)} + \mathcal{O}(\varepsilon), \quad (4.56)$$

$$\dot{w} \sim \dot{w}^{(0)} + \mathcal{O}(\varepsilon), \quad (4.57)$$

$$\sigma_{rr} \sim \sigma_{rr}^{(0)} + \mathcal{O}(\varepsilon), \quad (4.58)$$

$$\sigma_{\theta\theta} \sim \sigma_{\theta\theta}^{(0)} + \mathcal{O}(\varepsilon), \quad (4.59)$$

$$\sigma_{rz} \sim \sigma_{rz}^{(0)} + \mathcal{O}(\varepsilon). \quad (4.60)$$

At leading order, the quasistatic force balances in the plastic medium in a frame moving with the stagnation point are

$$\frac{\partial \sigma_{rr}}{\partial r} + \frac{\sigma_{rr} - \sigma_{\theta\theta}}{r} = 0, \quad (4.61)$$

$$\frac{\partial \sigma_{rz}}{\partial r} + \frac{\sigma_{rz}}{r} = 0. \quad (4.62)$$

We immediately see from the second equation that

$$\sigma_{rz}^{(0)} = \frac{f(z, t)}{r}. \quad (4.63)$$

However, the boundary condition (4.50) on $r = R_1(z, t)$ gives that $f(z, t) = 0$. Note that even if we tried an expansion for σ_{rz} starting at $\mathcal{O}(\frac{1}{\varepsilon})$ as hinted at by (4.40), the boundary condition would quickly show that σ_{rz} was again zero at leading-order.

Turning again to (4.40), we see that $\frac{\partial \dot{w}^{(0)}}{\partial r} = 0$, thus

$$\dot{w}^{(0)} = \dot{w}^{(0)}(z, t). \quad (4.64)$$

We can now integrate the incompressibility condition (4.43) with respect to r to obtain

$$\dot{u}^{(0)} = -\frac{1}{2} \frac{\partial \dot{w}^{(0)}}{\partial z}(z, t)r + \frac{g(z, t)}{r}, \quad (4.65)$$

for some unknown function $g(z, t)$. Substituting this into the boundary conditions (4.54) and (4.55) gives us that

$$g(z, t) = \frac{1}{2} \frac{\partial}{\partial z}(R_2^2 \dot{w}^{(0)}). \quad (4.66)$$

Further, we also obtain the plastic ‘conservation’ of mass (*c.f.* (4.29)),

$$\frac{\partial}{\partial t}(-R_1^2) + \frac{\partial}{\partial z}(\dot{w}^{(0)}(R_2^2 - R_1^2)) = 0. \quad (4.67)$$

In using the yield condition (4.35), we need to know which of σ_{rr} and $\sigma_{\theta\theta}$ is greater. Again, we appeal to the cylinder-expansion literature [36] or to numerical simulations,

which tell us that $\sigma_{rr} < \sigma_{\theta\theta}$. Hence using (4.37), (4.38) with (4.65), we see that the Lagrange multiplier is

$$\Lambda(r, z, t) = \frac{r^2}{\frac{\partial}{\partial z}(R_2^2 \dot{w}^{(0)})}. \quad (4.68)$$

Note that if both R_2 and $\dot{w}^{(0)}$ are not functions of z , there will be no radial flow (it is constrained by the boundary R_2) and we just have a uniform axial flow. Substituting the yield condition into (4.61) gives

$$\frac{\partial \sigma_{rr}^{(0)}}{\partial r} = \frac{1}{r}. \quad (4.69)$$

Integrating this and using the boundary condition (4.49) leads to

$$\sigma_{rr}^{(0)} = -\alpha P + \log \left(\frac{r}{R_1} \right). \quad (4.70)$$

Using the expressions for $\dot{w}^{(0)}$, Λ and $g(z, t)$, we can write down the deviatoric stresses as

$$\sigma'_{rr} = -\frac{1}{2} \left(1 + \frac{\frac{\partial \dot{w}^{(0)}}{\partial z}}{\frac{\partial}{\partial z}(R_0^2 \dot{w}^{(0)})} r^2 \right), \quad (4.71)$$

$$\sigma'_{\theta\theta} = \frac{1}{2} \left(1 - \frac{\frac{\partial \dot{w}^{(0)}}{\partial z}}{\frac{\partial}{\partial z}(R_0^2 \dot{w}^{(0)})} r^2 \right), \quad (4.72)$$

$$\sigma'_{zz} = \frac{\frac{\partial \dot{w}^{(0)}}{\partial z}}{\frac{\partial}{\partial z}(R_0^2 \dot{w}^{(0)})} r^2. \quad (4.73)$$

The hydrostatic pressure is hence given as

$$\begin{aligned} p &= \sigma'_{rr} - \sigma_{rr} \\ &= \alpha P - \log \frac{r}{R_1} - \frac{1}{2} \left(1 + \frac{\frac{\partial \dot{w}^{(0)}}{\partial z}}{\frac{\partial}{\partial z}(R_0^2 \dot{w}^{(0)})} r^2 \right). \end{aligned} \quad (4.74)$$

The other unknown stresses are written

$$\sigma_{\theta\theta} = -\alpha P + 1 + \log \frac{r}{R_1}, \quad (4.75)$$

$$\sigma_{zz} = -\alpha P + \log \frac{r}{R_1} + \frac{1}{2} \left(1 + \frac{3 \frac{\partial \dot{w}^{(0)}}{\partial z}}{\frac{\partial}{\partial z}(R_0^2 \dot{w}^{(0)})} r^2 \right). \quad (4.76)$$

The unknown functions will be determined by matching into the elastic region.

4.1.3 Inner elastic region

The stresses in the elastic region are generated from the plastic stresses. Hence, we again nondimensionalise the components of the stress tensor by scaling with σ_Y . In order to

choose the correct scale for the elastic displacements, we recall the principal radial stress component

$$\sigma_{rr} = (\lambda + 2\mu) \frac{\partial u}{\partial r} + \lambda \frac{u}{r} + \lambda \frac{\partial w}{\partial z}. \quad (4.77)$$

Hence, scaling $z \sim L$ and $r \sim r_j$ motivates scaling $u \sim \frac{\sigma_Y r_j}{\lambda + 2\mu}$ and $w \sim \frac{\sigma_Y L}{\lambda + 2\mu}$. Thus, in a frame moving with the stagnation point, Navier's equations for elasticity (3.28) and (3.29) become

$$\left(\frac{\partial^2 u}{\partial r^2} + \frac{\partial}{\partial r} \left(\frac{u}{r} \right) \right) + \left(\frac{\lambda + \mu}{\lambda + 2\mu} \right) \frac{\partial^2 w}{\partial r \partial z} + \frac{\mu}{\lambda + 2\mu} \left(\frac{\partial^2 u}{\partial z^2} \right) \varepsilon^2 = \varepsilon^2 M_p^2 \left(\frac{\partial}{\partial t} - \tilde{U} \frac{\partial}{\partial z} \right)^2 u, \quad (4.78)$$

$$\frac{\mu}{\lambda + 2\mu} \left(\frac{1}{r} \frac{\partial}{\partial r} \left(r \frac{\partial w}{\partial r} \right) \right) + \left(\frac{\lambda + \mu}{\lambda + 2\mu} \right) \frac{1}{r} \frac{\partial^2 (ur)}{\partial r \partial z} \varepsilon^2 + \frac{\partial^2 w}{\partial z^2} \varepsilon^2 = \varepsilon^2 M_p^2 \left(\frac{\partial}{\partial t} - \tilde{U} \frac{\partial}{\partial z} \right)^2 w. \quad (4.79)$$

M_p is the Mach number with respect to the primary wave speed $c_p^2 = (\lambda + 2\mu)/\rho$, defined by

$$M_p = \frac{U_0}{c_p}. \quad (4.80)$$

From Table 3.1, we see that this is $\mathcal{O}(1)$ and so inertia does not play a leading role in the inner elastic region.

Nondimensional boundary conditions

The nondimensional boundary conditions on $r = R_2(z, t)$ are (4.54), continuity of displacement and the traction balances (4.51)-(4.52). We also have boundary conditions arising from matching with the outer elastic region.

Asymptotic expansion

Expanding the displacements

$$u \sim u^{(0)} + \mathcal{O}(\varepsilon), \quad (4.81)$$

$$w \sim w^{(0)} + \mathcal{O}(\varepsilon), \quad (4.82)$$

with corresponding stresses

$$\sigma_{rr} \sim \sigma_{rr}^{(0)} + \mathcal{O}(\varepsilon), \quad (4.83)$$

$$\sigma_{\theta\theta} \sim \sigma_{\theta\theta}^{(0)} + \mathcal{O}(\varepsilon), \quad (4.84)$$

$$\sigma_{zz} \sim \sigma_{zz}^{(0)} + \mathcal{O}(\varepsilon), \quad (4.85)$$

$$\sigma_{rz} \sim \sigma_{rz}^{(0)} + \mathcal{O}(\varepsilon), \quad (4.86)$$

the rescaled Navier equations become, at leading order,

$$\left(\frac{\partial^2 u^{(0)}}{\partial r^2} + \frac{\partial}{\partial r} \left(\frac{u^{(0)}}{r} \right) \right) + \left(\frac{\lambda + \mu}{\lambda + 2\mu} \right) \frac{\partial^2 w^{(0)}}{\partial r \partial z} = 0, \quad (4.87)$$

$$\frac{\partial^2 w^{(0)}}{\partial r^2} + \frac{1}{r} \frac{\partial w^{(0)}}{\partial r} = 0. \quad (4.88)$$

Integrating the second equation,

$$w^{(0)} = A_e(z, t) \log r + B_e(z, t), \quad (4.89)$$

and hence

$$u^{(0)} = C_e(z, t)r + \frac{D_e(z, t)}{r} - \left(\frac{\lambda + \mu}{\lambda + 2\mu} \right) \frac{1}{4} \frac{\partial A_e}{\partial z} r (2 \log r - 1). \quad (4.90)$$

Using these expressions for displacement, we can write down the stresses via (A.15)-(A.18). We start by writing down

$$\sigma_{rz} = \mu \left(\varepsilon \frac{\partial u^{(0)}}{\partial z} + \frac{1}{\varepsilon} \frac{\partial w^{(0)}}{\partial r} \right) \quad (4.91)$$

At leading order, we only get the contribution

$$\mu \frac{\partial w^{(0)}}{\partial r} = \mu \frac{A_e(z, t)}{r}. \quad (4.92)$$

However, the leading-order term from the tangential component of the traction boundary condition (4.52) tells us that $\sigma_{rz}(R_2) = 0$. Hence $A_e(z, t) = 0$ and

$$w^{(0)} = w^{(0)}(z, t). \quad (4.93)$$

Before performing further matching with the plastic region, we move to the outer elastic problem.

4.2 Outer region

The outer region is far away from where the penetration is taking place, and sees the inner region as a slender body. Although inertia will undoubtedly play a role in this region in the form of waves from the tip, we will initially consider solutions to the quasistatic equations of elasticity in order to gain intuition. These solutions will be matched asymptotically into the inner slender region, as in classic slender body theory (§1.2.4). We will then attempt to generalise the matching to the full hyperbolic equations of elasticity.

4.2.1 Quasistatic outer region

The crucial observation in attaining a solution is the assumption of axisymmetry; the displacement is the same in all planes through the axis of symmetry and so there exists a stress function, χ , which satisfies the biharmonic equation,

$$\nabla^4 \chi = 0. \quad (4.94)$$

All of the unknown quantities (C.2)-(C.7) can be expressed in terms of it. Recall that we term this the *Love stress function*, as in §1.2.1.4. Ultimately, we will need to reformulate the inner elastic region in terms of the Love stress function so that we can match the outer χ and its derivatives into the inner region.

From the point of view of the outer solution, we could consider the cavity as a series of holes. These holes can be modelled by considering singularities of the incompatibility tensor (the tensor we get when applying the curl operator to the rows and columns of the strain tensor). This is currently being investigated [57]. We adopt an approach using classic potential theory. This dictates that we can write the outer solution using a Green's function representation. We introduce the outer coordinates $\mathbf{x} = (R, \theta, z)$ and $\boldsymbol{\xi} = (0, \theta, z')$, where \mathbf{x} is a vector for a point outside the slender body and $\boldsymbol{\xi}$ is a point on the slender body. By considering $\nabla^4 G_{bih}(\mathbf{x}, \boldsymbol{\xi}) = \delta(\mathbf{x} - \boldsymbol{\xi})$, the Green's function for the biharmonic operator is found to be

$$G_{bih} = |\mathbf{x} - \boldsymbol{\xi}| = \sqrt{R^2 + (z - z')^2}. \quad (4.95)$$

Noting that any harmonic solution is automatically biharmonic, we write our Love stress (potential) function in terms of the biharmonic Green's function and a contribution from the Laplace Green's function,

$$G_{lap} = \frac{1}{|\mathbf{x} - \boldsymbol{\xi}|} = \frac{1}{\sqrt{R^2 + (z - z')^2}}. \quad (4.96)$$

Hence

$$\chi(R, z, t) = \int_{\partial S} G_{bih}(R, z, z') f(z', t) dz' + \int_{\partial S} G_{lap}(R, z, z') g(z', t) dz' \quad (4.97)$$

$$= \int_{\partial S} \sqrt{R^2 + (z - z')^2} f(z', t) dz' + \int_{\partial S} \frac{g(z', t) dz'}{\sqrt{R^2 + (z - z')^2}}, \quad (4.98)$$

where $f(z, t)$ and $g(z, t)$ are unknown functions to be determined by boundary conditions and matching, and ∂S is the free boundary determining cavity shape. For completeness, we could include other integral terms involving the derivatives of the Green's functions. However, we know from the inner elastic solution for the displacements that there are no singularities as $r \rightarrow 0$ other than those in (4.95) and (4.96).

Scaling $z', r \sim L$, $\chi \sim L^3 \sigma_Y$, $f \sim L \sigma_Y$ and $g \sim L^3 \sigma_Y$, we obtain a nondimensional version where all the terms are now $\mathcal{O}(1)$. In this representation, the cavity is regarded as a line of point sources (of some unknown nature), where $f(z, t)$ and $g(z, t)$ are a measure of the strength of these sources with respect to the biharmonic and Laplace's equation, respectively. We now parameterize the cavity as a line $a < z' < b$, where a is taken to be sufficiently large and negative. We note that in writing this formulation down, we have

implicitly included the boundary conditions of zero stress at infinity as the stress is given in terms of the derivatives of χ . Bearing this in mind, we calculate the derivative

$$\frac{\partial \chi}{\partial R} = \int_a^b \frac{Rf(z', t)dz'}{(R^2 + (z - z')^2)^{\frac{1}{2}}} - \int_a^b \frac{Rg(z', t)dz'}{(R^2 + (z - z')^2)^{\frac{3}{2}}}. \quad (4.99)$$

In order to match this to the inner solution, we briefly reformulate the inner solution in terms of the Love stress function.

4.2.1.1 Inner elastic solution via Love stress function

The inner scalings from §4.1.3 are

$$r = r_j \bar{r}, z = L \bar{z}, \boldsymbol{\sigma} = \sigma_Y \bar{\boldsymbol{\sigma}}, u = \frac{\sigma_Y r_j}{\lambda + 2\mu} \bar{u}, w = \frac{\sigma_Y L}{\lambda + 2\mu} \bar{w}. \quad (4.100)$$

From (C.2) and noting that $\frac{\mu}{\lambda + 2\mu} \sim \mathcal{O}(1)$, we see that the inner scaling for the Love stress function is

$$\chi = r_j^2 L \sigma_Y \bar{\chi}. \quad (4.101)$$

Dropping hats, and recalling the boundary conditions (4.51)-(4.52), the inner problem becomes

$$\left(\frac{1}{r} \frac{\partial}{\partial r} \left(r \frac{\partial}{\partial r} \right) + \epsilon^2 \frac{\partial^2}{\partial z^2} \right)^2 \chi = 0 \text{ for } r \geq R_2(z, t), \quad (4.102)$$

$$\frac{\partial}{\partial z} \left(\frac{\lambda}{2(\lambda + \mu)} \left(\frac{1}{r} \frac{\partial}{\partial r} \left(r \frac{\partial \chi}{\partial r} \right) + \epsilon^2 \frac{\partial^2 \chi}{\partial z^2} \right) - \frac{\partial^2 \chi}{\partial r^2} \right) = \sigma_{rr}^{(p)}(R_2(z, t)) \text{ on } r = R_2(z, t), \quad (4.103)$$

$$\frac{\partial}{\partial r} \left(\frac{\lambda + 2\mu}{2(\lambda + \mu)} \left(\frac{1}{r} \frac{\partial}{\partial r} \left(r \frac{\partial \chi}{\partial r} \right) + \epsilon^2 \frac{\partial^2 \chi}{\partial z^2} \right) - \epsilon^2 \frac{\partial^2 \chi}{\partial z^2} \right) = 0 \text{ on } r = R_2(z, t). \quad (4.104)$$

Instead of using the boundary condition (4.103), it may be more convenient mathematically to use the fact that the material on the elastic-plastic boundary is at yield, and hence say that

$$1 = \frac{\partial}{\partial z} \left(\frac{\partial^2 \chi}{\partial r^2} - \frac{1}{r} \frac{\partial \chi}{\partial r} \right) \text{ on } r = R_2. \quad (4.105)$$

We also observe that, by virtue of the yield condition, continuity of σ_{rr} over the elastic-plastic boundary tells us that $\sigma_{\theta\theta}$ is automatically continuous.

The natural expansion for χ is in powers of ϵ^2 and so we expand

$$\chi \sim \chi_0(r, z, t) + \chi_2(r, z, t)\epsilon^2 + \mathcal{O}(\epsilon^4). \quad (4.106)$$

At leading order,

$$\left(\frac{1}{r} \frac{\partial}{\partial r} \left(r \frac{\partial}{\partial r} \right) \right)^2 \chi_0 = 0. \quad (4.107)$$

Integrating this with respect to r , we find that

$$\chi_0(r, z, t) = \alpha_0(z, t) \log r + \beta_0(z, t) + \gamma_0(z, t)r^2 + \delta_0(z, t)r^2 \log r, \quad (4.108)$$

for some unknown functions $\alpha_0(z, t)$, $\beta_0(z, t)$, $\delta_0(z, t)$ and $\gamma_0(z, t)$. The leading-order nondimensional inner displacements and stresses can now be written as follows:

$$u = -\frac{\sigma_Y}{2\mu} \left(\frac{1}{r} \frac{\partial \alpha_0}{\partial z} + \left(2 \frac{\partial \gamma_0}{\partial z} + \frac{\partial \delta_0}{\partial z} \right) r + 2 \frac{\partial \delta_0}{\partial z} r \log r \right), \quad (4.109)$$

$$w = \frac{2\sigma_Y}{\mu} \frac{(3\mu + \lambda)}{(\lambda + 2\mu)} (\gamma_0 + \delta_0 + \delta_0 \log r), \quad (4.110)$$

$$\sigma_{rr} = \frac{\partial}{\partial z} \left(\frac{2\lambda}{\lambda + \mu} (\gamma_0 + \delta_0) - 3\delta_0 - \frac{2\mu}{\lambda + \mu} \delta_0 \log r + \frac{\alpha_0}{r^2} \right), \quad (4.111)$$

$$\sigma_{\theta\theta} = \frac{\partial}{\partial z} \left(\frac{2\lambda}{\lambda + \mu} (\gamma_0 + \delta_0) - \delta_0 - \frac{2\mu}{\lambda + \mu} \delta_0 \log r - \frac{\alpha_0}{r^2} \right), \quad (4.112)$$

$$\sigma_{zz} = \frac{\lambda + 2\mu}{2(\lambda + \mu)} \frac{\partial}{\partial z} (\gamma_0 + \delta_0 + \delta_0 \log r), \quad (4.113)$$

$$\sigma_{rz} = \frac{1}{\varepsilon} \frac{\lambda + 2\mu}{2(\lambda + \mu)} \frac{\delta_0}{r}. \quad (4.114)$$

At $\mathcal{O}(1)$, equation (4.104) gives us that

$$\frac{\delta_0(z, t)}{a} = 0, \quad (4.115)$$

and so $\delta_0(z, t) = 0$, simplifying (4.109)-(4.114). Similarly, if we were to consider the next-order expansion, we would find that $\delta_1 = 0$, in the obvious notation. The continuity of normal stress equation (4.103) now reduces to

$$\frac{\partial}{\partial z} \left(4\nu\gamma_0(z, t) + \frac{\alpha_0(z, t)}{r^2} + 2\gamma_0(z, t) \right) = \sigma_{rr}^{(p)} \text{ on } r = R_2. \quad (4.116)$$

4.2.1.2 Matching

We now write the outer derivative $\frac{\partial \chi}{\partial R}$ in inner variables, considering each integral in (4.99) individually as $R \rightarrow 0$. Firstly, consider the Laplace term

$$\int_a^b \frac{\varepsilon r g(z', t) dz'}{(\varepsilon^2 r^2 + (z - z')^2)^{\frac{3}{2}}}. \quad (4.117)$$

The main contribution to this integral will be when $z - z' = \mathcal{O}(\varepsilon)$, the resultant integral being $\mathcal{O}(\frac{1}{\varepsilon r})$. We thus approximate $g(z', t) \sim g(z, t)$ and split the integral into a local region of size δ around $z' = z$, where $\varepsilon \ll \delta \ll 1$, assuming that z is not within $\mathcal{O}(\varepsilon)$ of the endpoints (which we may do, as the tip $z' = b$ is not in the slender region, and a is sufficiently negative):

$$\int_a^b \frac{\varepsilon r g(z', t) dz'}{(\varepsilon^2 r^2 + (z - z')^2)^{\frac{3}{2}}} \sim \varepsilon r g(z, t) \left(\int_a^{z-\delta} + \int_{z-\delta}^{z+\delta} + \int_{z+\delta}^b \right) \left(\frac{dz'}{(\varepsilon^2 r^2 + (z - z')^2)^{\frac{3}{2}}} \right). \quad (4.118)$$

Rescaling $z - z' = \varepsilon Z$, the second (local) integral becomes

$$\begin{aligned} \varepsilon r g(z, t) \int_{-\frac{\delta}{\varepsilon}}^{\frac{\delta}{\varepsilon}} \frac{\varepsilon dZ}{(\varepsilon^2 r^2 + \varepsilon^2 Z^2)^{\frac{3}{2}}} &= \frac{r g(z, t)}{\varepsilon} \left[\frac{Z}{r^2 \sqrt{r^2 + Z^2}} \right]_{-\frac{\delta}{\varepsilon}}^{\frac{\delta}{\varepsilon}} \\ &= \frac{2g(z, t)}{\varepsilon r} \frac{\frac{\delta}{\varepsilon}}{\sqrt{r^2 + \frac{\delta^2}{\varepsilon^2}}}. \end{aligned} \quad (4.119)$$

Expanding in terms of $\frac{\varepsilon}{\delta} \ll 1$, this becomes

$$\frac{2g(z, t)}{\varepsilon r} \frac{1}{\sqrt{1 + \left(\frac{\varepsilon r}{\delta}\right)^2}} \sim \frac{2g(z, t)}{\varepsilon r} - g(z, t) \frac{\varepsilon r}{\delta^2}. \quad (4.120)$$

The first “non-local” term of (4.118) is

$$\begin{aligned} \varepsilon r g(z, t) \int_a^{z-\delta} \frac{dz'}{(\varepsilon^2 r^2 + (z - z')^2)^{\frac{3}{2}}} &= -\varepsilon r g(z, t) \left[\frac{z - z'}{\varepsilon^2 r^2 \sqrt{\varepsilon^2 r^2 + (z - z')^2}} \right]_a^{z-\delta} \\ &= -\frac{g(z, t)}{\varepsilon r} \left(\frac{\delta}{\sqrt{\varepsilon^2 r^2 + \delta^2}} - \frac{z - a}{\sqrt{\varepsilon^2 r^2 + (z - a)^2}} \right) \\ &\sim \frac{1}{2} g(z, t) \frac{\varepsilon r}{\delta^2} - \frac{1}{2} g(z, t) \frac{\varepsilon r}{(z - a)^2}. \end{aligned} \quad (4.121)$$

We get a similar expression for the third term of (4.118) and sum the three terms to arrive at

$$\begin{aligned} \int_a^b \frac{\varepsilon r g(z', t) dz'}{(\varepsilon^2 r^2 + (z - z')^2)^{\frac{3}{2}}} &= \frac{2g(z, t)}{\varepsilon r} \left(1 - \frac{(\varepsilon r)^2}{4} \left(\frac{1}{(z - a)^2} + \frac{1}{(b - z)^2} \right) \right) \\ &\sim \frac{2g(z, t)}{\varepsilon r} + \mathcal{O}(\varepsilon r). \end{aligned} \quad (4.122)$$

Hence the Laplace contribution to $\frac{\partial \chi}{\partial r}$ is locally determined by z and, at leading order, independent of the endpoints.

We now turn our attention to the biharmonic part of $\frac{\partial \chi}{\partial r}$. To assess the relative sizes of the global and local contributions, we again split up the range of integration as

$$\int_a^b \frac{\varepsilon r f(z', t) dz'}{(\varepsilon^2 r^2 + (z - z')^2)^{\frac{1}{2}}} \sim \varepsilon r \left(\int_a^{z-\delta} + \int_{z-\delta}^{z+\delta} + \int_{z+\delta}^b \right) \left(\frac{f(z', t) dz'}{(\varepsilon^2 r^2 + (z - z')^2)^{\frac{1}{2}}} \right), \quad (4.123)$$

where $0 \leq \varepsilon \ll \delta \ll 1$. The (second) local part of the integral is dominated when $z - z' \sim \mathcal{O}(\varepsilon)$, and so we rewrite $z - z' = \varepsilon Z$. Thus $f(z', t) \sim f(z, t)$ and the integral becomes

$$\begin{aligned} \varepsilon r f(z, t) \int_{-\frac{\delta}{\varepsilon}}^{\frac{\delta}{\varepsilon}} \frac{dZ}{\sqrt{r^2 + Z^2}} &= 2\varepsilon r f(z, t) \left[\log(Z + \sqrt{r^2 + Z^2}) \right]_0^{\frac{\delta}{\varepsilon}} \\ &= 2\varepsilon r f(z, t) \left(\log \left(1 + \sqrt{1 + \frac{\varepsilon^2 r^2}{\delta^2}} \right) - \log \left(\frac{\varepsilon r}{\delta} \right) \right) \\ &\sim 2\varepsilon r f(z, t) \left(\log \left(\frac{1}{\varepsilon r} \right) + \log \frac{1}{\delta} + \frac{\varepsilon^2 r^2}{4\delta^2} \right) \end{aligned} \quad (4.124)$$

The main contributions from the first and third integrals are [38]

$$-\varepsilon r f(z, t) \left(\log \frac{1}{\delta} + \mathcal{O}(1) \right), \quad (4.125)$$

in both cases, and so

$$\int_a^b \frac{\varepsilon r f(z', t) dz'}{(\varepsilon^2 r^2 + (z - z')^2)^{\frac{1}{2}}} \sim 2\varepsilon r f(z, t) \left(\log \frac{1}{\varepsilon} + \mathcal{O}(1) \right). \quad (4.126)$$

Putting these two together, our outer solution as $R \rightarrow 0$ is

$$\frac{\partial \chi}{\partial R} \sim 2R f(z, t) \left(\log \frac{1}{R} + \mathcal{O}(1) \right) + \frac{2g(z, t)}{R}. \quad (4.127)$$

We need to match this to the inner expression for $\frac{\partial \chi}{\partial r}$, which is given by (4.108) as

$$\frac{\partial \chi}{\partial r} = \frac{\alpha_0(z, t)}{r} + 2r\gamma_0(z, t). \quad (4.128)$$

Introduce the intermediate variable

$$s = \frac{R}{\varepsilon^j} = \varepsilon^{1-j} r, \quad (4.129)$$

where $0 < j < 1$. This leads to the following expressions for the outer and inner radial derivative of χ :

$$\text{Outer: } \frac{\partial \chi}{\partial R} = 2f(z, t)s\varepsilon^j \left(-\log s + j \log \frac{1}{\varepsilon} + \mathcal{O}(1) \right) + \frac{2\varepsilon^{-j}g(z, t)}{s} \dots \quad (4.130)$$

$$\text{Inner: } \varepsilon \frac{\partial \chi_0}{\partial r} = \frac{\alpha_0(z, t)}{s} \varepsilon^{2-j} + 2s\varepsilon^j \gamma_0(z, t) + \dots, \quad (4.131)$$

where we multiply the inner expression by ε to match as we have an r derivative. Matching at leading order, we immediately see that the leading-order term in $g(z, t)$ dominates everything, with nothing to match to in the inner expansion. Hence $g(z, t)$ is zero at leading order, which leads us to pose

$$g(z, t) \sim 0 + \varepsilon^2 g_2(z, t) + \mathcal{O}(\varepsilon^3). \quad (4.132)$$

Continuing with the matching,

$$2g_2(z, t) = \alpha_0(z, t). \quad (4.133)$$

Expanding $f(z, t) \sim f_0(z, t) + \mathcal{O}(\varepsilon)$, matching the logarithmic term tells us that

$$f_0(z, t) = 0, \quad (4.134)$$

and hence

$$\gamma_0(z, t) = 0. \quad (4.135)$$

We observe that these latter two coefficients are nonzero if δ_0 is nonzero in the inner expansion (4.108) for χ . *i.e.* nonzero if the shear stress in the plastic region, σ_{rz} , is nonzero on the elastic-plastic boundary². The inner function $\beta_0(z, t)$ is still undetermined, but not important when writing down expressions for stress and displacement as derivatives with respect to r need to be taken.

The boundary condition (4.116) now yields

$$\frac{\partial \alpha_0}{\partial z} = \sigma_{rr}^{(p)}(R_2, t) R_2^2 = 2 \frac{\partial g_2}{\partial z}. \quad (4.136)$$

Hence we can now give the physical interpretation of the way that the outer solution views the inner solution; the outer sees the inner as a line of point pressure sources, where the pressure is given from the plastic region. Similarly, the canonical fully-elastic problem would have an outer solution which viewed the inner as a line of point pressure sources with strength related to the cavity pressure P .

Continuing the analysis, we elect to use the yield condition (4.105) on the boundary $R_2(z, t)$ and discover that

$$\frac{\partial \alpha_0}{\partial z} = -\frac{1}{2} R_2(z, t)^2. \quad (4.137)$$

Thus the nondimensional leading-order stresses and displacements in the inner elastic region become:

$$u = \frac{\sigma_Y R_2^2}{4\mu r}, \quad (4.138)$$

$$w = 0, \quad (4.139)$$

$$\sigma_{rr} = -\frac{R_2^2}{2r^2} = -\sigma_{\theta\theta}, \quad (4.140)$$

$$\sigma_{rz} = 0 = \sigma_{zz}. \quad (4.141)$$

This is the solution we would get if we considered plane-stress elastic-plastic expansion of a radially-symmetric cavity under internal pressure.

4.2.2 Matching with a fully inertial outer region

In the quasistatic case, the inner solution for the Love stress function is

$$\chi_0 \sim \alpha_0(z, t) \log r + \beta_0(z, t) + \gamma_0(z, t) r^2. \quad (4.142)$$

When searching for an outer solution, we considered a Green's function representation in which the stress decayed at infinity. Matching these solutions together gave us that

²Indeed, if there is a nonzero plastic shear stress, we would match $f_0 = -\delta_0$ by looking at the coefficient of $\varepsilon^j \log \frac{1}{\varepsilon}$. Performing further matching, we would discover that f_0 is actually smaller than we thought, and should be rescaled $f_0 = \frac{2\gamma_0}{1+2\log \frac{1}{\varepsilon}} \sim \frac{\gamma_0}{\log \frac{1}{\varepsilon}} \left(1 - \frac{1}{2\log \frac{1}{\varepsilon}} + \dots\right)$.

$\gamma_0(z, t) = 0$, and so we effectively recovered a two-dimensional solution in the inner. We could perhaps have seen this with little work. The outer solution for χ must satisfy $\chi_r \rightarrow 0$ as $\mathbf{r} \rightarrow \infty$, and χ_r must match with the inner. The $\gamma_0(z, t)r^2$ in the inner is the dominant term when matching into the outer giving the boundary condition on the outer that $\chi_r \sim 2\gamma_0(z, t)r$ as $r \rightarrow 0$. Since (unlike the log terms), such a condition gives no singularity in the biharmonic equation, the outer solution is $\gamma_0 = 0$ by uniqueness.

A similar argument applies if waves are present. Consider, as a paradigm, the wave equation outside a slender body:

$$\nabla^2 \phi = \frac{1}{c^2} \frac{\partial^2 \phi}{\partial t^2}, \quad (4.143)$$

with boundary condition

$$\phi \rightarrow 0 \text{ as } \mathbf{r} \rightarrow \infty, \quad (4.144)$$

and an inner slender solution of

$$\phi_0 \sim A(z, t) + B(z, t) \log r, \quad (4.145)$$

for some arbitrary functions $A(z, t)$ and $B(z, t)$. We assume that all waves are outgoing. Suppose that there are no singularities in the wave-field, so that $B(z, t) = 0$. Uniqueness of solutions to the wave equation on a domain with no singularities then tells us that the only solution is the zero solution.

The same idea holds in the case of the full Navier equations. Equation (4.142) still holds in the inner elastic region, even with inertia. Assuming that there is no incoming radiation and given that the outer is dominated by the $\gamma_0(z, t)r^2$ and sees no singularities, we can use the principle of reciprocity (as the Green's functions are self-adjoint) and uniqueness of solutions to the Navier equations to determine that $\gamma_0 = 0$. Hence, the analysis of the previous section is still valid, and we can now match between the inner plastic and elastic regions. Note that we have not solved the outer problem; we have merely used decaying stress, matching and uniqueness to set an inner coefficient to zero.

4.2.2.1 Matching between different regions

Using continuity of the radial stress (4.70) over the elastic-plastic boundary, R_2 , we can get an expression for the position of the free boundary in terms of the fluid-plastic boundary, R_1 , viz:

$$R_2(z, t) = R_1(z, t) \exp\left(\alpha P - \frac{1}{2}\right). \quad (4.146)$$

Using this in conjunction with the plastic mass flux equation (4.67), we obtain

$$\frac{\partial}{\partial z} (\dot{w} R_1^2 (\exp(2\alpha P - 1) - 1)) = \frac{\partial}{\partial t} R_1^2. \quad (4.147)$$

In order to fully determine the plastic velocities and displacements, we need to consider the axial stresses in both plastic and elastic regions, as discussed in detail by Hill [36]. In a *finite* gun-barrel problem, say $a_0 < r < b_0$, these are determined via an axial force balance. We suppose that a longitudinal force L is applied on each end of the barrel, so that the force balance becomes

$$L = \int_{\theta=0}^{2\pi} \int_{r=a_0}^{b_0} \sigma_{zz} r dr d\theta. \quad (4.148)$$

The parameter L can depend on whether the ends of the gun-barrel are open ($L = 0$, which corresponds to plane-stress), closed ($L = \pi a_0^2$) or whether some intermediate mathematically-convenient rule such as plane-strain is chosen. In the case of a partially-plastic gun-barrel, we can see that this integral will have a plastic contribution and an elastic contribution for the axial stress. Hence, as σ_{zz} should really be determined by Reuss' equations, it must depend on the strain-history. On applying Reuss' equations and changing to coordinates following an element, one can derive a hyperbolic system of equations. The boundary conditions for these equations are continuity of σ_{zz} and continuity of velocity (following a particle) on the elastic-plastic boundary. Alas, the hyperbolic system can rarely be solved explicitly and one often needs to resort to numerical methods. Fortunately, approximations can be made when considering the expansion of a cavity into an infinite elastic medium. It transpires that using the Lèvy-Mises equations with the aforementioned boundary conditions does not lead to significant errors in this case. This is discussed in detail in [35, 36, 37]. Hence we apply continuity of σ_{zz} over $R_2(z, t)$ and, using (4.146), we see from (4.76) that

$$\frac{1}{2} \frac{\frac{\partial \dot{w}^{(0)}}{\partial z}}{\frac{\partial}{\partial z}(R_0^2 \dot{w}^{(0)})} R_2^2 = 0. \quad (4.149)$$

Thus the plastic axial velocity satisfies, at leading order,

$$\dot{w}(z, t) = \dot{W}(t). \quad (4.150)$$

This velocity must be determined by matching into the tip region.

In summary, dropping numeric superscripts which denoted leading order, the elastic displacements and stresses are given by (4.138)-(4.141), whilst the plastic displacements

and stresses are

$$\dot{w}^{(p)} = \dot{W}(t), \quad (4.151)$$

$$\dot{u}^{(p)} = \frac{\dot{W}(t)}{2r} \frac{\partial}{\partial z}(R_2^2) = \frac{\dot{W}(t)}{2r} \frac{\partial}{\partial z}(R_1^2 \exp(2\alpha P - 1)), \quad (4.152)$$

$$\sigma'_{rr} = -\frac{1}{2} = -\sigma'_{\theta\theta}, \quad (4.153)$$

$$\sigma'_{zz} = 0, \quad (4.154)$$

$$\sigma_{rr}^{(p)} = -\alpha P + \log \frac{r}{R_1}, \quad (4.155)$$

$$\sigma_{\theta\theta}^{(p)} = -\alpha P + 1 + \log \frac{r}{R_1}, \quad (4.156)$$

$$\sigma_{zz}^{(p)} = -\alpha P + \frac{1}{2} + \log \frac{r}{R_1}, \quad (4.157)$$

where P is the pressure from the fluid region. We observe from this that σ_{zz} is indeed the intermediate principal stress and so the solution is self-consistent.

4.2.3 Comments

We have derived a model for penetration far from the tip, valid when the slender plastic velocities are small compared to the jet velocity. Analysis of the fluid region yielded a conservation of mass equation (4.29), an ‘eikonal’ equation (4.31), and an expression for the pressure on the free boundary $r = R_1(z, t)$, (4.33). These equations are written in terms of the unknowns $\phi_0(z, t)$, $R_0(z, t)$, $R_1(z, t)$, $U(t)$ and $P(z, t)$. Matching into the plastic region furnished us with an evolution-equation, (4.147), for the free boundary $r = R_1(z, t)$ in terms of the axial plastic velocity component, whilst matching into the inner and outer elastic regions revealed that the axial component of plastic velocity is a constant function of time, sadly unknown. Hence we have four coupled equations and six unknowns. The extra conditions must come from matching with the intricate tip region. Indeed, we expect tip matching to provide equations for the leading-order fluid velocity potential and the axial component of the plastic velocity. Such analysis is highly non-trivial. However, we can gain some intuition regarding the behaviour of our system of equations by considering the possibility of travelling-wave solutions.

4.3 Travelling-wave solution

In this section, we attempt to find a travelling-wave solution to the system of the equations in which the tip moves with constant velocity. This velocity must be the same order of magnitude as the plastic axial velocity by conservation of mass, as the target material is excavated on the same timescale as the penetration occurs. Hence, we introduce a

travelling wave variable

$$\xi = z - \delta U t, \quad (4.158)$$

where z and t are with respect to the original frame, and $\delta \ll \varepsilon^{\frac{1}{2}}$ is a scale for the travelling-wave velocity. We nondimensionalise the axial scale with L , time with $L/(\delta U)$ and velocity with U , so that the derivatives become

$$\frac{\partial}{\partial t} = -\delta \frac{d}{d\xi}, \quad (4.159)$$

$$\frac{\partial}{\partial z} = \frac{d}{d\xi}. \quad (4.160)$$

Mirroring the analysis of the jet, we introduce a nondimensional potential function in the travelling-wave frame, defined by

$$\psi(r, \xi, t) = \phi(r, z, t) - \delta \xi. \quad (4.161)$$

The boundary condition (3.7) on $R_0(z, t)$ and (4.17) on $R_1(z, t)$ thus become, at leading order,

$$\frac{\partial \psi}{\partial r} - \varepsilon^2 \frac{\partial R_0}{\partial \xi} \frac{\partial \psi}{\partial \xi} = 0 \text{ on } r = R_0, \quad (4.162)$$

$$\frac{\partial \psi}{\partial r} - \varepsilon^2 \frac{\partial R_1}{\partial \xi} \left(\frac{\partial \psi}{\partial \xi} + \delta \right) = 0 \text{ on } r = R_1. \quad (4.163)$$

Expanding this in powers of ε^2 , we again find from Laplace's equation that $\psi_0 = \psi_0(\xi, t)$, and so the $\mathcal{O}(\varepsilon^2)$ boundary conditions on $r = R_0$ and $r = R_1$ give the modified mass conservation (*c.f.* (4.29))

$$\frac{\partial}{\partial \xi} \left(\frac{\partial \psi_0}{\partial \xi} (R_1^2 - R_0^2) \right) = 0. \quad (4.164)$$

Recall Bernoulli's equation in the rest frame, (3.2). In nondimensional travelling-wave variables, this becomes

$$-\delta \frac{\partial}{\partial \xi} (\delta \xi + \psi) + p + \frac{1}{2} \left(\frac{1}{\varepsilon^2} \left(\frac{\partial \psi}{\partial r} \right)^2 + \left(\delta + \frac{\partial \psi}{\partial \xi} \right)^2 \right) = G. \quad (4.165)$$

We quickly substitute the asymptotic expansion for ψ and apply the boundary condition $p(R_0) = 0$ to discover, at leading order,

$$\frac{1}{2} \left(\frac{\partial \psi_0}{\partial \xi} \right)^2 = G. \quad (4.166)$$

We determine G by considering the far-field solution. Consider, in the rest frame, the incoming jet with nondimensional velocity $\bar{V} = V/U$ with corresponding nondimensional penetration velocity δ (moving with the stagnation point). Changing to a frame moving

with the stagnation point and dropping bars, the incoming jet has relative velocity $V - \delta \sim V$. By applying steady-Bernoulli to the inner free boundary on which the pressure $p = 0$, we see that the returning jet must have speed V at leading order in the negative z -direction. Thus, in our travelling wave formulation, the velocity for large negative ξ must be $-V$ and so, up to an additive constant, $\psi = -V\xi$ for large negative ξ . Thus

$$G = \frac{1}{2}V^2. \quad (4.167)$$

We can now solve for ψ , and, taking the negative root to satisfy the flow for large negative ξ , we see that

$$\psi_0(\xi) = -V\xi + \text{constant}, \quad (4.168)$$

and so we have plug flow. Substituting into the mass conservation equation (4.164) tells us that

$$R_1^2 = A + R_0^2, \quad (4.169)$$

where A is a positive constant. Continuing with the analysis, the $\mathcal{O}(\varepsilon^2)$ correction to velocity potential is given by (*c.f.* (4.26))

$$\psi_2(\xi, r, t) = C(\xi, t) \log r + D(\xi, t). \quad (4.170)$$

Applying the $\mathcal{O}(\varepsilon^2)$ boundary conditions (4.162)-(4.163) determines

$$C(\xi, t) = \frac{1}{2} \frac{\partial}{\partial \xi} (V R_0^2) = \frac{1}{2} \frac{\partial}{\partial \xi} (V R_1^2). \quad (4.171)$$

Hence the $\mathcal{O}(\varepsilon^2)$ pressure equation gives the inflation pressure for the plastic region as

$$\begin{aligned} p(R_1) - p(R_0) &= -\frac{\varepsilon^2}{2} \left[\left(\frac{\partial \psi_2}{\partial r} \right)^2 + 2 \frac{\partial \psi_0}{\partial \xi} \frac{\partial \psi_2}{\partial \xi} \right]_{R_0}^{R_1} \\ &= \left(\frac{1}{2} C(\xi, t)^2 \left(\frac{1}{R_0^2} - \frac{1}{R_1^2} \right) + V \frac{\partial C}{\partial \xi} \log \left(\frac{R_1}{R_0} \right) \right) \varepsilon^2, \end{aligned} \quad (4.172)$$

We now eliminate R_0 , letting $R_1^2(\xi) = f(\xi)$. The inflation pressure thus becomes

$$p(R_1) = \frac{V^2 \varepsilon^2}{8} \left(\frac{A f'^2}{f(f-A)} + 2 \log \left(\frac{f}{f-A} \right) f'' \right). \quad (4.173)$$

When coupling the jet equations with the elasto-plastic analysis, we expect that the nondimensional travelling-wave speed δ will play a more prominent part in the plastic region. Indeed, the mass equation (4.67) becomes

$$-\delta \frac{\partial}{\partial \xi} (-R_1^2) + \frac{\partial}{\partial \xi} (\delta \dot{w} (R_2^2 - R_1^2)) = 0. \quad (4.174)$$

Recall that the nondimensional axial velocity is constant, W , say, in the rest frame. For a physical solution, this constant must be negative or zero, as any plastic flow will be driven by back-flow from the tip. On integration, we discover that

$$(1 - W)R_1^2 + WR_2^2 = Q, \quad (4.175)$$

for some constant Q .

We initially consider the case of $W = 0$. This gives that $R_1^2 = Q$, and so, using (4.171), $C(\xi, t) = 0$. From equation (4.172), we deduce that the fluid pressure $p(R_1) \sim \mathcal{O}(\varepsilon^4)$, which is insufficient to yield the surrounding target material. This contradicts the assumption of a plastic region in our model, and so we must consider $W < 0$.

The crucial observation for $W < 0$ is that the plastic region cannot terminate. This is because the plastic normal velocity at this termination point is still finite and so cannot equal the zero normal velocity in the elastic region (and so the termination point is a singularity). This will be discussed in a later chapter. Differentiation of (4.175) gives

$$(1 - W)R_1R_1' + WR_2R_2' = 0, \quad (4.176)$$

and so the signs of R_1' and R_2' are the same. From the previous paragraph, we know that $C(\xi, t) = 0$ corresponds to the termination of the plastic region at some point, which is not physically permissible. However, equation (4.176) tells us that if either of the derivatives of R_1 and R_2 is zero, then so is the other. We can see from equation (4.171) that this would lead to $C(\xi, t) = 0$, and thus deduce that all the free boundaries must be strictly monotonic. Furthermore, we can see that the free boundaries must be monotonically decreasing. This is because all free boundaries tend to zero for sufficiently large negative z if the derivatives are positive, corresponding to the termination of both jet and plastic regions.

Rearranging (4.175), we see that

$$R_2^2 - R_1^2 = -\frac{1}{W}(R_1^2 - Q), \quad (4.177)$$

thus $R_1^2 > Q$. After some algebra, equation (4.146) gives

$$P = \frac{1}{2\alpha} \left(1 + \log \left(\frac{1}{\beta} + \frac{Q}{Wf} \right) \right), \quad (4.178)$$

where $\beta = -W/(1 - W) > 0$ and the logarithmic term is well-defined. Coupling this with (4.173) results in the following nonlinear second-order equation:

$$2f'' \log \left(\frac{f}{f - A} \right) + \frac{Af'^2}{f(f - A)} = \gamma \left(1 + \log \left(\frac{1}{\beta} + \frac{Q}{Wf} \right) \right), \quad (4.179)$$

Introducing $X(\xi) = f(\xi)$ and $Y(\xi) = f'(\xi)$, the second-order equation decomposes into the following system of two first-order equations:

$$X' = Y, \quad (4.180)$$

$$Y' = \frac{1}{2 \log \frac{X}{X-A}} \left(\gamma \left(1 + \log \left(\frac{1}{\beta} + \frac{Q}{WX} \right) \right) - \frac{AY^2}{X(X-A)} \right). \quad (4.181)$$

From equation (4.169) we note that, for a physical solution, $X > A$ and so Y' is well-defined. The equilibrium point (X_c, Y_c) is given by

$$X_c = \frac{Qe}{e - W(e - 1)}, \quad (4.182)$$

$$Y_c = 0. \quad (4.183)$$

Note that $|X_c| < |Q|$. We linearise the system about this point and discover that the eigenvalues of the linear system are determined by the roots of

$$\lambda^2 + \frac{\gamma Qe}{2(-W)X^2} \left(\log \left(\frac{X_c - A}{X_c} \right) \right)^{-1} = 0. \quad (4.184)$$

The nullclines are given by

$$Y = 0 \text{ and } Y = \pm \sqrt{\frac{\gamma}{A} X(X-A) \left(1 + \log \left(\frac{1}{\beta} + \frac{Q}{WX} \right) \right)}. \quad (4.185)$$

We are hence presented with four possible phase planes, depending on the relative sizes of Q , X_c and A . However, we can make deductions about the system without detailed analysis of these phase planes and without determination of the equilibrium point by arguing as follows. Suppose that a trajectory starts from (X_0, Y_0) . Firstly, we know that $Y_0 < 0$ as the derivatives of the free boundaries are negative. Secondly, from (4.177), we must have that $X_0 > Q$ for existence of the plastic region. Hence, any physical trajectory must start with $X_0 > Q$ and $Y_0 < 0$. Such trajectories, shown in Fig. 4.3, will always travel along paths with decreasing X . There are three separate possibilities:

- A trajectory meets $Y = 0$ before reaching $X = Q$ or $X = A$ and then moves with increasing X in the upper-half plane;
- A trajectory meets $X = Q$ for some $Y < 0$ (if $Q > A$);
- A trajectory meets $X = A$ for some $Y < 0$ (if $Q < A$).

The first case corresponds to the termination of the plastic region (zero pressure), which we know cannot happen owing to the mismatch in velocities at the termination point. From equation (4.177), we deduce that the second possibility results in $R_2 \rightarrow R_1$, and so is again invalid owing to the termination of the plastic region. Finally, using equation (4.169), we discover that the third possibility results in the jet region terminating, again physically unacceptable and so, ineluctably, the travelling-wave formulation fails for $W < 0$.

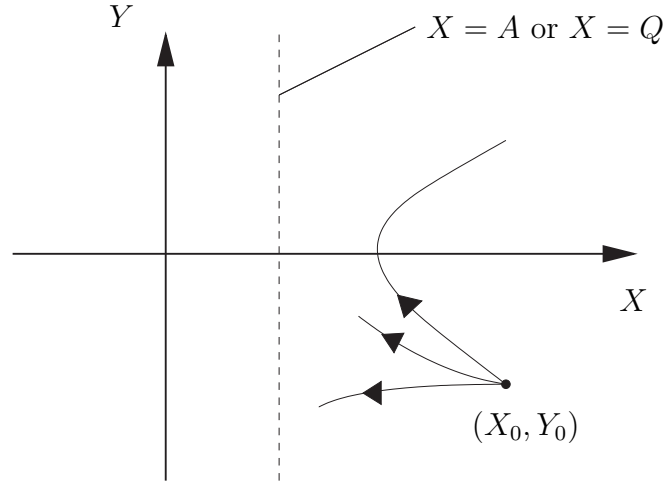


Figure 4.3: A schematic phase-plane of possible trajectories from (X_0, Y_0) .

4.4 Inertial effects

We have considered a parameter regime in which the plastic velocities in the slender region were significantly smaller than the jet velocity. This was motivated by supposing that the plastic velocity matching from the tip to the slender region was small. In this section, we allow the slender plastic velocity-scale to be comparable to the jet velocity.

4.4.1 Modified inertial equations

Most of the slender jet equations are unchanged; the only difference is that there is no longer a mismatch in velocity scales over $r = R_1(z, t)$, so the kinematic boundary condition on $r = R_1(z, t)$ in the moving frame is (*c.f.* (4.16))

$$\frac{\partial \phi}{\partial r} - \varepsilon^2 \frac{\partial R_1}{\partial z} \frac{\partial \phi}{\partial z} = \varepsilon^2 \frac{\partial R_1}{\partial t} \quad \text{on } r = R_1(z, t). \quad (4.186)$$

This results in (4.27)-(4.28) being replaced by

$$C(z, t) = \frac{1}{2} \frac{\partial}{\partial t} (R_j^2) + \frac{1}{2} \frac{\partial}{\partial z} \left(\frac{\partial \phi_0}{\partial z} R_j^2 \right), \quad j = 0, 1. \quad (4.187)$$

Conservation of mass is thus given by

$$\frac{\partial}{\partial t} (R_1^2 - R_0^2) + \frac{\partial}{\partial z} \left(\frac{\partial \phi_0}{\partial z} (R_1^2 - R_0^2) \right) = 0. \quad (4.188)$$

Note that we could have obtained this expression directly by considering mass flux through the annulus $R_0(z, t) \leq r \leq R_1(z, t)$ via the relation

$$\frac{\partial}{\partial t} \int_0^{2\pi} \int_{R_0}^{R_1} r dr d\theta + \frac{\partial}{\partial z} \int_0^{2\pi} \int_{R_0}^{R_1} \left(\frac{\partial \phi_0}{\partial z} \right) r dr d\theta = 0. \quad (4.189)$$

The Bernoulli equation (giving (4.31)) and expression for the pressure P on the boundary $r = R_1(z, t)$ are unchanged, albeit with $C(z, t)$ given by (4.187).

The plastic region beholds more significant changes. Firstly, recall that we need to assume that $\varepsilon^2 \alpha \sim \mathcal{O}(1)$ for the material by the cavity to be plastic, where $\alpha = \rho_t U_0^2 / \sigma_Y$. Writing this parameter as α_* , the nondimensional force-balance equations (4.44)-(4.45) become

$$\frac{\partial \sigma_{rr}}{\partial r} + \varepsilon \frac{\partial \sigma_{rz}}{\partial z} + \frac{\sigma_{rr} - \sigma_{\theta\theta}}{r} = \alpha_* \frac{\partial \dot{u}}{\partial t}, \quad (4.190)$$

$$\frac{\partial \sigma_{rz}}{\partial r} + \varepsilon \frac{\partial \sigma_{zz}}{\partial z} + \frac{\sigma_{rz}}{r} = \frac{\alpha_*}{\varepsilon} \frac{\partial \dot{w}}{\partial t}. \quad (4.191)$$

The flow law (4.37)-(4.40) is unchanged. The second of the force-balance equations, in addition to (4.40), indicates that the shear stress should have the expansion

$$\sigma_{rz} = \frac{1}{\varepsilon} \sigma_{rz}^{(-1)} + \mathcal{O}(1). \quad (4.192)$$

The leading-order force-balance equations now become

$$\frac{\partial \sigma_{rr}}{\partial r} + \frac{\partial \sigma_{rz}^{(-1)}}{\partial z} + \frac{\sigma_{rr} - \sigma_{\theta\theta}}{r} = \alpha_* \frac{\partial \dot{u}}{\partial t}, \quad (4.193)$$

$$\frac{\partial \sigma_{rz}^{(-1)}}{\partial r} + \frac{\sigma_{rz}^{(-1)}}{r} = \alpha_* \frac{\partial \dot{w}}{\partial t}. \quad (4.194)$$

The boundary conditions on the inner boundary $r = R_1(z, t)$ remain as (4.49)-(4.50), whereas inertial terms now need to be included on the elastic-plastic boundary $r = R_2(z, t)$. These are written nondimensionally as

$$[\dot{u}_n]_{-}^{+} = 0, \quad (4.195)$$

$$\left[\sigma_{in}^{(-1)} - \frac{\rho_t}{\rho_j} \alpha_* (\dot{u}_n - \frac{\partial R_2}{\partial t}) \dot{u}_i \right]_{-}^{+} = 0. \quad (4.196)$$

We can rearrange the flow law to obtain

$$\frac{2\sigma_{rz}^{(-1)}}{\frac{\partial \dot{w}}{\partial r}} = \Lambda = \frac{1}{\frac{\dot{u}}{r} - \frac{\partial \dot{u}}{\partial r}}. \quad (4.197)$$

Thus we have the following three nondimensional equations for \dot{w} , \dot{u} and $\sigma_{rz}^{(-1)}$:

$$\frac{1}{r} \frac{\partial}{\partial r} (r \dot{u}) + \frac{\partial \dot{w}}{\partial z} = 0, \quad (4.198)$$

$$2 \frac{\partial}{\partial r} \left(\frac{\dot{u}}{r} \right) r \sigma_{rz}^{(-1)} + \frac{\partial \dot{w}}{\partial r} = 0, \quad (4.199)$$

$$\frac{1}{r} \frac{\partial}{\partial r} (r \sigma_{rz}^{(-1)}) = \frac{\partial \dot{w}}{\partial t}. \quad (4.200)$$

The remaining components of the stress tensor decouple and are given by the yield condition, which we write as

$$\sigma_{\theta\theta} - \sigma_{rr} = 1, \quad (4.201)$$

and

$$\frac{\partial \sigma_{rr}}{\partial r} + \frac{\partial \sigma_{rz}^{(-1)}}{\partial z} = \frac{1}{r} + \alpha_* \frac{\partial \dot{u}}{\partial t}. \quad (4.202)$$

We can eliminate $\sigma_{rz}^{(-1)}$ from the system (4.198)-(4.200) to reach

$$\begin{aligned} \frac{\partial \dot{w}}{\partial t} &= -\frac{1}{r} \frac{\partial}{\partial r} \left(\frac{1}{2 \frac{\partial}{\partial r} \left(\frac{\dot{u}}{r} \right)} \frac{\partial \dot{w}}{\partial r} \right) \\ &= -\frac{1}{2r} \left(\frac{\dot{w}_{rr}}{(\dot{u}/r)_r} - \frac{\dot{w}_r}{((\dot{u}/r)_r)^2} \left(\frac{\dot{u}}{r} \right)_{rr} \right). \end{aligned} \quad (4.203)$$

Using (4.198), this can be rewritten as an equation for $\dot{w}(r, z, t)$ as

$$\dot{w}_t = f(r, \dot{u}, \dot{u}_r, \dot{w}_z) \dot{w}_{rr} + g(r, \dot{u}, \dot{u}_r, \dot{w}_z) \dot{w}_{rz}, \quad (4.204)$$

for some functions f and g . This equation has two real characteristics in space, and can be transformed to an equation of the form

$$\frac{\partial \dot{w}}{\partial t} = \tilde{f} \frac{\partial^2 \dot{w}}{\partial r^2} - \tilde{g} \frac{\partial^2 \dot{w}}{\partial z^2}, \quad (4.205)$$

for some \tilde{f} and \tilde{g} such that $\tilde{f}\tilde{g} > 0$. We could attempt to solve this novel partial differential equation using a travelling-wave variable. However, we can think of this rather nasty equation as forward diffusion in one spatial variable, and backward diffusion in the other. Thus it is likely to be ill-posed³.

4.5 Comments on elastic-plastic modelling

We have developed elastic-plastic models based on the traditional Birkhoff impact models (see §2.1.1). Initially, we considered a model in which the scales for the plastic velocities were significantly smaller than the velocity scale for the returning jet. The result of this was a quasistatic model, with a partial solution in need of information from matching with the tip. We attempted a travelling-wave solution, even though it would predict an infinite cavity-depth. This was to gain intuition into the penetration. Sadly, this approach failed, suggesting that either the free boundary $R_0 \rightarrow 0$ (unphysical) or the termination of the plastic region ($R_2 \rightarrow R_1$). Attempts at a model in which the plastic velocities were

³We could try this plastic velocity-scale with constant \dot{w} . This remedies the problem with the equation being ill-posed, but the matching conditions into the inner elastic region are still inertial, leading to another non-trivial problem.

comparable to the jet velocity also had limited success. We discovered that the effects of inertia in the plastic region now became important, but the equations resulted in an ill-posed partial differential equation. This suggests we were correct in neglecting plastic inertia, although warrants further investigation. Finally, our estimate on the size of $\alpha\epsilon^2$ shows that the pressure is insufficient to induce plasticity in the slender region unless the yield stress of the target is sufficiently low. This indicates that the plasticity should be confined to a region near the tip for a more realistic yield stress.

We could embark on several routes to a solution. For example, we could construct a model in which the plastic region has finite extent (Fig. 4.4), as suggested by the earlier travelling-wave formulation and the previous comment. Depending on the extent of the

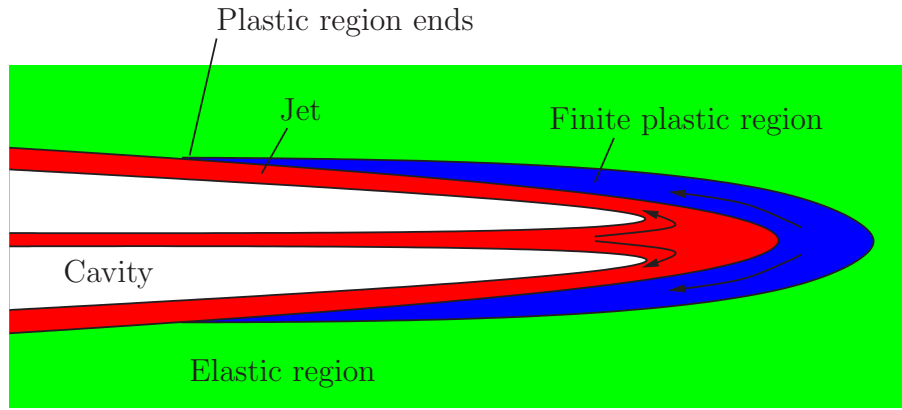


Figure 4.4: Penetration with finite plastic region.

plastic region, this could lead to two slender regions, one with a plastic zone and one without, separated by some transition region. We could also try a similarity solution or numerical solutions for different scalings of both the radii of the separate regions and for different velocity scales (recall Fig. 3.7 and Fig. 3.8). However, before wading in with detailed analysis, it is prudent to make some important observations:

- Neglecting any spall effects, there is no apparent mass loss in the target material after penetration [93]. More explicitly, this means that little or no target material gets ejected from the point of entry.
- Before penetration, the target is pristine. The jet exerts a high pressure on the target on impact and as it penetrates. This applied pressure, however, returns to zero as the penetration terminates. Hence, in view of the previous observation, use of a linear elasticity model⁴ predicts that the cavity radius must return to zero!

⁴Linear elasticity cannot be responsible for the initial opening of the cavity in the target either. It is likely that the target is immediately plastic on impact, although nonlinear elasticity effects could be partially responsible for the initial excavation of the cavity.

- When looking at a penetrated target block, we observe that all four unpenetrated sides have bowed. This adds weight to the previous observation, and is shown in Fig. 4.5.

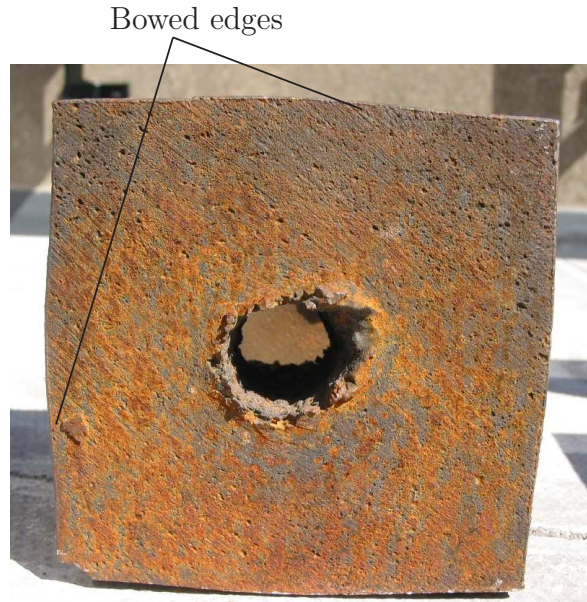


Figure 4.5: A photograph of a penetrated block, showing clear bowing of the edges.

These three observations all indicate that accurate modelling will require some method of ‘locking in’ residual stresses and displacements after the penetration has finished. Clearly, this cannot be a result of linear elasticity theory and must occur as a result of the severe deformation in the plastic region. This suggests that we need to carefully consider the paradigm cavity expansion problem in more detail.

Chapter 5

Gun-barrel mechanics

When a gun is fired, its barrel is put under high stress by high-pressure gases. Eventually, this will lead to fatigue in the gun-barrel, which will ultimately be rendered useless. It was known at least as early as the second world war that by cyclically loading and unloading the gun-barrel, one can introduce beneficial residual stresses which considerably improve the fatigue life of the gun-barrel [90]. This process is known as *autofrettage*, literally meaning “self-hooping”. The basic idea is that the cavity pressure is increased so that the material yields, and then increased further past the yield limit. When the pressure is eventually released, some of the material will have been plastic and some of the material was always elastic. It is in the former that we “lock in” plastic stress and displacement. Thus, when returning the cavity pressure to zero, we have introduced some residual stresses. This process is also of great importance in high pressure pump cylinders and other vessels that are subjected to high pressures.

The theory of finite autofrettaged cylinders has been studied with various plasticity models, such as perfect plasticity with the Bauschinger effect [80], Hencky’s equations [101] and a constitutive power-law with Bauschinger effect [48]. Numerical solutions have also been investigated [66]. Our slender model of the previous chapter essentially treated the returning jet as a pseudo-pressure source to enable a two-dimensional, radially-symmetric, elastic-plastic expansion of the target material. We implicitly assumed that the same equations would hold irrespective of the history of the position of the elastic-plastic boundary and of whether the plastic region is expanding ($\dot{P} > 0$) or contracting ($\dot{P} < 0$). In this chapter, we wish to write down a model that allows us to lock in plastic stress, thus taking into account some history. To do this, we consider the paradigm two-dimensional, radially-symmetric cavity expansion problem in an infinite elastic medium in some detail. We will start by considering infinitesimal displacement of the inner cavity, using the equations of linear elasticity. We will then use the linear model as a mould for a nonlinear model and attempt to reconcile it with Fig. 4.5 to formulate a better theory

for penetration, before considering simple asymmetric problems.

5.1 Linear elastic perfect-plastic cavity model

5.1.1 Elastic expansion

Consider a circular cavity of radius a in an infinite linear elastic medium. We let the internal cavity pressure be $P(t)$, so that the internal boundary condition is

$$\sigma_{rr}(a) = -P(t). \quad (5.1)$$

We also impose zero stress at infinity (so zero displacement). By virtue of the inherent radial symmetry, we can immediately write down $\sigma_{r\theta} = 0$. If $P(t)$ is not sufficiently large to induce yield, the medium remains elastic, and the remaining nonzero components of the stress tensor are well-known to be [49]

$$\sigma_{rr} = -\frac{a^2 P(t)}{r^2}, \quad (5.2)$$

$$\sigma_{\theta\theta} = \frac{a^2 P(t)}{r^2}. \quad (5.3)$$

The corresponding displacements are

$$u = \frac{a^2 P(t)}{2\mu r}, \quad (5.4)$$

$$v = 0. \quad (5.5)$$

5.1.2 Elastic-plastic expansion

We now increase the pressure so that the material yields. We will again use the Tresca yield condition for the plastic region,

$$|\sigma_{\theta\theta} - \sigma_{rr}| = \sigma_Y. \quad (5.6)$$

From (5.2)-(5.3), it is clear that the maximum of $\sigma_{\theta\theta} - \sigma_{rr} = \frac{2a^2 P}{r^2}$ occurs on the inner boundary $r = a$ and so the elastic medium yields from the centre. We denote the elastic-plastic free boundary by $r = c(t)$, shown in Fig. 5.1, and will use superscripts ‘p’ and ‘e’ to denote ‘plastic’ and ‘elastic’, respectively.

5.1.2.1 Plastic Region

In addition to the Tresca yield condition, we use an incompressible flow law to represent plastic flow,

$$\sigma'_{ij} = \Lambda \dot{\epsilon}_{ij}, \quad (5.7)$$

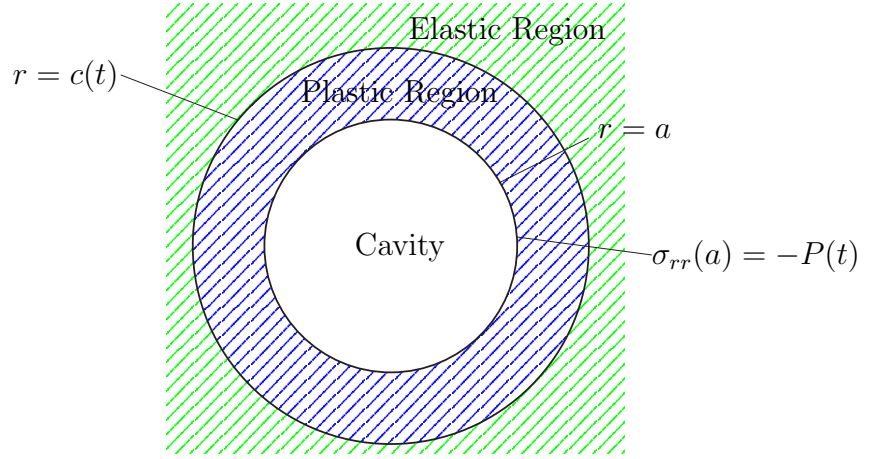


Figure 5.1: Expansion of a gun-barrel under applied pressure $P(t)$.

so that conservation of mass is

$$\frac{\partial \dot{u}}{\partial r} + \frac{\dot{u}}{r} = 0. \quad (5.8)$$

The usual quasistatic radial force balance is

$$\frac{\partial \sigma_{rr}^{(p)}}{\partial r} + \frac{\sigma_{rr}^{(p)} - \sigma_{\theta\theta}^{(p)}}{r} = 0. \quad (5.9)$$

The boundary conditions are

$$\sigma_{rr}^{(p)}(a) = -P(t), \quad (5.10)$$

$$\sigma_{r\theta}^{(p)}(a) = 0, \quad (5.11)$$

$$[\sigma_{rr}]_{r=c-}^{r=c+} = 0, \quad (5.12)$$

$$[\dot{u}]_{r=c-}^{r=c+} = 0, \quad (5.13)$$

$$[u]_{r=c-}^{r=c+} = 0. \quad (5.14)$$

We can immediately solve for the stresses and see that the nonzero components of the plastic stress tensor are

$$\sigma_{rr}^{(p)} = -P(t) + \sigma_Y \log\left(\frac{r}{a}\right), \quad (5.15)$$

$$\sigma_{\theta\theta}^{(p)} = -P(t) + \sigma_Y \left(\log\left(\frac{r}{a}\right) + 1 \right). \quad (5.16)$$

Before looking at the flow law, we need to gain some information from the elastic region.

5.1.2.2 Elastic Region

In the elastic region $r > c(t)$, we again solve the quasistatic versions of (B.1)-(B.2). Apart from the continuity conditions (5.12)-(5.14), we impose zero stress at infinity. Solving the

equilibrium equations, we obtain the usual Lamé solution

$$u^{(e)} = Ar + \frac{B}{r}, \quad (5.17)$$

with corresponding nonzero components of stress

$$\sigma_{rr}^{(e)} = 2(\lambda + \mu)A - \frac{2\mu B}{r^2}, \quad (5.18)$$

$$\sigma_{\theta\theta}^{(e)} = 2(\lambda + \mu)A + \frac{2\mu B}{r^2}. \quad (5.19)$$

Use of the boundary conditions gives us $A = 0$, $B = \frac{\sigma_Y c(t)^2}{4\mu}$ and hence

$$u^{(e)} = \frac{\sigma_Y c(t)^2}{4\mu r}, \quad (5.20)$$

$$\sigma_{rr}^{(e)} = -\frac{\sigma_Y c(t)^2}{2r^2}, \quad (5.21)$$

$$\sigma_{\theta\theta}^{(e)} = \frac{\sigma_Y c(t)^2}{2r^2}. \quad (5.22)$$

Note that continuity of stress also allows us to express the position of the free boundary $r = c(t)$ in terms of the inflation pressure $P(t)$, namely¹

$$c(t) = a \exp\left(\frac{P(t)}{\sigma_Y} - \frac{1}{2}\right). \quad (5.23)$$

5.1.2.3 Flow law in plastic region

We can now use the flow law (5.7) to calculate the plastic velocities and the associated displacement. The deviatoric stresses are given as

$$\sigma'_{rr} = \Lambda \frac{\partial \dot{u}}{\partial r}, \quad (5.24)$$

$$\sigma'_{\theta\theta} = \Lambda \frac{\dot{u}}{r}. \quad (5.25)$$

The hydrostatic pressure is

$$p = -\frac{1}{2}(\sigma_{rr}^{(p)} + \sigma_{\theta\theta}^{(p)}). \quad (5.26)$$

Using the flow law (5.7), mass conservation (5.8) and the yield condition in the form

$$\sigma'_{\theta\theta} - \sigma'_{rr} = \sigma_Y, \quad (5.27)$$

we arrive at an explicit expression for Λ , given in terms of the radial velocity:

$$\Lambda \frac{\dot{u}}{r} = \frac{\sigma_Y}{2}. \quad (5.28)$$

Note that in the expansion phase, we expect $\dot{u} > 0$ for a physical solution and so $\Lambda > 0$. This will be shown shortly. We also note that the characteristics of the mass conservation (5.8) are $r = \text{constant}$ and $t = \text{constant}$, and so we can visualise the expansion phase for the plastic displacements in the $r - t$ plane, shown in Fig. 5.2.

¹Normally, when doing a finite gun-barrel expansion model, one would get a transcendental equation for the position of the free boundary, $c(t)$.

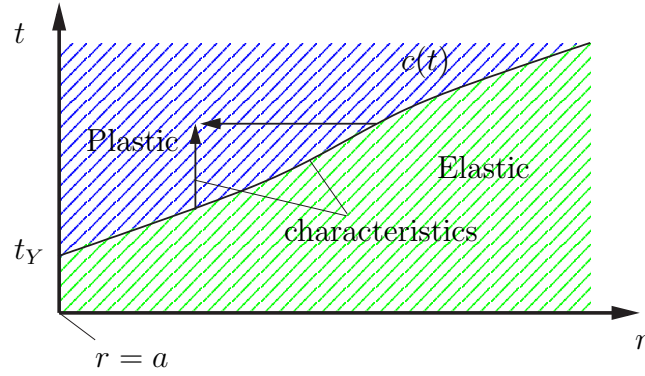


Figure 5.2: An $r-t$ graph showing elastic and plastic regions for expansion of a gun-barrel for some applied pressure $P(t)$. The inner surface of the gun-barrel yields at time $t = t_Y$.

Integrating the mass equation (5.8) with respect to r , the radial velocity in the plastic region is

$$\dot{u}^{(p)} = \frac{D(t)}{r}. \quad (5.29)$$

We now integrate this equation with respect to time between the time when the material was first plastic, $c^{-1}(r)$, and the current time, t , to arrive at

$$u^{(p)} = \frac{1}{r} \int_{c^{-1}(r)}^t D(\tau) d\tau + f(r), \quad (5.30)$$

for some function $f(r)$, which will be determined by using continuity of u on $r = c(t)$. The velocity of the elastic part on the boundary $c(t)$ is given from (5.20) as

$$\dot{u}^{(e)}(r) = \frac{\sigma_Y c \dot{c}}{2\mu r}, \quad (5.31)$$

which fixes

$$D(t) = \frac{\sigma_Y}{4\mu} \frac{d}{dt}(c^2). \quad (5.32)$$

This is positive for $\dot{P} > 0$ and so both \dot{u} and Λ are strictly positive in the expansion phase, as expected. Continuing with the analysis with knowledge of $D(t)$, we obtain

$$u^{(p)} = \frac{\sigma_Y}{4\mu r} (c(t)^2 - r^2) + f(r). \quad (5.33)$$

Finally, using continuity of u across $r = c(t)$ we see that

$$f(c(t)) = u^{(e)}(c(t)) = \frac{\sigma_Y c(t)}{4\mu}, \quad (5.34)$$

thus

$$u^{(p)} = \frac{\sigma_Y}{4\mu r} (c^2 - r^2) + \frac{\sigma_Y r}{4\mu} = \frac{\sigma_Y c^2}{4\mu r} = u^{(e)}. \quad (5.35)$$

From the expression for the radial plastic velocity, we see that there is only plastic ‘flow’ when the free boundary $r = c(t)$ is moving. This will only happen (when talking about expansion) when the cavity pressure is increasing. This is intuitively obvious, as we have imposed conservation of mass along with radial symmetry. We might expect to get some plastic flow in the azimuthal direction for fixed cavity pressure if our symmetry restriction is relaxed.

5.1.3 Simple plastic contraction with no residual stress

We now release the cavity pressure gradually for the previous elastic-plastic model. Suppose the cavity pressure reached $P_* > \sigma_Y/2$ at time t_* , say, and let $c_* = c(t_*)$. If we naively apply the flow-law and assume that the material in $r < c_*$ is still behaving plastically, we would see that the Lagrange multiplier Λ becomes infinite when $\dot{u} = 0$. Furthermore, in a similar manner to the expansion phase, we would easily find that, using incompressibility, the radial plastic flow is

$$\dot{u} = \frac{\sigma_Y \tilde{c}}{2\mu r} \frac{d\tilde{c}}{dt}, \quad (5.36)$$

where \tilde{c} is the new position of the elastic-plastic boundary, given by

$$\tilde{c} = a \exp\left(\frac{\tilde{P}}{\sigma_Y} - \frac{1}{2}\right). \quad (5.37)$$

Here \tilde{P} is the decreasing cavity pressure, satisfying $0 \leq \tilde{P} \leq P_* = \tilde{P}(t_*) = P(t_*)$. Hence \tilde{c} is decreasing, so that $\dot{u} < 0$ for strictly decreasing pressure. Using the flow law and incompressibility,

$$\Lambda = \frac{\sigma_Y}{\frac{\dot{u}}{r} - \frac{\partial \dot{u}}{\partial r}} = \frac{\sigma_Y \mu r^2}{\tilde{c} \dot{\tilde{c}}} < 0. \quad (5.38)$$

This is unphysical (equivalent to a negative viscosity when modelling a viscous fluid), and so this model for ‘plastic contraction’ is incorrect. This observation, in addition to the fact that plastic strain is not recoverable, suggests that we need some condition which allows us to ‘lock in’ the plastic stress and displacement. It is not immediately obvious how we do this, as there are various possibilities.

5.1.4 A possible model for cavity-contraction permitting a residual stress

At first sight, it might seem that we need to proceed in a manner similar to a melding or welding process, where the elastic-plastic boundary is analogous to a solid-liquid boundary that represents a melting-setting front. To model a liquid material setting to form

a solid, one can consider the equations of hypo-thermo-elasticity²[33]. These equations are, basically, the time derivatives of the thermoelasticity equations. The boundary conditions on the setting front that one uses and, indeed, expects are continuity of velocity, displacement, a Stefan condition and continuity of normal stress. However, by integrating the elasticity equations with respect to time, we gain a new unknown function of space for which we need another boundary condition. This function (equivalent to our locked in stress) is determined by arguing that the stress at the front is purely hydrostatic, so the whole stress tensor is continuous. However, in doing the elastic-plastic problem, we already know that the whole stress tensor is continuous as continuity of normal stress and the Tresca yield condition automatically give us continuity of the hoop stress and so we must consider a different condition or idea.

One obvious approach is to divide the problem into five different regions, shown in Fig. 5.3 and permit the possibility of locking in stress from the plastic region during inflation. We shall see that this approach fails, but give the analysis to see why it is incorrect. In

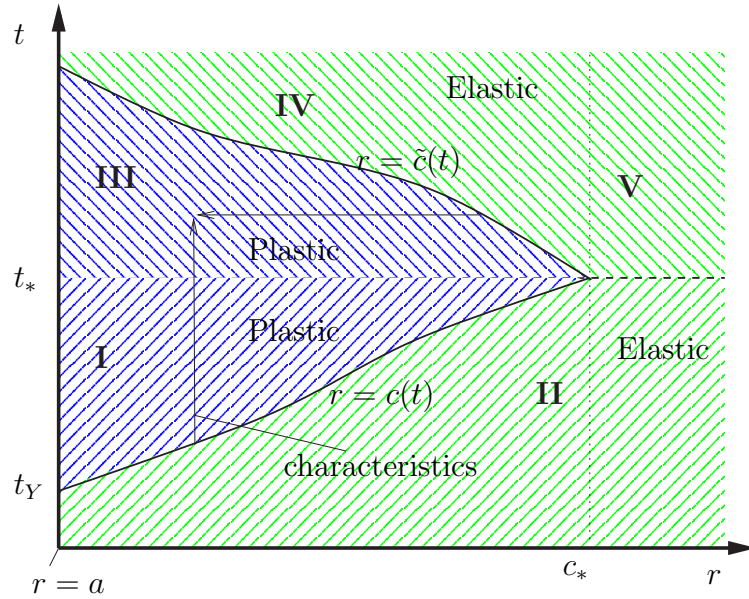


Figure 5.3: A schematic $r - t$ graph showing elastic and plastic regions for expansion and a possible idea for contraction of a gun-barrel for some applied pressure $P(t)$.

this set-up, regions I and II are those already considered in the expansion phase. Region III is a new plastic region; region IV is an elastic region in which there is a residual plastic stress and displacement; region V is elastic and knows nothing of the initial plasticity in $r < c_*$. The boundary conditions are continuity of total normal displacement, total

²Hypoelasticity models are used to model nonlinear stress-strain relations where the strain is infinitesimal. Essentially, the plastic flow law of an elastic-plastic material is replaced by a nonlinear elastic law in this regime. The ‘thermo’ part just refers to the usual temperature dependence in thermoelasticity.

normal stress and of normal velocity between these regions.

Region III

Applying the plasticity equations in region III, we get the ‘usual’ solution in terms of logarithm and the inflation pressure, \tilde{P} , thus

$$\sigma_{rr}^{(p)} = -\tilde{P} + \sigma_Y \log\left(\frac{r}{a}\right), \quad (5.39)$$

$$\sigma_{\theta\theta}^{(p)} = -\tilde{P} + \sigma_Y \left(1 + \log\left(\frac{r}{a}\right)\right). \quad (5.40)$$

The radial velocity is, by incompressibility,

$$\dot{u} = \frac{\tilde{D}(t)}{r}, \quad (5.41)$$

for some $\tilde{D}(t)$, determined by matching over the elastic-plastic boundary $r = \tilde{c}(t)$ into region III.

Region IV

Region IV is the elastic region confining the plastic region III. The difference between this region and region II is that the initial state is now unknown in advance. Thus we try splitting up the displacement in region IV into an elastic part and a “locked-in”, spatially-dependent plastic part,

$$u(r, t) = u^p(r) + u^e(r, t). \quad (5.42)$$

We decompose the stress in the same manner. The residual part of the displacement is the displacement when the material was last plastic,

$$u^p(r) = u^{(p)}(r, \tilde{c}^{-1}(r)), \quad (5.43)$$

with corresponding residual stresses

$$\sigma_{rr}^p(r) = -\tilde{P}(\tilde{c}^{-1}(r)) + \sigma_Y \log\left(\frac{r}{a}\right), \quad (5.44)$$

$$\sigma_{\theta\theta}^p(r) = -\tilde{P}(\tilde{c}^{-1}(r)) + \sigma_Y \left(1 + \log\left(\frac{r}{a}\right)\right). \quad (5.45)$$

The elastic part of the stresses and displacement are the classical Lamé solutions, thus

$$u^e(r, t) = \tilde{F}r + \frac{\tilde{G}}{r}, \quad (5.46)$$

$$\sigma_{rr}^e = 2(\lambda + \mu)\tilde{F} - \frac{2\mu\tilde{G}}{r^2}, \quad (5.47)$$

$$\sigma_{\theta\theta}^e = 2(\lambda + \mu)\tilde{F} + \frac{2\mu\tilde{G}}{r^2}, \quad (5.48)$$

for unknown constants \tilde{F} and \tilde{G} . Now, on the boundary $r = \tilde{c}(t)$, the total stress must satisfy the yield condition. Hence

$$\sigma_{\theta\theta}^e - \sigma_{rr}^e = \sigma_Y - (\sigma_{\theta\theta}^p - \sigma_{rr}^p) = 0, \quad (5.49)$$

and so $\tilde{G} = 0$ and the total stress satisfies $\sigma_{\theta\theta} - \sigma_{rr} = \sigma_Y$ everywhere in region IV. We can also use continuity of (total) σ_{rr} and (total) u over $r = \tilde{c}(t)$, giving the boundary conditions

$$u^e(\tilde{c}(t), t) = \sigma_{rr}^e(\tilde{c}(t), t) = 0. \quad (5.50)$$

Hence $\tilde{F} = 0$, and so the elastic part in region IV is zero. This means that all of the material in this region has zero velocity, and thus applying continuity of velocity into region III gives, from (5.41), that $\tilde{D}(t) = 0$ and hence the velocity in the plastic region III is zero. The flow law and yield condition lead to the expression (5.38), from which we conclude that Λ is infinite (equivalent to an infinite viscosity if we were considering a viscous fluid). This is our contradiction. Furthermore, it suggests that the material should be treated as elastic unless we are forced to do otherwise by the yield condition, and so we now consider elastic contraction with residual stresses from plastic expansion.

5.1.5 “Elastic contraction”

We wish to write down a model in which the plastic stress is locked in immediately after the elastic-plastic free boundary has passed through it. This is perhaps best visualised by supposing that we increase the cavity pressure beyond the pressure needed to yield the material, and then hold it constant. Whilst the pressure is constant, the material in the plastic region is static. Hence, it will effectively behave like an elastic material if the pressure is relaxed, with an initial state of stress given by the plastic stress we had from expansion. We will term this material as *plasticised*, as it was at one time a plastic, but on contraction, is elastic. This is described for a finite gun-barrel in [12]. Indeed, at $t = t_*$, the information that pressure is decreasing is carried along the horizontal constant t characteristics. This suggests that the elastic-plastic boundary $c(t)$ immediately goes back to zero.

Thus, we once more assume that the the cavity pressure is increased up to a pressure $P = P_* > \frac{\sigma_Y}{2}$ at time t_* with corresponding “elastic-plastic boundary” at $c_* = c(t_*)$. We then slowly release the pressure. For the moment, we assume that the material only behaves elastically when the pressure is released. Using linearity of the stresses, the solution in $r \geq c_*$ is

$$\sigma_{rr} = -\frac{\sigma_Y c_*^2}{2r^2} + \frac{a^2(P_* - \tilde{P})}{r^2}, \quad (5.51)$$

$$\sigma_{\theta\theta} = \frac{\sigma_Y c_*^2}{2r^2} - \frac{a^2(P_* - \tilde{P})}{r^2}. \quad (5.52)$$

with the same notation as in the previous section. The corresponding solution for the stresses in $a < r < c_*$ is

$$\sigma_{rr} = \sigma_Y \left(\log \frac{r}{c_*} - \frac{1}{2} \right) + \frac{a^2(P_* - \tilde{P})}{r^2}, \quad (5.53)$$

$$\sigma_{\theta\theta} = \sigma_Y \left(\log \frac{r}{c_*} + \frac{1}{2} \right) - \frac{a^2(P_* - \tilde{P})}{r^2}. \quad (5.54)$$

The first term is the solution for the stresses from the elastic-plastic expansion, whereas the second term is the classical Lamé solution for the contraction. Similarly for $r \geq c_*$, the first terms in (5.51)-(5.52) can be regarded as the elastic response to the residual plastic stress. When the internal cavity pressure \tilde{P} reaches zero, we thus obtain the residual stresses. When this happens, there will be a corresponding residual displacement. We can write down an expression for the displacement using linearity of the displacements from expansion/contraction. Hence

$$u = \frac{\sigma_Y c_*^2}{4\mu r} - \frac{a^2(P_* - \tilde{P}(t))}{2\mu r}. \quad (5.55)$$

This will hold everywhere, as the solution for the displacements is the same in both elastic and plastic regions during expansion. Rewriting c_* in terms of P_* via (5.23), the final residual displacement is given by

$$u_{res} = \frac{\sigma_Y a}{4\mu} \left(\exp \left(\frac{2P_*}{\sigma_Y} - 1 \right) - \frac{2P_*}{\sigma_Y} \right). \quad (5.56)$$

5.1.5.1 A note on incremental expansion

We have just argued that the material should be considered as elastic unless the yield condition dictates otherwise. We have shown that this results in a consistent solution when considering elastic-plastic expansion followed by an elastic contraction. In this brief section, we will show that our model for expansion in §5.1.2 is consistent within this framework. We thus suppose that we increase the cavity pressure up to a constant P_* , say, where $P_* > \sigma_Y$, with corresponding elastic-plastic boundary c_* . The material is thus plasticised in $a < r < c_*$. We then hold the pressure constant, before increasing it again to $P_* + \bar{P}$. We suppose, for a contradiction, that the plastic stress we had before is locked in, and all of the applied stress contributes to an elastic response, *i.e.*

$$\sigma_{rr} = \begin{cases} \sigma_{rr}^p(r) + \sigma_{rr}^{(e)}(r, t) & a \leq r \leq c_*, \\ -\frac{\sigma_Y c_*^2}{4\mu r} + \sigma_{rr}^{(e)}(r, t) & r \geq c_*. \end{cases}, \quad (5.57)$$

with similar expressions for $\sigma_{\theta\theta}$ and u . Note that the elastic response is the same for $a < r < c_*$ and $r > c_*$ as it satisfies the same equations and both displacement and

normal stress are continuous over $r = c_*$. Using bounded stress at infinity and continuity of normal stress and displacement over $r = c_*$, we thus obtain the classical Lamé solution

$$\sigma_{rr}^{(e)} = -\frac{a^2 \bar{P}}{r^2}, \quad (5.58)$$

which results in

$$\sigma_{\theta\theta} - \sigma_{rr} = \begin{cases} \sigma_Y + \frac{2a^2}{r^2} \bar{P} & a \leq r \leq c_*, \\ \frac{\sigma_Y c_*^2}{r^2} + \frac{2a^2}{r^2} & r \geq c_*. \end{cases} \quad (5.59)$$

In $r < (c_*^2 + 2a^2/\sigma_Y)^{\frac{1}{2}}$, the yield condition is exceeded (giving us our contradiction), and so we must treat this region as plastic rather than elastic. This will modify the elastic response, so that we need to consider where the yield condition is exactly met given an inner plastic solution, which will then determine the new elastic-plastic boundary, exactly as we did in §5.1.2. Iteration of this procedure for increasing P gives us the position of the elastic-plastic boundary at time t .

This analysis may seem trivially obvious given the work of the previous section. However, we shall see in §5.4 a more complicated situation of which this trivial analysis is the simplest example.

5.1.6 Elastic-plastic contraction

The model for elastic contraction in the previous section is not the end of the story, as we have assumed that the material will always behave elastically when the pressure is released. This may not necessarily be true, as indicated by the expression

$$\sigma_{\theta\theta} - \sigma_{rr} = \begin{cases} \frac{\sigma_Y c_*^2}{r^2} - \frac{2a^2(P_* - \tilde{P})}{r^2} & r \geq c_*, \\ \sigma_Y - \frac{2a^2(P_* - \tilde{P})}{r^2} & a < r \leq c_*. \end{cases} \quad (5.60)$$

Clearly, if P_* is suitably large, the yield condition $|\sigma_{\theta\theta} - \sigma_{rr}| = \sigma_Y$ can again be satisfied as \tilde{P} decreases to zero. As the maximum of $|\sigma_{\theta\theta} - \sigma_{rr}|$ occurs on the inner surface $r = a$, the material will again yield on the inner surface. Some quick algebra reveals that

$$P_* - \tilde{P} > \sigma_Y \Rightarrow \sigma_{\theta\theta} - \sigma_{rr} < -\sigma_Y. \quad (5.61)$$

Thus, as $\tilde{P} \in (0, P_*)$, the material re-yields³ when $P_* \geq \sigma_Y$ at time $t = t_{RY}$, say, when $\tilde{P} = P_* - \sigma_Y$. In such a case, we will get another plastic region once \tilde{P} decreases sufficiently far enough. Hence the previous analysis gives us the solution for $P_* < \sigma_Y$, whereas we need to consider a more complicated set-up for $P_* > \sigma_Y$. We denote the new elastic-plastic boundary by $r = d(t)$. This is shown graphically in Fig. 5.4. Regions I and II are

³This is sometimes called *reverse yielding*, as the yield condition takes the opposite sign to the normal one.

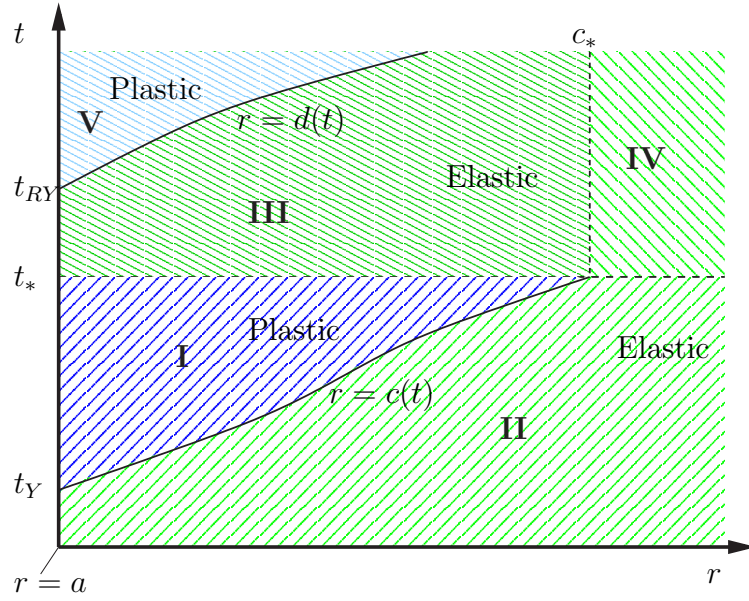


Figure 5.4: An $r-t$ graph showing elastic and plastic regions for expansion and contraction of a gun-barrel for some applied pressure $P(t)$. The inner surface yields once on expansion, then again when the cavity pressure is being decreased.

just the usual elastic and plastic regions during expansion as in §5.1.1. Region III is the region that now has residual plastic stresses locked in, over which we superimpose elastic stresses and displacements, as in (5.51)-(5.52). Region IV is, and always has been, elastic and so will have some classic Lamé solution. Region V is the new plastic region, with the reference stress state including the locked-in plastic stress from expansion.

In order to calculate the stresses and displacements in each region, we split the total stress into two components, one arising solely from the expansion and one from the contraction,

$$\boldsymbol{\sigma} = \boldsymbol{\sigma}^{\text{exp}} + \boldsymbol{\sigma}^{\text{con}}. \quad (5.62)$$

In the plastic region V, the total stress satisfies $\sigma_{\theta\theta} - \sigma_{rr} = -\sigma_Y$ whilst the locked in component from plastic expansion must satisfy $\sigma_{\theta\theta}^{\text{exp}} - \sigma_{rr}^{\text{exp}} = \sigma_Y$. Hence the new pseudo-yield condition for $\boldsymbol{\sigma}^{\text{con}}$ is

$$\sigma_{\theta\theta}^{\text{con}} - \sigma_{rr}^{\text{con}} = -2\sigma_Y. \quad (5.63)$$

Using the boundary condition $\sigma_{rr}(a) = -\tilde{P}$ for the total stress, and “initial” condition $\sigma_{rr}^{\text{exp}}(a) = -P_*$ at time t_* , we see that

$$\sigma_{rr}^{\text{con}}(a) = -\tilde{P}(t) + P_*. \quad (5.64)$$

Treating $-2\sigma_Y$ as some kind of pseudo-yield stress, the stresses in the plastic region are

given by

$$\sigma_{rr}^{\text{con}} = -\tilde{P}(t) + P_* - 2\sigma_Y \log\left(\frac{r}{a}\right), \quad (5.65)$$

$$\sigma_{\theta\theta}^{\text{con}} = -\tilde{P}(t) + P_* - 2\sigma_Y \left(\log\left(\frac{r}{a}\right) + 1\right). \quad (5.66)$$

Region III should really be subdivided further into two regions. Firstly, for $t_* < t < t_{RY}$, we recover the stresses in (5.51)-(5.54) with the corresponding displacement (5.52). For $t > t_{RY}$, we have a new elastic-plastic boundary, $r = d(t)$, to worry about. For $r > d(t)$, the material is behaving as an elastic, some with locked in plastic stress ($d(t) < r < c_*$) and some without ($r > c_*$). The stress components purely from the contraction phase are again given by Lamé's solution (applying zero stress at infinity), so

$$\sigma_{rr}^{\text{con}} = \frac{\sigma_Y d(t)^2}{r^2}, \quad (5.67)$$

$$\sigma_{\theta\theta}^{\text{con}} = -\frac{\sigma_Y d(t)^2}{r^2}. \quad (5.68)$$

Continuity of the total normal stress σ_{rr} over $r = d(t)$ (and hence of $\sigma_{\theta\theta}$ using the yield condition) and continuity of the locked-in components of the stress (from the expansion phase) tells us that σ^{con} must be continuous over $r = d(t)$, and so we can solve for $d(t)$, namely

$$d(t) = a \exp\left(\frac{-\tilde{P} + P_*}{2\sigma_Y} - \frac{1}{2}\right). \quad (5.69)$$

From this, we see that, as expected, the position of the free boundary $d(t)$ increases as the cavity pressure, \tilde{P} , decreases from P_* to zero. Note that when the cavity pressure, \tilde{P} , returns to zero, the final location of the boundary is

$$d_f = a \exp\left(\frac{P_*}{2\sigma_Y} - \frac{1}{2}\right) < c_*. \quad (5.70)$$

Using this expression for $d(t)$, we can rewrite the stresses in $a < r < d(t)$ in a simpler form as

$$\sigma_{rr}^{\text{con}} = \sigma_Y \left(1 + \log\left(\frac{d^2}{r^2}\right)\right), \quad (5.71)$$

$$\sigma_{\theta\theta}^{\text{con}} = \sigma_Y \left(-1 + \log\left(\frac{d^2}{r^2}\right)\right). \quad (5.72)$$

Armed with these formulae, we can now solve for the total stresses in each of the regions in Fig. 5.4 in the contraction phase (namely $a < r < d(t)$, $d(t) < r < c_*$ and $r > c_*$) using linearity of the stresses. In the plastic region V for $t > t_{RY}$ (and automatically $r < d(t)$),

the stresses are given by

$$\begin{aligned}\sigma_{rr} &= -\tilde{P}(t) + P_* - 2\sigma_Y \log\left(\frac{r}{a}\right) - P_* + \sigma_Y \log\left(\frac{r}{a}\right) \\ &= -\tilde{P}(t) - \sigma_Y \log\left(\frac{r}{a}\right),\end{aligned}\tag{5.73}$$

$$\begin{aligned}\sigma_{\theta\theta} &= -\tilde{P}(t) + P_* - 2\sigma_Y \left(\log\left(\frac{r}{a}\right) + 1\right) - P_* + \sigma_Y \left(\log\left(\frac{r}{a}\right) + 1\right) \\ &= -\tilde{P}(t) - \sigma_Y \left(\log\left(\frac{r}{a}\right) + 1\right).\end{aligned}\tag{5.74}$$

For the elastic part of region III with $t > t_{RY}$, we have $d(t) < r < c_*$, and the stresses are

$$\sigma_{rr} = \frac{\sigma_Y d^2}{r^2} - P_* + \sigma_Y \log\left(\frac{r}{a}\right),\tag{5.75}$$

$$\sigma_{\theta\theta} = -\frac{\sigma_Y d^2}{r^2} - P_* + \sigma_Y \left(\log\left(\frac{r}{a}\right) + 1\right).\tag{5.76}$$

With the obvious notation, the corresponding displacements are

$$\begin{aligned}u &= u_{(p)}^{\text{exp}} + u_{(e)}^{\text{con}} \\ &= \frac{\sigma_Y}{4\mu r} (c_*^2 - 2d(t)^2).\end{aligned}\tag{5.77}$$

In the elastic region $r > c_*$ and $t > t_{RY}$, the stresses are

$$\sigma_{rr} = \frac{\sigma_Y d(t)^2}{r^2} - \frac{\sigma_Y c_*^2}{2r^2},\tag{5.78}$$

$$\sigma_{\theta\theta} = -\frac{\sigma_Y d(t)^2}{r^2} + \frac{\sigma_Y c_*^2}{2r^2},\tag{5.79}$$

with displacement

$$u = \frac{\sigma_Y}{4\mu r} (c_*^2 - 2d(t)^2).\tag{5.80}$$

This is the same as in (5.77) as the residual component of the stress is the same.

To work out the displacement in the plastic region V, we once more use a flow-law and use incompressibility. Since we know that the locked-in part of the stress is already continuous throughout this region, the incompressibility condition is, once more,

$$\frac{\partial \dot{u}^{\text{con}}}{\partial r} + \frac{\dot{u}^{\text{con}}}{r} = 0\tag{5.81}$$

and so⁴

$$\dot{u}^{\text{con}} = \frac{C(t)}{r}.\tag{5.82}$$

Considering (5.80), continuity of velocity over $d(t)$ leads to

$$\dot{u}^{\text{con}} = -\frac{\sigma_Y}{2\mu} \frac{d}{dt} (d(t)^2).\tag{5.83}$$

⁴The Lagrange multiplier Λ is still positive, as effective yield stress and velocity are now both negative.

Integrating with respect to time,

$$u^{\text{con}} = \frac{1}{r} \int_{d^{-1}(r)}^t -\frac{\sigma_Y}{2\mu} \frac{d}{d\tau} (d(\tau)^2) d\tau + g(r). \quad (5.84)$$

By computing the integral and matching the displacements over $d(t)$, we eventually end up with a total displacement in the plastic region of

$$u = \frac{\sigma_Y}{4\mu r} (c_*^2 - 2d(t)^2). \quad (5.85)$$

Thus the residual displacement is given by

$$\begin{aligned} u(a) &= \frac{\sigma_Y}{4\mu a} (c_*^2 - 2d_f^2) \\ &= \frac{\sigma_Y a}{4\mu} \left(\exp\left(\frac{2P_*}{\sigma_Y} - 1\right) - 2 \exp\left(\frac{P_*}{\sigma_Y} - 1\right) \right). \end{aligned} \quad (5.86)$$

As $P_* > \sigma_Y$, this expression is positive.

A schematic diagram to summarise the solutions for stresses, displacements and velocities for each of the regions during the expansion and contraction phases, equivalent to Fig. 5.4, is shown in Fig. 5.5, with the physical effect on the gun-barrel shown in Fig. 5.6.

5.1.7 Cyclic loading-unloading

An interesting, albeit academic, observation from this analysis is what happens when if the cavity pressure is increased and decreased several times. Suppose we increase the cavity pressure past the yield condition and stop at some pressure P_* at time t_* . If we then decrease the pressure so that the material behaves only elastically, then increase back up to P_* at time t_{**} . As the expansion for $t \in (t_*, t_{**})$ is purely elastic, we recover the elastic stress that has just been generated. Thus the stress tensor and displacement is just the same as it was at $t = t_*$, the system ‘forgetting’ about the motion for $t \in (t_*, t_{**})$. Further, if we raise the pressure past P_* , the system ‘remembers’ where it was before, and continues expanding plastically. Once again, this is best illustrated graphically, shown in Fig. 5.7.

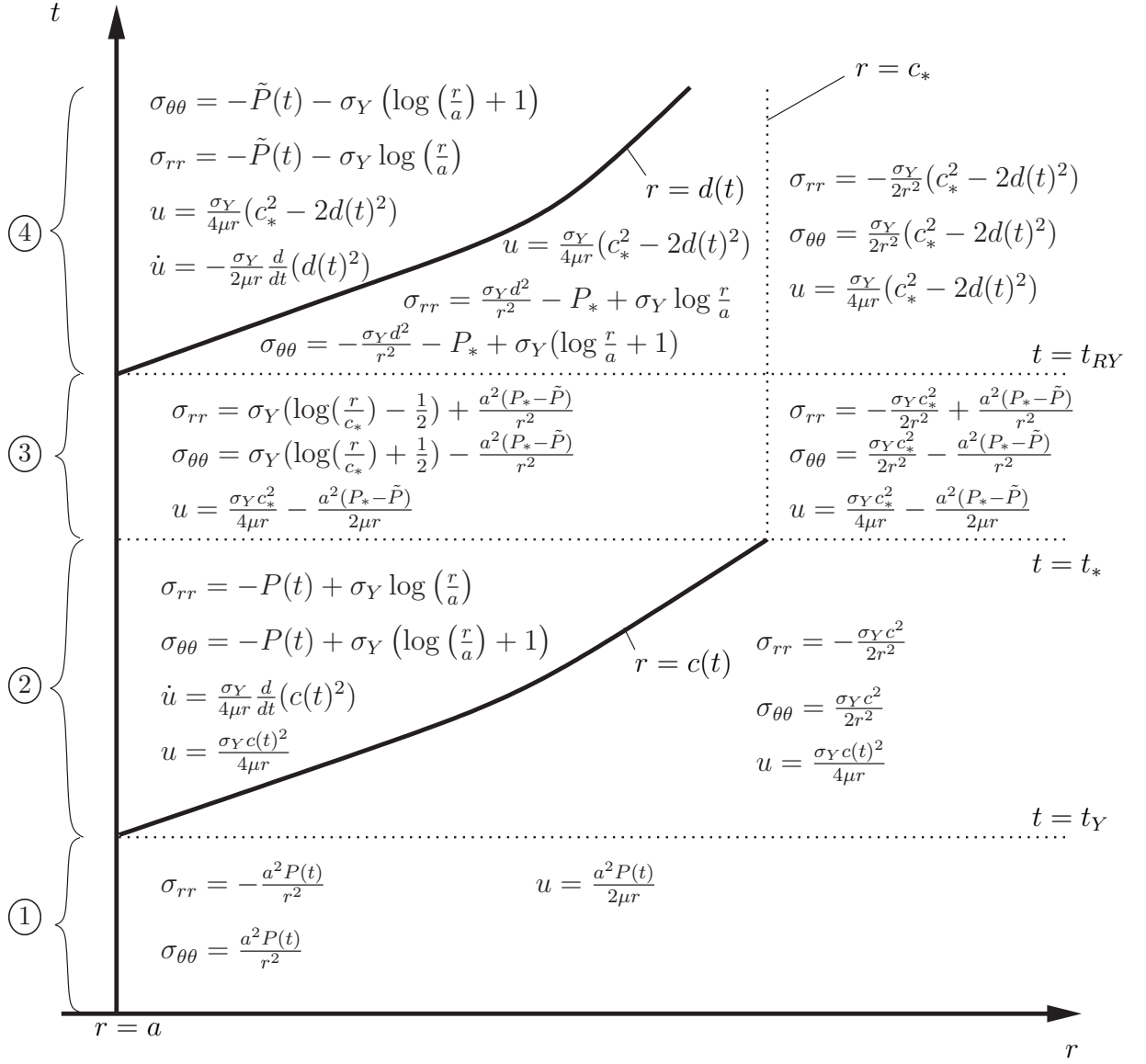


Figure 5.5: An $r - t$ graph showing the stresses and displacements when cavity pressure is increased up to $P_* > \frac{\sigma_Y}{2}$, leading elastic expansion of the medium (①) and then elastic-plastic expansion (②). When the cavity pressure is decreased, the medium firstly contracts elastically (③). For $P_* > \sigma_Y$, there is elastic-plastic contraction until $\tilde{P} = 0$ (④). For any $P_* > \frac{\sigma_Y}{2}$, there are residual stresses and displacements.

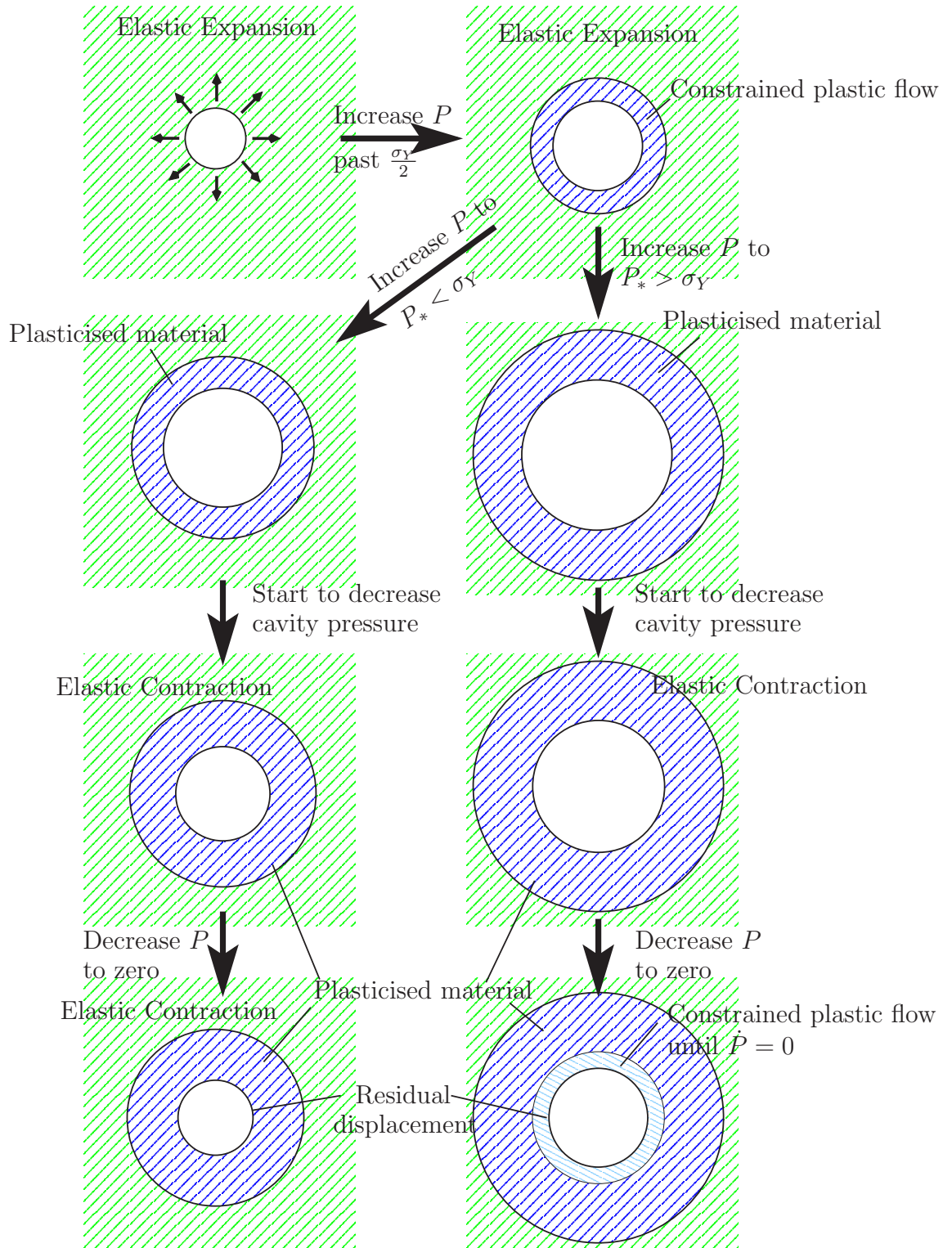


Figure 5.6: A schematic of gun-barrel expansion/contraction. The two different paths depend on the relative sizes of P_* and σ_Y , thus allowing the possibility of the gun-barrel reyielding on contraction.

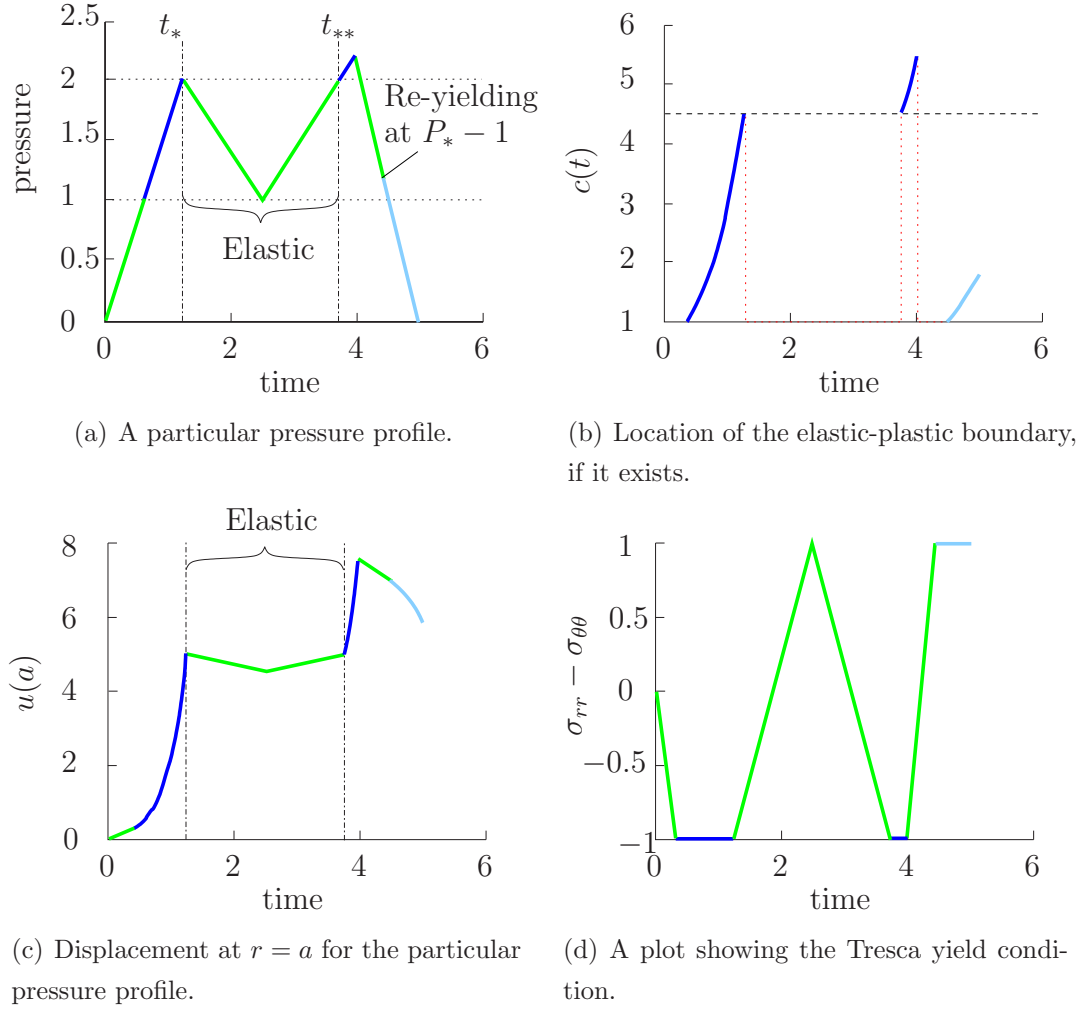


Figure 5.7: Four diagrams depicting different quantities during repeated expansion and contraction of a gun-barrel, produced from MATLAB. We take $\mu = 1$, $\sigma_Y = 1$ and $a = 1$. The colours correspond to the shaded regions in Fig. 5.6. Note that the maximum cavity pressure is greater than the yield stress, and so the material re-yields on contraction.

5.2 A nonlinear problem

Up until now, we have demonstrated that applying a radial pressure to a circular cavity then releasing it again will lead to residual displacements and stresses if plastic flow has occurred. These residual displacements are infinitesimal as a result of the linear-elasticity theory used. It is likely that there are residual displacements and stresses if a finite-displacement elasticity theory is used in place of the linear theory. Indeed, it was hinted at the end of the last chapter that we may need to consider nonlinear elasticity, as linear elasticity cannot be a good model for the opening of the initial cavity. Hence, using the theory outlined in §1.2.1.5, we emulate the previous analysis using finite-(nonlinear)-elasticity. We expect that the calculations will be significantly messier and may mean that numerical solutions are needed to complete the problem. However, with the goal of applying this paradigm to the shaped-charge problem, we only need to demonstrate that the concept works for such a framework⁵.

Suppose a vector \mathbf{X} in the undeformed reference frame is deformed to a vector \mathbf{x} in the deformed frame, so that $\mathbf{x} = \mathbf{X} + \mathbf{u}(\mathbf{X})$. In cylindrical polars, we let $\mathbf{x} = (r, \theta, z)$ and $\mathbf{X} = (R, \Theta, Z)$. Noting that a small arc-length dS in undeformed coordinates satisfies

$$(dS)^2 = (dR)^2 + (Rd\Theta)^2 + (dZ)^2, \quad (5.87)$$

we may write

$$\mathbf{u}(\mathbf{X}) = \left(u, \frac{v}{R}, w \right), \quad (5.88)$$

and relate the two frames via $d\mathbf{x} = \mathbf{F}d\mathbf{X}$, where $F_{ij} = \frac{\partial x_i}{\partial X_j}$ is the deformation tensor. Owing to radial symmetry, we can write this tensor as

$$\mathbf{F} = \begin{pmatrix} 1 + \frac{\partial u}{\partial R} & 0 & 0 \\ 0 & 1 + \frac{u}{R} & 0 \\ 0 & 0 & 1 \end{pmatrix}. \quad (5.89)$$

Note that \mathbf{F} is diagonal, so that $\mathbf{F} = \mathbf{F}^T$. Motivated by the fact that for radial displacements in the linear elastic model considered previously it turns out that $\nabla \cdot \mathbf{u} = 0$, we assume for simplicity that the elastic material is incompressible. Thus $\det \mathbf{F} = 1$, and so

$$\frac{\partial u}{\partial R} = -\frac{u}{u + R}. \quad (5.90)$$

⁵It is possible to modify the previous linear-elastic-perfect-plastic model by changing the inner boundary condition to $\sigma_{rr}(a + u(a)) = -P$. In doing so, we would find similar explicit expressions for stress and displacement, obtained by solving a quadratic. This analysis is not, however, consistent with the equations of linear elasticity, where we have already neglected quadratic terms, and so is not mathematically justifiable.

We integrate this expression with respect to R to give

$$u = -R \pm \sqrt{R^2 + \alpha(t)}, \quad (5.91)$$

for some unknown $\alpha(t)$, to be determined. For large R ,

$$u \sim -R \pm R \left(1 + \frac{\alpha(t)}{2R^2} \right). \quad (5.92)$$

Thus, for finite displacement at infinity, we take the positive root, giving

$$u(R, t) = -R + R \sqrt{1 + \frac{\alpha(t)}{R^2}}. \quad (5.93)$$

We define the reference configuration by $A \leq R < \infty$ and $0 \leq \Theta < 2\pi$, with current (Eulerian) configuration $a \leq r < \infty$ and $0 \leq \theta < 2\pi$. By definition, $r = u(R) + R$, and so

$$R^2 = r^2 - \alpha(t). \quad (5.94)$$

This gives the displacement

$$u = r - \sqrt{r^2 - \alpha}. \quad (5.95)$$

To determine the stresses, we need to introduce a strain-energy function, W . The simplest such representation is to assume that the material is Neo-Hookean, hence

$$W = \frac{\mu}{2}(I_1 - 3), \quad (5.96)$$

where I_1 , the first invariant of the Green's deformation tensor $\mathbf{C} = \mathbf{F}^T \mathbf{F}$, is

$$I_1 = \text{tr}(\mathbf{F}^T \mathbf{F}). \quad (5.97)$$

We recall that the constraint of incompressibility leads us to express the first Piola-Kirchhoff stress tensor \mathbf{S} as

$$\mathbf{S} = \frac{\partial W}{\partial \mathbf{F}} - p(\mathbf{F}^{-1})^T, \quad (5.98)$$

where p , termed the hydrostatic pressure, is the Lagrange multiplier for the constraint. The true stress tensor $\boldsymbol{\sigma}$ is given by

$$\boldsymbol{\sigma} = \mathbf{S} \mathbf{F}^T = \frac{\partial W}{\partial \mathbf{F}} \mathbf{F} - p \mathbf{I}, \quad (5.99)$$

where \mathbf{I} is the identity tensor. Substituting for I_1 and using tensor identities [39], we find that

$$\boldsymbol{\sigma} = \mu \mathbf{F}^2 - p \mathbf{I}. \quad (5.100)$$

Thus

$$\sigma_{rr} = \mu \left(1 + \frac{\partial u}{\partial R} \right)^2 - p = \frac{\mu R^2}{R^2 + \alpha} - p = \mu \left(\frac{r^2 - \alpha}{r^2} \right) - p, \quad (5.101)$$

$$\sigma_{\theta\theta} = \mu \left(1 + \frac{u}{R} \right)^2 - p = \mu \left(1 + \frac{\alpha}{R^2} \right) - p = \mu \left(\frac{r^2}{r^2 - \alpha} \right) - p. \quad (5.102)$$

5.2.1 Elastic expansion

We have seen that the elastic stresses are (5.101)-(5.102), with radial displacement (5.93). The unknown pressure $p(r, t)$ is determined by the usual quasistatic, radially-symmetric force-balance equation

$$\frac{\partial \sigma_{rr}}{\partial r} + \frac{\sigma_{rr} - \sigma_{\theta\theta}}{r} = 0, \quad (5.103)$$

whence

$$p(r, t) = \frac{\mu}{2} \log \left(\frac{r^2}{r^2 - \alpha(t)} \right) - \frac{\mu \alpha(t)}{2r^2} + \beta(t), \quad (5.104)$$

for some $\beta(t)$. The unknown functions $\alpha(t)$ and $\beta(t)$ are determined by imposing the boundary conditions

$$\sigma_{rr}(a) = -P(t), \quad (5.105)$$

where $a = u(A) + A$ is unknown, and

$$\sigma_{rr}, \sigma_{\theta\theta} \rightarrow 0 \text{ as } r \rightarrow \infty. \quad (5.106)$$

The second boundary condition reveals that $\beta(t) = \mu$, whilst the first tells us that the function $\alpha(t)$ must satisfy some transcendental equation. Without writing this down, we can still deduce, properties of $A(t)$ from the large r expansion of σ_{rr} :

$$\sigma_{rr} = -\frac{\mu \alpha(t)}{2r^2} + \frac{\mu}{2} \log \left(1 - \frac{\alpha(t)}{r^2} \right) \sim -\frac{\mu \alpha(t)}{r^2}. \quad (5.107)$$

As we are applying a stress to the inner boundary, the elastic body must be in compression (radially), hence $\alpha(t) > 0$.

5.2.2 Elastic-plastic expansion

We now suppose that the inflation pressure is great enough to yield the material, resulting in an inner plastic annulus surrounded by elastic material. With the usual analysis, the plastic stresses and plastic radial velocity are

$$\sigma_{rr}^{(p)} = -P(t) + \sigma_Y \log \left(\frac{r}{a} \right), \quad (5.108)$$

$$\sigma_{\theta\theta}^{(p)} = -P(t) + \sigma_Y \left(1 + \log \left(\frac{r}{a} \right) \right), \quad (5.109)$$

$$\dot{u}^{(p)}(r, t) = \frac{D(t)}{r}. \quad (5.110)$$

Recall, once more, the general elastic solution given by (5.95), (5.101) and (5.102). Continuity of the radial velocity over the elastic-plastic boundary $r = c(t)$ gives

$$D(t) = \frac{\dot{\alpha}}{2\sqrt{1 - \frac{\alpha(t)}{c(t)^2}}}. \quad (5.111)$$

We now need to apply continuity of stress. We can do so without explicitly using the expression (5.104) for $p(r, t)$, as the material on the elastic-plastic boundary must satisfy the yield condition. Thus,

$$\mu \left(\frac{c(t)^2}{c(t)^2 - \alpha(t)} - \frac{c(t)^2 - \alpha(t)}{c(t)^2} \right) = \sigma_Y, \quad (5.112)$$

eventually leading to

$$\alpha(t) = \left(1 + \frac{\sigma_Y}{2\mu} - \sqrt{1 + \frac{\sigma_Y^2}{4\mu^2}} \right) c(t)^2, \quad (5.113)$$

where the negative square root is taken so that $D(t)$ is well-defined. Substituting into the expression for $D(t)$ yields

$$D(t) = \frac{1 + \sigma_Y/(2\mu) - \sqrt{1 + \sigma_Y^2/(4\mu^2)}}{2\sqrt{\sqrt{1 + \sigma_Y^2/(4\mu^2)} - \sigma_Y/(2\mu)}} \frac{d}{dt}(c^2) = E \frac{d}{dt}(c^2), \quad (5.114)$$

say, where E is defined in the obvious manner. We now directly match the radial stress across the elastic-plastic boundary. Using (5.104),

$$-\frac{\mu}{2} \log \left(\frac{c^2}{c^2 - \alpha} \right) - \frac{\mu\alpha}{2c^2} = -P + \sigma_Y \log \left(\frac{c}{a} \right). \quad (5.115)$$

After substituting for $\alpha(t)$ from (5.113), we see that the left-hand side is independent of $c(t)$, and so

$$\frac{\mu}{2} \left(\log \left(\sqrt{1 + \frac{\sigma_Y^2}{4\mu^2}} - \frac{\sigma_Y}{2\mu} \right) - 1 - \frac{\sigma_Y}{2\mu} + \sqrt{1 + \frac{\sigma_Y^2}{4\mu^2}} \right) + P - \frac{\sigma_Y}{2} = \sigma_Y \log \left(\frac{c(t)}{a} \right), \quad (5.116)$$

thus determining $c(t)$ in terms of the unknown $a = A + u(A)$, which is calculated by evaluation of $u^{(p)}(a)$. To do so, we integrate the plastic velocity, giving

$$u^{(p)} = \int_{c^{-1}(r)}^t \frac{D(\tau)}{r} d\tau + f(r) = \frac{E}{r}(c^2 - r^2) + f(r), \quad (5.117)$$

where E is given in (5.114). To determine $f(r)$, we use continuity of displacement on $r = c(t)$. Thus, substituting for $\alpha(t)$ in (5.95),

$$f(c(t)) = c(t) \left(1 - \left(\sqrt{1 + \frac{\sigma_Y^2}{4\mu^2}} - \frac{\sigma_Y}{2\mu} \right)^{\frac{1}{2}} \right). \quad (5.118)$$

The plastic displacement can now be written

$$u^{(p)}(r, t) = \frac{Ec^2}{r} - Er + r \left(1 - \left(\sqrt{1 + \frac{\sigma_Y^2}{4\mu^2}} - \frac{\sigma_Y}{2\mu} \right)^{\frac{1}{2}} \right). \quad (5.119)$$

Using $a = A + u(a)$, we can calculate $u(a)$, and substitute into (5.115). This results in a quadratic for $c(t)$. This can be solved to give a rather messy explicit expression for $c(t)$ and hence for the whole system.

5.2.3 Contraction with no re-yielding

We now suppose that we have increased the cavity pressure to P_* at time t_* , say, and now slowly decrease it. We firstly assume that the inner boundary does not reyield, as in §5.1.5. We will use tildes to denote the particular variables with respect to the reference state at time t_* , and start by decomposing the displacements as

$$u(r, t) = \begin{cases} u_{res}^p(r) + \tilde{u}^e(r, t) & \tilde{a} < r \leq c_*, \\ u_{res}^e(r) + \tilde{u}^e(r, t) & r \geq c_*. \end{cases} \quad (5.120)$$

We denote the position of the elastic-plastic boundary at time t_* by c_* , and the position of the inner boundary by $\tilde{a} = A + \tilde{u}(A)$. The residual displacement $u_{res}^p(r)$ is the displacement when the material was last plastic, given by (5.119) (with $c = c_*$), whereas the elastic response to the residual displacement is given by (5.93), where $\alpha(t_*) = \alpha_*$, say, is known in terms of c_* . The new component of displacement $\tilde{u}^e(r, t)$ is the displacement relative to the new reference state of stress and displacement at time t_* , and hence

$$\tilde{u}^e(r, t) = r - \sqrt{r^2 - \tilde{\alpha}(t)}. \quad (5.121)$$

We decompose the stresses in the same manner, so that the locked in radial stresses are

$$\sigma_{rr}(r, t) = \begin{cases} -P_* + \sigma_Y \log\left(\frac{r}{a_*}\right) + \tilde{\sigma}_{rr}^e(r, t) & \tilde{a} < r \leq c_*, \\ -\frac{\mu}{2}(\log\left(\frac{r^2}{r^2 - \alpha_*}\right) + \frac{\alpha_*}{r^2}) + \tilde{\sigma}_{rr}^e(r, t) & r \geq c_*. \end{cases} \quad (5.122)$$

Similar expressions for $\sigma_{\theta\theta}$ are also easy to write down. The unknown part of the stress from contraction $\sigma_{rr}^e(r, t)$ must satisfy (*c.f.* (5.107))

$$\tilde{\sigma}_{rr}^e(r, t) = -\frac{\mu}{2} \left(\log \left(\frac{r^2}{r^2 - \tilde{\alpha}(t)} \right) + \frac{\tilde{\alpha}(t)}{r^2} \right). \quad (5.123)$$

To determine $\tilde{\alpha}(t)$, we use the boundary condition (for *total* stress)

$$\sigma_{rr}(\tilde{a}, t) = -\tilde{P}(t), \quad (5.124)$$

or, in terms of the locked in plastic stress and recoverable elastic part from contraction,

$$-P_* + \tilde{\sigma}_{rr}^e(\tilde{a}, t) = -\tilde{P}(t). \quad (5.125)$$

Thus

$$\tilde{\sigma}_{rr}^e(\tilde{a}, t) = -\tilde{P}(t) + P_*. \quad (5.126)$$

This gives an implicit expression for $\tilde{\alpha}(t)$ in terms of \tilde{a} ,

$$-\tilde{P} + P_* = -\frac{\mu}{2} \left(\log \left(\frac{\tilde{a}^2}{\tilde{a}^2 - \tilde{\alpha}(t)} \right) + \frac{\tilde{\alpha}(t)}{\tilde{a}^2} \right), \quad (5.127)$$

resulting in two equations for unknowns $\tilde{\alpha}(t)$ and \tilde{a} which have to be solved numerically. Finally, the residual displacement at the cavity when the applied pressure returns to zero (and residual stresses) can be calculated by setting $\tilde{P} = 0$.

5.2.4 Contraction with further plastic flow

As was the case with the linear theory, we observe that the material can yield again on contraction. This is apparent when considering the difference of total stresses on the cavity boundary:

$$\sigma_{\theta\theta} - \sigma_{rr} = (\sigma_{\theta\theta}^p - \sigma_{rr}^p) + (\tilde{\sigma}_{\theta\theta}^e - \tilde{\sigma}_{rr}^e) \quad (5.128)$$

$$= \sigma_Y - \mu\tilde{\alpha} \left(\frac{1}{r^2 - \tilde{\alpha}} + \frac{1}{r^2} \right). \quad (5.129)$$

Hence, if $\tilde{\alpha}$ is sufficiently large enough, we can have $\sigma_{\theta\theta} - \sigma_{rr} \leq -\sigma_Y$, leading to further yielding. Based on our analysis with linear elasticity and on (5.127), we see that $\tilde{\alpha}$ depends on P_* , and so it is again likely that the criterion for reyielding is directly related to a critical value of P_* (*c.f.* (5.61)). Hence, we have a model similar to that of Fig. 5.5. To write down a full solution, we firstly decompose the stresses and displacement in a manner similar to (5.120). After this point, the material re-yields at some \tilde{P} , and we need to consider solutions of the form

$$u(r, t) = \begin{cases} u_{res}^p(r) + \tilde{u}^p(r, t) & \tilde{\alpha} \leq r \leq d(t), \\ u_{res}^p(r) + \tilde{u}^e(r, t) & d(t) \leq r \leq c_*, \\ u_{res}^e(r) + \tilde{u}^e(r, t) & r > c_*. \end{cases} \quad (5.130)$$

with corresponding expressions for the stresses. The new plastic part \tilde{u}^p will have a form similar to (5.119), with associated stresses

$$\tilde{\sigma}_{rr}^p = P_* - \tilde{P}(t) + \sigma_Y \log \left(\frac{r}{\tilde{\alpha}} \right), \quad (5.131)$$

$$\tilde{\sigma}_{\theta\theta}^p = P_* - \tilde{P}(t) + \sigma_Y \left(1 + \log \left(\frac{r}{\tilde{\alpha}} \right) \right). \quad (5.132)$$

The elastic part of the displacement \tilde{u}^e will have the form of (5.93), with stresses (5.101)-(5.102). The boundary conditions are⁶ continuity of total stress and total displacement over the elastic-plastic boundary $r = d(t)$, continuity of total stress and total displacement over $r = c_*$ and zero stress at infinity. Some of these quantities can be calculated explicitly, whereas others have to be evaluated numerically. We omit this analysis, as it is just an exercise in algebra.

5.2.5 Comment

The crux of this section is that a perfect-plastic-nonlinear-elastic model will also lead to residual displacements and stresses after plastic expansion. In the linear model, these displacements were (inherently) infinitesimal; we have shown that the idea still works for finite-displacement elasticity.

⁶We have implicitly used $\sigma_{rr}(\tilde{\alpha})$ in the expressions for $\tilde{\sigma}_{rr}^p$ and $\tilde{\sigma}_{\theta\theta}^p$.

5.3 Application to shaped-charge penetration

We have seen that both the linear theory and nonlinear theory predict residual stresses and displacements after plastic flow. Recall the residual displacement predicted by the linear elastic model, detailed in equations (5.56) and (5.86). We note that, even though the predicted residual displacement is small in the linear theory, it may be significant if the plastic region is large enough, since a displacement of $\mathcal{O}(\varepsilon)$ at $r = c_*$ gives a displacement of $\mathcal{O}(\varepsilon c_*/a)$ at $r = a$. Explicitly, we need $c_* \sim a(\mu/\sigma_Y)^{\frac{1}{2}}$ for the residual displacement to be $\mathcal{O}(a)$. Using $P_* \sim \frac{1}{2}\rho_t(V - U)^2$, order of magnitude estimates for the residual displacement in equation (5.56) give unfeasibly large displacements (as $2P_*/\sigma_Y \sim 100$). However, we must remember that this estimate is based on the maximum pressure in the tip, where there is a significant axial flow. Hence, we expect that the residual displacement will always be overestimated if we use the maximum tip pressure. A detailed analysis of the tip should provide an effective pressure P_* , thus furnishing us with residual displacements and stresses and so giving an estimate for the cavity width.

We can now develop a model in which the cavity is considered as a series of two-dimensional radially-symmetric gun-barrel problems, permitting residual stresses and displacements. We model the jet as a pressure pulse moving from the tip to the rear of the cavity. Each point in the target will thus experience an increase then decrease in cavity pressure, resulting in residual displacements along the length of the cavity. In reality, the pressure profile is a function of both position and time, but, in order to illustrate a concept, we suppose that the pressure profile is a travelling-wave. This model thus contains an extra boundary between the plasticised region (in which the applied pressure is decreasing) and the plastic region (positive applied pressure gradient). This boundary is a straight line, as we are effectively stitching two-dimensional slices together. We denote this boundary by $z = z_*$ and provide a schematic of the model in Fig. 5.8. With the pressure profile and z_* given, we can write down the solution for $z < z_*$ based on previous analysis, as all the material here is either elastic, plasticised-elastic, or plasticised-plastic (if the material re-yields), with known P_* . We observe that this model says that all of the important mechanics takes place in the tip region where the plastic flow takes place. The main problem with the model is that the tip region is not slender, and so cannot be considered as a series of two-dimensional slices. Indeed, we expect that there will be significant axial plastic flow near the tip. However, as we shall see in Chapter 6, this model serves as a simple template for a far more complicated model.

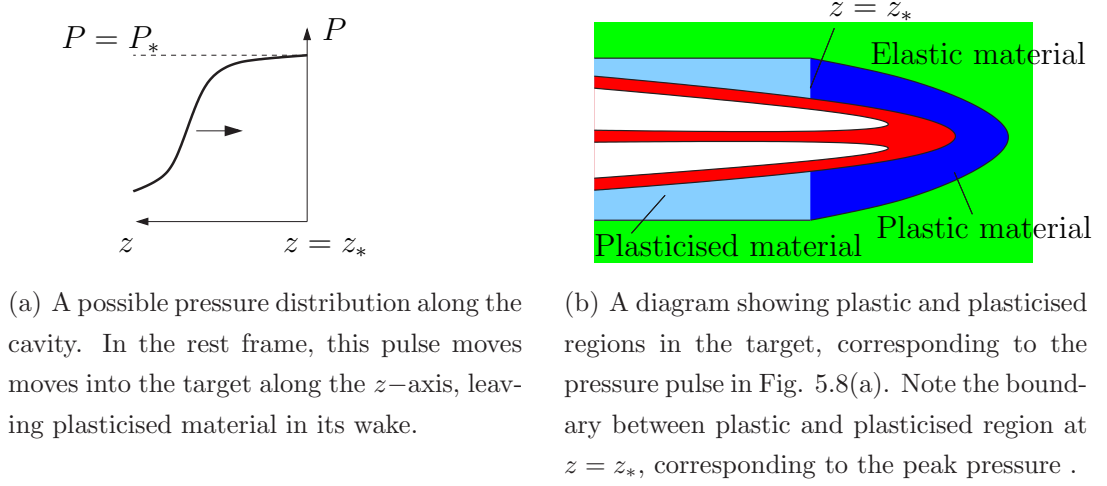


Figure 5.8: Two schematic diagrams for modelling the penetration as a series of two-dimensional gun-barrel problems.

5.3.1 Remarks

Normally, linear elasticity is used to model metal solids, as, if the applied traction is sufficient, the metal will become plastic before nonlinear elasticity becomes important. In the previous sections, we have discussed two possible mechanisms to explain the presence of the bowed edges (evident in Fig. 4.5) and the size of the cavity. Either they are a consequence of residual displacements from linear elasticity theory, in which case the plastic region must be large enough so that the elastic residual displacements are $\mathcal{O}(a)$, or they are a result of nonlinear residual displacements, in which case a smaller plastic region is permissible. It is possible that a combination of nonlinear effects and the high pressure in the jet are responsible for the initial opening of the cavity, before the extreme pressure of the jet creates a large plastic region hence resulting in observable bowing via residual displacements. So far, the notion of residual stresses and displacements has only been applied to the problem of expansion/contraction of a two-dimensional radially-symmetric gun-barrel. Our analysis shows that it is crucial to include these effects when developing a full elastic-plastic model for the penetration. This will be discussed in Chapter 6. Before doing so, we present more preliminary work on the gun-barrel as a paradigm to tip-modelling.

5.4 An asymmetric perturbation to the gun-barrel problem

In order to model the tip, we wish to model the response of an elastic-plastic material to a stress applied in a cavity with known geometry. This stress is mainly directed along the z -axis. To gain some intuition about the response of the material to such a force, we begin by considering the simplest non-symmetric configuration by perturbing the stress applied on the inner surface for the classical gun-barrel expansion problem (as discussed in §5.1.2). We assume that the gun-barrel has already yielded under application of a radially-symmetric cavity pressure, which results in a plastic annulus. We now perturb the cavity pressure, applying the following boundary conditions:

$$\sigma_{rr}(a) = -P(t) - \varepsilon Y(\theta, t), \quad (5.133)$$

$$\sigma_{r\theta}(a) = 0. \quad (5.134)$$

Here, we assume that the prescribed function $Y(t, \theta)$ is 2π -periodic and non-negative. The latter means that the applied pressure is decreased nowhere around the cavity, and so the initially plastic material will still behave plastically (recall the trivial example in §5.1.5.1). Later, we will permit the sign of $Y(t, \theta)$ to depend on θ , which will result in a plasticised region with residual stresses and a plastic region (still flowing). We again use the linear theory so that the boundary conditions are applied at $r = a$. Ideally, we would like to apply an $\mathcal{O}(1)$ -periodic perturbation. In doing so, we would find that a general solution for the stress field is possible, although we would also discover that the position of the elastic-plastic boundary must satisfy a transcendental equation and so the complete problem can only be solved numerically. This will become apparent in solving the simpler problem which has boundary conditions (5.133)-(5.134). To avoid confusion, we will consistently use superscripts e and p to denote ‘elastic’ and ‘plastic’, respectively, and superscripts 0 and 1 to refer to leading-order and first order corrections in an asymptotic expansion, respectively, so that, for example, the principal radial component of the plastic total stress will be written

$$\sigma_{rr}^p = \sigma_{rr}^{p0} + \varepsilon \sigma_{rr}^{p1} + \mathcal{O}(\varepsilon^2). \quad (5.135)$$

We start the analysis with the plastic region. As usual, we have the quasistatic stress balances in the plastic region, written in terms of the total stresses as

$$\frac{\partial \sigma_{rr}^p}{\partial r} + \frac{1}{r} \frac{\partial \sigma_{r\theta}^p}{\partial \theta} + \frac{\sigma_{rr}^p - \sigma_{\theta\theta}^p}{r} = 0, \quad (5.136)$$

$$\frac{\partial \sigma_{r\theta}^p}{\partial r} + \frac{1}{r} \frac{\partial \sigma_{\theta\theta}^p}{\partial \theta} + \frac{2\sigma_{r\theta}^p}{r} = 0. \quad (5.137)$$

Now, given the form of the boundary condition (5.133), we might expect that a nonzero $\sigma_{r\theta}$ will affect the principal stresses and hence the yield condition. We thus consider the

eigenvalues of the stress tensor by calculating

$$0 = \det(\lambda \mathbf{I} - \boldsymbol{\sigma}) = \begin{vmatrix} \lambda - \sigma_{rr}^p & -\varepsilon \sigma_{r\theta}^{p1} - \dots \\ -\varepsilon \sigma_{r\theta}^{p1} - \dots & \lambda - \sigma_{\theta\theta}^p \end{vmatrix}, \quad (5.138)$$

and discover that they are given by

$$\lambda = \frac{\sigma_{rr}^p + \sigma_{\theta\theta}^p}{2} \pm \frac{\sigma_{rr}^p - \sigma_{\theta\theta}^p}{2} + \mathcal{O}(\varepsilon^2). \quad (5.139)$$

Hence the principal stresses are still σ_{rr}^p and $\sigma_{\theta\theta}^p$ (up to $\mathcal{O}(\varepsilon^2)$) and so the yield condition is unchanged as

$$\sigma_{\theta\theta}^p - \sigma_{rr}^p = \sigma_Y. \quad (5.140)$$

The final set of equations for the plastic region are given by the incompressible flow law,

$$\sigma_{ij}^{p'} = \Lambda \dot{\varepsilon}_{ij}^p. \quad (5.141)$$

Meanwhile, in the elastic region, the stresses must satisfy the equilibrium equations

$$\frac{\partial \sigma_{rr}^e}{\partial r} + \frac{1}{r} \frac{\partial \sigma_{r\theta}^e}{\partial \theta} + \frac{\sigma_{rr}^e - \sigma_{\theta\theta}^e}{r} = 0, \quad (5.142)$$

$$\frac{\partial \sigma_{r\theta}^e}{\partial r} + \frac{1}{r} \frac{\partial \sigma_{\theta\theta}^e}{\partial \theta} + \frac{2\sigma_{r\theta}^e}{r} = 0. \quad (5.143)$$

The elastic displacements $\mathbf{u}^e = (u^e, v^e)$ are given via the relations

$$\sigma_{rr}^e = (\lambda + 2\mu) \frac{\partial u^e}{\partial r} + \lambda \left(\frac{u^e}{r} + \frac{1}{r} \frac{\partial v^e}{\partial \theta} \right), \quad (5.144)$$

$$\sigma_{\theta\theta}^e = \lambda \frac{\partial u^e}{\partial r} + (\lambda + 2\mu) \left(\frac{u^e}{r} + \frac{1}{r} \frac{\partial v^e}{\partial \theta} \right), \quad (5.145)$$

$$\sigma_{r\theta}^e = \mu \left(\frac{\partial v^e}{\partial r} - \frac{v^e}{r} + \frac{1}{r} \frac{\partial u^e}{\partial \theta} \right). \quad (5.146)$$

Clearly, the leading-order solution is unchanged by the small perturbation, and so we can write the elastic-plastic boundary as $r = c_0(t) + \varepsilon c_1(\theta, t)$. The boundary conditions over this boundary are continuity of traction, velocity and displacement. The elastic stress must also satisfy the yield condition (5.140) here. The other boundary conditions are (5.133)-(5.134) and zero stress at infinity.

We expand the stresses, velocities and displacements in powers of ε and find that the leading-order solution is unchanged from §5.1.2. The first-order correction is found by considering a linear combination of separable solutions for the stresses, velocities and displacements. Expanding the plastic stresses as

$$\sigma_{rr}^p = \sigma_{rr}^{p0} + \varepsilon \sigma_{rr}^{p1} + \dots, \quad (5.147)$$

$$\sigma_{\theta\theta}^p = \sigma_{\theta\theta}^{p0} + \varepsilon \sigma_{\theta\theta}^{p1} + \dots, \quad (5.148)$$

$$\sigma_{r\theta}^p = \varepsilon \sigma_{r\theta}^{p1} + \dots, \quad (5.149)$$

we can apply the boundary condition $\sigma_{r\theta}^{p1}(a) = 0$ and hence, omitting much of the analysis, the plastic first-order corrections can be written as

$$\sigma_{rr}^{p1} = D_0 + \left(\log \frac{r}{a} + 1\right) \left(\frac{B_1}{r} \cos \theta - \frac{A_1}{r} \sin \theta\right) - 2A_0\theta \quad (5.150)$$

$$+ \sum_{j=2}^{\infty} \left(\sin(\sqrt{j^2 - 1} \log \frac{r}{a}) + \cos(\sqrt{j^2 - 1} \log \frac{r}{a}) \sqrt{j^2 - 1} \right) \left(\frac{D_j}{jr} \cos j\theta - \frac{C_j}{jr} \sin j\theta \right),$$

$$\sigma_{r\theta}^{p1} = (A_1 \cos \theta + B_1 \sin \theta) \frac{1}{r} \log \frac{r}{a} + A_0 \left(1 - \frac{a^2}{r^2}\right) + \sum_{j=2}^{\infty} \frac{1}{r} \sin(\sqrt{j^2 - 1} \log \frac{r}{a}) (C_j \cos j\theta + D_j \sin j\theta), \quad (5.151)$$

where A_j, B_j, C_j, D_j are constants, and, using the yield condition, $\sigma_{\theta\theta}^{p1} = \sigma_{rr}^{p1}$. We note, by linearity, this expansion would be valid at leading order had we tried an $\mathcal{O}(1)$ perturbation to the inner boundary condition instead of the current $\mathcal{O}(\varepsilon)$ perturbation, providing that the condition $\sigma_{\theta\theta} > \sigma_{zz} > \sigma_{rr}$ is still satisfied.

We now prescribe particular expressions for $Y(\theta, t)$. We consider the following two separable forms in the following two subsections:

- $Y(\theta, t) = (1 + \cos \theta)Q(t)$,
- $Y(\theta, t) = (1 + \cos N\theta)Q(t)$,

where $Q(t)$ is an increasing function with dimensions of pressure and N is an integer greater than unity.

5.4.1 Perturbation $\varepsilon Y(\theta, t) = \varepsilon(1 + \cos \theta)Q(t)$ to the cavity pressure

For such a $Y(\theta, t)$, we know by symmetry that σ_{rr}^{p1} must be an even function of θ whereas $\sigma_{r\theta}^{p1}$ must be an odd function of θ . Using orthogonality, the higher harmonics must vanish and we reach the following solution for the total plastic stresses:

$$\sigma_{rr}^p = -P(t) + \sigma_Y \log \left(\frac{r}{a}\right) - \varepsilon \frac{aQ(t)}{r} \cos \theta \left(1 + \log \frac{r}{a}\right) - \varepsilon Q(t), \quad (5.152)$$

$$\sigma_{\theta\theta}^p = -P(t) + \sigma_Y + \sigma_Y \log \left(\frac{r}{a}\right) - \varepsilon \frac{aQ(t)}{r} \cos \theta \left(1 + \log \frac{r}{a}\right) - \varepsilon Q(t), \quad (5.153)$$

$$\sigma_{r\theta}^p = -\frac{\varepsilon Q(t)a}{r} \log \left(\frac{r}{a}\right) \sin \theta. \quad (5.154)$$

We also expand the $\mathcal{O}(\varepsilon)$ elastic stresses in cosine and sine series and exploit the symmetry. After much tortuous algebra and writing Q for $Q(t)$, we arrive at the following

expressions:

$$\sigma_{rr}^e = -\frac{\sigma_Y c_0^2}{2r^2} - \left(\frac{c_0^2 \log \frac{c_0}{a}}{r^3} + \frac{3\mu + 2\lambda}{2(\lambda + 2\mu)r} + \frac{c_0^2 \mu}{2(\lambda + 2\mu)r^3} \right) \varepsilon a Q \cos \theta - \frac{c_0^2}{r^2} \varepsilon Q, \quad (5.155)$$

$$\sigma_{\theta\theta}^e = \frac{\sigma_Y c_0^2}{2r^2} + \left(\frac{c_0^2 \log \frac{c_0}{a}}{r^3} + \frac{\mu}{2(\lambda + 2\mu)r} + \frac{c_0^2 \mu}{2(\lambda + 2\mu)r^3} \right) \varepsilon a Q \cos \theta + \frac{c_0^2}{r^2} \varepsilon Q, \quad (5.156)$$

$$\sigma_{r\theta}^e = - \left(\frac{c_0^2 \log \frac{c_0}{a}}{r^3} - \frac{\mu}{2(\lambda + 2\mu)r} + \frac{c_0^2 \mu}{2(\lambda + 2\mu)r^3} \right) \varepsilon a Q \sin \theta. \quad (5.157)$$

The position of the elastic-plastic boundary is determined by knowledge that the elastic stresses on this boundary must satisfy the Tresca yield condition, thus

$$\begin{aligned} c(\theta, t) &\sim c_0 + \frac{aQ(t) \cos \theta}{\sigma_Y} \left(\frac{3\mu + \lambda}{2(\lambda + 2\mu)} + \log \left(\frac{c_0}{a} \right) \right) \varepsilon + \frac{Q c_0}{\sigma_Y} \varepsilon \\ &= c_0 + \frac{aQ \cos \theta}{\sigma_Y} \left(\frac{\mu}{2(\lambda + 2\mu)} + \frac{P}{\sigma_Y} \right) \varepsilon + \frac{Q(t) c_0}{\sigma_Y} \varepsilon. \end{aligned} \quad (5.158)$$

We expand the elastic displacements in powers of ε , thus

$$u = \frac{\sigma_Y c_0^2}{4\mu r} + \varepsilon u^{e1}(r, \theta, t), \quad (5.159)$$

$$v = \varepsilon v^{e1}(r, \theta, t). \quad (5.160)$$

To solve for the $\mathcal{O}(\varepsilon)$ correction, we try for solutions of the form

$$u^{e1}(r, \theta, t) = E_0(r, t) + \sum_{j=1}^{\infty} (E_j(r, t) \cos j\theta + F_j(r, t) \sin j\theta), \quad (5.161)$$

$$v^{e1}(r, \theta, t) = G_0(r, t) + \sum_{j=1}^{\infty} (G_j(r, t) \cos j\theta + H_j(r, t) \sin j\theta), \quad (5.162)$$

for unknown functions of space and time, $E_j(r, t), F_j(r, t), G_j(r, t), H_j(r, t)$. After even more messy algebra involving the equations of equilibrium, the unknown functions can be determined to give general solutions. Firstly, the θ -independent terms are given by

$$E_0(r, t) = \alpha_0(t)r + \frac{\beta_0(t)}{r}, \quad (5.163)$$

$$G_0(r, t) = \gamma_0(t)r, \quad (5.164)$$

for unknown temporal functions $\alpha_0(t), \beta_0(t)$; $E_1(r, t), F_1(r, t), G_1(r, t), H_1(r, t)$ have the form

$$\alpha_1(t) + \beta_1(t) \log r + \gamma_1(t)r^2 + \frac{\delta_1(t)}{r^2}, \quad (5.165)$$

for different $\alpha_1(t), \beta_1(t), \gamma_1(t), \delta_1(t)$; for $j \geq 2$, $E_j(r, t), F_j(r, t), G_j(r, t)$ and $H_j(r, t)$ are of the form

$$\alpha_j(t)r^{j+1} + \beta_j(t)r^{j-1} + \frac{\gamma_j(t)}{r^{j+1}} + \frac{\delta_j(t)}{r^{j-1}}, \quad (5.166)$$

again, for different $\alpha_j(t), \beta_j(t), \gamma_j(t)$ and $\delta_j(t)$. We substitute these expressions into the equations (5.144)-(5.146). Exploiting the orthogonality of the $\cos j\theta$ and $\sin j\theta$ and matching into the plastic region, we arrive at the expressions

$$u^{e1} = \left(-E_1(t) + \frac{aQ(\lambda + \mu)}{4\mu(\lambda + 2\mu)} - \frac{(3\mu + \lambda)aQ \log r}{4\mu(\lambda + 2\mu)} + \frac{aQc_0^2}{8r^2} \left(\frac{1}{\lambda + 2\mu} + \frac{2 \log \frac{c_0}{a}}{\mu} \right) \right) \cos \theta + F_1(t) \sin \theta + \frac{c_0^2 Q}{2\mu r}, \quad (5.167)$$

$$v^{e1} = F_1(t) \cos \theta + \left(E_1(t) + \frac{(3\mu + \lambda)aQ \log r}{4(\lambda + 2\mu)\mu} + \frac{aQc_0^2}{8r^2} \left(\frac{1}{\lambda + 2\mu} + \frac{2 \log \frac{c_0}{a}}{\mu} \right) \right) \sin \theta. \quad (5.168)$$

The significance of the unknown functions $E_1(t)$ and $F_1(t)$ can be explained as follows. Consider a small displacement given by

$$\delta r = F_1(t) \sin \theta - E_1(t) \cos \theta, \quad (5.169)$$

$$r\delta\theta = F_1(t) \cos \theta + E_1(t) \sin \theta. \quad (5.170)$$

Writing $x = r \cos \theta$ and $y = r \sin \theta$, we can write these small displacements in Cartesian coordinates:

$$\delta x = \delta r \cos \theta - r\delta\theta \sin \theta, \quad (5.171)$$

$$\delta y = \delta r \sin \theta + r\delta\theta \cos \theta. \quad (5.172)$$

We thus substitute for δr and $r\delta\theta$ and discover that

$$\delta x = -E_1(t), \quad (5.173)$$

$$\delta y = F_1(t). \quad (5.174)$$

Hence, these terms represent a shift of origin, and so we set them to zero without loss of generality. The $\mathcal{O}(\varepsilon)$ corrections are now given in the slightly simpler form

$$u^{e1} = \left(\frac{aQ(\lambda + \mu)}{4\mu(\lambda + 2\mu)} - \frac{(3\mu + \lambda)aQ \log r}{4\mu(\lambda + 2\mu)} + \frac{aQc_0^2}{8r^2} \left(\frac{1}{\lambda + 2\mu} + \frac{2 \log \frac{c_0}{a}}{\mu} \right) \right) \cos \theta + \frac{c_0^2 Q}{2\mu r}, \quad (5.175)$$

$$v^{e1} = \left(\frac{(3\mu + \lambda)aQ \log r}{4\mu(\lambda + 2\mu)} + \frac{aQc_0^2}{8r^2} \left(\frac{1}{\lambda + 2\mu} + \frac{2 \log \frac{c_0}{a}}{\mu} \right) \right) \sin \theta. \quad (5.176)$$

Note that these expressions contain logarithmic terms in r , which are clearly unbounded as $r \rightarrow \infty$. This implies that the expansion is not valid for large r , and that an outer region is required for a full asymptotic solution.

We now solve for the plastic velocities and so expand

$$\dot{u}^p = \frac{\sigma_Y}{4\mu r} \frac{d}{dt}(c_0^2) + \varepsilon \dot{u}^{p1}, \quad (5.177)$$

$$\dot{v}^p = 0 + \varepsilon \dot{v}^{p1}, \quad (5.178)$$

where

$$\dot{u}^{p1} = \alpha(r) + \beta(r) \cos \theta + \gamma(r) \sin \theta, \quad (5.179)$$

$$\dot{v}^{p1} = \kappa(r) + \chi(r) \cos \theta + \psi(r) \sin \theta, \quad (5.180)$$

$$\Lambda(r, t) \sim \Lambda_0(r, t) + \varepsilon \Lambda_1(r, t) + \mathcal{O}(\varepsilon^2). \quad (5.181)$$

In the usual manner, the plasticity equations are incompressibility, the Tresca yield condition, the associated flow law, and knowledge of $\sigma_{r\theta}^p$ via (5.154). Incompressibility and the flow law hence give that the $\mathcal{O}(\varepsilon)$ corrections to the plastic velocities must satisfy

$$\frac{\partial \dot{u}^{p1}}{\partial r} + \frac{\dot{u}^{p1}}{r} + \frac{1}{r} \frac{\partial \dot{v}^{p1}}{\partial \theta} = 0, \quad (5.182)$$

$$\frac{\Lambda_0}{2} \left(\frac{\partial \dot{v}^{p1}}{\partial r} + \frac{1}{r} \frac{\partial \dot{u}^{p1}}{\partial \theta} - \frac{\dot{v}^{p1}}{r} \right) = -\frac{Q(t)a}{r} \log\left(\frac{r}{a}\right) \sin \theta. \quad (5.183)$$

Use of the yield condition merely determines $\Lambda_1(r, t)$. Substituting the expansions for the velocities and using continuity of velocity over the elastic-plastic boundary, we immediately reach $\gamma = \kappa = \chi = 0$. We also obtain

$$\alpha(r) = \frac{1}{2\mu r} \frac{d}{dt} (c_0^2 Q), \quad (5.184)$$

$$\beta(r) = K(t) \log \frac{r}{a} + L(t) + \frac{aQ}{4\mu r^2} \frac{d}{dt} (c_0^2) \left(\log \frac{r}{a} + 1 \right), \quad (5.185)$$

$$\psi(r) = -K(t) - L(t) - K(t) \log \frac{r}{a} + \frac{aQ}{4\mu r^2} \frac{d}{dt} (c_0^2) \log \frac{r}{a}, \quad (5.186)$$

where $K(t)$ and $L(t)$ are unknown functions of time, which we now fully determine by further utilising continuity of velocity over the elastic-plastic boundary. After much toil, the remaining unknown functions can finally be calculated:

$$K(t) = -a \left(\frac{\dot{Q}}{4\mu} \left(1 + 2 \log \left(\frac{c_0}{a} \right) \right) + \frac{Q \dot{c}_0}{2(\lambda + 2\mu)c_0} \right), \quad (5.187)$$

$$\begin{aligned} L(t) = & a \dot{Q} \left(\frac{2\lambda + 3\mu}{8\mu(\lambda + 2\mu)} + \frac{\log \left(\frac{c_0}{a} \right)}{2\mu} \left(1 + \log \left(\frac{c_0}{a} \right) \right) - \frac{(3\mu + \lambda) \log c_0}{4\mu(\lambda + 2\mu)} \right) \\ & + \frac{a \dot{c}_0 Q}{4c_0(\lambda + 2\mu)} \left(2 \log \left(\frac{c_0}{a} \right) - \frac{\lambda}{\mu} - 1 \right). \end{aligned} \quad (5.188)$$

To visualise the flow, we nondimensionalise the velocities, scaling all stresses and Lamé constants with σ_Y , and lengthscales with a . The resultant plots are shown in Fig. 5.9. As expected, the main difference to the purely radial solution of the earlier section is that the elastic-plastic boundary is perturbed. Indeed, given the form of (5.158), we could have noticed earlier that this boundary would be circular with centre to the right of the origin. This solution is not very illustrative of material being ‘squeezed’ in the azimuthal

direction as we had hoped. However, we do observe the elastic-plastic boundary being displaced as a result of the perturbation. This is a consequence of the confinement from the surrounding elastic material. The other possible boundary condition involves a $\cos N\theta$ term (for integer $N \geq 2$), and so should yield more interesting results.

5.4.2 Perturbation $\varepsilon Y(\theta, t) = \varepsilon(1 + \cos N\theta)Q(t)$, $N \geq 2$ to the cavity pressure

We can quickly write down the plastic stresses using orthogonality and (5.150)-(5.151) as

$$\begin{aligned} \sigma_{rr}^p &= -P + \sigma_Y \log\left(\frac{r}{a}\right) - \varepsilon Q \\ &\quad - \frac{\varepsilon Q a}{\sqrt{N^2 - 1}} \left(\sin\left(\sqrt{N^2 - 1} \log \frac{r}{a}\right) + \cos\left(\sqrt{N^2 - 1} \log \frac{r}{a}\right) \sqrt{N^2 - 1} \right) \frac{\cos N\theta}{r}, \end{aligned} \quad (5.189)$$

$$\begin{aligned} \sigma_{\theta\theta}^p &= -P + \sigma_Y + \sigma_Y \log\left(\frac{r}{a}\right) - \varepsilon Q \\ &\quad - \frac{\varepsilon Q a}{\sqrt{N^2 - 1}} \left(\sin\left(\sqrt{N^2 - 1} \log \frac{r}{a}\right) + \cos\left(\sqrt{N^2 - 1} \log \frac{r}{a}\right) \sqrt{N^2 - 1} \right) \frac{\cos N\theta}{r}, \end{aligned} \quad (5.190)$$

$$\sigma_{r\theta}^p = -\varepsilon \frac{Q a N}{\sqrt{N^2 - 1}} \sin\left(\sqrt{N^2 - 1} \log \frac{r}{a}\right) \frac{\sin N\theta}{r}, \quad (5.191)$$

After a significant amount of tedious algebra on equations (5.161)-(5.162) and on the equations of equilibrium, the solutions for the elastic stresses that decay for large r are

$$\sigma_{rr}^e = -\frac{\sigma_Y c_0^2}{2r^2} + \left((N+2)\alpha - \frac{\beta}{r^2} \right) \frac{\cos N\theta}{r^N} \varepsilon - \frac{c_0^2}{r^2} \varepsilon Q, \quad (5.192)$$

$$\sigma_{\theta\theta}^e = \frac{\sigma_Y c_0^2}{2r^2} + \left(-(N-2)\alpha + \frac{\beta}{r^2} \right) \frac{\cos N\theta}{r^N} \varepsilon + \frac{c_0^2}{r^2} \varepsilon Q, \quad (5.193)$$

$$\sigma_{r\theta}^e = \left(N\alpha - \frac{\beta}{r^2} \right) \frac{\sin N\theta}{r^N} \varepsilon, \quad (5.194)$$

where the unknown constants are determined by matching with the plastic region as

$$\alpha = \frac{c_0^{N-1} Q a}{2} \left(\sqrt{\frac{N-1}{N+1}} \sin\left(\sqrt{N^2 - 1} \log \frac{c_0}{a}\right) - \cos\left(\sqrt{N^2 - 1} \log \frac{c_0}{a}\right) \right), \quad (5.195)$$

$$\beta = c_0^{N+1} \frac{Q a N}{2} \left(\sqrt{\frac{N+1}{N-1}} \sin\left(\sqrt{N^2 - 1} \log \frac{c_0}{a}\right) - \cos\left(\sqrt{N^2 - 1} \log \frac{c_0}{a}\right) \right). \quad (5.196)$$

The $\mathcal{O}(\varepsilon)$ correction to the position of the elastic-plastic boundary can now be calculated by using the yield condition on $c_0 + \varepsilon c_1$,

$$0 = \left(-2N\alpha + \frac{2\beta}{c_0^2} \right) \frac{\cos N\theta}{c_0^N} - \frac{2c_1}{c_0} + \frac{2Q}{\sigma_Y}, \quad (5.197)$$

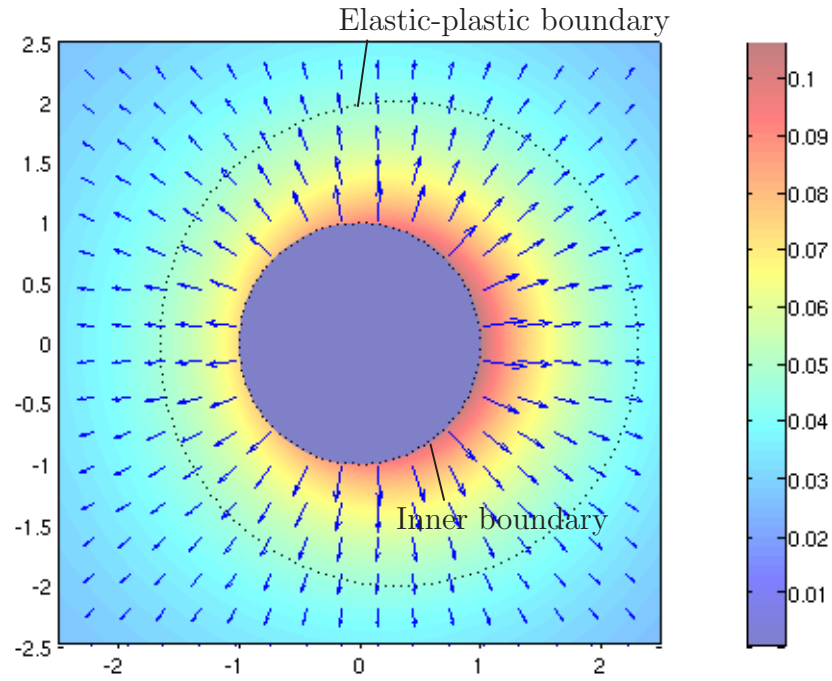
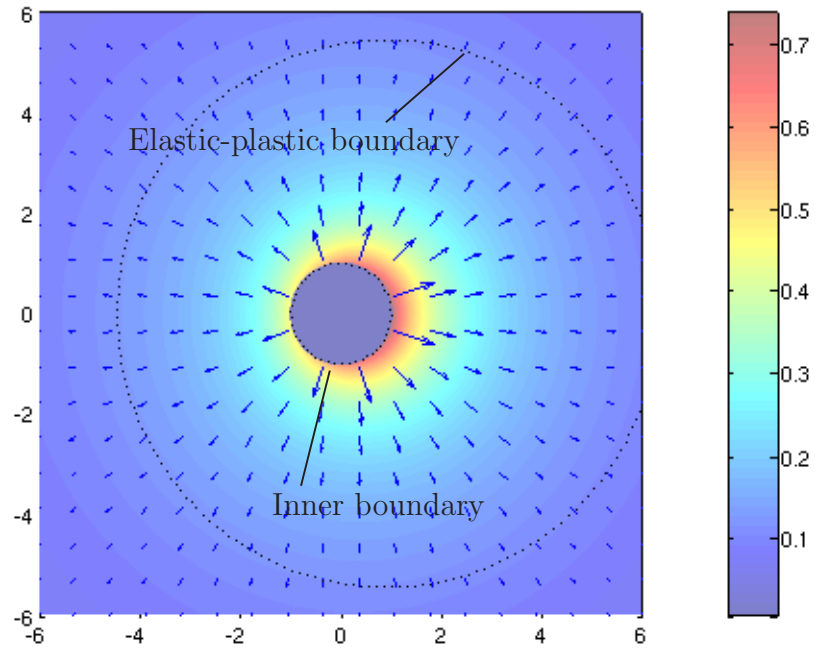
(a) A vector plot of velocity at $t = 0.15\text{s}$.(b) A vector plot of velocity at $t = 0.44\text{s}$.

Figure 5.9: Vector plots of the nondimensional velocity from MATLAB. The colouring represents the magnitude of the velocity. The nondimensional parameter values used were $\varepsilon = 0.2$, $\mu = 70$, $\lambda = 32$, $Q = 1 + 3t$ and $P = \frac{1}{2} + 3t$. The elastic-plastic boundary is denoted by the outer dotted black line.

thus

$$\begin{aligned} c_1(\theta, t) &= \frac{NaQ}{2\sigma_Y} \sin\left(\sqrt{N^2-1} \log \frac{c_0}{a}\right) \left(\sqrt{\frac{N+1}{N-1}} - \sqrt{\frac{N-1}{N+1}} \right) \cos N\theta + \frac{Q(t)c_0}{\sigma_Y} \\ &= \frac{NaQ}{\sigma_Y \sqrt{N^2-1}} \sin\left(\sqrt{N^2-1} \log \frac{c_0}{a}\right) \cos N\theta + \frac{Q(t)c_0}{\sigma_Y}. \end{aligned} \quad (5.198)$$

The $\mathcal{O}(\varepsilon)$ corrections to the elastic displacements corresponding to the stresses (5.192)-(5.194) are

$$u^{e1} = \left(\frac{\beta}{2\mu(N+1)r^{N+1}} - \frac{\alpha}{2(N-1)r^{N-1}} \left(\frac{2}{\lambda+\mu} + \frac{N}{\mu} \right) \right) \cos N\theta + \frac{c_0^2 Q}{2\mu r}, \quad (5.199)$$

$$v^{e1} = \left(\frac{\beta}{2\mu(N+1)r^{N+1}} + \frac{\alpha}{2(N-1)r^{N-1}} \left(\frac{2}{\lambda+\mu} - \frac{N-2}{\mu} \right) \right) \sin N\theta. \quad (5.200)$$

In deriving these expressions, we have implicitly set the linear coefficients of $\cos \theta$ and $\sin \theta$ to zero, as before. In contrast to the earlier perturbed solution, these displacements are valid for large r and tend to zero as $r \rightarrow \infty$.

To solve for the $\mathcal{O}(\varepsilon)$ corrections for the plastic velocities, we once again look for cosine and sine series solutions. These expansions must satisfy

$$\frac{\partial \dot{u}^{p1}}{\partial r} + \frac{1}{r} \frac{\partial \dot{u}^{p1}}{\partial \theta} + \frac{\dot{u}^{p1}}{r} = 0, \quad (5.201)$$

and

$$\frac{\Lambda_0}{2} \left(\frac{\partial \dot{v}^{p1}}{\partial r} + \frac{1}{r} \frac{\partial \dot{v}^{p1}}{\partial \theta} - \frac{\dot{v}^{p1}}{r} \right) = -\frac{QaN}{\sqrt{N^2-1}} \frac{\sin(\sqrt{N^2-1} \log \frac{r}{a})}{r} \sin N\theta, \quad (5.202)$$

where

$$\Lambda_0 = \frac{\mu r^2}{c_0 \dot{c}_0}. \quad (5.203)$$

Bearing in mind the matching that has to be done with the elastic region and the equations that the velocities must satisfy, we can deduce that the only terms in the expansions will be those terms involving $\cos N\theta$, $\sin N\theta$ and an arbitrary function of r . Hence we may write

$$u^{e1}(r, \theta) = \alpha_1(r) + \beta_1(r) \cos N\theta + \gamma_1(r) \sin N\theta, \quad (5.204)$$

$$v^{e1}(r, \theta) = \chi_1(r) + \eta_1(r) \cos N\theta + \nu_1(r) \sin N\theta. \quad (5.205)$$

Further work reveals that $\alpha_1(r) = \frac{1}{2\mu r} \frac{d}{dt}(c_0^2 Q)$, $\gamma_1 = \chi_1 = \eta_1 = 0$, and β_1 satisfies

$$\beta_1(r) = C_1 \cos \Theta(r) + C_2 \sin \Theta(r) + \frac{2c_0 \dot{c}_0 Q a N^2}{\mu(N^2-1)} (\sin \Theta(r) I_1(r) - \cos \Theta(r) I_2(r)), \quad (5.206)$$

where C_1 and C_2 are unknown constants,

$$\Theta(r) = \sqrt{N^2-1} \log(r/a), \quad (5.207)$$

and the remaining functions are given by the following integrals:

$$I_1(r) = \int \frac{\cos \Theta(r) \sin \Theta(r)}{r^3} dr, \quad (5.208)$$

$$I_2(r) = \int \frac{\sin^2 \Theta(r)}{r^3} dr. \quad (5.209)$$

Fortunately, these integrals can be easily computed, eventually giving the plastic velocities as

$$\begin{aligned} \dot{u}^{p1}(r, \theta) = & \frac{\frac{d}{dt}(c_0^2 Q)}{2\mu r} + \left(C_1 \cos \Theta(r) + C_2 \sin \Theta(r) \right. \\ & \left. + \frac{Qac_0\dot{c}_0}{2\mu r^2} \left(\frac{\sin \Theta(r)}{\sqrt{N^2 - 1}} + \cos \Theta(r) \right) \right) \cos N\theta, \end{aligned} \quad (5.210)$$

$$\begin{aligned} \dot{v}^{p1}(r, \theta) = & \left(\frac{NQac_0\dot{c}_0 \sin \Theta(r)}{2\sqrt{N^2 - 1}\mu r^2} + \frac{1}{4N} \left((C_1\sqrt{N^2 - 1} - C_2) \sin \Theta(r) \right. \right. \\ & \left. \left. - (C_1 + C_2\sqrt{N^2 - 1}) \cos \Theta(r) \right) \right) \sin N\theta, \end{aligned} \quad (5.211)$$

where C_1 and C_2 are determined using continuity of velocity with equations (5.199)-(5.200). We omit explicit expressions for these constants owing to their inherent complexity.

A vector plot of the material velocity is shown in Fig. 5.10. This shows an important difference in the shape of the elastic-plastic boundary. Furthermore, it demonstrates the expected result that the velocity of the material is significantly greater in the vicinity of where the material is being pushed harder. This disturbance has a much smaller effect on the elastic region owing to the $1/r^{N-1}$ decay of the elastic displacements.

5.4.3 Remarks

Our principal objective in perturbing the inner boundary condition was to investigate its effect on the plastic flow of the material. Sadly, this result was not realised as the perturbation was not strong enough, although our results did show the effect of the perturbation on the position of the free elastic-plastic boundary. This motivates modifying the form of the boundary condition (5.133) to

$$\sigma_{rr}(a) = -P - Q(\cos N\theta + 1). \quad (5.212)$$

Indeed, we can obtain the same general solutions for stresses and for the elastic displacement. Furthermore, we can derive explicit solutions for the plastic stresses (by merely taking the $\mathcal{O}(\varepsilon)$ correction to be at leading order). However, when it comes to determining the position of the elastic-plastic boundary, $c(\theta, t)$, by exploiting the Tresca yield

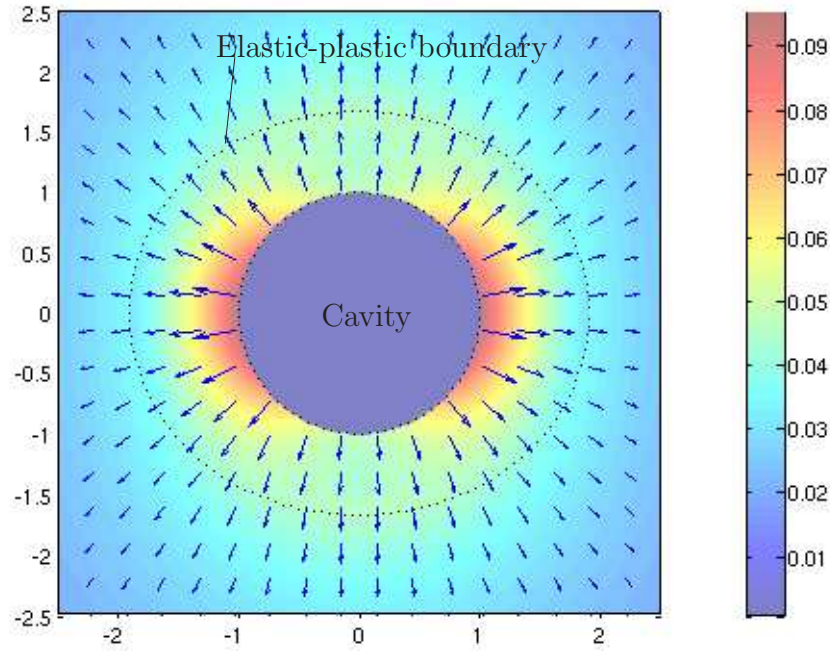


Figure 5.10: A vector plot of nondimensional velocity at $t = 0.15\text{s}$ for $N = 2$. The colouring represents the magnitude of the velocity. The nondimensional parameter values used were $\varepsilon = 0.1$, $\mu = 70$, $\lambda = 32$, $Q = 1 + 3t$ and $P = \frac{1}{2} + 3t$. The elastic-plastic boundary is denoted by the outer dotted black line.

condition on equations (5.155)-(5.156), it is clear that we obtain a transcendental equation for $c(\theta, t)$, and so a numerical solution is needed for a full solution.

5.4.4 Effects of applying a non-radially-symmetric perturbation with varying sign as a function of θ to a plasticised annulus

We have argued that residual stresses and displacements are of paramount importance in shaped charge penetration. As a final stepping-stone to posing a tractable model, we consider a similar set-up to the previous section, but allow the sign of the perturbation to vary around the cavity. Little analytical progress has been made with this problem, although we present numerical solutions using a finite-element formulation in FEMLAB. We consider a cavity of radius unity centred at the origin in a steel material occupying the grid $-15 \leq x, y \leq 15$. The yield stress of the steel is chosen to be $2 \times 10^8 \text{kg m}^{-1} \text{s}^{-1}$. We then divide the domain into 2668 finite elements and then, using a perfect-plastic-elastic model, plasticise an annulus by applying zero traction on the outer boundaries, zero shear stress on $r = 1$, and $\sigma_{rr} = -3.5 \times 10^8 \text{kg m}^{-1} \text{s}^{-1}$ on $r = 1$. The solution to this symmetric problem is shown in Fig. 5.11 in a Von-Mises stress plot. To investigate

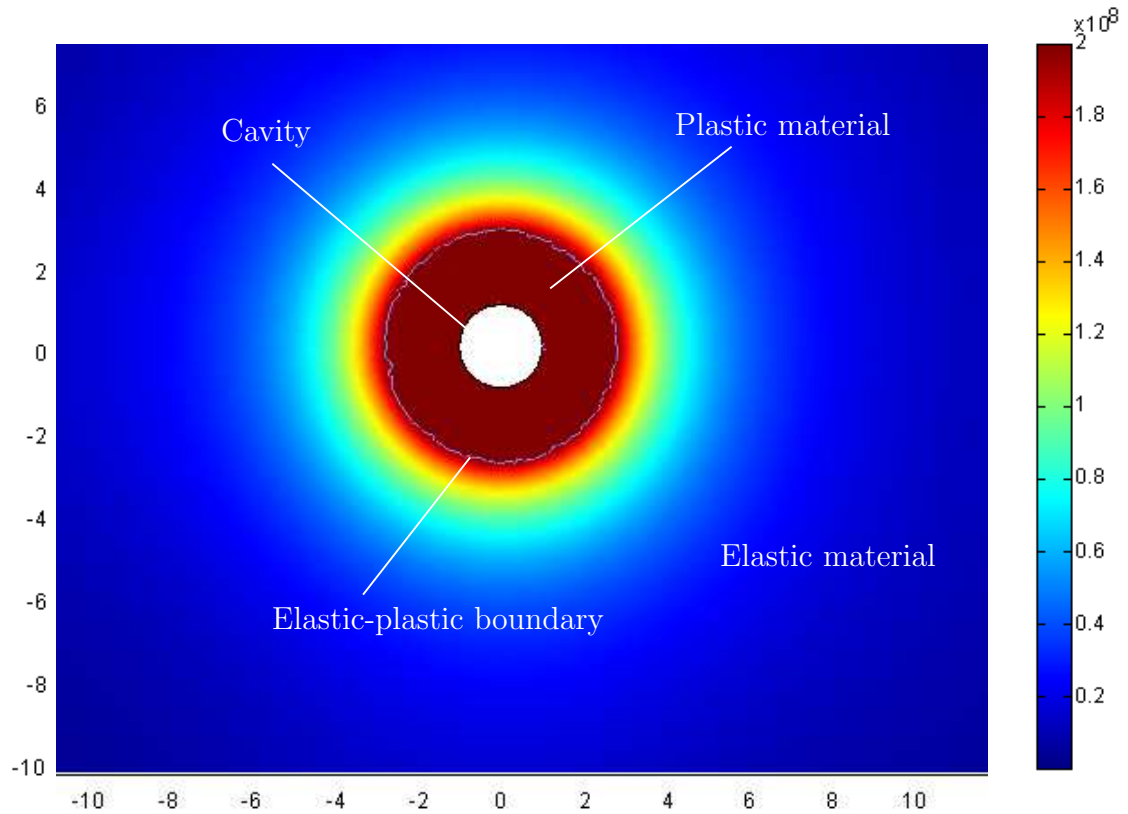


Figure 5.11: Von-Mises stress contours from FEMLAB modelling plasticised steel.

unloading phenomena, we continue to increase the cavity pressure when $x > 0$, whilst decreasing it for $x < 0$, thus introducing a Heaviside-discontinuity at $\theta = \pm\pi/2$. We expect the response to the unloading in $x < 0$ to be elastic, whilst the plastic region will extend further in $x > 0$, with some free boundary separating these regions. Furthermore, we expect that if we unload sufficiently in $x < 0$ (assuming the initial inflation pressure is sufficiently great, as in §5.1.6), then the steel will reyield. Indeed, choosing suitable parameters, these observations can be realised, and are shown in Fig. 5.12 and Fig. 5.13. Observe the position and shape of the elastic-plastic free boundary and the possibility of reverse yielding.

5.4.5 Remarks

The results from FEMLAB emphasise the important role of residual stresses that arise from loading and unloading. It is clear that, even when the radial cavity stress boundary condition is a simple Heaviside discontinuity, the response of the material is complex and only a numerical solution is sensible. However, we are now in a good position to exploit the ideas from this chapter to formulate a model for shaped-charge penetration.

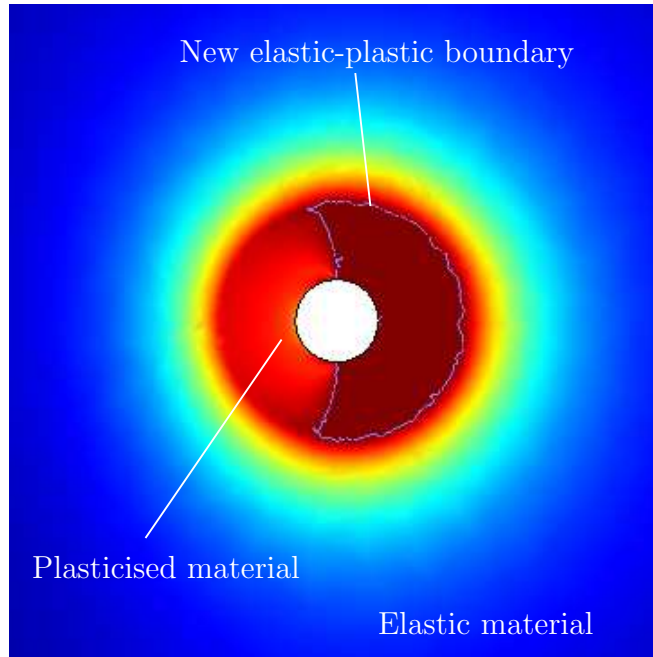


Figure 5.12: A Von-Mises plot from FEMLAB on the same scale as Fig. 5.11. The outer boundary is stress-free, whereas the boundary conditions on the cavity are zero shear stress and $\sigma_{rr} = -3.78 \times 10^8 \text{ kg m}^{-1} \text{ s}^{-1}$ for $x > 0$, $\sigma_{rr} = -3 \times 10^8 \text{ kg m}^{-1} \text{ s}^{-1}$ for $x < 0$.

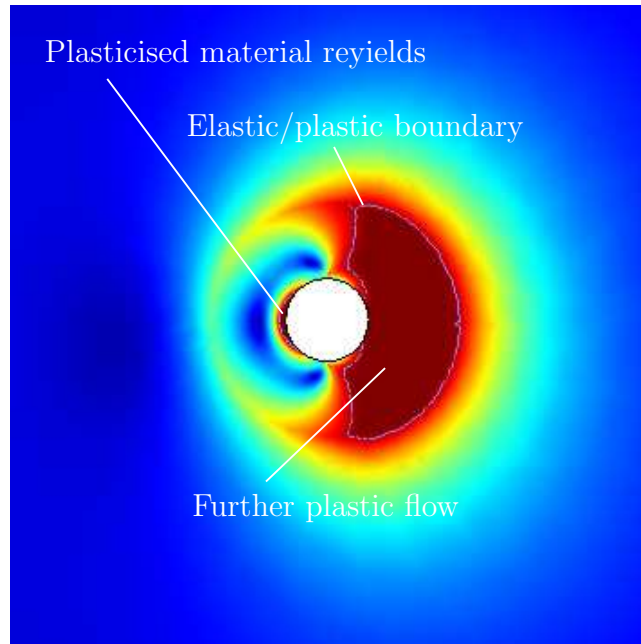


Figure 5.13: A Von-Mises plot from FEMLAB on the same scale as Fig. 5.11, now illustrating the possibility of reverse yielding. The cavity boundary conditions are $\sigma_{r\theta} = 0$ and $\sigma_{rr} = -3.78 \times 10^8 \text{ kg m}^{-1} \text{ s}^{-1}$ for $x > 0$, $\sigma_{rr} = -3 \times 10^7 \text{ kg m}^{-1} \text{ s}^{-1}$ for $x < 0$, and the outer boundary remains stress-free.

Chapter 6

Ideas for a full elastic-plastic model

In the previous chapter, we analysed, in some detail, the expansion and contraction of a circular cavity under applied pressure. We discovered that ‘locking in’ plastic stresses resulted in residual displacements and stresses and that asymmetric boundary conditions lead to novel free boundary problems. In this chapter, we wish to write down a full elastic-plastic model that takes the plastic history of the material into account, based on the previous gun-barrel analysis. We will conclude this chapter by discussing a possible mechanism of moving plastic material via a squeeze film analogy.

6.1 A full elastic-plastic model for the tip

Given the complexity of the elastic-plastic model developed for penetration with a slender region far from the tip, it is likely that a full axisymmetric model will be impossible to solve analytically. However, it is important to present such a model for completion and to understand the intricate nature of the penetration.

Our proposed model is best viewed pictorially, and is shown in Fig. 6.1. As one might expect, we consider the usual plastic, elastic and jet regions. The extra region is the *plasticised* region. This is motivated by the work of the previous chapter, and is a region containing residual stresses and displacements. We will thus split the stress into a residual part and non-residual part in this region; it is the former component of the stress tensor that accounts for the plastic history of the material. Based on the gun-barrel analysis, there will be a free boundary separating the plasticised material from the surrounding elastic material, and a free boundary with the plastic region where the yield condition is satisfied and new plastic stress is still being created. Furthermore, we expect the radius of the free boundary between plasticised material and purely elastic material to increase towards the initial entry point of penetration. This is because the pressure at the tip will decrease as the charge penetrates, resulting in a plastic zone decreasing in size with

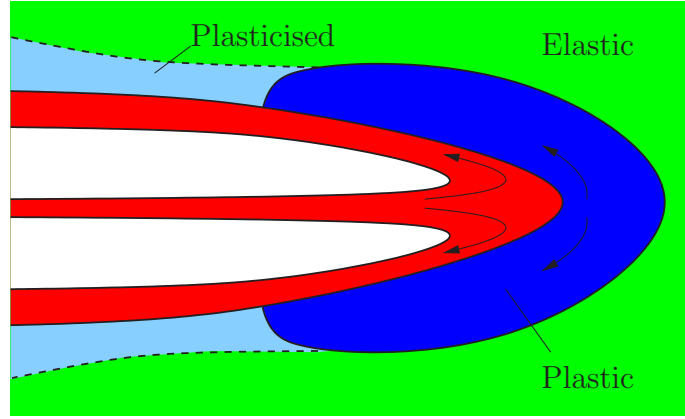


Figure 6.1: The proposed elastic-plastic model showing jet, elastic, plastic and plasticised regions of the penetration.

time around the tip. The geometry of the plastic-plasticised free boundary is not clear; the analysis of Chapter 4 indicates that this boundary is near the tip for targets with a high yield stress, as the plastic region cannot be maintained by the pressure of the jet sufficiently far into the slender region. However, even for softer targets where we might have expected the plastic region to extend further back towards the entry point of the charge, we still expect this boundary to be in the vicinity of the tip. This is because the stresses applied from the jet far from the tip, although great enough to induce yield on virgin material, are significantly less than the large stresses that were exerted as the tip passed this point. Thus they will contribute to the residual part of the stress, rather than producing yield, an important point that was illustrated by Fig. 5.7.

We now write down the nondimensional equations in each region, essentially using ideas from Chapter 4 without the small parameter. Again, we assume that the penetration has already begun so that we can ignore the difficult initial impact problem.

6.1.1 Tip jet region

Making the usual assumptions about incompressibility and of an irrotational flow, the equations governing the motion of the jet are Laplace's equation and Bernoulli's equation. We write the velocity potential as φ , then change to a frame moving with the stagnation point which has new velocity potential ϕ . With the notation of Chapter 3, we scale $\mathbf{q} \sim U_0$, $z, r \sim r_j$, $t \sim r_j/U_0$ and $p \sim \rho_j U_0^2$ and thus obtain the following nondimensional equations:

$$\frac{1}{r} \frac{\partial}{\partial r} \left(r \frac{\partial \phi}{\partial r} \right) + \frac{\partial^2 \phi}{\partial z^2} = 0, \quad (6.1)$$

$$p + \frac{\partial \phi}{\partial t} + \dot{U}z + \frac{1}{2} \left(\left(\frac{\partial \phi}{\partial z} \right)^2 + \left(\frac{\partial \phi}{\partial r} \right)^2 \right) = 0. \quad (6.2)$$

We again write the inner free boundary as $r = R_0(z, t)$ and the outer free boundary as $r = R_1(z, t)$, so that the nondimensional boundary conditions in a frame moving with the tip are

$$p = 0 \text{ on } r = R_0(z, t), \quad (6.3)$$

and,

$$\frac{\partial R_j}{\partial t} = \frac{\partial \phi}{\partial r} - \frac{\partial \phi}{\partial z} \frac{\partial R_j}{\partial z} \text{ on } r = R_j, \quad j = 0, 1. \quad (6.4)$$

Sufficiently far away from the tip, the boundary condition on $r = R_1$ may have to change to a zero normal flow (if the plastic velocities are significantly smaller than the jet velocities). Also, different asymptotic regions may be needed depending on how near the turnaround point the flow is. Possibilities for such regions will form the backbone for the next chapter. The final condition is a matching condition from knowledge of the initial radius and velocity V of the incoming jet.

6.1.2 Plastic region

The extreme pressure from the jet leads to a plastic region near the tip. Whilst this applied pressure is increasing, we are locking in plastic stress. For consistency, we use the Tresca yield condition, and a perfect-plastic flow law. Scaling all the stresses with the yield stress and lengthscales with r_j , the nondimensional equations are, in the initial frame,

$$\max(|\sigma_{rr} - \sigma_{\theta\theta}|, |\sigma_{rr} - \sigma_{zz}|, |\sigma_{zz} - \sigma_{\theta\theta}|) = 1, \quad (6.5)$$

$$\sigma'_{ij} = \Lambda \dot{\epsilon}_{ij}, \quad (6.6)$$

in addition to the inertial force-balance equations

$$\frac{\partial \sigma_{rr}}{\partial r} + \frac{\partial \sigma_{rz}}{\partial z} + \frac{\sigma_{rr} - \sigma_{\theta\theta}}{r} = \frac{\partial \dot{u}}{\partial t}, \quad (6.7)$$

$$\frac{\partial \sigma_{rz}}{\partial r} + \frac{\partial \sigma_{zz}}{\partial z} + \frac{\sigma_{rz}}{r} = \frac{\partial \dot{w}}{\partial t}. \quad (6.8)$$

Numerical analysis of a point force moving into a solid medium [57] suggests that the intermediate stress is σ_{rr} , so that the yield condition in the tip is $\sigma_{\theta\theta} - \sigma_{zz} = 1$.

As well as being important in the force balance equations, inertia must now be included in the boundary conditions. Firstly, continuity of traction on $r = R_1(z, t)$ is written

$$\mathbf{n} \cdot (\boldsymbol{\sigma} \cdot \mathbf{n}) = -\frac{\rho_j U_0^2}{\sigma_Y} p, \quad \mathbf{t} \cdot (\boldsymbol{\sigma} \cdot \mathbf{n}) = 0 \text{ on } r = R_1(z, t), \quad (6.9)$$

where p is the nondimensional pressure from the jet. The other condition on this boundary is kinematic, so

$$\dot{u} - \frac{\partial R_1}{\partial z} \dot{w} = \frac{\partial R_1}{\partial t} \text{ on } r = R_1(z, t). \quad (6.10)$$

We denote the elastic-plastic boundary by $r = R_2(z, t)$. Again, the normal velocity must be continuous on this non-material boundary, so that

$$\dot{u} - \frac{\partial R_2}{\partial z} \dot{w} = 0 \text{ on } r = R_2(z, t), \quad (6.11)$$

whereas the nondimensional traction vector satisfies (3.21), *i.e.*

$$\left[\sigma_{in} - \frac{\rho_t U_0^2}{\sigma_Y} (\dot{u}_n - V) \dot{u}_i \right]_-^+ = 0, \quad (6.12)$$

which can be simplified in line with (6.11). We defer writing down the boundary condition with the plasticised region until we have described the region's equations.

6.1.3 Elastic region

The nondimensional Navier equations for the displacements in a frame moving with the stagnation point, similar in nature to (4.78)-(4.79), are

$$\left(\frac{\partial^2 u}{\partial r^2} + \frac{\partial}{\partial r} \left(\frac{u}{r} \right) \right) + \left(\frac{\lambda + \mu}{\lambda + 2\mu} \right) \frac{\partial^2 w}{\partial r \partial z} + \frac{\mu}{\lambda + 2\mu} \left(\frac{\partial^2 u}{\partial z^2} \right) = M_p^2 \left(\frac{\partial}{\partial t} - U \frac{\partial}{\partial z} \right)^2 u, \quad (6.13)$$

$$\frac{\mu}{\lambda + 2\mu} \left(\frac{1}{r} \frac{\partial}{\partial r} \left(r \frac{\partial w}{\partial r} \right) \right) + \left(\frac{\lambda + \mu}{\lambda + 2\mu} \right) \frac{1}{r} \frac{\partial^2 (ur)}{\partial r \partial z} + \frac{\partial^2 w}{\partial z^2} = M_p^2 \left(\frac{\partial}{\partial t} - U \frac{\partial}{\partial z} \right)^2 w, \quad (6.14)$$

where M_p is the Mach number with respect to the primary wave speed. The elastic stresses are given via the relations (3.25). In addition to the boundary conditions with the plastic region already mentioned, we also have

$$\sigma_{ij} \rightarrow 0 \text{ as } \mathbf{r} \rightarrow \infty, \quad (6.15)$$

and we impose a radiation condition of no incoming waves. There is also some matching condition with the plasticised region, which will be described in the next section.

6.1.4 'Plasticised' elastic region

Recall that the plasticised region arises when the applied pressure starts decreasing. In this region, we split the total stress and the total displacement into a plastic residual part from the expansion and an elastic part for the contraction, viz:

$$\boldsymbol{\sigma} = \boldsymbol{\sigma}^p(r, z) + \boldsymbol{\sigma}_{\text{con}}^e(r, z, t), \quad (6.16)$$

$$\mathbf{u} = \mathbf{u}^p(r, z) + \mathbf{u}_{\text{con}}^e(r, z, t). \quad (6.17)$$

The elastic parts of the stress and displacement satisfy the usual force balance equations and Navier equations, as in the fully elastic region above. The residual part of the stress is the stress field from when the material was last plastic, which occurred whilst the

plastic region was increasing in size (equivalent to the applied pressure gradient being positive in the radially-symmetric gun-barrel problem). Similarly, the residual part of the displacement is the displacement of the material when it was last plastic¹. These residual parts are calculated whilst the region is still plastic ($\frac{\partial P}{\partial t} > 0$).

We denote the free boundary of this region with the fully-elastic region as $r = R_3(z, t)$ and the part in contact with the plastic region as $r = R_4(z, t)$. The nondimensional boundary conditions over the plasticised-elastic-elastic boundary $r = R_3(z, t)$ are thus

$$[\mathbf{n} \cdot (\boldsymbol{\sigma} \cdot \mathbf{n})]_{-}^{+} = 0, \quad (6.18)$$

$$[\mathbf{t} \cdot (\boldsymbol{\sigma} \cdot \mathbf{n})]_{-}^{+} = 0, \quad (6.19)$$

$$[\mathbf{u}]_{-}^{+} = 0, \quad (6.20)$$

$$[\dot{\mathbf{u}}]_{-}^{+} = 0. \quad (6.21)$$

The boundary $r = R_4(z, t)$ is an elastic-plastic boundary, so has boundary conditions

$$[\dot{\mathbf{u}} \cdot \mathbf{n}]_{-}^{+} = 0, \quad (6.22)$$

$$\left[\sigma_{in} - \frac{\rho_t U_0^2}{\sigma_Y} (\dot{u}_n - \dot{v}_n) \dot{u}_i \right]_{-}^{+} = 0, \quad (6.23)$$

where σ_{ij} is the total stress, u_i is the total displacement and \dot{v}_n is the normal velocity of the free boundary. We can of course simplify these boundary conditions knowing that $\boldsymbol{\sigma}^{(e)} = 0$ on $r = R_4(z, t)$, as this is the boundary where material stops getting locked in and any change in stress occurs in the (recoverable) elastic part.

6.1.5 Remarks

We have written down a novel model with four free boundaries. This model is nontrivial and it is likely that it can only be solved numerically. Furthermore, depending on the parameter regime, it is possible that a fifth free boundary is needed to include the effect of reyielding (as $P_* \gg \sigma_Y$), shown in Fig. 6.2. The equations for this region are no harder to write down than for the ‘plasticised elastic’ region; all we need to do is decompose the stress into a residual part (known from the plastic history when the plastic region was still advancing) and a new plastic part, $\tilde{\boldsymbol{\sigma}}^p(\mathbf{r}, t)$. The latter must satisfy the usual associated flow law, force balances and yield condition with suitable boundary conditions,

¹Note that we *could* split the stresses and displacements into residual (*i.e.* elastic response to residual plastic) and elastic parts in the elastic region, as we did in the gun-barrel expansion-contraction. However, since both elastic and residual parts satisfy the same governing equations, we can just solve for the total stress. In the case of the gun-barrel, this is apparent by noting that both residual and elastic parts of the stress have general solution $\sigma_{rr} = A(t)/r^2$.

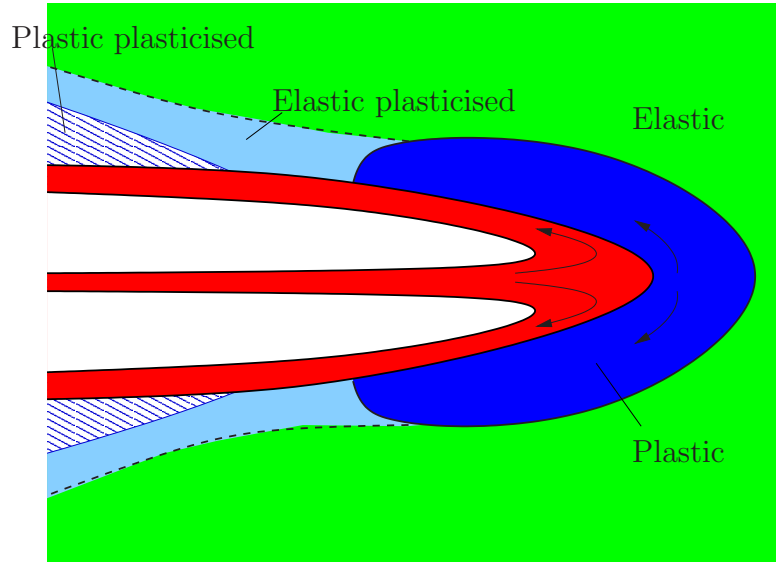


Figure 6.2: A modification to the previous figure (Fig. 6.1), permitting residual stresses and including reyielding effects.

and occurs when the total stress satisfies the yield condition (see §5.1.6). We can now summarise the determination of the stress tensor as

$$\boldsymbol{\sigma}(\mathbf{r}, t) = \begin{cases} \boldsymbol{\sigma}^e(\mathbf{r}, t) & \text{if } \mathcal{Y}(\boldsymbol{\sigma}(\mathbf{r}, t)) < \sigma_Y \text{ and } \max_{t>0} \mathcal{Y}(\boldsymbol{\sigma}(\mathbf{r}, t)) < \sigma_Y, \\ \boldsymbol{\sigma}^p(\mathbf{r}, t) & \text{if } \mathcal{Y}(\boldsymbol{\sigma}(\mathbf{r}, t)) = \sigma_Y \text{ and } \boldsymbol{\sigma}_{\text{con}}^e = 0, \\ \boldsymbol{\sigma}^p(\mathbf{r}, t_c) + \boldsymbol{\sigma}_{\text{con}}^e(\mathbf{r}, t) & \text{if } \mathcal{Y}(\boldsymbol{\sigma}(\mathbf{r}, t)) < \sigma_Y, \text{ and } \max_{0 < t < t_c} \mathcal{Y}(\boldsymbol{\sigma}(\mathbf{r}, t)) = \sigma_Y, \\ \boldsymbol{\sigma}^p(\mathbf{r}, t_c) + \tilde{\boldsymbol{\sigma}}^p(\mathbf{r}, t) & \text{if } \mathcal{Y}(\boldsymbol{\sigma}(\mathbf{r}, t)) = \sigma_Y, \max_{0 < t < t_c} \mathcal{Y}(\boldsymbol{\sigma}(\mathbf{r}, t)) = \sigma_Y, \\ & \text{and } \mathcal{Y}(\boldsymbol{\sigma}^p(\mathbf{r}, t_c + \delta t)) < \sigma_Y. \end{cases}$$

Here, we write $\mathcal{Y}(\boldsymbol{\sigma})$ to denote that $\boldsymbol{\sigma}$ satisfies one of the nonlinear yield conditions (1.38), δt for some small time, and t_c to denote the last time at which the material was plastic on expansion. Using the notation “ $\mathcal{N}\boldsymbol{\sigma} = 0$ ” to mean that $\boldsymbol{\sigma}$ satisfies Navier’s equations of linear elasticity and “ $\mathcal{P}\boldsymbol{\sigma} = 0$ ” to mean that $\boldsymbol{\sigma}$ satisfies the quasistatic equations of perfect-plasticity, the equations for the stresses are thus

$$\mathcal{N}(\boldsymbol{\sigma}^e) = 0, \quad (6.24)$$

$$\mathcal{N}(\boldsymbol{\sigma}_{\text{con}}^e) = 0, \quad (6.25)$$

$$\mathcal{P}(\boldsymbol{\sigma}^p) = 0, \quad (6.26)$$

$$\tilde{\mathcal{P}}(\tilde{\boldsymbol{\sigma}}^p) = 0, \quad (6.27)$$

where the operator $\tilde{\mathcal{P}}$ in the final equation means that $\tilde{\boldsymbol{\sigma}}^p$ satisfies the plasticity equations with modified yield condition (see §5.1.6).

Our model views the final cavity as being held open by residual stresses, a consequence of the plastic deformation it underwent during penetration. It is clear that the motion of

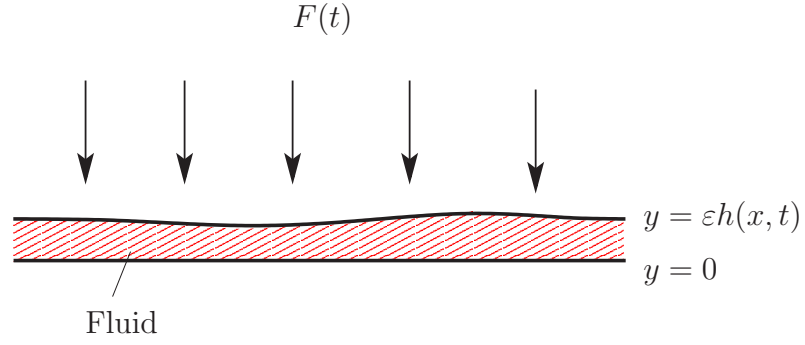
the tip is of major importance, as the residual stress is locked in where the pressure from the jet peaks, *i.e.* in the vicinity of the jet. However, we saw that even with the relatively simple geometry in §5.4.4, the resultant stress field is complex, and so a full solution to the penetration model can only be numerical. On a positive note, the model is successful in providing an explanation for the observed bowed edges, namely, that they are the elastic response to the residual stresses and displacements in the plasticised region.

6.2 Squeeze film analogy

We have just seen the high degree of complexity involved in an elastic-perfect-plastic model for penetration, even with the presence of a small parameter in the slender region. In this section, we develop a simpler model in order to visualise the plastic flow field and to see how the applied pressure affects the size of the plastic region. We initially consider a two-dimensional elastic-plastic squeeze film between two flat plates under a horizontal tension to see how the plastic flow evolves under some applied pressure P . We will then consider the similar set-up of when the block is under horizontal compression to model the confinement of the target. We will then cultivate this model, briefly discussing the case when the upper plate is slowly varying, before considering a squeeze film with no fixed base in general curvilinear coordinates. Our aim is to see the effect of a pressure P over a fixed interval on the height of the plastic region. Note that this is not directly applicable to the flow in the target, as, in doing a squeeze film, we assume that the elastic part of the squeeze film is free to move horizontally; in reality, it is part of the target, and so is confined by the surrounding elastic material. In addition to evaluating the flow field, we also wish to investigate the possibility of solutions in which the height of the squeeze film goes to zero. This represents the termination of the plastic region, as in Fig. 6.1. Before embarking upon such a voyage, we outline the analysis for a simple viscous squeeze film.

6.2.1 Viscous squeeze film

Consider a two-dimensional squeeze film on $-L < x < L$. We fix the lower surface $y = 0$ and prescribe the upper surface $y = \varepsilon h(x, t)$, where $0 < \varepsilon \ll 1$ is the ratio of a typical vertical lengthscale to a typical horizontal lengthscale (say L). A spatially-constant force $F(t) > 0$ is applied on the upper surface. This is shown in Fig. 6.3. We use the Navier-Stokes equations and incompressibility to model the viscous fluid. Writing $\mathbf{u} = (u, v)$ for the fluid velocity, we nondimensionalise these equations, summarised in (D.2). As in classic boundary-layer theory, $\varepsilon \ll 1$ motivates us to rescale $y = \varepsilon y'$ and the vertical velocity $v = \varepsilon v'$. By also assuming that the “reduced Reynold’s number”, $\mathcal{R}\varepsilon^2 \ll 1$

**Figure 6.3:** A viscous squeeze film.

(where \mathcal{R} is the Reynold's number), we can neglect inertia in the momentum equation. We rescale $p = \frac{1}{\varepsilon^2} p'$ to avoid the trivial solution and hence, at leading order, we recover the *lubrication equations* (dropping dashes):

$$0 = -\frac{\partial p}{\partial x} + \frac{\partial^2 u}{\partial y^2}, \quad (6.28)$$

$$0 = -\frac{\partial p}{\partial y}, \quad (6.29)$$

$$\frac{\partial u}{\partial x} + \frac{\partial v}{\partial y} = 0. \quad (6.30)$$

The boundary conditions are zero flow on the bottom plate and that the only nonzero component of the velocity on the upper plate is the normal velocity, which must balance the velocity of the upper surface. We also know that the external force imposed must balance the force from the fluid. Thus

$$u = v = 0 \quad \text{on } y = 0, \quad (6.31)$$

$$u = 0, v = \frac{\partial h}{\partial t} \quad \text{on } y = h(x, t), \quad (6.32)$$

$$\int_{\text{top}} p(x, t) dx = F(t). \quad (6.33)$$

Briefly, we integrate the vertical component of the momentum equation to get that $p = p(x, t)$ and hence, by integrating the horizontal momentum balance, we find that

$$u = \frac{1}{2} \frac{\partial p}{\partial x} y(y - h). \quad (6.34)$$

Finally, integration of the mass conservation equation between 0 and $h(x, t)$ leads us to

$$\frac{\partial h}{\partial t} = \frac{\partial}{\partial x} \left(\frac{h^3}{12} \frac{\partial p}{\partial x} \right). \quad (6.35)$$

Using incompressibility along with the boundary conditions for v and (6.33), we can find v in terms of $p(x, t)$, $h(x, t)$ and hence $F(t)$.

6.2.1.1 Solution for $h = h(t)$

In the case where h is a function of time only, we can write down explicit solutions for bounded $F(t)$. Suppose that the squeeze film is on the nondimensional interval $-1 < x < 1$ (and that the two plates are also described by $-1 < x < 1$). We can integrate (6.35) with respect to x and use $p(\pm 1, t) = 0$ (taking atmospheric pressure to be zero) to obtain

$$p(x, t) = \frac{6}{h^3} \frac{dh}{dt} (x^2 - 1), \quad (6.36)$$

and, on using (6.33),

$$F(t) = -\frac{8}{h^3} \frac{dh}{dt} = 4 \frac{d}{dt} \left(\frac{1}{h^2} \right). \quad (6.37)$$

We denote $h(0) = h_0$, and so the top-boundary is given by

$$h(t) = \frac{1}{\sqrt{\int_0^t \frac{F(\tau)}{4} d\tau + \frac{1}{h_0^2}}}. \quad (6.38)$$

Note that, for monotonic, bounded $F(t)$, $h(t)$ remains finite and so the two plates do not meet in finite time. The corresponding velocities are

$$u = \frac{3F}{4} y(y - h)x, \quad (6.39)$$

$$v = \frac{3F}{4} y \left(\frac{y^2}{3} - \frac{hy}{2} \right). \quad (6.40)$$

6.2.2 Elasto-plastic squeeze film under horizontal tension

We now wish to develop a plastic equivalent to the viscous squeeze film. Before looking at a direct analogy with the viscous squeeze film, we quickly outline the circumstances in which a plastic squeeze film may arise. The problem concerning the compression of an elastic block between two *rough* plates is discussed by Hill [36]. Initially, he considers compression in which the plates are not as wide as the width of the block being compressed, and so there is an overhang. He assumes the experimentally observed fact, namely that the elastic block begins to yield at the four sharp edges, and then spreads inwards as the pressure on the block is increased (Fig. 6.4). Note that the overhang must always remain elastic as it satisfies a stress-free boundary condition. The bug-bear of solving this kind of system is that the block does not remain geometrically similar and so the rheology must be tracked as time progresses.

The equations can be simplified when the (finite) block is a lot wider than it is tall. Hill argues that the slip-lines must become uniform far from the edge, and essentially solves the leading-order problem for the stresses (but not velocities) sufficiently far away from the overhang. The resulting solution (involving a coefficient of friction for the rough blocks) is known as *Prandtl's cycloid solution*.

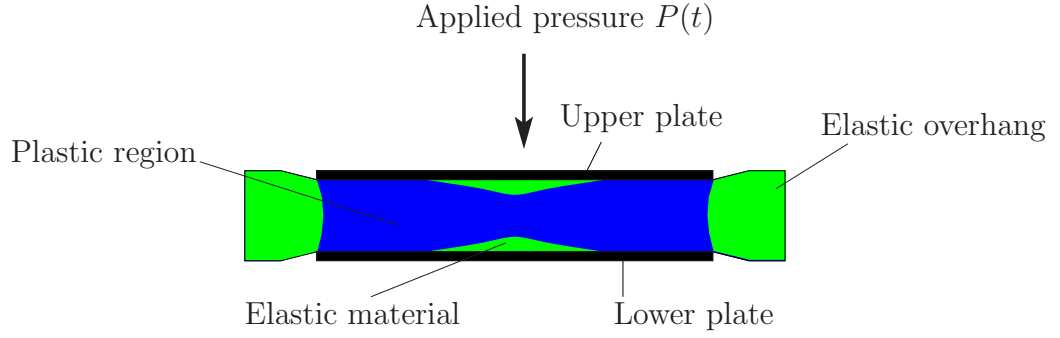


Figure 6.4: Hill's squeeze film [36]. Observe that the plasticity spreads from the four sharp corners into the middle, and that the overhang is elastic.

This solution motivates us to consider a thin material initially lying in $-L < x < L$ and $0 < y < h_0$, where h_0 is known and $h_0 \ll L$. We apply sufficient pressure $P(t) > 0$ on the upper surface for $|x| \leq 1$, so that the material in $|x| \leq 1$ is plastic, where $L \gg 1$. Thus we allow the upper surface $y = h_p(x, t)$ to vary with space and time in this plastic region. This initial set-up is shown in Fig. 6.5. Given suitable applied pressure and horizontal

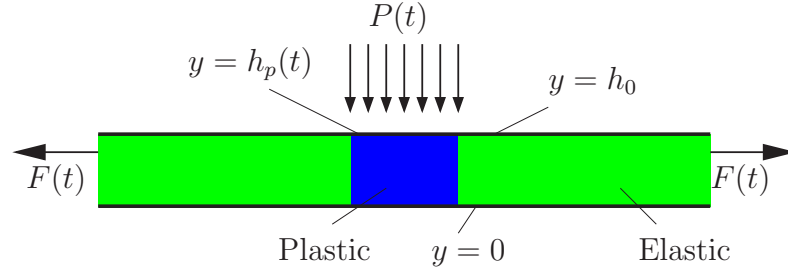


Figure 6.5: A simple plastic squeeze film under tension.

tensile force $F(t) > 0$, the material in $|x| < 1$ will remain plastic and neck, whilst the remaining elastic material will move horizontally as a rigid body. The necked part of the material in $|x| > 1$ that was once plastic will have residual stresses. As the material is thin, we can assume that all the horizontal components of displacement, velocity and stress will be independent of y . We hence denote the boundary between the plasticised region and the elastic region as $x = \pm c(t)$, and present a schematic diagram in Fig. 6.6. Note the analogy with cold-rolling [54]. Our aim is to solve for the height $h_p(x, t)$ and the displacement, velocity and stress in each region for a given initial profile and with prescribed $F(t) > 0$ and $P(t) > 0$. We will assume that all of the surfaces are shear-free².

Rescaling the y -component of the plastic velocity with ε (to avoid the trivial solution),

²To allow for a rough surface, Hill uses the boundary condition $\sigma_{xy}(\varepsilon h) = mk$ on $y = \varepsilon h_p(t)$, for $0 \leq m \leq 1$ ($m = 1$ being a completely rough surface), where $k = \sigma_Y/2$ for the Tresca yield condition and $k = \sigma_Y/\sqrt{3}$ for Von-Mises' yield condition.

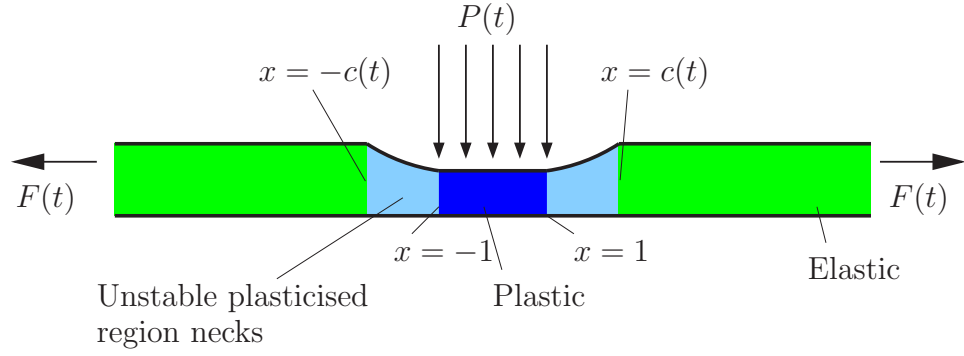


Figure 6.6: Necking of the unstable plastic squeeze film. The curved part of the elastic region is determined by the height when it was last plastic.

the boundary conditions in the plastic region are

$$v(x, 0, t) = 0, \quad (6.41)$$

$$\sigma_{xy}(x, t) = 0, \quad (6.42)$$

$$\mathbf{n} \cdot (\boldsymbol{\sigma} \cdot \mathbf{n}) = -P(t) \text{ on } y = h_p(x, t), \quad (6.43)$$

$$\mathbf{t} \cdot (\boldsymbol{\sigma} \cdot \mathbf{n}) = 0 \text{ on } y = h_p(x, t), \quad (6.44)$$

$$\dot{v}(x, h_p, t) = \frac{\partial h_p}{\partial t}(x, t), \quad (6.45)$$

$$\dot{u}(\pm 1, t) = \pm \dot{c}(t). \quad (6.46)$$

and continuity of traction over $|x| = 1$. In writing the last boundary condition down, we assume that the elastic displacement is small compared with the rigid body displacement in both the elastic and plasticised regions. In the usual manner, we decompose the stress and displacement in the plasticised region $1 < |x| < c(t)$ as

$$\sigma_{xx}(x, t) = \sigma_{xx}^p(x, \tau(x)) + \sigma_{xx}^e(x, t), \quad (6.47)$$

and so on for the remaining stress and displacement components, where $\tau(x)$ is the time at which the material at x was last plastic. Denoting the height of this region by $y = h_e(x, t)$, the boundary conditions are

$$v(x, 0, t) = 0, \quad (6.48)$$

$$\sigma_{xy}(x, 0, t) = 0, \quad (6.49)$$

$$\mathbf{n} \cdot (\boldsymbol{\sigma} \cdot \mathbf{n}) = 0 \text{ on } y = h_e(x, t), \quad (6.50)$$

$$\mathbf{t} \cdot (\boldsymbol{\sigma} \cdot \mathbf{n}) = 0 \text{ on } y = h_e(x, t), \quad (6.51)$$

$$\sigma_{xx}(\pm c(t), t) = \sigma_{xx}^E(\pm c(t), t), \quad (6.52)$$

$$\sigma_{xy}(\pm c(t), y, t) = \sigma_{xy}^E(\pm c(t), y, t), \quad (6.53)$$

along with continuity of traction into the elastic region $|x| > c(t)$. The superscripts ‘E’ refer to the elastic region, which has boundary conditions

$$v^E(x, 0, t) = 0, \quad (6.54)$$

$$\sigma_{xy}^E(x, 0, t) = 0, \quad (6.55)$$

$$\sigma_{xy}^E(x, h_0, t) = 0, \quad (6.56)$$

$$\sigma_{yy}^E(x, h_0, t) = 0, \quad (6.57)$$

$$\sigma_{xx}^E(\pm L, t) = F(t) > 0, \quad (6.58)$$

$$\sigma_{xy}^E(\pm L, y, t) = 0. \quad (6.59)$$

Note that we have deferred writing down the traction continuity conditions explicitly – this will be remedied when we have exploited the thinness of the medium.

Plastic region $|x| < 1$

We are looking for a quasistatic solution, and so the equations for the plastic region are the equations of equilibrium,

$$\frac{\partial \sigma_{xx}}{\partial x} + \frac{\partial \sigma_{xy}}{\partial y} = 0, \quad (6.60)$$

$$\frac{\partial \sigma_{xy}}{\partial x} + \frac{\partial \sigma_{yy}}{\partial y} = 0, \quad (6.61)$$

a yield condition,

$$\frac{1}{4}(\sigma_{xx} - \sigma_{yy})^2 + \sigma_{xy}^2 = k^2, \quad (6.62)$$

where $k = \sigma_Y/2$ for the Tresca yield condition and $k = \sigma_Y/\sqrt{3}$ for Von-Mises’ yield condition, and a flow law,

$$\sigma'_{ij} = \Lambda \dot{\varepsilon}_{ij}, \quad (6.63)$$

where $\Lambda(x, y, t)$ is an unknown Lagrange multiplier for the yield constraint, which we assume to be $\mathcal{O}(1)$ *a priori*. This flow law automatically implies incompressibility, which is written in terms of the deviatoric stresses as

$$\sigma'_{xx} + \sigma'_{yy} = 0. \quad (6.64)$$

We nondimensionalise the components of the yield stress with $2k$, the horizontal length-scale with L , the vertical height with h_0 and the horizontal force with $2kh_0$. Writing the ratio $h_0/L = \varepsilon \ll 1$, the equilibrium equations become

$$\frac{\partial \sigma_{xx}}{\partial x} + \frac{1}{\varepsilon} \frac{\partial \sigma_{xy}}{\partial y} = 0, \quad (6.65)$$

$$\frac{\partial \sigma_{xy}}{\partial x} + \frac{1}{\varepsilon} \frac{\partial \sigma_{yy}}{\partial y} = 0. \quad (6.66)$$

We expand the plastic stresses as an asymptotic series in ε , so

$$\sigma_{xx} = \sigma_{xx}^{(0)} + \mathcal{O}(\varepsilon), \quad (6.67)$$

$$\sigma_{yy} = \sigma_{yy}^{(0)} + \mathcal{O}(\varepsilon), \quad (6.68)$$

$$\sigma_{xy} = \sigma_{xy}^{(0)} + \varepsilon \sigma_{xy}^{(1)} + \mathcal{O}(\varepsilon^2). \quad (6.69)$$

At leading order, the equations of equilibrium (6.65)-(6.66), along with the boundary conditions (6.41)-(6.43), give that

$$\sigma_{yy}^{(0)} = -\bar{P}(t) \quad (6.70)$$

and

$$\sigma_{xy}^{(0)} = 0. \quad (6.71)$$

The yield condition now gives

$$\sigma_{xx}^{(0)} = 1 - \bar{P}(t), \quad (6.72)$$

where $\bar{P} = P/2k$ is the nondimensional pressure. This must hold everywhere in the plastic region. At $\mathcal{O}(\varepsilon)$, (6.65) gives a horizontal force balance, which we integrate to

$$\int_0^{h_p} \frac{\partial \sigma_{xx}^{(0)}(t)}{\partial x} dy = -\sigma_{xy}^{(1)}(x, h_p, t). \quad (6.73)$$

However, we know that the left-hand side is zero, and that, from (6.44),

$$-\frac{\partial h}{\partial x} \sigma_{xx}^{(0)} + \sigma_{xy}^{(1)} + \frac{\partial h}{\partial x} \sigma_{yy}^{(0)} = 0 \text{ on } y = h_p(x, t). \quad (6.74)$$

Hence $h_p = h_p(t)$.

To calculate the flow field, we use incompressibility (6.64) and the yield condition in the nondimensional form

$$\sigma_{xx}^{(0)} - \sigma_{yy}^{(0)} = 1, \quad (6.75)$$

and find that

$$\sigma'_{xx} = \frac{1}{2}, \quad (6.76)$$

$$\sigma'_{yy} = -\frac{1}{2}. \quad (6.77)$$

Recalling that \dot{v} has been rescaled by ε , the incompressibility condition (6.64) becomes, at leading order,

$$\frac{\partial \dot{u}}{\partial x} + \frac{\partial \dot{v}}{\partial y} = 0. \quad (6.78)$$

The flow law yields

$$\frac{\partial \dot{u}}{\partial x} = \frac{1}{2\Lambda(x, y, t)} = -\frac{\partial \dot{v}}{\partial y}. \quad (6.79)$$

The flow law also gives that

$$0 = \sigma_{xy} = \sigma'_{xy} = \frac{\Lambda}{2} \left(\frac{1}{\varepsilon} \frac{\partial \dot{u}}{\partial y} + \varepsilon \frac{\partial \dot{v}}{\partial x} \right), \quad (6.80)$$

so that, at leading order, $\dot{u} = \dot{u}(x, t)$. In terms of the velocities, the yield condition is

$$\Lambda(x, y, t) \left(\frac{\partial \dot{u}}{\partial x} - \frac{\partial \dot{v}}{\partial y} \right) = 1. \quad (6.81)$$

However, the incompressibility condition (6.78) now tells us that $\frac{\partial \dot{v}}{\partial y} = \frac{\partial \dot{v}}{\partial y}(x, t)$, and hence $\Lambda = \Lambda(x, t)$. We now integrate (6.79) to obtain

$$\dot{v} = -\frac{y}{2\Lambda(x, t)}, \quad (6.82)$$

where we have used no flow on $y = 0$ to fix the constant of integration to zero. The other boundary condition on the vertical velocity gives that

$$\Lambda(t) = -\frac{h_p(t)}{2\dot{h}_p(t)}. \quad (6.83)$$

This is positive for $\dot{h}_p < 0$, and so the material is only plastic whilst the film is getting thinner. The velocity field can be written as

$$\dot{u} = -\frac{\dot{h}_p(t)}{h_p(t)}x, \quad (6.84)$$

$$\dot{v} = \frac{\dot{h}_p(t)}{h_p(t)}y, \quad (6.85)$$

where we have fixed the constant of integration in the horizontal velocity to be zero by symmetry. This is stagnation flow.

Elastic region $|x| > c(t)$

Firstly, we note that, by arguing as we did in the plastic region, the rescaled equations of equilibrium give us the leading-order stresses

$$\sigma_{yy}^E = 0 = \sigma_{xy}^E. \quad (6.86)$$

Instead of integrating the equilibrium equations further, we exploit the plane-stress elasticity and introduce the Airy stress function, $A(x, y, t)$, which is biharmonic. Nondimensionally, the biharmonic equation becomes

$$\frac{\partial^4 A}{\partial y^4} = 0, \quad (6.87)$$

and so the leading-order solution is

$$A_0(x, y, t) = \frac{\alpha(x, t)y^3}{6} + \frac{\beta(x, t)y^2}{2} + \gamma(x, t)y + \delta(x, t). \quad (6.88)$$

The stresses are determined via $\sigma_{xx}^E = A_{yy}$, $\sigma_{yy}^E = A_{xx}$ and $\sigma_{xy}^E = -A_{xy}$. We already know that $\sigma_{xy}^E = 0$, and so α and β are functions of t only. The boundary condition (6.58) is independent of y , and so, using

$$\sigma_{xx}^E(y, t) = \alpha(t)y + \beta(t), \quad (6.89)$$

we must have that $\alpha(t) = 0$. The final unknown component of the stress tensor is hence

$$\sigma_{xx}^E(t) = F(t). \quad (6.90)$$

The horizontal force balance into the plasticised region is now

$$\sigma_{xx}(\pm c(t), t) = F(t). \quad (6.91)$$

Plasticised region $1 < |x| < c(t)$

Recall that we decompose $\boldsymbol{\sigma}$ and \mathbf{u} into a plastic residual part and an elastic part. The plastic parts of the stress are determined by the plastic analysis (which is independent of y) as

$$\sigma_{xy}^p = 0, \quad \sigma_{xx}^p = 1 - P(\tau(x)), \quad \sigma_{yy}^p = -P(\tau(x)), \quad (6.92)$$

where $\tau(x)$ is the time at which the material at x was last plastic. From (6.48)-(6.53), the leading-order boundary conditions on the elastic parts of the stress are now

$$\sigma_{yy}^e(x, h_e(x, t), t) = P(\tau(x)), \quad (6.93)$$

$$\sigma_{xy}^e(x, 0, t) = \sigma_{xy}^e(x, h_e(x, t), t) = v^e(x, 0, t) = 0. \quad (6.94)$$

By arguing as we did in the plastic region, the rescaled equations of equilibrium give us the leading-order stresses

$$\sigma_{yy}^e = P(\tau(x)), \quad \sigma_{xy}^e = 0, \quad (6.95)$$

and so the (total) stress $\sigma_{yy} = 0$.

We can now draw conclusions from the system without further analysis of the plasticised region by performing a global horizontal force balance; using continuity of the horizontal force throughout the plasticised region, we have

$$h_p(t)(1 - P(t)) = h_0 F(t). \quad (6.96)$$

This determines the velocity field (6.84)-(6.85), from which we deduce the velocity of the rigid body at $|x| = 1$ and hence the height h_e and stress σ_{xx}^e everywhere in the elastic

region. This solution works if $F(t) = 1 - P(t)$. However, we suppose that $F(0) = 1 - P(0)$, and then slowly increase $F(t)$ whilst holding P constant. The height of the plastic region cannot increase, as the Lagrange multiplier Λ becomes negative. Also, if the pressure $P > 1$, the predicted height becomes negative. Clearly, this solution is unphysical – if we pull harder at the ends, the plastic region should get thinner. We deduce that there is no quasistatic plasticity solution for this set-up – the stress exerted by the elastic region is too great for the plastic region, and so the motion of the plastic region is unstable, leading to necking. A similar result will also hold if we apply a variable pressure in the plastic region, allowing the upper boundary to be slowly-varying as the leading-order stress field is unchanged. This analysis is omitted.

6.2.3 Elastic-plastic squeeze film under horizontal compression

We now consider a similar squeeze-film, but now under horizontal compression. This is motivated by the fact that the plastic region is under confinement from the surrounding target. The only change to the boundary conditions from before is that (6.58) must now be replaced by

$$\sigma_{xx}^E(\pm L, t) = -F(t), \quad (6.97)$$

where $F(t) > 0$. This now gives that $\sigma_{xx}^E = -F(t)$. A global force-balance now leads to

$$h_p(t) = -\frac{h_0 F(t)}{1 - P(t)}, \quad (6.98)$$

from which we can derive expressions for the plastic velocities from (6.84)-(6.85). Using the boundary condition (6.46) and initial conditions on $c(t)$ and $h_p(t)$, we deduce that

$$c(t) = 1 - \log \left(\frac{h_p(t)}{h_0} \right). \quad (6.99)$$

The elastic part of the stress in the plasticised region and hence the height $h_e(x, t)$ can now be calculated using continuity of height and total stress into the different regions. This analysis is omitted. For this solution to make sense, we must have $P(t) > 1$ for the plastic region to be at yield. We suppose that this is true, and then increase the magnitude of F to $F + \delta$ for constant P and small, positive δ . The difference $\sigma_{xx} - \sigma_{yy} < 1$, and so the material is elastic everywhere. This tells us that the higher the confining stress, the greater the pressure we have to apply for the material to remain plastic. Conversely, suppose that we hold F constant and increase the magnitude of P . We can easily see that the material in $|x| < 1$ is still at yield, and the height of the plastic region decreases according to (6.98). This solution is consistent with the Lagrange multiplier for the flow law being positive and makes sense physically. Thus we have derived a simple relationship between

the height of the plastic region and the applied pressure $P(t)$ for a constant confining pressure. Furthermore, observe the similarity with the viscous squeeze-film; the height of the material cannot go to zero for finite applied pressure $P(t)$.

6.2.4 Elasto-plastic squeeze film under compression, with known, varying base

We wish to incorporate the curvature of the tip in to a squeeze film model and so consider a thin plastic squeeze film in which the lower surface is a known fixed function of space under compression. We elect to use the curvilinear coordinate system (s, n) defined by

$$\mathbf{x} = \mathbf{X}_0(s) + n\mathbf{n}, \quad (6.100)$$

where $\mathbf{X}_0(s)$ is the lower curved-surface, s is arc-length, and \mathbf{n} is the unit normal from the surface $\mathbf{X}_0(s)$. We suppose that the upper surface is initially given by $n = h_0$, and that the body is symmetric about the horizontal axis. We again suppose that all of the surfaces are shear-free, and that the thinness of the medium allows us to assume that the s -components of the unknowns are independent of n . Following the analysis of Chapman *et al* [13], we can write the derivatives as

$$\frac{\partial \mathbf{x}}{\partial s} = (1 + \kappa n)\mathbf{t}, \quad (6.101)$$

$$\frac{\partial \mathbf{x}}{\partial n} = \mathbf{n}, \quad (6.102)$$

where κ is the curvature of the boundary $X_0(s)$. The equations of equilibrium in these orthogonal curvilinear coordinates become

$$\frac{\partial}{\partial s}\sigma_{ss} + \frac{\partial}{\partial n}((1 + \kappa n)\sigma_{ns}) + \left(\frac{\partial}{\partial n}(1 + \kappa n)\right)\sigma_{ns} = 0, \quad (6.103)$$

$$\frac{\partial}{\partial s}\sigma_{ns} + \frac{\partial}{\partial n}((1 + \kappa n)\sigma_{nn}) - \left(\frac{\partial}{\partial n}(1 + \kappa n)\right)\sigma_{ss} = 0. \quad (6.104)$$

To mimic the flat squeeze-film problem, we assume that the inner boundary is symmetric about $s = 0$, without loss of generality, and apply sufficiently great normal stress on the inner boundary so that the material in $|s| < 1$ is plastic. The boundary conditions for $|s| < 1$ are

$$\sigma_{nn}(s, 0, t) = -P(t), \quad (6.105)$$

$$\mathbf{u}(s, 0, t) = \mathbf{0}, \quad (6.106)$$

$$\sigma_{ns}(s, 0, t) = 0 \quad (6.107)$$

$$\mathbf{t}_h \cdot (\boldsymbol{\sigma} \cdot \mathbf{n}_h) = 0 \text{ on } n = h_p(s, t), \quad (6.108)$$

$$\dot{v}(s, h, t) = \dot{h}_p(t), \quad (6.109)$$

along with suitable continuity conditions over $|s| = 1$. Here, we write $\dot{v}(s, n)$ for the normal component of the plastic velocity, $\mathbf{n}_h(s, t)$ for the normal to $h(s, t)$ and $\mathbf{t}_h(s, t)$ for tangent to $h(s, t)$. The medium will again neck, a result of the plasticity, resulting in a plasticised region, $1 < |s| < c(t)$, say, and an elastic region, $|s| > c(t)$. The boundary conditions for the plasticised region are continuity of traction over the boundaries $|s| = 1$ and $|s| = c(t)$, and

$$\sigma_{nn}(s, 0, t) = 0, \quad (6.110)$$

$$\mathbf{u}(s, 0, t) = \mathbf{0}, \quad (6.111)$$

$$\mathbf{t}_h \cdot (\boldsymbol{\sigma} \cdot \mathbf{n}_h) = 0 \text{ on } n = h_e(s), \quad (6.112)$$

$$\mathbf{n}_h \cdot (\boldsymbol{\sigma} \cdot \mathbf{n}_h) = 0 \text{ on } n = h_e(s), \quad (6.113)$$

$$\dot{u}(\pm c(t), t) = \pm \dot{c}(t), \quad (6.114)$$

where we again assume that the elastic displacement is small compared with the plastic velocity and rigid body displacement. Finally, the boundary conditions in the elastic region $|s| > c(t)$ are

$$\sigma_{nn}(s, 0, t) = 0, \quad (6.115)$$

$$\mathbf{u}(s, 0, t) = \mathbf{0}, \quad (6.116)$$

$$\mathbf{t}_h \cdot (\boldsymbol{\sigma} \cdot \mathbf{n}_h) = 0 \text{ on } n = h_e(s), \quad (6.117)$$

$$\mathbf{n}_h \cdot (\boldsymbol{\sigma} \cdot \mathbf{n}_h) = 0 \text{ on } n = h_e(s), \quad (6.118)$$

$$\sigma_{ss}(\pm L, t) = -F(t), \quad (6.119)$$

$$\sigma_{ns}(\pm L, n, t) = 0, \quad (6.120)$$

where $F(t) > 0$. This is shown in Fig. 6.7.

Plastic region

We nondimensionalise the stresses and applied pressure with the yield stress, scale the normal distances with h_0 , and tangential distances with L , where $0 < h_0/L = \varepsilon \ll 1$. Writing the nondimensional normal distance as ρ , the equations of equilibrium become

$$\frac{\partial \sigma_{ss}}{\partial s} + (1 + \kappa \varepsilon \rho) \frac{1}{\varepsilon} \frac{\partial \sigma_{ns}}{\partial \rho} + 2\kappa \sigma_{ns} = 0, \quad (6.121)$$

$$\frac{\partial \sigma_{ns}}{\partial s} + (1 + \kappa \varepsilon \rho) \frac{1}{\varepsilon} \frac{\partial \sigma_{nn}}{\partial \rho} + \kappa(\sigma_{nn} - \sigma_{ss}) = 0. \quad (6.122)$$

Expanding the stresses in powers of ε gives the following leading-order nondimensional equations:

$$\frac{\partial \sigma_{ns}^{(0)}}{\partial \rho} = 0, \quad \frac{\partial \sigma_{nn}^{(0)}}{\partial \rho} = 0. \quad (6.123)$$

We integrate these expressions and use the boundary conditions to recover the leading-order stresses

$$\sigma_{nn}^{(0)} = -P, \quad (6.124)$$

$$\sigma_{ns}^{(0)} = 0. \quad (6.125)$$

We write the nondimensional Tresca yield condition with respect to the principal stresses as

$$|\sigma_{nn} - \sigma_{ss}| = 1, \quad (6.126)$$

so that

$$\sigma_{ss}^{(0)} = -P(t) + 1, \quad (6.127)$$

where the sign of the yield criterion is chosen so that the material is in tension in the x -direction immediately prior to yielding.

Considering the velocities, the flow law is

$$\sigma'_{ij} = \Lambda \dot{\epsilon}_{ij}, \quad (6.128)$$

for some unknown multiplier $\Lambda(\rho, s, t)$. Using expressions for the strains from Hill [36],

$$\sigma'_{nn} = \frac{\Lambda}{\varepsilon} \frac{\partial \dot{v}}{\partial \rho}, \quad (6.129)$$

$$\sigma'_{ss} = (1 + \varepsilon \kappa \rho) \frac{\partial \dot{u}}{\partial s}, \quad (6.130)$$

$$\sigma'_{ns} = (1 + \varepsilon \kappa \rho) \frac{\partial \dot{v}}{\partial s} + \left(\frac{1}{1 + \varepsilon \kappa \rho} \right) \frac{1}{\varepsilon} \frac{\partial}{\partial \rho} ((1 + \varepsilon \kappa \rho) \dot{u}). \quad (6.131)$$

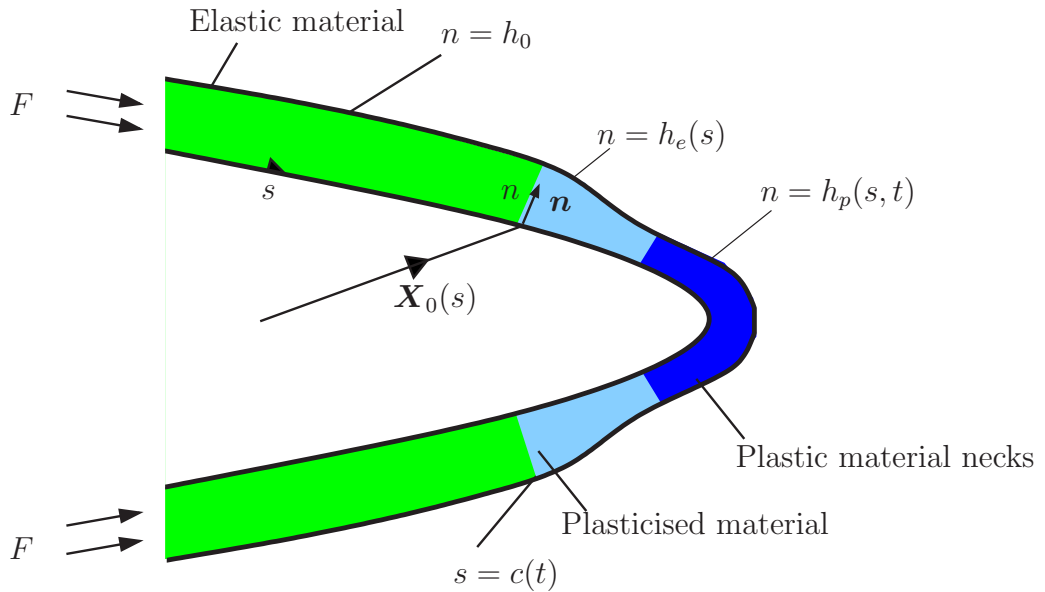


Figure 6.7: A curved squeeze film parametrised with arc length, s and normal distance, n , from the lower surface.

Incompressibility $\sigma'_{ii} = 0$ dictates that the normal velocity \dot{v} needs to be rescaled with ε , so that

$$\frac{\partial \dot{v}}{\partial \rho} + \frac{\partial \dot{u}}{\partial s} = 0, \quad (6.132)$$

at leading order. The expression for σ_{ns} hence gives that

$$\dot{u} = \dot{u}(s, t), \quad (6.133)$$

We now use the velocity boundary conditions and find that

$$\dot{u} = -\frac{\partial h_p}{\partial t} \frac{s}{h_p}, \quad (6.134)$$

$$\dot{v} = \frac{\partial h_p}{\partial t} \frac{\rho}{h_p}, \quad (6.135)$$

where $h_p(s, t)$ will be determined by the horizontal force balance with the elastic region and we have used symmetry about $s = 0$ to set a constant of integration to zero.

Elastic and plasticised regions

The stresses in the elastic region and the unknown elastic part of the stress in the plasticised region are once more determined by solving the rescaled biharmonic equation

$$\frac{\partial^4 A}{\partial \rho^4} = 0. \quad (6.136)$$

The analysis is identical to the flat-bottomed squeeze film, and so, omitting much of the analysis, we use a global force balance in the s -direction (which again holds throughout the plasticised region) to relate the plastic and elastic heights via

$$h_p(t) = -\frac{h_0 F(t)}{1 - P(t)}, \quad (6.137)$$

thus determining the plastic velocities (6.134)-(6.135), elastic stress and the profile of the medium for given $F(t)$ and $P(t)$.

6.2.5 Remarks

Equation (6.137) gives us an idea of how the plastic region behaves as a result of confinement. Of course, the whole squeeze-film in Fig. 6.7 is really surrounded by elastic material, which confines both the thin elastic region and the thin plastic region. This must restrict the inner thin elasto-plastic layer, and so our results are at most qualitative. This observation, however, leads us to comment on mass conservation in the plastic region. In a frame moving with the stagnation point, the plastic region moves through the target. If the elastic response is small by comparison to the cavity radius a , then to leading order,

the flow of material into/out of the plastic region is $U\mathbf{i}\cdot\mathbf{n}$ at the interface between elastic and plastic regions. Since there is no flow of material through the plastic-jet boundary, more material enters the plastic region than leaves it, as shown in Fig. 6.8. We could

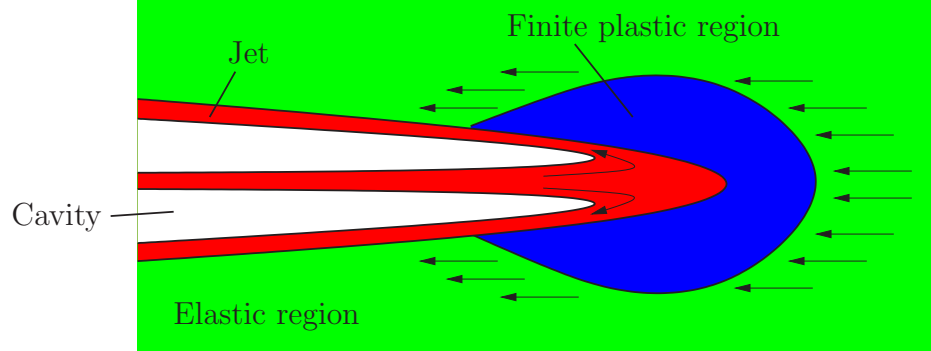


Figure 6.8: A diagram illustrating a problem with mass conservation in incompressible plasticity and infinitesimal elasticity.

recover from this contradiction by introducing compressibility into the plastic region, although this would mean that the tip region is getting more and more dense as the charge penetrates, which seems unlikely. Alternatively, we need the elastic displacement around the boundary of the plastic region to be finite and $\mathcal{O}(a/c_*)$, where c_* is the radius of the plastic region. Note that this is the same scale that we required in §5.3.

Chapter 7

Paradigm tip models for the jet

We have seen the Gordian nature of a full elastic-plastic model in the previous chapter. In this chapter, we wish to derive tractable models to represent the flow of the jet in the tip. We motivate the geometry of the jet in the tip by the arguments of Chapter 3. In particular, for the scalings shown in Fig. 3.7(a) and Fig. 3.7(d), the tip region has a radial scale of ε and an axial scale of $\mathcal{O}(1)$. Performing a naive rescaling of r with ε and solving Laplace's equation for the flow in the jet will lead to problems. This is because the incoming jet is in the positive z -direction, whilst the outgoing jet flows in the negative z -direction and hence, when we get an equation like (4.24), we will arrive at a contradiction. For non-trivial solutions of Laplace's equation, the r and z coordinates must scale the same way and so the fluid of the jet has to turn back on itself over a region of $\mathcal{O}(\varepsilon)$. Indeed, Peregrine *et al.* [67] consider such flows when modelling cliff erosion (and when investigating so-called “cleaning flows”). The basic idea in modelling cliff erosion is that a violent jet enters a crevice and starts to fill it. The jet, which nearly fills the cross-section of the cavity, then rapidly turns back on itself (“flip-around”) when it reaches the end of the cavity, causing a much thinner jet to flow back out of the cavity. This is known as a *filling flow* and is depicted in Fig. 7.1. Observe that the flip-around of the jet produces a free boundary between the fluid and the air. Clearly, for such a flow, some of the incoming fluid will go into filling the cavity, whereas some will be rapidly turned around and expelled as the cavity fills and the free boundary moves in the opposite direction of the incoming jet. This gives birth to a stagnation point in a frame moving with the jet turnaround point and a dividing streamline. We note that if we reverse the signs of the velocities, we have an “emptying-flow”, in which the turnaround point now moves deeper *into* the cavity.

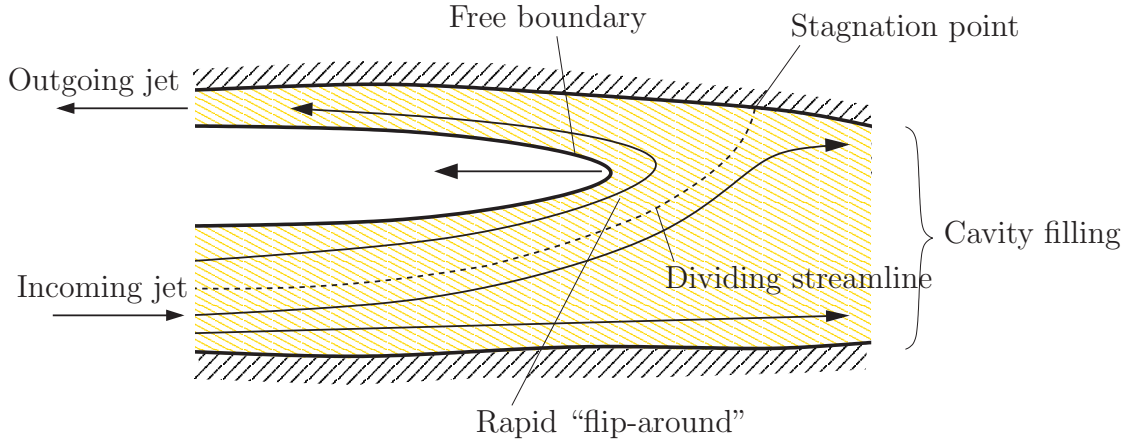


Figure 7.1: A schematic of a filling flow.

7.1 Simple two-dimensional filling-flow models for the jet

In order to develop a model for the jet region of shaped-charge penetration, we briefly outline the analysis of Peregrine [67], and initially consider a two-dimensional flow between two parallel plates. It is assumed that the violence of the flow dominates any gravity effects, and that the flow is incompressible with density ρ (although compressible effects are considered in [68]), steady, and impacts a fluid at rest with pressure P . We introduce the following notation:

Height of incoming jet:	h_j ,
Height of returning jet:	h_r ,
Cavity height:	H ,
Velocity of incoming jet:	V ,
Velocity of returning jet:	V_r ,
Position of the “turnaround point”:	$X_0(t)$,
Velocity potential:	ϕ ,
Nondimensional parameter:	$k^2 = \frac{h_j}{H}$,

where we will find that $\frac{1}{2} \leq k < 1$. We consider global balances representing conservation of mass, a force balance and steady Bernoulli’s equation over the region. In doing so, we will find that the velocity of the turnaround point \dot{X}_0 is undetermined. Changing to a frame moving with the turnaround point $X_0(t)$, mass conservation becomes

$$h_j(V - \dot{X}_0) = h_r(V_r + \dot{X}_0) - \dot{X}_0 H. \quad (7.1)$$

The force on the region must equal the rate of change of momentum. Hence, as the pressure on the cavity is zero, only the fluid filling the cavity upstream of the stagnation

point exerts a force, and so the force balance is

$$PH = \rho \left((V - \dot{X}_0)^2 h_j + (V_r + \dot{X}_0)^2 h_r - \dot{X}_0^2 H \right). \quad (7.2)$$

Finally, use of Bernoulli's condition gives

$$\frac{P}{\rho} = \frac{1}{2}(V - \dot{X}_0)^2 - \frac{1}{2}\dot{X}_0^2. \quad (7.3)$$

In order to represent a filling flow rather than an emptying flow, we must impose $V > \dot{X}_0$ so that the incoming flow velocity has positive sign in the moving frame (note that $\dot{X}_0 < 0$ for a filling flow). The boundary conditions are no normal flow on the walls, and $p = 0$ on the free boundary. This set-up is shown in Fig. 7.2. Using Bernoulli's condition on

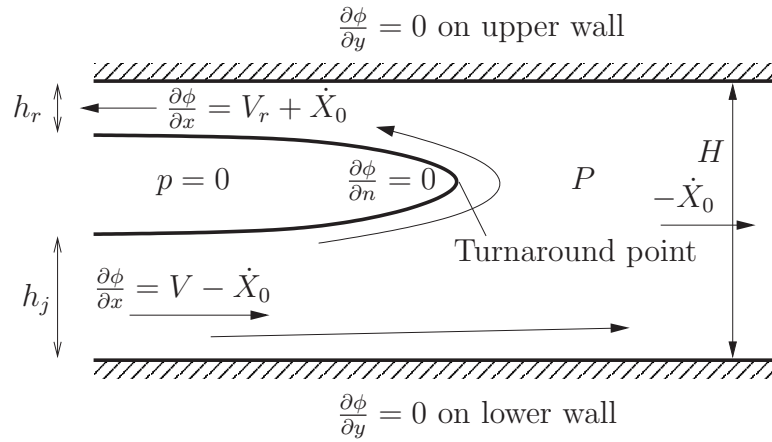


Figure 7.2: A filling flow in a frame moving with the turnaround point $X_0(t)$.

the free streamline along with the boundary conditions immediately tells us that

$$V_r + \dot{X}_0 = V - \dot{X}_0. \quad (7.4)$$

This simplifies our balances and allows us to rearrange the three global balances above to give solutions for V_r , \dot{X}_0 , h_r and P in terms of H , k and V . These solutions can also be obtained by using complex variable techniques (as in [67]) akin to the hydrodynamic fluid-fluid impact in §2.1.1 (e.g. using a Schwarz-Christoffel transform). This will give us an explicit equation for the free boundary, although it loses some of the physical intuition. Note that the physical balances can also be used for an axisymmetric filling flow (whereas the complex variable methods using conformal mappings cannot).

7.1.1 A filling flow in a channel with constant height with various end-conditions

We will construct some very simple models in attempt to apply the ideas from two-dimensional filling flows to shaped-charge penetration. We start by looking at fully hydrodynamic models in two dimensions to gain intuition. The most rudimentary model is

to consider the turnaround region in the tip as a filling flow, which is sufficiently far away (axially) from where the jet-tip ends, at $x = b(t)$, say. We will initially assume that the flow occurs between two flat plates with constant separation H , before considering the more general and representative flow where the upper surface H is a free boundary. We also assume that the flow has already impacted the target and so has already turned back on itself.

Following the scaling analogies, we assume that the height of the cavity (equivalent to the radius in the axisymmetric model) is $\mathcal{O}(\varepsilon)$. We now divide the flow up into two regions. We label the inner filling flow region I, where $x \sim \mathcal{O}(\varepsilon)$, and the outer region II, where $x \sim \mathcal{O}(1)$. This is shown in Fig. 7.3.

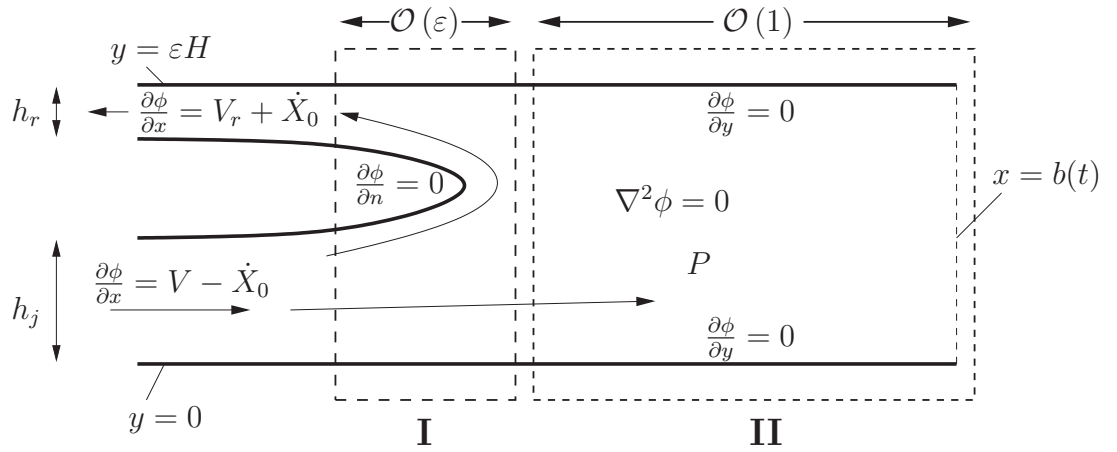


Figure 7.3: Inner and outer regions for a filling flow moving with the turnaround point, $X_0(t)$.

7.1.1.1 Region I

In a similar manner to the previous section, we wish to write mass, force and Bernoulli balances for the flow in the inner region in a frame moving with the turnaround point, $X_0(t)$, and hence introduce the inner coordinates $\bar{\xi}$, \bar{y} and τ , where

$$\varepsilon \bar{\xi} = x - X_0(\tau), \quad (7.5)$$

$$\varepsilon \bar{y} = y, \quad (7.6)$$

$$\tau = t. \quad (7.7)$$

The associated derivatives are

$$\frac{\partial}{\partial x} = \frac{1}{\varepsilon} \frac{\partial}{\partial \bar{\xi}}, \quad (7.8)$$

$$\frac{\partial}{\partial y} = \frac{1}{\varepsilon} \frac{\partial}{\partial \bar{y}}, \quad (7.9)$$

$$\frac{\partial}{\partial t} = \frac{\partial}{\partial \tau} - \frac{X'_0(\tau)}{\varepsilon} \frac{\partial}{\partial \bar{\xi}}. \quad (7.10)$$

We start by considering Bernoulli's equation, which, in the frame moving with $X_0(t)$, becomes

$$\frac{\partial \phi}{\partial \tau} - \frac{X'_0(\tau)}{\varepsilon} \frac{\partial \phi}{\partial \bar{\xi}} + \frac{1}{2} \frac{1}{\varepsilon^2} \left(\frac{\partial \phi}{\partial \bar{\xi}} \right)^2 + \frac{p}{\rho} = G(\tau). \quad (7.11)$$

We also need to rescale the velocity potential ϕ in this region so that the velocity is order one. Clearly, the appropriate scaling is $\phi = \varepsilon \varphi$, and so the leading-order Bernoulli equation becomes

$$-X'_0(\tau) \frac{\partial \varphi}{\partial \bar{\xi}} + \frac{1}{2} \left(\frac{\partial \varphi}{\partial \bar{\xi}} \right)^2 + \frac{p}{\rho} = G(\tau). \quad (7.12)$$

When matching into the outer region, the first term is a function of τ only, and so a local Bernoulli balance similar to (7.3) is valid. Let $u_0(\tau)$ denote the far-field velocity of the fluid in the inner region as the outer region is approached in the original frame. Writing 'dot' for derivatives with respect to τ , the Bernoulli condition is thus written in inner variables as

$$\frac{P}{\rho} + \frac{1}{2} (u_0(\tau) - \dot{X}_0)^2 = \frac{1}{2} (V - \dot{X}_0)^2, \quad (7.13)$$

where P is the far-field pressure of the inner region as $\xi \rightarrow \infty$. Similarly, mass and force balances are written as

$$h_j(V - \dot{X}_0) = h_r(V_r + \dot{X}_0) + (u_0(\tau) - \dot{X}_0)H, \quad (7.14)$$

$$(P + \rho(u_0(\tau) - \dot{X}_0)^2)H = \rho(V - \dot{X}_0)^2(h_j + h_r), \quad (7.15)$$

where we have implicitly used (7.4). These physical balances (7.13)-(7.15) are the inner equations in certain *slamming* models [45] and also represent the inner equations used to model *surf-skimming* [91].

Recalling that $k^2 = \frac{h_j}{H}$, we rearrange these three expressions and find ourselves with two possible roots for \dot{X}_0 when $k \neq \frac{1}{2}$, namely

$$V - \dot{X}_0 = \frac{\dot{X}_0 - u_0(\tau)}{1 - 2k}, \quad (7.16)$$

or

$$V - \dot{X}_0 = -\frac{\dot{X}_0 - u_0(\tau)}{1 + 2k}. \quad (7.17)$$

The latter root results in a negative pressure P and so we discard it on physical grounds. Using the first one, we see that $k \geq \frac{1}{2}$ and find that

$$P = 2\rho k(1-k)(V - \dot{X}_0)^2 = \frac{k}{2(1-k)}\rho(V - u_0(\tau))^2, \quad (7.18)$$

$$\dot{X}_0 = V + \frac{u_0(\tau) - V}{2(1-k)}. \quad (7.19)$$

Expressions for h_r and V_r can also be derived from these equation by making a trivial modification to the global balances of Peregrine. These provide boundary conditions for the flow in the returning jet, applied at $x = X_0(t)$. This jet is modelled using the zero-gravity shallow-water equations, with no normal flow on the upper and lower boundaries, and zero pressure on the free boundary.

In deriving these equations, we have assumed that there is a constant jet with velocity V flowing into this region, corresponding to an infinite jet. The natural consequence of this assumption is likely to be the existence of travelling-wave solutions. To proceed with a solution, we move to consider the outer region.

7.1.1.2 Region II

The fluid in the outer region is assumed to be incompressible and irrotational. Thus, we can introduce a potential function ϕ such that

$$\nabla^2\phi = 0. \quad (7.20)$$

The boundary conditions are no normal flow on $y = 0$ and $y = \varepsilon H$, the fluid velocity equalling the velocity of $b(t)$ at $x = b(t)$, some further condition (to be discussed) at $x = b(t)$, and matching conditions with the inner region. Moving with the turnaround point, the outer coordinates are

$$\xi = x - X_0(\tau), \quad (7.21)$$

$$y = \varepsilon\bar{y}, \quad (7.22)$$

$$\tau = t, \quad (7.23)$$

with derivatives

$$\frac{\partial}{\partial x} = \frac{\partial}{\partial \xi}, \quad (7.24)$$

$$\frac{\partial}{\partial y} = \frac{1}{\varepsilon} \frac{\partial}{\partial \bar{y}}, \quad (7.25)$$

$$\frac{\partial}{\partial t} = \frac{\partial}{\partial \tau} - X'_0(\tau) \frac{\partial}{\partial \xi}. \quad (7.26)$$

Thus, the boundary conditions are

$$\frac{\partial \phi}{\partial \bar{y}} = 0 \text{ on } \bar{y} = 0, H, \quad (7.27)$$

$$\hat{u} = \dot{b}(\tau) - \dot{X}_0(\tau) \text{ on } \xi = b(\tau) - X_0(\tau), \quad (7.28)$$

along with the velocity matching into the inner region,

$$\hat{u} + \dot{X}_0 = u_0(\tau) \text{ at } \xi = 0, \quad (7.29)$$

where \hat{u} is the horizontal velocity component in the moving frame.

We return to the momentum equation in order to derive an outer version of Bernoulli's equation in a moving frame. In the rest frame, the momentum balance is

$$\frac{\partial \mathbf{u}}{\partial t} + (\mathbf{u} \cdot \nabla) \mathbf{u} = -\frac{1}{\rho} \nabla p. \quad (7.30)$$

We introduce the new potential $\hat{\phi} = \phi - \dot{X}_0 \xi$, and hence the ξ -component of the momentum equation is, with respect to the outer variables, (*c.f.* 4.9)

$$\frac{\partial}{\partial \xi} \left(\frac{\partial \hat{\phi}}{\partial \tau} + \frac{1}{2} |\hat{u}|^2 + \frac{p}{\rho} \right) = -\ddot{X}_0(\tau). \quad (7.31)$$

We can integrate this with respect to ξ to reach the Bernoulli condition in an accelerating frame. We now expand the velocity potential $\hat{\phi}$:

$$\hat{\phi}(\xi, \bar{y}, \tau) = \hat{\phi}_0(\xi, \bar{y}, \tau) + \varepsilon \hat{\phi}_1(\xi, \bar{y}, \tau) + \varepsilon^2 \hat{\phi}_2(\xi, \bar{y}, \tau) + \mathcal{O}(\varepsilon^3), \quad (7.32)$$

From Laplace's equation 7.20, we see that the leading-order term is

$$\frac{\partial^2 \hat{\phi}_0}{\partial \bar{y}^2} = 0. \quad (7.33)$$

The boundary conditions are

$$\frac{\partial \hat{\phi}}{\partial \bar{y}} = 0 \text{ on } \bar{y} = 0, H, \quad (7.34)$$

at all orders, which tell us that the leading-order velocity potential $\hat{\phi}_0$ is a function of ξ and τ only. Continuing the analysis up to $\mathcal{O}(\varepsilon^2)$ yields

$$\frac{\partial^2 \hat{\phi}_2}{\partial \bar{y}^2}(\xi, \bar{y}, \tau) = -\frac{\partial^2 \hat{\phi}_0}{\partial \xi^2}(\xi, \tau). \quad (7.35)$$

Integrating with respect to \bar{y} twice and again imposing the zero vertical flow on the walls leads us to the familiar expression

$$\hat{\phi}_0(\xi, \tau) = \hat{u}(\tau)\xi + A(\tau), \quad (7.36)$$

for unknown functions $\hat{u}(\tau)$ and $A(\tau)$. Thus we have plug flow where the horizontal velocity is just a function of time only, given by $\hat{u} = \hat{u}(\tau)$. This velocity is easily determined by applying the boundary condition (7.28), so

$$\hat{u}(\tau) = \dot{b}(\tau) - \dot{X}_0(\tau). \quad (7.37)$$

Applying the matching condition (7.29) now gives $u_0(\tau) = \dot{b}(\tau)$, from which (7.19) can be integrated with respect to τ to give

$$X_0(\tau) = -\alpha V \tau + \frac{b(\tau) - b_0}{2(1-k)} + x_0, \quad (7.38)$$

where $\alpha = \frac{2k-1}{2(1-k)}$ is a positive nondimensional parameter, and the other constants are defined by $x_0 = X_0(0)$ and $b_0 = b(0)$, with $b_0 - x_0 = \mathcal{O}(1)$. Further, the pressure difference between $x = b(\tau)$ and the turnaround point is given by integrating (7.31) between $\xi = 0$ and $\xi = b(\tau) - X_0(\tau)$ as

$$P_b(\tau) - P(\tau) = -\rho \ddot{b}(\tau)(b(\tau) - X_0(\tau)), \quad (7.39)$$

where $P_b(\tau) = p(b(\tau) - X_0(\tau))$ is the pressure exerted on the end $x = b(\tau)$ by the fluid in the outer region, and $P(\tau) = \frac{k}{2(1-k)}\rho(V - \dot{b}(\tau))^2$.

When $k = \frac{1}{2}$, the solution simplifies to

$$P = \frac{\rho}{2}(V - \dot{X}_0)^2, \quad (7.40)$$

and $\dot{X}_0 = u_0(\tau) = \dot{b}(\tau)$. Hence the turnaround point X_0 and end point always remain a fixed distance apart, and the pressure on the end $x = b(\tau)$ is given from the expression

$$P_b = P - \rho \ddot{X}_0 s_0, \quad (7.41)$$

where $s_0 = b_0 - x_0$ is the constant separation between the turnaround point and the ‘tip’. This set-up corresponds to all the incoming fluid turning around, with no net flow into region II. For completeness, we note that the solution procedure also yields that $h_j = h_r$ for such k .

7.1.1.3 End conditions

In order to close equations (7.38) and (7.39) for $X_0(\tau)$ and $b(\tau)$, we need a constitutive law at the end $x = b(\tau)$ to represent the confinement of the elastic medium. Although they are rather simple, we elect to use the following three end conditions at $x = b(\tau)$ to gain intuition:

- (i) Model a filling flow impacting a **spring**. The boundary condition is then

$$m\ddot{b}(\tau) = -K(b(\tau) - b_e) + P_b H, \quad (7.42)$$

where m is a measure of the spring's inertia (equivalent to inertia in the elastic medium), K is a positive spring constant and b_e is the equilibrium position of the spring such that the initial position of the spring satisfies $b_0 \geq b_e$ to model the initial elasticity of the target. This is perhaps the simplest model we could use.

- (ii) Model the end $b(\tau)$ as a **dashpot**, hence the force on the end $b(t)$ is proportional to the velocity. This is perhaps a better analogy than the spring model, as the spring can only be pushed a finite amount for nonzero spring constant and so the 'penetration' would have to stop. The boundary condition for this end condition is

$$m\ddot{b}(\tau) + D\dot{b}(\tau) = P_b H \text{ on } x = b(\tau), \quad (7.43)$$

where D is a positive constant and m is the mass of the dashpot.

- (iii) Model the end $b(\tau)$ via some kind of '**yield pressure**' analogy. This is motivated by the fact that the plastic material around the tip will satisfy a yield condition, and so we pose

$$P_b = \sigma_Y \text{ on } x = b(\tau). \quad (7.44)$$

7.1.1.4 (i) Spring model

For $k \neq \frac{1}{2}$, we couple the expression for the pressure on the end $b(\tau)$, (7.39), with the boundary condition (7.42) and the expression for $X_0(\tau)$, (7.38), to reach the following nonlinear and non-autonomous ordinary differential equation:

$$\left(\frac{m}{H\rho} + \left(\alpha Vt - x_0 + \frac{b_0}{2(1-k)} - \alpha b \right) \right) \ddot{b} = -\frac{K}{H\rho}(b - b_e) + \frac{k}{2(1-k)}(V - \dot{b})^2. \quad (7.45)$$

To nondimensionalise this equation, we need to pick a suitable lengthscale. We choose the steady state solution for $b(\tau)$, which gives a lengthscale of

$$L = b_e + \frac{\rho H k V^2}{2(1-k)K}. \quad (7.46)$$

Writing a typical timescale as T , we introduce the following nondimensional parameters:

$$M = \frac{m}{\rho H L}, \quad (7.47)$$

$$R = \frac{T}{L} V, \quad (7.48)$$

$$I = \left(-\frac{x_0}{L} + \frac{b_0}{2(1-k)L} \right), \quad (7.49)$$

$$C = \frac{K T^2}{\rho H L}. \quad (7.50)$$

Scaling $b(\tau) = L\bar{b}(\bar{\tau})$ and $\tau = T\bar{\tau}$ and dropping bars for convenience, the ordinary differential equation now becomes,

$$(M + \alpha R\tau + I - \alpha b(\tau))\ddot{b}(\tau) = -C(b(\tau) - 1) + \frac{k}{2(1-k)}\dot{b}(\tau)^2 - \frac{Rk}{1-k}\dot{b}(\tau). \quad (7.51)$$

Given the number of nondimensional parameters in this equation, there are numerous different parameter regimes that we could investigate. In an attempt to at least weakly represent the penetration, we attempt to choose some realistic parameters relating to the penetration process. Firstly, we pick a timescale consistent with the chosen lengthscale L and with the penetration velocity, so try $T = L/V$, say. Typical values from Table 3.1 motivate choosing $V \sim 4 \times 10^3 \text{ms}^{-1}$, $\rho \sim 8 \times 10^3 \text{kg m}^{-3}$, $k = 0.55$ (using *a posteriori* estimates for the cavity size), $\alpha \sim 0.1$ and $b_e = 0.7\text{m}$. We choose $x_0 = 0$ without loss of generality. We wish to keep inertial terms in the tip. It is sensible to balance M with the effect of the spring, so we suppose that $M \sim C$. Thus the nondimensional constants become $I \sim \frac{b_0}{L}$, $R = 1$ and $C \sim \frac{L}{\rho V^2 H} = \frac{1}{2}(1 + \frac{K}{\rho H V^2})$.

A key parameter in this model is the ratio $\frac{\rho H V^2}{K}$. If the spring constant K is large compared to the ‘force’ $\rho H V^2$, the lengthscale is dominated by the equilibrium position of the spring and so we might expect oscillatory solutions. This behaviour is confirmed numerically for $b(\tau)$ using MAPLE, shown in Fig. 7.4. We omit similar plots for pressure and position of the turnaround point that also demonstrate oscillatory behaviour about limiting values.

Bearing this numerical solution in mind, we can calculate the large- κ limit for $b(\tau)$. For sufficiently large τ , (7.51) is

$$\alpha\tau\ddot{b} = -C(b(\tau) - 1) + \frac{k}{2(1-k)}\dot{b}(\tau)^2 - \frac{k}{1-k}\dot{b}(\tau). \quad (7.52)$$

Substituting $d(\tau) = b(\tau) - 1$, we neglect quadratic terms in \dot{d} (since the solution oscillates about an equilibrium point) and the equation becomes

$$\tau\ddot{d}(\tau) \approx -\lambda d(\tau) - \mu\dot{d}(\tau), \quad (7.53)$$

where the constants λ and μ are defined by $\lambda = \frac{C}{\alpha}$ and $\mu = \frac{k}{(1-k)\alpha}$. The unintuitive substitution $d(t) = t^{\frac{1-\mu}{2}}f(t)$, where $t = \sqrt{\tau}$ leads to the more familiar equation

$$t^2 f'' + t f' + (4\lambda t^2 - (1 - \mu)^2) = 0, \quad (7.54)$$

where $' = \frac{d}{dt}$. The solutions to this equation are the Bessel function J_ν and modified Bessel function Y_ν , where $\nu = \mu - 1$. Thus the large time limit solutions of the original equation is a linear sum of the two Bessel functions:

$$\tau^{-\frac{\nu}{2}}J_\nu(\sqrt{4\lambda\tau}) \text{ and } \tau^{-\frac{\nu}{2}}Y_\nu(\sqrt{4\lambda\tau}). \quad (7.55)$$

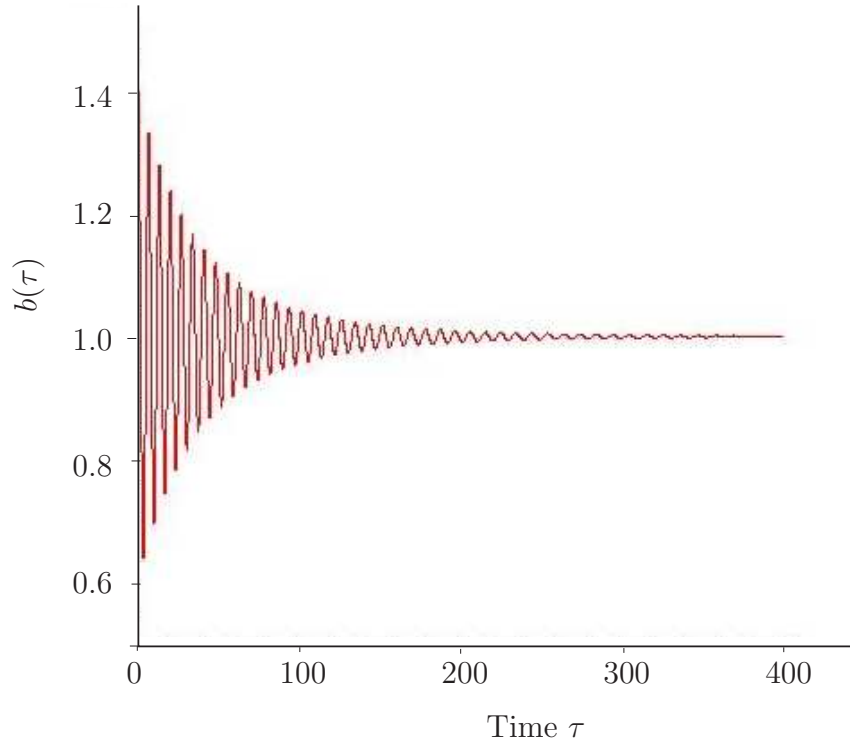


Figure 7.4: A numerical plot of the solution of (7.51) (from MAPLE). The parameters taken are $M = 20$, $k = 0.55$, $I = \frac{b_0}{L} \sim \frac{b_0}{b_e} = 1$, $C = 20$, $R = 1$, $b_0 = 0.7$ and $b_e = 0.7$.

We can expand the Bessel functions for large τ (see *e.g.* [1]) as

$$J_\nu(\sqrt{4\lambda\tau}) \sim \frac{1}{\sqrt{\pi\sqrt{\lambda}}} \tau^{-\frac{1}{4}} \cos(2\sqrt{\lambda\tau} - \frac{\nu\pi}{2} - \frac{\pi}{4}), \quad (7.56)$$

$$Y_\nu(\sqrt{4\lambda\tau}) \sim \frac{1}{\sqrt{\pi\sqrt{\lambda}}} \tau^{-\frac{1}{4}} \sin(2\sqrt{\lambda\tau} - \frac{\nu\pi}{2} - \frac{\pi}{4}). \quad (7.57)$$

Thus the solution will decay like $\tau^{-\frac{1}{4}-\frac{\nu}{2}}$. In terms of the original constants, this power is $-\frac{2k+1}{4(2k-1)} < 0$. This is in agreement with the numerical solution (graphically) when $k = 0.55$.

Conversely, suppose the spring constant K is small so that $C \sim \frac{1}{2}$. The lengthscale L is thus very large and so $I \sim 0$. With the other parameters remaining unchanged, a numerical plot reveals the behaviour shown in Fig. 7.5. This solution settles down to the equilibrium position far quicker than the large K case and does not oscillate with an $\mathcal{O}(1)$ amplitude. Hence, this is a preferred parameter regime when comparing it to shaped-charge penetration, albeit unrepresentative of the physics.

7.1.1.5 Special case of $k = \frac{1}{2}$

The case when $k = \frac{1}{2}$ is a special limit. Recall that the physical interpretation is of no net flow into the outer region from the inner, and that the pressure is given by (7.40).

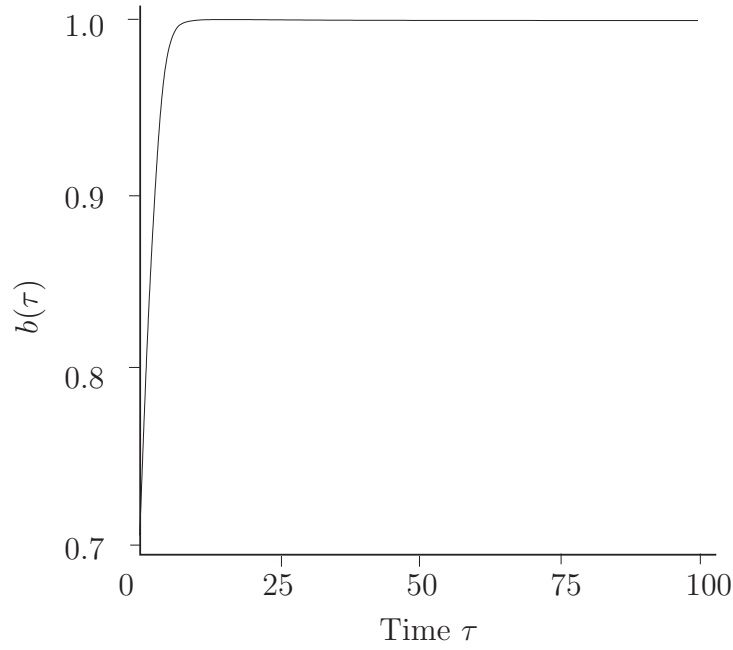


Figure 7.5: A numerical plot of the solution of 7.51 for small C (from MAPLE). The parameters taken are $M = 0.5$, $k = 0.55$, $I \sim 0$, $R = 1$, $C = 0.5$, $b_0 = 0.7$ and $b_e = 0.7$.

This results in the following far simpler ordinary differential equation:

$$(H\rho s_0 + m)\ddot{b} = -K(b - b_e) + \frac{1}{2}\rho(V - \dot{b})^2 H. \quad (7.58)$$

We nondimensionalise this equation by choosing the steady-state solution (from (7.46)) as the lengthscale and by choosing the timescale T so that the inertia of the spring balances the stiffness. Thus the equation becomes, in nondimensional variables,

$$\ddot{b} = (1 - b) + \beta \dot{b}^2 - \gamma \dot{b}, \quad (7.59)$$

where $\beta = \rho H L / (H\rho s_0 + m)$ and $\gamma = \rho H / K^{\frac{1}{2}} (H\rho s_0 + m)^{\frac{1}{2}}$ are both constants, assumed to be $\mathcal{O}(1)$. To convert this nonlinear second order differential equation into a system of two first-order equations, we introduce $X = b$ and $Y = \dot{X} = \dot{b}$ so that the system is

$$\dot{X} = Y, \quad (7.60)$$

$$\dot{Y} = 1 - X + \beta Y^2 - \gamma Y. \quad (7.61)$$

This system has one equilibrium point, at $(1, 0)$. We linearise the system about the equilibrium point and find that its nature is determined by the eigenvalues of the following matrix:

$$\begin{pmatrix} 0 & 1 \\ -1 & -\gamma \end{pmatrix}. \quad (7.62)$$

The eigenvalues, λ_{\pm} , are given by

$$2\lambda_{\pm} = -\gamma \pm \sqrt{\gamma^2 - 4}. \quad (7.63)$$

Hence, the nature of the equilibrium point depends on the sign of $\gamma - 2$, although, in either case, the real part of the eigenvalues is always negative and so the equilibrium point is always stable. The two cases separate cases are:

- $\gamma > 2$, in which both of the eigenvalues are real and negative. The equilibrium point is thus a stable node.
- $\gamma < 2$, where the eigenvalues are complex (with nonzero real part). The equilibrium point is thus a stable spiral.

In either case, the nullclines are also simple to write down as

$$Y = 0 \text{ and } X - 1 + \frac{\gamma^2}{4\beta} = \beta \left(Y - \frac{\gamma}{2\beta} \right)^2, \quad (7.64)$$

and so we can plot the phase planes for $\gamma > 2$ (Fig. 7.6) and for $\gamma < 2$ (Fig. 7.7).

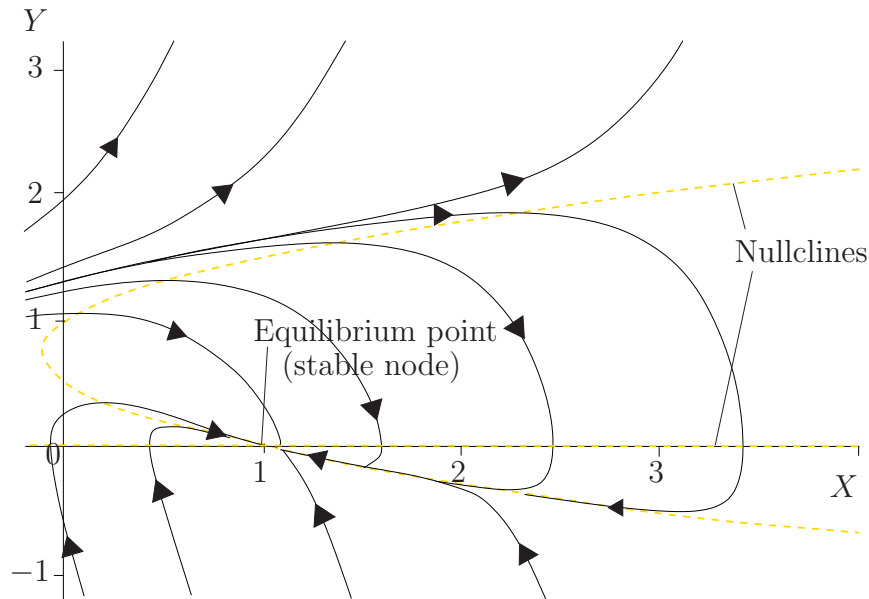


Figure 7.6: Phase plane for the case $\gamma > 2$. The values taken are $\gamma = 3$ and $\beta = 2$ (from MATLAB).

Suppose $\dot{b}(0) = 0$ so that the trajectories start from $Y = 0$ for some X . In both cases we see that, for a certain parameter regime with $b_0 > b_e + \frac{\rho H V^2}{2K}$, all trajectories will end up at the equilibrium point, and so the ‘penetration’ stops in finite time. Differing parameter regimes with $Y(0) = 0$ can lead to the penetration speed increasing monotonically. This is unphysical, and so there are some restrictions on β and γ in this ‘toy’ model.

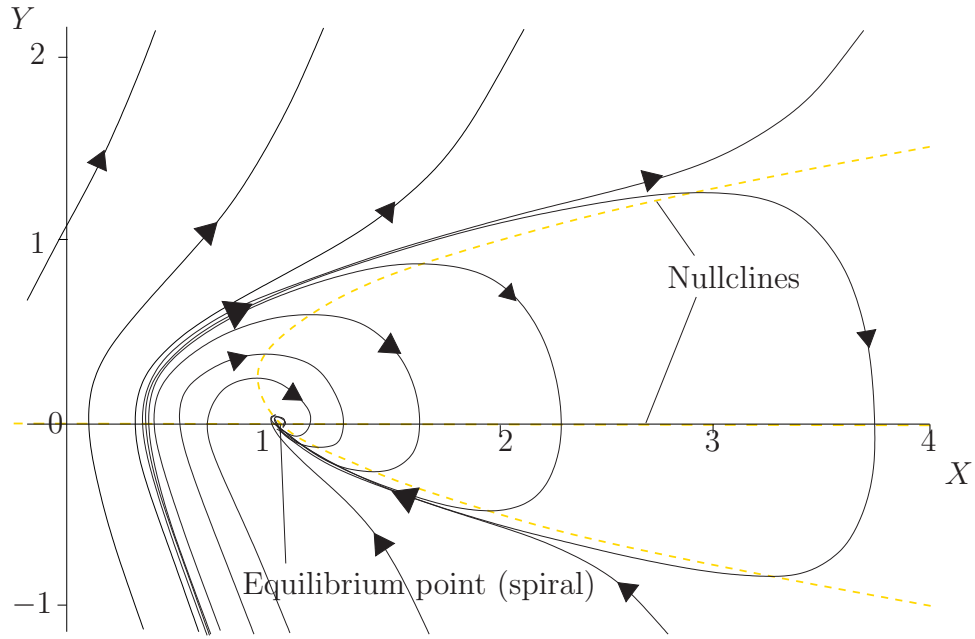


Figure 7.7: Phase plane for the case $\gamma < 2$. The values taken are $\gamma = 1$ and $\beta = 2$ (from MATLAB).

We observe that these phase planes are consistent with the $k \neq \frac{1}{2}$ solutions: in the $\gamma < 2$ regime, the spring term K is more dominant which permits the possibility of decaying oscillatory solutions; when $\gamma > 2$, the spring constant K is below a critical value which denies the existence of any oscillatory solutions.

7.1.1.6 (ii) Dashpot model

In a similar manner to using the spring boundary condition (7.42), employing the dashpot boundary condition (7.43) with $k \neq \frac{1}{2}$ leads to an ordinary differential equation for $b(\tau)$,

$$\frac{m}{H\rho}\ddot{b} + \frac{D}{H\rho}\dot{b} + \left(\alpha V\tau - x_0 + \frac{b_0}{2(1-k)} - \alpha b\right)\ddot{b} = \frac{k}{2(1-k)}(V - \dot{b})^2. \quad (7.65)$$

Crucially, unlike the ‘spring equation’ (7.45), we can simplify this equation by substituting $f(\tau) = V\tau - b(\tau)$ to arrive at an autonomous differential equation,

$$\frac{D}{H\rho}(V - \dot{f}) - \left(\alpha f - x_0 + \frac{m}{H\rho} + \frac{b_0}{2(1-k)}\right)\ddot{f} = \frac{k}{2(1-k)}\dot{f}^2. \quad (7.66)$$

We transform this equation into a system of two first order equations by setting $X = f$ and $Y = \dot{X} = \dot{f}$, so

$$\dot{X} = Y, \quad (7.67)$$

$$\dot{Y} = \frac{1}{C + (2k-1)X} \left(\frac{2(1-k)DV}{H\rho} - kY^2 - \frac{2D(1-k)}{H\rho}Y \right), \quad (7.68)$$

where $C = b_0 + \frac{2(1-k)m}{H\rho}$ and, without loss of generality, $x_0 = 0$. It is trivial to see that there are no fixed points. The nullclines, however, are

$$Y = 0 \quad \text{and} \quad Y = Y_{\pm}, \quad (7.69)$$

where

$$Y_{\pm} = -\frac{D(1-k)}{H\rho k} \pm \frac{1}{k} \sqrt{\left(\frac{D(1-k)}{H\rho} + kV\right)^2 - (kV)^2}. \quad (7.70)$$

The phase plane is shown in Fig. (7.8).

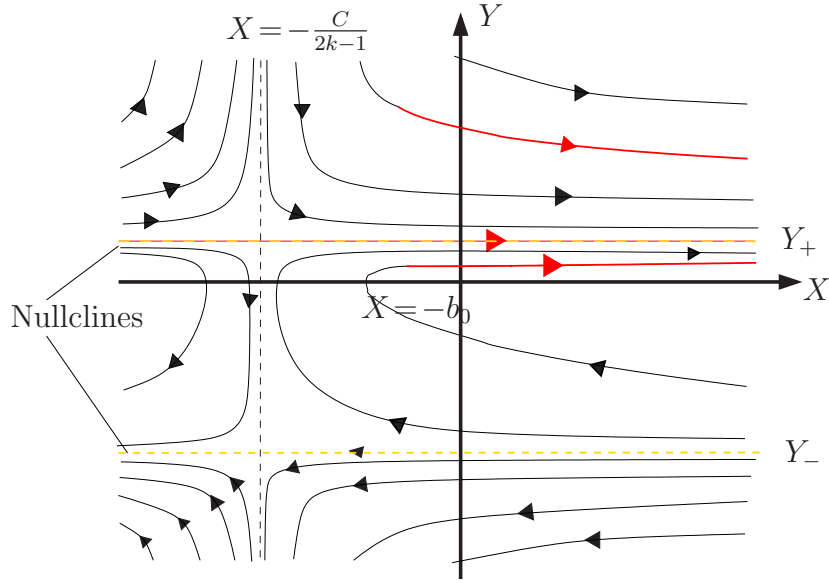


Figure 7.8: A schematic phase plane plot for the system (7.67)-(7.68). The trajectories appropriate to our initial conditions are highlighted in red.

We know that, initially, $X(0) = -b_0 > -C/(2k-1)$. Hence, by following the trajectories starting at $(-b_0, Y_0)$ for some Y_0 (shown in red), we can deduce that $Y \rightarrow Y_+$ for large τ (either from above or below). This corresponds to a large time solution of

$$b(\tau) = V\tau + \frac{D(1-k)}{H\rho k}\tau - \frac{\tau}{k} \sqrt{\left(\frac{D(1-k)}{H\rho} + kV\right)^2 - (kV)^2} + b_0. \quad (7.71)$$

Substituting into (7.38) gives us that

$$X_0 \sim V\tau + \frac{D}{2H\rho k}\tau - \frac{\tau}{2(1-k)k} \sqrt{\left(\frac{D(1-k)}{H\rho} + kV\right)^2 - (kV)^2}, \quad (7.72)$$

and the separation

$$b(\tau) - X_0(\tau) \sim b_0 + \frac{2k-1}{2(1-k)} \frac{\tau}{k} \sqrt{\left(\frac{D(1-k)}{H\rho} + kV\right)^2 - (kV)^2} - \frac{D(2k-1)}{2H\rho k}\tau. \quad (7.73)$$

This separation remains positive if and only if

$$\sqrt{\left(\frac{D(1-k)}{H\rho} + kV\right)^2 - (kV)^2} - \frac{D(1-k)}{H\rho} > 0, \quad (7.74)$$

which is true for all positive D . The fact that $X_0(\tau)$ and $b(\tau)$ are linear at large τ means that the pressure on the dashpot also tends to a constant (by virtue of (7.18) and (7.39)). Numerical solutions illustrate these features (Fig. 7.9).

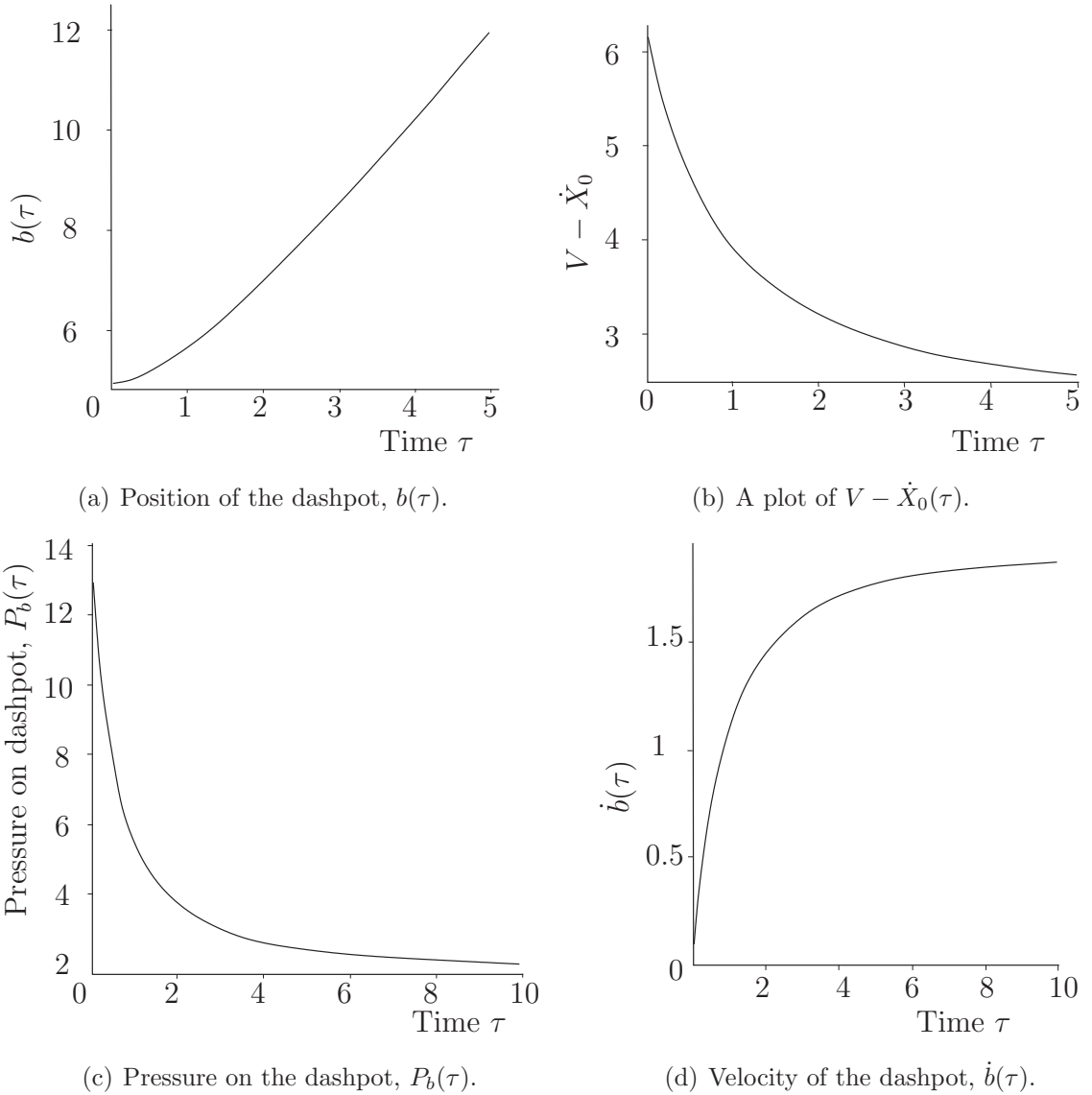


Figure 7.9: Four numerical plots (using MAPLE) showing $b(\tau)$, $V - \dot{X}_0$, $P_b(\tau)$ and $\dot{b}(\tau)$ all against time τ . We have taken $b_0 = 5$, $k = 0.76$, $\rho = 1$, $m = 1$, $H = 1$, $x_0 = 0$, $V = 5$ and $D = 1$.

7.1.1.7 Special case of $k = \frac{1}{2}$

When $k = \frac{1}{2}$, the equation for the motion of the dashpot is

$$(H\rho b_0 + m)\ddot{b} + D\dot{b} = \frac{1}{2}\rho(V - \dot{b})^2 H. \quad (7.75)$$

We introduce the lengthscale $L = 2b_0 + 2m/\rho H$ and timescale $T = L/V$, so that the nondimensional version of this equation is

$$\ddot{b} + \lambda\dot{b} = 1 + \dot{b}^2, \quad (7.76)$$

where $\lambda = 2 + \frac{2D}{\rho HV}$ is a nondimensional parameter. Imposing $b(0) = b_0$, the general solution is now

$$b(\tau) = \frac{1}{2}(\lambda + \mu)\tau - \frac{1}{2}\log((\exp(\mu\tau - b_0) + b_1(\exp(\mu\tau) - 1))^2), \quad (7.77)$$

where $\mu = \sqrt{\lambda^2 - 4}$ is a real constant, and b_1 is a constant determined by $\dot{b}(0)$. For large τ , the logarithmic term is dominated by the exponential, and so

$$b(\tau) \sim \frac{1}{2}(\lambda + \mu)\tau - \mu\tau = \frac{1}{2}(\lambda - \sqrt{\lambda^2 - 4})\tau. \quad (7.78)$$

The argument of τ is positive, and so we have linear growth again at large time¹.

7.1.1.8 (iii) “Yield pressure” model

Our last toy model states that the pressure at the tip is constant, say $P_b = \sigma_Y$. For $k \neq \frac{1}{2}$, the equation (without inertia²) is

$$\frac{\sigma_Y}{H\rho} + \left(\alpha V\tau - x_0 + \frac{b_0}{2(1-k)} - \alpha b\right)\ddot{b} = \frac{k}{2(1-k)}(V - \dot{b})^2. \quad (7.79)$$

This equation is very similar in nature to (7.65) and so we analyse it accordingly. Thus we let $f(\tau) = V\tau - b(\tau)$, set $x_0 = 0$ and transform the resulting second order differential equation into a two dimensional system via $X = f$ and $Y = \dot{X} = \dot{f}$:

$$\dot{X} = Y, \quad (7.80)$$

$$\dot{Y} = \frac{1}{b_0 + (2k-1)X}(2(1-k)\frac{\sigma_Y}{H\rho} - kY^2). \quad (7.81)$$

There are no stationary points, and the nullclines are given by $Y = 0$ and $Y = \pm Y_*$, where

$$Y_* = \sqrt{\frac{2(1-k)\sigma_Y}{H\rho k}}. \quad (7.82)$$

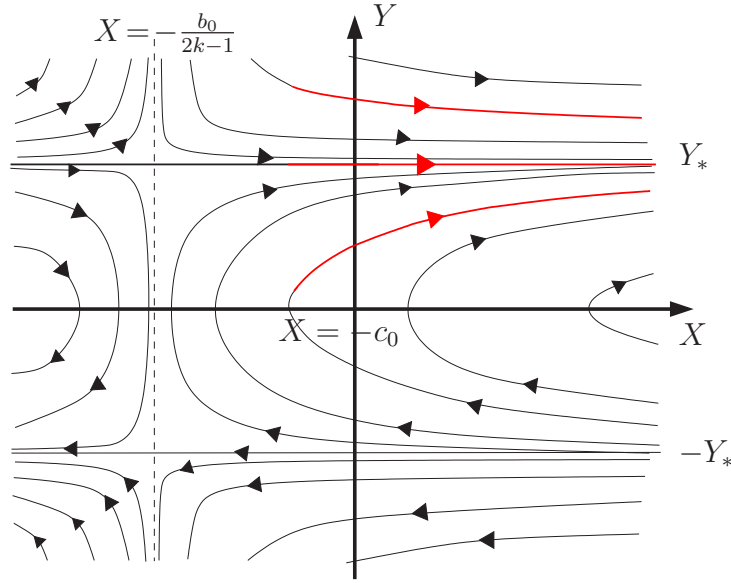


Figure 7.10: A schematic phase plane plot for the system (7.80)-(7.81). The trajectories appropriate to our initial conditions are again highlighted in red.

Thus, we can now plot the phase plane, shown in Fig. 7.10.

Initially, $X(0) = -b_0 < 0 = x_0$. More crucially, $-b_0 > -b_0/(2k-1)$ and, since $V - \dot{X}_0 > 0$, $Y(0) > 0$. From this, we deduce that all appropriate trajectories start with $X > -b_0/(2k-1)$ and $Y > 0$. Such trajectories tend to $Y = Y_*$, and so, for large τ ,

$$b(\tau) \sim V\tau - \sqrt{\left(\frac{2(1-k)\sigma_Y}{H\rho k}\right)}\tau + b_0. \quad (7.83)$$

For a realistic notion of penetration, we must have $\dot{b} > 0$, and so we demand that³

$$V^2 > \frac{2(1-k)\sigma_Y}{H\rho k}. \quad (7.84)$$

Concluding the analysis for large τ , the turnaround point is given by

$$X_0 \sim V\tau - \frac{\tau}{2(1-k)}\sqrt{\left(\frac{2(1-k)\sigma_Y}{H\rho k}\right)}, \quad (7.85)$$

and the separation

$$b(\tau) - X_0(\tau) = \frac{2k-1}{2(k-1)}\tau + b_0. \quad (7.86)$$

This is a positive and increasing function of τ , and shows that the yield stress and X_0 are related quadratically for large τ . Plots of $b(\tau)$ and $V - \dot{X}_0$ are given in Fig. 7.11.

¹This nondimensional result is consistent with the large-time limit derived in (7.71) with $k = \frac{1}{2}$.

²We could add inertia to this problem. In doing so, we would find that we gain little as it is a trivial modification of the $m = 0$ case.

³*c.f.* the yield condition, where we demand $P > \sigma_Y/2$ for plastic flow.

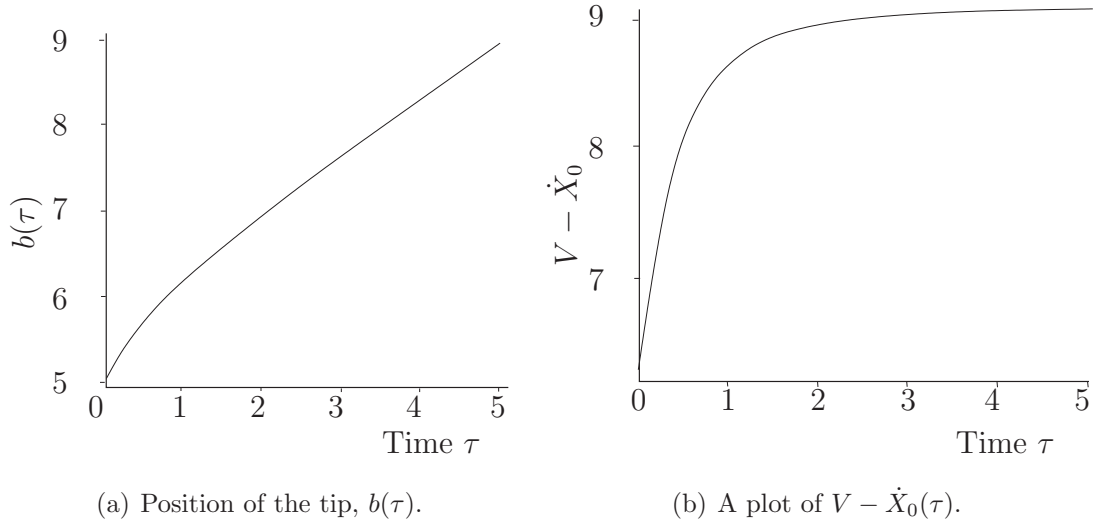


Figure 7.11: Two numerical plots (using MAPLE) showing $b(\tau)$ and $V - \dot{X}_0$ against time τ . We have taken $b_0 = 5$, $k = 0.76$, $\rho = 1$, $H = 1$, $x_0 = 0$, $V = 5$ and $\sigma_Y = 30$.

7.1.1.9 Special case of $k = \frac{1}{2}$

Consideration of the special case of $k = \frac{1}{2}$ leads to a simpler differential equation for $b(\tau)$, namely

$$b_0 \ddot{b} = \frac{1}{2}(V - \dot{b})^2 - \frac{\sigma_Y}{H\rho}. \quad (7.87)$$

This has an explicit solution,

$$b(\tau) = \left(V + \sqrt{\frac{2\sigma_Y}{H\rho}} \right) \tau - 2b_0 \log \left(D_1 \exp \left(\frac{1}{b_0} \sqrt{\frac{2\sigma_Y}{H\rho}} \tau \right) - D_2 \right), \quad (7.88)$$

for some constants D_1 and D_2 . Imposing $b(0) = b_0$ fixes $D_1 = 1/e + D_2$. We can solve for D_2 by prescribing some initial velocity. For large time,

$$b(\tau) \sim \left(V + \sqrt{\frac{2\sigma_Y}{H\rho}} \right) \tau - 2\sqrt{\frac{2\sigma_Y}{H\rho}} \tau = \left(V - \sqrt{\frac{2\sigma_Y}{H\rho}} \right) \tau. \quad (7.89)$$

Thus the final velocity is determined by the sign of $V - \sqrt{2\sigma_Y/H\rho}$, in agreement with (7.85) with $k = \frac{1}{2}$.

7.1.2 Comments

We have seen that even the simplest of end-conditions can exhibit disparate behaviour. Firstly, we considered the end $b(\tau)$ as a spring, which, in a particular parameter regime, demonstrated oscillatory behaviour. This is clearly a nonsensical situation when comparing it to shaped-charge penetration. A different parameter regime led to a solution in

which the trajectories in the phase-plane reach a stable equilibrium point, and so penetration effectively comes to a halt. This is a more realistic analogy with shaped-charge penetration and corresponds to a small contribution from the spring. The analysis demonstrates the main problem in choosing a spring end-condition: the resulting equilibrium point strongly depends on the equilibrium position of the spring, which must be chosen *a priori* based on *a posteriori* estimates!

Conversely, the dashpot and ‘yield-pressure’ models both suggest a travelling-wave type solution, in which the penetration velocity tends to a positive value (when V is sufficiently great). This is the other type of solution we may hope to reach when solving a fuller model. In these formulations, the initial conditions are effectively ‘forgotten’ for large time whilst the pressure and fluid velocities equilibrate.

It is a trivial exercise to modify this analysis for an axisymmetric jet, in which the height of the cavity merely gets replaced by the cross-sectional area in the global mass, force and Bernoulli balances.

7.2 A model for a filling flow impacting a pre-stressed membrane

The approach taken in the previous section was to develop simple ideas as stepping-stones *en route* to fuller, more representative models. In this section, we again consider the jet in the tip region as a filling flow. A key difference to the last section is that we will now derive a two-dimensional model in which we permit the upper boundary to be free, whilst the lower boundary still remains fixed at $y = 0$. The latter boundary is equivalent to the axis of penetration ($r = 0$) in the axisymmetric model. The upper boundary represents the jet-target boundary, and consequently must taper down to zero at the tip. We wish this boundary to model the confinement of the surrounding target material. The simplest method for doing so is to consider it as a membrane (or string) with position $y = \varepsilon H(x, t)$, where $0 < \varepsilon \ll 1$ is a nondimensional parameter (equal to the ratio of a typical y -scale to a typical x -scale), under applied positive pressure P . This is shown in Fig. 7.12. When the contact point moves in the positive x -direction, the membrane ‘peels back’ from the surface and we have penetration. Note that we could alternatively model it as a beam, whose stiffness is equivalent to the target elasticity. This will be considered in the next section.

Before writing down the fluid equations for a filling flow impacting on a membrane, we will derive the boundary condition on the membrane and appropriate initial conditions to determine the initial profile of the membrane. We suppose that the height of the

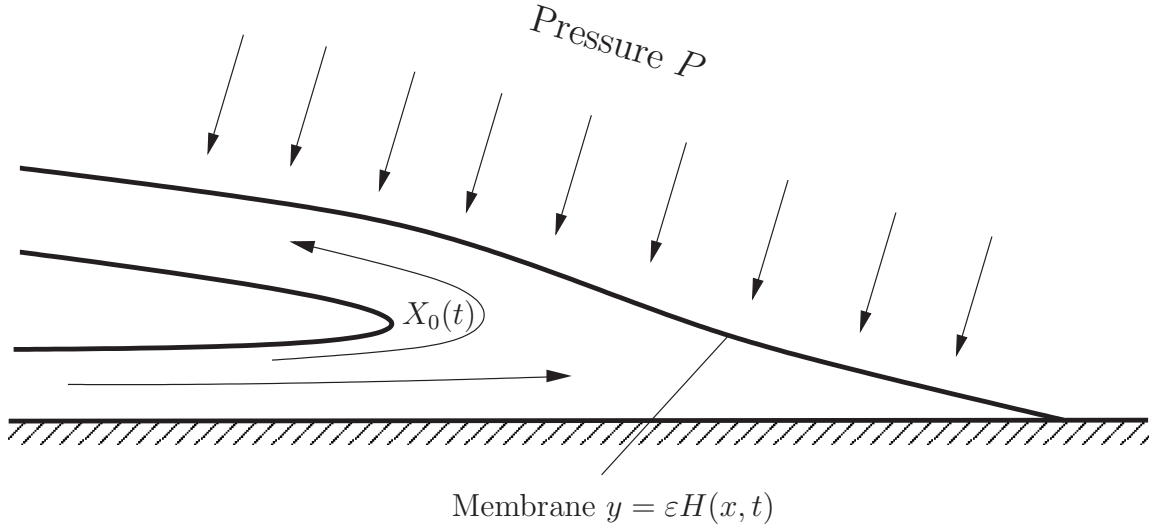


Figure 7.12: A filling flow impacting on a membrane.

membrane $H(x, t)$ is fixed at endpoints $x = 0$ and $x = L$, such that

$$H(0, t) = H_0, \quad (7.90)$$

$$H(L, t) = 0, \quad (7.91)$$

where H_0 is small compared to L . We assume that the membrane is initially under constant pressure P from above. We are thus faced with a *contact problem* (see *e.g.* [24]), shown in Fig. 7.13. We denote the contact point as $x = C$. The equation of the membrane

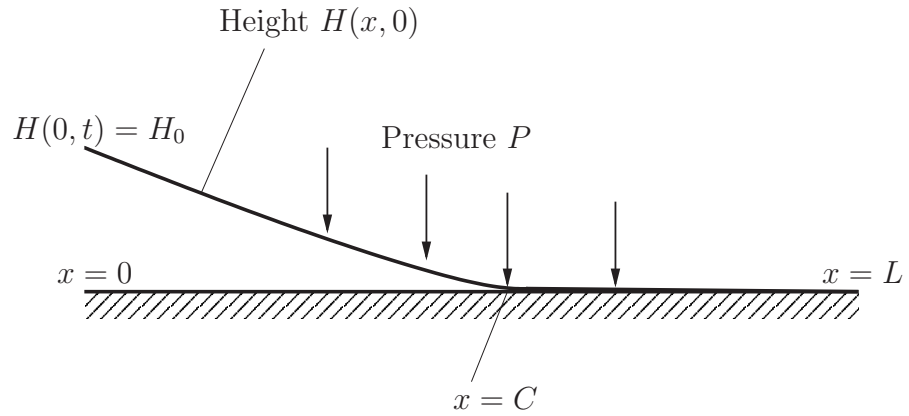


Figure 7.13: Initial conditions for the jet-membrane impact problem.

is

$$T \frac{\partial^2 H}{\partial x^2} = -N + P, \quad (7.92)$$

where T is the tension in the membrane (assumed constant) and the normal reaction N

is given by

$$N = \begin{cases} 0 & 0 \leq x < C \\ P & C < x \leq L \end{cases}. \quad (7.93)$$

Note that we need to assume that $N \geq 0$, so that $P - TH_{xx} \geq 0$. The boundary conditions are (7.90)-(7.91), and the continuity conditions⁴

$$H(C, t) = H_x(C, t) = 0. \quad (7.94)$$

We solve these equations and boundary conditions to discover that the displacement at time $t = 0$ satisfies

$$H(x, 0) = \begin{cases} \frac{P}{2T} \left(x - \sqrt{\frac{2H_0T}{P}} \right)^2 & 0 \leq x \leq \sqrt{\frac{2H_0T}{P}} \\ 0 & \sqrt{\frac{2H_0T}{P}} \leq x \leq L \end{cases}. \quad (7.95)$$

We now need to write down an equation for the evolution of the membrane displacement as a result of the pressure p of the fluid. For small H , a force balance leads to the following wave-equation for the membrane:

$$\frac{1}{c^2} \frac{\partial^2 H}{\partial t^2} = \frac{\partial^2 H}{\partial x^2} + \frac{p - P}{T}, \quad (7.96)$$

where $c = \sqrt{T/\rho_m}$ is the wave speed.

7.2.1 Inner and outer analysis

We are now in good shape to divide the model up into four separate regions. Firstly, region I is where the incoming jet enters the thin channel, $y = \varepsilon H(x, t)$, before entering the inner region (region II). This inner region is where the fluid rapidly turns around, and so we will use a filling-flow model here. Region III is the outer shallow region, where the fluid exerts a pressure on the membrane and the membrane comes down to zero. Finally, region IV consists of returning jet material. This set-up is depicted in Fig. 7.14.

When deriving the equations for the flow, we will once more change to coordinates moving with the turnaround point, $X_0(t)$, in the inner region. We start by looking at the equations in the individual regions, concentrating on the all-important regions II, III and IV.

⁴There will be a Heaviside-type discontinuity in w_{xx} at $x = C$ which leads to a δ -function in the third derivative of w . If the first derivative was discontinuous, there would have to be a δ -function in the second derivative, which we clearly do not have.

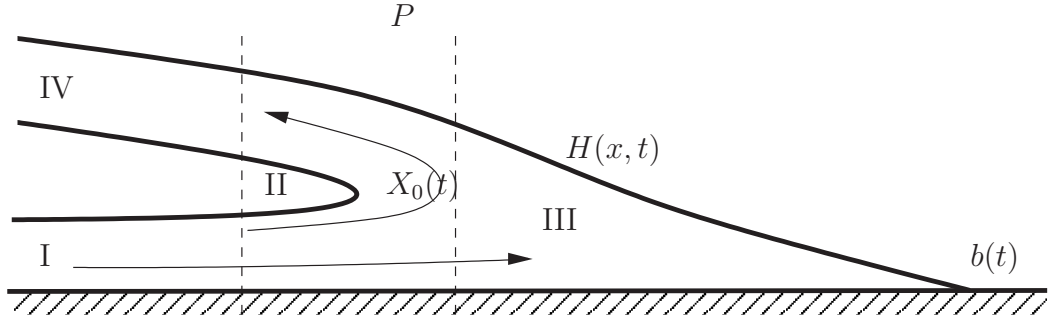


Figure 7.14: A schematic of the filling flow impacting a membrane, showing four separate asymptotic regions.

7.2.1.1 Region I

In region I, we assume that a steady, infinite jet with velocity V and height h_j flows in the positive x -direction. The fluid in the jet is assumed to be irrotational and incompressible, so that there exists a velocity potential satisfying Laplace's equation. We also assume that a filling flow develops almost instantaneously, thus neglecting any effects of turbulent flow in the initial impact. Hence, region I merely provides the boundary conditions for the incoming jet in region II.

7.2.1.2 Region II

Recall that, for nontrivial solutions of Laplace's equation, the aspect ratio must be of order unity. We thus introduce coordinates $\bar{\xi}$, \bar{y} and τ for a frame moving with $x = X_0(t)$ defined by

$$\varepsilon \bar{\xi} = x - X_0(t), \quad (7.97)$$

$$y = \varepsilon \bar{y}, \quad (7.98)$$

$$\tau = t. \quad (7.99)$$

We write the inner membrane height as H_{II} and expand it in powers of ε

$$H_{\text{II}} = H_{\text{II}}^0 + \varepsilon H_{\text{II}}^1 + \mathcal{O}(\varepsilon^2). \quad (7.100)$$

We can now see that the effects of these inner scalings are immediately felt at leading-order and at $\mathcal{O}(\varepsilon)$ in the membrane equation (7.96), giving

$$\frac{\partial^2 H_{\text{II}}^0}{\partial \bar{\xi}^2} = 0 \quad \text{and} \quad \frac{\partial^2 H_{\text{II}}^1}{\partial \bar{\xi}^2} = 0. \quad (7.101)$$

The matching conditions on H_{II} into the outer regions III and IV are on H and its derivative. At leading order, we have

$$\lim_{\bar{\xi} \rightarrow \infty} H_{\text{II}}^0 = \lim_{\xi \rightarrow 0} H_{\text{III}}^0 \quad \text{and} \quad \lim_{\bar{\xi} \rightarrow -\infty} H_{\text{II}}^0 = \lim_{\xi \rightarrow 0} H_{\text{IV}}^0 \quad (7.102)$$

and

$$\lim_{\bar{\xi} \rightarrow \infty} \frac{1}{\varepsilon} \left(\frac{\partial H_{\text{II}}^0}{\partial \bar{\xi}} + \varepsilon \frac{\partial H_{\text{II}}^1}{\partial \bar{\xi}} \right) = \lim_{\xi \rightarrow 0} \frac{\partial H_{\text{III}}^0}{\partial \xi}, \quad (7.103)$$

$$\lim_{\bar{\xi} \rightarrow -\infty} \frac{1}{\varepsilon} \left(\frac{\partial H_{\text{II}}^0}{\partial \bar{\xi}} + \varepsilon \frac{\partial H_{\text{II}}^1}{\partial \bar{\xi}} \right) = \lim_{\xi \rightarrow 0} \frac{\partial H_{\text{IV}}^0}{\partial \xi}. \quad (7.104)$$

We can immediately integrate (7.101) and use the matching condition on derivatives to find that

$$H_{\text{II}}(\bar{\xi}, \tau) = H_{\text{II}}(\tau). \quad (7.105)$$

Furthermore, we also find that $\frac{\partial^2 H_{\text{II}}^1}{\partial \bar{\xi}^2}$ is a constant function of τ , and so

$$\frac{\partial H_{\text{III}}}{\partial \xi}(0, \tau) = \frac{\partial H_{\text{IV}}}{\partial \xi}(0, \tau). \quad (7.106)$$

We can now use the knowledge that H_{II} does not vary with $\bar{\xi}$ to recapitulate the usual filling flow balances of §7.1.1.1:

$$\frac{p_0}{\rho} + \frac{1}{2}(u_0(\tau) - \dot{X}_0)^2 = \frac{1}{2}(V - \dot{X}_0)^2, \quad (7.107)$$

$$h_j(V - \dot{X}_0) = h_r(V - \dot{X}_0) + H_{\text{II}}(u_0(\tau) - \dot{X}_0), \quad (7.108)$$

$$(p_0 + \rho(u_0(\tau) - \dot{X}_0)^2)H_{\text{II}} = \rho(V - \dot{X}_0)^2(h_j + h_r). \quad (7.109)$$

Here, p_0 is the far-field pressure as $\bar{\xi} \rightarrow \infty$, $u_0 - \dot{X}_0$ is the far-field velocity as $\bar{\xi} \rightarrow \infty$ and $k(\tau) = \sqrt{\frac{h_j}{H_{\text{II}}(\tau)}}$ is now a function of τ . Solving (7.107)-(7.109) leads to the familiar expressions for the far-field pressure p_0 and velocity $u_0 - \dot{X}_0$:

$$p_0 = 2\rho k(\tau)(1 - k(\tau))(V - \dot{X}_0)^2, \quad (7.110)$$

$$u_0 - \dot{X}_0 = (2k(\tau) - 1)(V - \dot{X}_0). \quad (7.111)$$

7.2.1.3 Region III

In region III, we use outer coordinates moving with the turnaround point $X_0(t)$ defined by

$$y = \varepsilon y', \quad (7.112)$$

$$\xi = x - X_0(t), \quad (7.113)$$

$$\tau = t, \quad (7.114)$$

with derivatives

$$\frac{\partial}{\partial x} = \frac{\partial}{\partial \xi}, \quad (7.115)$$

$$\frac{\partial}{\partial y} = \frac{1}{\varepsilon} \frac{\partial}{\partial y'}, \quad (7.116)$$

$$\frac{\partial}{\partial t} = \frac{\partial}{\partial \tau} - X_0'(\tau) \frac{\partial}{\partial \xi}. \quad (7.117)$$

The flow in this region is assumed to be irrotational and incompressible, so there exists a velocity potential, ϕ , that satisfies Laplace's equation with respect to a rest frame,

$$\nabla^2 \phi = 0, \quad (7.118)$$

with fluid velocity given by $\mathbf{u} = \nabla \phi$. With the benefit of hindsight and §4.1.1, we introduce a new velocity potential defined by $\hat{\phi} = \phi - \dot{X}_0 \xi$ so that the fluid velocity in the new frame is

$$\mathbf{u} = (\hat{u}, \hat{v}) = \left(\frac{\partial \hat{\phi}}{\partial \xi}, \frac{1}{\varepsilon} \frac{\partial \hat{\phi}}{\partial y'} \right). \quad (7.119)$$

Hence we can rewrite Laplace's equation in these coordinates as

$$\varepsilon^2 \frac{\partial^2 \hat{\phi}}{\partial \xi^2} + \frac{\partial^2 \hat{\phi}}{\partial y'^2} = 0. \quad (7.120)$$

The boundary conditions for the fluid will be no normal flow on the base $y' = 0$, a kinematic condition on $y' = H_{\text{III}}$, matching conditions for the fluid velocity and pressure from the inner region and a condition on the fluid velocity at the tip $\xi = b(\tau) - X_0(\tau)$. The first two of these boundary conditions can be written as

$$\frac{\partial \hat{\phi}}{\partial y'} = 0 \text{ on } y' = 0, \quad (7.121)$$

$$\varepsilon^2 \frac{\partial H_{\text{III}}}{\partial \tau} = \frac{\partial \hat{\phi}}{\partial y'} - \varepsilon^2 \frac{\partial H_{\text{III}}}{\partial \xi} \frac{\partial \hat{\phi}}{\partial \xi} \text{ on } y' = H_{\text{III}}. \quad (7.122)$$

From equations (7.110) and (7.111), the matching conditions on the fluid are

$$p(0, \tau) = p_0(0, \tau) = 2\rho \sqrt{\frac{h_j}{H_{\text{II}}(\tau)}} \left(1 - \sqrt{\frac{h_j}{H_{\text{II}}(\tau)}} \right) (V - \dot{X}_0)^2, \quad (7.123)$$

$$\hat{u}(0, \tau) = \left(2\sqrt{\frac{h_j}{H_{\text{II}}(\tau)}} - 1 \right) (V - \dot{X}_0). \quad (7.124)$$

Intuitively, the fluid velocity should equal the tip velocity at the tip, and so we expect that the boundary condition on the fluid at the tip is

$$\hat{u} = \dot{b} - \dot{X}_0 \text{ at } \xi = b - X_0. \quad (7.125)$$

We will see that this is the case, but will have to justify it after performing some analysis.

The fluid must also satisfy a version of Bernoulli's equation in the moving frame, as in §4.1.1 and §7.1.1. Integration of the ξ -component of Euler's equation (momentum conservation) allows us to write this as

$$\frac{\partial}{\partial \xi} \left(\frac{\partial \hat{\phi}}{\partial \tau} + \frac{1}{2} |\hat{\mathbf{u}}|^2 + \frac{p}{\rho} \right) = -\ddot{X}_0, \quad (7.126)$$

where \hat{u} is the velocity in the moving frame.

Transforming the membrane equation (7.96) into outer coordinates, we find that

$$\frac{1}{c^2} \left(\frac{\partial}{\partial \tau} - \dot{X}_0 \frac{\partial}{\partial \xi} \right)^2 H_{\text{III}} = \frac{\partial^2 H_{\text{III}}}{\partial \xi^2} + \frac{p - P}{T}. \quad (7.127)$$

We also impose the tip boundary conditions

$$H_{\text{III}}, \frac{\partial H_{\text{III}}}{\partial \xi} = 0 \text{ at } \xi = b(\tau) - X_0(\tau), \quad (7.128)$$

as we did when deriving the initial conditions for the problem⁵. The final conditions on the membrane are the matching conditions (7.106) and

$$H_{\text{III}}(0, \tau) = H_{\text{II}}(\tau). \quad (7.129)$$

The rescaled Laplace equation (7.120) suggests an asymptotic series in powers of $\mathcal{O}(\varepsilon^2)$. Dropping dashes for convenience, we expand the velocity potential

$$\hat{\phi} = \hat{\phi}_0 + \varepsilon^2 \hat{\phi}_2 + \mathcal{O}(\varepsilon^4). \quad (7.130)$$

and find, at leading order,

$$\frac{\partial^2 \hat{\phi}_0}{\partial y^2} = 0. \quad (7.131)$$

Expanding the boundary conditions (7.121)-(7.122) to leading order, we easily obtain

$$\hat{\phi}_0 = \hat{\phi}_0(\xi, \tau). \quad (7.132)$$

Continuing the analysis to $\mathcal{O}(\varepsilon^2)$,

$$\hat{\phi}_2(\xi, y, \tau) = -\frac{1}{2} \frac{\partial^2 \hat{\phi}_0}{\partial \xi^2} y^2 + A(\xi, \tau)y + B(\xi, \tau), \quad (7.133)$$

with boundary conditions

$$\frac{\partial \hat{\phi}_2}{\partial y} = 0 \text{ on } y = 0, \quad (7.134)$$

$$\frac{\partial \hat{\phi}_2}{\partial y} = \frac{\partial H_{\text{III}}}{\partial \tau} + \frac{\partial H_{\text{III}}}{\partial \xi} \frac{\partial \hat{\phi}_0}{\partial \xi} \text{ on } y = H_{\text{III}}. \quad (7.135)$$

Thus $A(\xi, \tau) = 0$ and, after some rearrangement,

$$\frac{\partial H_{\text{III}}}{\partial \tau} + \frac{\partial}{\partial \xi} \left(\frac{\partial \hat{\phi}_0}{\partial \xi} H_{\text{III}} \right) = 0. \quad (7.136)$$

⁵Here, we implicitly assume that $H_{\text{III}} = 0$ for $\xi > b(\tau) - X_0(\tau)$. This is the informal equivalent of saying that the normal reaction N is non-negative for $\xi > b(\tau) - X_0(\tau)$.

This is conservation of mass.

At leading order, Bernoulli's equation becomes

$$\frac{\partial}{\partial \xi} \left(\frac{\partial \hat{\phi}_0}{\partial \tau} + \frac{1}{2} |\hat{u}|^2 + \frac{p}{\rho} \right) = -\ddot{X}_0, \quad (7.137)$$

where, in a slight abuse of notation, $\hat{u} = \frac{\partial \hat{\phi}_0}{\partial \xi}$.

We can now derive the boundary condition (7.125) formally. Integrating the mass conservation equation (7.136) with respect to ξ , and noting that $\hat{u} = \frac{\partial \hat{\phi}_0(\xi, \tau)}{\partial \xi}$ is not a function of y , we see that

$$\hat{u} H_{\text{III}} = \int_0^{H_{\text{III}}} \hat{u} dy = \int_{\xi}^{b(\tau) - X_0(\tau)} \frac{\partial H_{\text{III}}}{\partial t}(\zeta, \tau) d\zeta + 0, \quad (7.138)$$

where the constant of integration is zero as H_{III} is zero at the tip. Changing to coordinates local to the tip, we let $\eta = \xi - (b(\tau) - X_0(\tau))$ and write $H_{\text{III}} = \bar{H}(\eta)$. Thus

$$\frac{\partial H_{\text{III}}}{\partial \tau} = -(\dot{b} - \dot{X}_0) \bar{H}'(\eta), \quad (7.139)$$

leading to the fluid velocity at the tip being given by

$$\begin{aligned} \hat{u} &= \frac{1}{\bar{H}} \int_{\xi - (b(\tau) - X_0(\tau))}^0 (-\dot{b} + \dot{X}_0) \bar{H}'(\zeta) d\zeta \\ &= \frac{1}{\bar{H}} (\dot{b} - \dot{X}_0) (\bar{H}(\eta) - \bar{H}(0)) \\ &= \dot{b} - \dot{X}_0. \end{aligned} \quad (7.140)$$

This is defined as $\bar{H} \rightarrow 0$ and so validates the boundary condition (7.125).

In summary, we have three equations for H_{III} , p and $\hat{\phi}_0$ (7.127), (7.136) and (7.137), with two boundary conditions on the membrane at the tip, whose position is unknown, (7.128), one boundary condition on the fluid at the tip (7.125), and four matching conditions as $\xi \rightarrow 0$, (7.106), (7.123), (7.124) and (7.129).

7.2.1.4 Region IV

Much of the analysis for the returning jet in region IV is similar to the outer analysis in region III, and so we use the outer coordinates (7.112)-(7.114). The main difference is that the returning jet is bounded by an upper free boundary, $y' = H_{\text{IV}}(\xi, \tau)$ and a lower free boundary, $y' = h_{\text{IV}}(\xi, \tau)$, say. Assuming an incompressible, irrotational fluid flow, there exists a velocity potential ϕ such that

$$\nabla^2 \phi = 0, \quad (7.141)$$

with fluid velocity $\mathbf{u} = \nabla\phi$ with respect to the rest frame. We again let $\hat{\phi} = \phi - \dot{X}_0\xi$ to get the following version of Laplace's equation in outer coordinates:

$$\varepsilon^2 \frac{\partial^2 \hat{\phi}}{\partial \xi^2} + \frac{\partial^2 \hat{\phi}}{\partial y'^2} = 0. \quad (7.142)$$

Similarly, Bernoulli's equation is

$$\frac{\partial}{\partial \xi} \left(\frac{\partial \hat{\phi}}{\partial \tau} + \frac{1}{2} |\hat{\mathbf{u}}|^2 + \frac{p}{\rho} \right) = -\ddot{X}_0. \quad (7.143)$$

The fluid boundary conditions on the upper and lower free boundaries are kinematic, so that (*c.f.* (7.122))

$$\varepsilon^2 \frac{\partial H_{\text{IV}}}{\partial \tau} = \frac{\partial \hat{\phi}}{\partial y'} - \varepsilon^2 \frac{\partial H_{\text{IV}}}{\partial \xi} \frac{\partial \hat{\phi}}{\partial \xi} \text{ on } y' = H_{\text{IV}}, \quad (7.144)$$

$$\varepsilon^2 \frac{\partial h_{\text{IV}}}{\partial \tau} = \frac{\partial \hat{\phi}}{\partial y'} - \varepsilon^2 \frac{\partial h_{\text{IV}}}{\partial \xi} \frac{\partial \hat{\phi}}{\partial \xi} \text{ on } y' = h_{\text{IV}}. \quad (7.145)$$

The equation for the membrane is

$$\frac{1}{c^2} \left(\frac{\partial}{\partial \tau} - \dot{X}_0 \frac{\partial}{\partial \xi} \right)^2 H_{\text{III}} = \frac{\partial^2 H_{\text{III}}}{\partial \xi^2} + \frac{p - P}{T}, \quad (7.146)$$

whilst the equation on the lower free boundary is

$$p = 0 \text{ on } y' = h_{\text{IV}}(\xi, \tau). \quad (7.147)$$

The matching conditions are concerning the height of the membrane and its derivative, the fluid velocity and the distance between the two free boundaries. Explicitly, we write

$$H_{\text{IV}}(0, \tau) = H_{\text{II}}(\tau), \quad (7.148)$$

$$\frac{\partial H_{\text{IV}}}{\partial \xi}(0, \tau) = \frac{\partial H_{\text{III}}}{\partial \xi}(0, \tau), \quad (7.149)$$

$$\hat{\mathbf{u}}(0, \tau) = -(V - \dot{X}_0), \quad (7.150)$$

$$(H_{\text{IV}}(0, \tau) - h_{\text{IV}}(0, \tau)) = h_r. \quad (7.151)$$

Finally, we suppose that the membrane is pinned at $x = -L$, say, where L is negative and of order unity, so

$$H_{\text{IV}}(-L, \tau) = H_p, \quad (7.152)$$

where H_p is a constant.

Dropping dashes, we expand the velocity potential in powers of ε^2 as

$$\hat{\phi} = \hat{\phi}_0 + \varepsilon^2 \hat{\phi}_2 + \mathcal{O}(\varepsilon^4). \quad (7.153)$$

We substitute this into Laplace's equation and use the kinematic boundary conditions to find that, at leading order,

$$\hat{\phi}_0 = \hat{\phi}_0(\xi, \tau), \quad (7.154)$$

and at $\mathcal{O}(\varepsilon^2)$, we obtain the mass conservation equation

$$\frac{\partial}{\partial \tau}(H_{\text{IV}} - h_{\text{IV}}) + \frac{\partial}{\partial \xi} \left(\frac{\partial \hat{\phi}_0}{\partial \xi} (H_{\text{IV}} - h_{\text{IV}}) \right) = 0. \quad (7.155)$$

The leading-order Bernoulli equation is more interesting. As $\hat{\phi}_0$ is a function of τ only, we find from the boundary condition (7.147) that, at leading order,

$$p = 0, \quad (7.156)$$

and that

$$\frac{\partial \hat{\phi}_0}{\partial \tau} + \frac{1}{2} \left(\frac{\partial \hat{\phi}_0}{\partial \xi} \right)^2 + \ddot{X}_0 \xi = 0, \quad (7.157)$$

as in (4.31). The leading-order membrane equation now simplifies to

$$\frac{1}{c^2} \left(\frac{\partial}{\partial \tau} - \dot{X}_0 \frac{\partial}{\partial \xi} \right)^2 H_{\text{IV}} = \frac{\partial^2 H_{\text{IV}}}{\partial \xi^2} - \frac{P}{T}. \quad (7.158)$$

We thus have a mass conservation equation for the fluid, (7.155), an “eikonal” equation for ϕ_0 , (7.157), and an equation for the evolution of the membrane, (7.158). We also have four matching conditions and a condition for the membrane at $x = -L$. In total, there are three unknowns in this region, $\hat{\phi}_0$, H_{IV} and h_{IV} , and five boundary conditions, which is enough to determine $X_0(t)$, given $X_0(0)$, and $b(t)$, given $b(0)$.

7.2.2 Global travelling wave solution

The simplest solution methodology is to attempt a global travelling wave solution, in which $\dot{X}_0 = \dot{b} = U$, say, where U is a constant such that $U < V$ (so that the flow is a filling flow). Note that we will have to replace the pinning condition (7.152) with a new condition fixed in the travelling-wave frame for the formulation to work. Before performing any detailed analysis, we can immediately predict that any such solution must be in the $k = \frac{1}{2}$ regime. This is because the outer region is “thin” so no extra mass can flow into this region if $\dot{X}_0 = \dot{b}$. With this in mind, we start the analysis in region III by introducing an outer travelling-wave variable ζ defined by

$$\zeta = x - Ut. \quad (7.159)$$

The derivatives are thus

$$\frac{\partial}{\partial x} = \frac{d}{d\zeta}, \quad (7.160)$$

$$\frac{\partial}{\partial t} = -U \frac{d}{d\zeta}. \quad (7.161)$$

In travelling-wave variables, and writing H for H_{III} , equation (7.136) for mass conservation becomes

$$\frac{\partial}{\partial \zeta}(uH) = 0, \quad (7.162)$$

and so the mass flux uH is constant through region III. This constant is easily determined to be zero by noting that the velocity u is finite at the tip where $H = 0$. For a valid solution, the height H cannot be zero everywhere in region III. Thus $u = 0$ in region III for a travelling wave, and so the velocity potential here is a constant. As $V > U$, the third matching condition (7.124) hence yields that $k = \frac{1}{2}$, as anticipated. This gives the inner height as

$$H_{\text{II}} = 4h_j. \quad (7.163)$$

Bernoulli's equation in region III trivially gives that the pressure p is constant. This constant will be determined by the second of the matching conditions, (7.123). We substitute $H_{\text{II}}(\tau)$ into this expression and hence find that the constant pressure in the outer region satisfies

$$p = \frac{1}{2}\rho(V - U)^2. \quad (7.164)$$

Finally, we transform the membrane equation (7.96) into the new travelling-wave coordinates. We nondimensionalise $H = 4h_j\hat{H}$ and $\xi = \xi_*\hat{\xi}$, where we have fixed $\xi = 0$ at the turnaround point $x = X_0(t)$ and $\xi = \xi_*$ at the tip $x = b(t)$. Dropping hats, the membrane equation (7.96) becomes

$$\frac{\partial^2 H}{\partial \xi^2} = \alpha, \quad (7.165)$$

where

$$\alpha = \frac{(\rho(V - U)^2 - 2P)\xi_*^2}{8Th_j} \left(\frac{c^2}{U^2 - c^2} \right). \quad (7.166)$$

Note that we have implicitly assumed that $U \neq c$. The case $U = c$ will be considered later. Also, this equation indicates that there is some constraint on the nondimensional constant α . The nondimensional boundary conditions are

$$H, H_\xi = 0 \text{ at } \xi = 1, \quad (7.167)$$

hence

$$H = \frac{\alpha(\xi - 1)^2}{2}. \quad (7.168)$$

The constraint on the solution being valid is that the quadratic must be positive, so $\alpha > 0$. Indeed, matching the membrane height into region II, using the nondimensional (7.163), we find that $\alpha = 2$ and so

$$H = (\xi - 1)^2. \quad (7.169)$$

We now transform the equations of region IV into travelling-wave variables, initially keeping the analysis dimensional. Firstly, mass conservation (7.155) becomes

$$\frac{\partial}{\partial \zeta}(u(H_{\text{IV}} - h_{\text{IV}})) = 0. \quad (7.170)$$

Using the matching conditions and the result $h_r = h_j$, we can integrate to obtain

$$u(H_{\text{IV}} - h_{\text{IV}}) = -h_j(V - U). \quad (7.171)$$

Bernoulli's equation is no longer an accelerating version, and so we have

$$\frac{1}{2} \left(\frac{\partial \hat{\phi}_0}{\partial \zeta} \right)^2 = \text{constant}. \quad (7.172)$$

Again, we use the matching conditions and then integrate to find

$$\hat{\phi}_0(\zeta, t) = -(V - U)\zeta + f(t), \quad (7.173)$$

for some $f(t)$, and so $u = -(V - U)$. Substituting back into the new mass flux equation, we see that

$$H_{\text{IV}} - h_{\text{IV}} = h_j \quad (7.174)$$

everywhere. This tells us that the two free boundaries must stay the same distance apart in the travelling-wave formulation. Now, using the same nondimensionalisation as before and dropping hats, the membrane equation (7.158) becomes

$$\frac{\partial^2 H_{\text{IV}}}{\partial \zeta^2} = \beta, \quad (7.175)$$

where

$$\beta = \frac{-P\xi_*^2}{4Th_j} \left(\frac{c^2}{U^2 - c^2} \right). \quad (7.176)$$

We integrate this twice, using the nondimensional matching conditions $H_{\text{IV}}(0) = 1$ and $H'_{\text{IV}}(0) = -2$ and discover that

$$H_{\text{IV}} = \frac{\beta \xi^2}{2} - 2\xi + 1. \quad (7.177)$$

Although, in reality, we would like to solve on an infinite region, it is sensible to pin the ends of the membrane in the moving frame for the travelling-wave formulation, and so (7.152) becomes

$$H_{\text{IV}}(-\tilde{L}) = \tilde{H}_p, \quad (7.178)$$

where $\tilde{L} = L/\xi_*$ and $\tilde{H}_p = H_p/4h_j$. This leads to

$$\tilde{H}_p = \frac{\beta \tilde{L}^2}{2} + 2\tilde{L} + 1. \quad (7.179)$$

The equations $\alpha = 2$ and (7.179) are enough to determine the unknown constants U and ξ_* . These lead to a quartic (note that ξ_* is hidden in the expression for \tilde{H}_p , and so the roots are nontrivial). To investigate possible solutions, we separately consider the three cases of $\beta > 0$, $\beta = 0$ and $\beta < 0$, corresponding to subsonic, sonic and supersonic penetration respectively. These may or may not be possible, and depend on choice of the unknown constants in α and β .

Subsonic penetration ($\beta > 0$)

From the constraint $\alpha > 0$, we see that subsonic penetration occurs when the applied pressure $P > \frac{1}{2}\rho(V - U)^2$. This bounds U via

$$V - \sqrt{\frac{2P}{\rho}} < U < c. \quad (7.180)$$

Interestingly, we note that the incoming jet speed can still satisfy $V > c$ in this regime. The profile in region IV is a positive quadratic, with ζ_* and U determined via $\alpha = 2$ and (7.179).

Sonic penetration ($\beta = 0$)

If we try $U = c$, the dimensional membrane equation in region IV in the form

$$\left(\frac{U^2 - c^2}{c^2}\right) \frac{\partial^2 H_{\text{IV}}}{\partial \zeta^2} = -\frac{P}{T} \quad (7.181)$$

leads to the contradiction $P = 0$, and so there is no non-trivial travelling-wave solution for such U .

Supersonic penetration ($\beta < 0$)

As $V - U > 0$, a supersonic travelling wave is only possible if the initial velocity of the jet is itself supersonic. Further, as $\alpha > 0$, we must have $P < \frac{1}{2}\rho(V - U)^2$ and so V must satisfy the stronger constraint of

$$V > U + \sqrt{\frac{2P}{\rho}} > c + \sqrt{\frac{2P}{\rho}}. \quad (7.182)$$

The profile is again quadratic in both regions III and regions IV, although the quadratic in region IV is now a negative quadratic (*i.e.* is bounded above). Analysis of this quadratic shows that it turns at

$$\zeta_c = \frac{2}{\beta} = \frac{\tilde{L}^2}{\tilde{H}_p - 2\tilde{L} - 1}, \quad (7.183)$$

which is negative by the assumption on β . The relative sizes of ζ_c and \tilde{L} are not known from this expression, and so we allow the possibility of the derivative of H_{IV} changing sign. This results in two possible profiles for subsonic penetration, depending on the unknown variables. Note that the inequality (7.182) makes sense physically. Firstly, we can see that a necessary condition for supersonic penetration is the initial jet to be itself supersonic (*c.f.* plasticity in §3.3). Furthermore, the inequality demonstrates the effect of the applied pressure P ; the greater the pressure P , the higher the velocity of the incoming jet V has to be above the sound speed of the membrane for supersonic penetration to occur.

7.2.2.1 Predictions using shaped-charge parameters

We can visualise these travelling-wave profiles using shaped-charge parameters from Table 3.1. We motivate choosing the pinning length-scale $L = 1\text{m}$ from a typical penetration depth, the confining pressure P by the yield stress, tension T by the Lamé constant λ , the density ρ by the density ρ_j of the copper jet, and choose the primary sound speed c_p . We can then vary the parameters H_p and V to generate one subsonic travelling-wave profile and two possible supersonic travelling-wave profiles. Recalling the constraints on P and V for a valid solution, we plot solutions in Fig. 7.15 and Fig. 7.16.

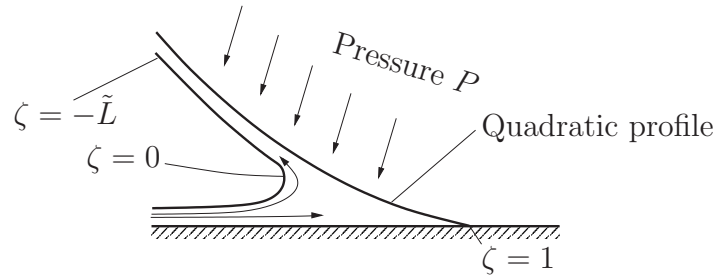
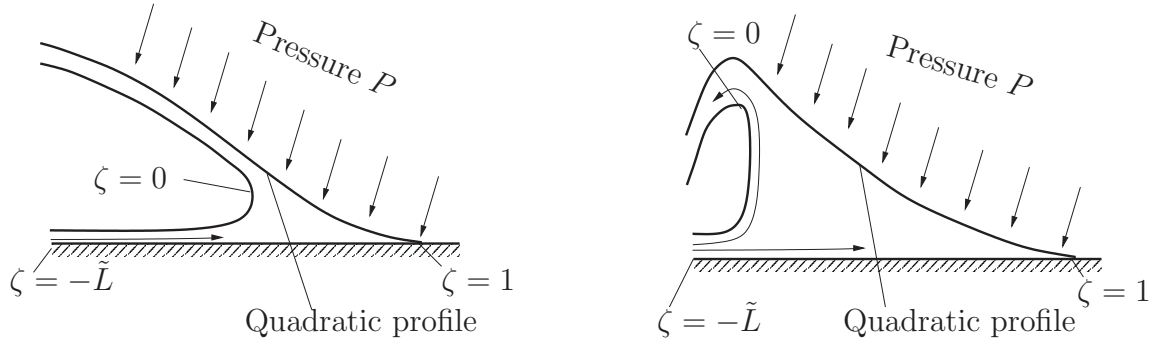


Figure 7.15: A subsonic travelling-wave profile, with $h_j = 2\text{mm}$, $\rho = 8920\text{kg m}^{-3}$, $c = 5000\text{ms}^{-1}$, $T = 1 \times 10^{11}\text{kgs}^{-2}$, $P = 2 \times 10^9\text{kg m}^{-1}\text{s}^{-2}$, $L = 0.5\text{m}$, $V = 2000\text{ms}^{-1}$ and $H_p = 20\text{mm}$. This leads to a solution $U = 2326\text{ms}^{-1}$ and $\xi_* = 0.91\text{m}$.



(a) Solution with $H_p = 20\text{mm}$. This leads to a valid solution with $U = 7920\text{ms}^{-1}$ and $\xi_* = 0.86\text{m}$. Observe that the height in region IV satisfies a negative quadratic with no turning point.

(b) Solution with $H_p = 5\text{mm}$. This leads to a valid solution with $U = 8320\text{ms}^{-1}$ and $\xi_* = 6.0\text{m}$. The height in region IV satisfies a negative quadratic with a turning point in the region.

Figure 7.16: The two supersonic travelling-wave profiles with $h_j = 2\text{mm}$, $\rho = 8920\text{kg m}^{-3}$, $c = 5000\text{ms}^{-1}$, $T = 1 \times 10^{11}\text{kgs}^{-2}$, $P = 2 \times 10^9\text{kg m}^{-1}\text{s}^{-2}$, $L = 1\text{m}$ and $V = 9000\text{ms}^{-1}$.

7.3 A model for a filling flow impacting a pre-stressed beam

In the previous section, we investigated representing the elasticity of the target via a membrane boundary condition (7.96). In this section, we use the stiffness of a bending beam as an analogy to the target elasticity. To do so, we replace the linearised membrane condition (7.96) with a linearised beam equation

$$m \frac{\partial^2 H}{\partial t^2} + EI \frac{\partial^4 H}{\partial x^4} = p - P, \quad (7.184)$$

where m is the mass of the beam, E is the Young's modulus of the beam and I is the area moment of inertia of the beam's cross section. These are all assumed to be constant.

To derive an initial state of the beam, we are faced with the contact problem

$$EI \frac{\partial^4 H}{\partial x^4} = N - P, \quad (7.185)$$

where, using the same notation of the previous section,

$$N = \begin{cases} 0 & 0 \leq x < C \\ P & C < x \leq L \end{cases}. \quad (7.186)$$

We clamp the beam at $x = L$, so that $H(L) = H_x(L) = H_{xx}(L) = 0$, and suppose that it is simply supported at $x = 0$, so that $H_{xx}(0) = 0$ and $H(0) = H_0$, say. The continuity

conditions at the contact point⁶ $x = C$ are continuity of H , H_x and H_{xx} . This will give us an initial profile, although we omit this analysis.

7.3.1 Inner and outer analysis

Once more, we consider four separate regions, as in Fig. 7.14. We omit much of the analysis, as it is identical to the previous membrane analysis.

7.3.1.1 Inner region II

Changing to the inner coordinates defined by (7.97)-(7.99), we expand the height of the beam as

$$H_{\text{II}} = H_{\text{II}}^0 + \varepsilon H_{\text{II}}^1 + \varepsilon^2 H_{\text{II}}^2 + \varepsilon^3 H_{\text{II}}^3 + \mathcal{O}(\varepsilon^4), \quad (7.187)$$

and find that the beam equation (7.184) becomes

$$\frac{\partial^4 H_{\text{II}}^j}{\partial \bar{\xi}^4} = 0, \quad (7.188)$$

for $j = 0, 1, 2, 3$. We integrate these equations and find the cubic solutions

$$H_{\text{II}}^j(\bar{\xi}, \tau) = A_j(\tau)\bar{\xi}^3 + B_j(\tau)\bar{\xi}^2 + C_j(\tau)\bar{\xi} + D_j(\tau), \quad (7.189)$$

for $j = 0, 1, 2, 3$. This is simplified by the matching conditions

$$\lim_{\bar{\xi} \rightarrow \infty} H_{\text{II}}^0 = \lim_{\xi \rightarrow 0} H_{\text{III}}^0, \quad (7.190)$$

$$\lim_{\bar{\xi} \rightarrow -\infty} H_{\text{II}}^0 = \lim_{\xi \rightarrow 0} H_{\text{IV}}^0, \quad (7.191)$$

$$\lim_{\bar{\xi} \rightarrow \infty} \frac{1}{\varepsilon} \left(\frac{\partial H_{\text{II}}^0}{\partial \bar{\xi}} + \varepsilon \frac{\partial H_{\text{II}}^1}{\partial \bar{\xi}} \right) = \lim_{\xi \rightarrow 0} \frac{\partial H_{\text{III}}^0}{\partial \xi}, \quad (7.192)$$

$$\lim_{\bar{\xi} \rightarrow -\infty} \frac{1}{\varepsilon} \left(\frac{\partial H_{\text{II}}^0}{\partial \bar{\xi}} + \varepsilon \frac{\partial H_{\text{II}}^1}{\partial \bar{\xi}} \right) = \lim_{\xi \rightarrow 0} \frac{\partial H_{\text{IV}}^0}{\partial \xi}, \quad (7.193)$$

$$\lim_{\bar{\xi} \rightarrow \infty} \frac{1}{\varepsilon^2} \left(\frac{\partial^2 H_{\text{II}}^0}{\partial \bar{\xi}^2} + \varepsilon \frac{\partial^2 H_{\text{II}}^1}{\partial \bar{\xi}^2} + \varepsilon^2 \frac{\partial^2 H_{\text{II}}^2}{\partial \bar{\xi}^2} \right) = \lim_{\xi \rightarrow 0} \frac{\partial^2 H_{\text{III}}^0}{\partial \xi^2}, \quad (7.194)$$

$$\lim_{\bar{\xi} \rightarrow -\infty} \frac{1}{\varepsilon^2} \left(\frac{\partial^2 H_{\text{II}}^0}{\partial \bar{\xi}^2} + \varepsilon \frac{\partial^2 H_{\text{II}}^1}{\partial \bar{\xi}^2} + \varepsilon^2 \frac{\partial^2 H_{\text{II}}^2}{\partial \bar{\xi}^2} \right) = \lim_{\xi \rightarrow 0} \frac{\partial^2 H_{\text{IV}}^0}{\partial \xi^2}. \quad (7.195)$$

Hence

$$H_{\text{II}}(\bar{\xi}, \tau) = H_{\text{II}}(\tau), \quad (7.196)$$

⁶The ‘Heaviside’ discontinuity at the contact point is now in the fourth derivative.

and, after a little algebra on H_{II}^0 , H_{II}^1 and H_{II}^2 , we obtain the simplified matching conditions

$$H_{\text{III}}^0(0, \tau) = H_{\text{IV}}(0, \tau) = H_{\text{II}}(\tau), \quad (7.197)$$

$$\frac{\partial H_{\text{III}}}{\partial \xi}(0, \tau) = \frac{\partial H_{\text{IV}}}{\partial \xi}(0, \tau), \quad (7.198)$$

$$\frac{\partial^2 H_{\text{III}}}{\partial \xi^2}(0, \tau) = \frac{\partial^2 H_{\text{IV}}}{\partial \xi^2}(0, \tau). \quad (7.199)$$

As the height of the inner region does not depend on $\bar{\xi}$, the remaining analysis is unchanged from the membrane analysis, giving equations (7.107)-(7.109) and far-field matching conditions (7.110)-(7.111).

7.3.1.2 Outer region III

The analysis in the outer region is mainly unchanged; the only differences are the beam equation and its boundary conditions. Hence, the equations for the fluid motion are mass conservation (7.136) and Bernoulli's equation (7.137). The unchanged boundary conditions are the condition (7.125) on the fluid velocity at the tip, whereas the membrane equation (7.127) with boundary conditions (7.128) are superseded by

$$m \left(\frac{\partial}{\partial \tau} - \dot{X}_0 \frac{\partial}{\partial \xi} \right)^2 H_{\text{III}} + EI \frac{\partial^4 H_{\text{III}}}{\partial \xi^4} = p - P \text{ for } 0 < \xi < b(\tau) - X_0(\tau), \quad (7.200)$$

$$H_{\text{III}} = 0 \text{ for } \xi > b(\tau) - X_0(\tau), \quad (7.201)$$

and

$$H_{\text{III}}, \frac{\partial H_{\text{III}}}{\partial \xi}, \frac{\partial^2 H_{\text{III}}}{\partial \xi^2} = 0 \text{ at } \xi = b(\tau) - X_0(\tau). \quad (7.202)$$

Along with the matching conditions (7.110)-(7.111), we have just the matching conditions (7.197)-(7.199).

7.3.1.3 Outer region IV

Mass conservation is unchanged at (7.155), and the eikonal equation (7.157) still holds as the result of $p = 0$ at leading order. The evolution equation (7.158) is replaced by

$$m \left(\frac{\partial}{\partial \tau} - \dot{X}_0 \frac{\partial}{\partial \xi} \right)^2 H_{\text{IV}} + EI \frac{\partial^4 H_{\text{IV}}}{\partial \xi^4} = -P. \quad (7.203)$$

The pinning condition (7.152) is unchanged, although we also suppose that the beam is simply-supported, so that

$$\frac{\partial^2 H_{\text{IV}}}{\partial \xi^2}(-L) = 0. \quad (7.204)$$

Finally, the matching conditions as $\xi \rightarrow 0$ are (7.150)-(7.151) for the pressure and fluid velocity, and (7.197)-(7.199) for the beam.

7.3.2 Global travelling wave solution

Once again, we search for a global travelling wave solution and so introduce the travelling-wave variable

$$\zeta = x - Ut. \quad (7.205)$$

Following through the previous analysis, we recover the same solution for the fluid velocity in region II, $u = 0$, the same outer pressure in III, $p = \frac{1}{2}\rho(V - U)^2$, and same inner height, $H_{\text{II}} = 4h_j$.

The first important difference is the beam equation (7.184), which, in the outer region III, transforms to

$$EI \frac{\partial^4 H_{\text{III}}}{\partial \xi^4} + mU^2 \frac{\partial^2 H_{\text{III}}}{\partial \xi^2} = \frac{\rho}{2}(V - U)^2 - P, \quad (7.206)$$

with boundary conditions

$$H_{\text{III}}, \frac{\partial H_{\text{III}}}{\partial \zeta}, \frac{\partial^2 H_{\text{III}}}{\partial \zeta^2} = 0 \text{ at } \zeta = \zeta_*. \quad (7.207)$$

We nondimensionalise this equation by scaling $\zeta = \zeta_* \tilde{\zeta}$ and $H_{\text{III}} = 4h_j \tilde{H}$, where ζ_* , the length of the outer region, will be determined by the solution procedure. By writing $' = \frac{d}{d\tilde{\zeta}}$ and then dropping tildes for convenience, we obtain the following nondimensional eigenvalue equation:

$$H'''' + \lambda^2 H'' = \mu, \quad (7.208)$$

where the unknown nondimensional constants λ and μ are given by

$$\lambda^2 = \frac{mU^2 \zeta_*^2}{EI}, \quad (7.209)$$

and

$$\mu = \frac{\zeta_*^4}{4EIh_j} \left(\frac{\rho}{2}(V - U)^2 - P \right). \quad (7.210)$$

The boundary conditions are now

$$H(0) = 1, \quad (7.211)$$

and

$$H(1) = H'(1) = H''(1) = 0. \quad (7.212)$$

The solution to this problem is

$$H(\zeta) = \frac{\mu}{2\lambda^4} \left(\lambda^2(1 - \zeta)^2 + \cos(\lambda(1 - \zeta)) - 1 \right), \quad (7.213)$$

where μ and λ satisfy the transcendental equation

$$2\lambda^4 = \mu(\lambda^2 + \cos \lambda - 1). \quad (7.214)$$

The first key observation we make about this solution is that since $z^2 + \cos z - 1 > 0$ for all $0 < z < 1$, the solution H is only positive if $\mu > 0$. Thus, in stark contrast to the membrane solution, there is no travelling wave solution unless

$$P < \frac{\rho}{2}(V - U)^2, \quad (7.215)$$

and so, for U to be positive, the velocity must satisfy

$$V^2 > \frac{2P}{\rho}. \quad (7.216)$$

Note that the constraint (7.215) ensures that $\mu > 0$ and so the transcendental equation for λ and μ is well-defined. Secondly, it is clear by looking at the first derivative that this function is monotonic increasing for $\zeta \in [0, 1]$.

A second equation for μ and λ must come from region IV. The nondimensional problem here becomes

$$H_{\text{IV}}'''' + \lambda^2 H_{\text{IV}}'' = \hat{\mu}, \quad (7.217)$$

where $\hat{\mu} = -\frac{P\xi_*^4}{4E\Gamma h_j}$, with nondimensional boundary conditions from (7.197)-(7.199)

$$H_{\text{IV}}(0) = 1, \quad (7.218)$$

$$H_{\text{IV}}'(0) = \frac{\mu}{2\lambda^3}(2\lambda + \sin \lambda), \quad (7.219)$$

$$H_{\text{IV}}''(0) = -\frac{\mu}{2\lambda^2}(2 + \cos \lambda), \quad (7.220)$$

$$H_{\text{IV}}(-\tilde{L}) = \frac{H_p}{4h_j} = \tilde{H}_p, \quad (7.221)$$

$$H_{\text{IV}}''(-\tilde{L}) = 0, \quad (7.222)$$

where the end $\zeta = -\tilde{L} = -L/\zeta_*$ is now simply-supported in the moving frame. Solving this, we find that

$$H_{\text{IV}} = A + B\zeta + \frac{\hat{\mu}\zeta^2}{2\lambda^4} + C \sin \lambda^2 \zeta + D \cos \lambda^2 \zeta, \quad (7.223)$$

where

$$A = 1 - \frac{1}{2\lambda^8} (\mu\lambda^2(2 + \cos \lambda) + 2\hat{\mu}), \quad (7.224)$$

$$B = -\left(\frac{\cot(\lambda^2 \tilde{L})}{\lambda^6} (\mu\lambda^2(2 + \cos \lambda) + 2\hat{\mu})\right) + \frac{\mu\lambda(2 + \sin \lambda)}{2\lambda^3} + \frac{\hat{\mu} \csc(\lambda^2 \tilde{L})}{\lambda^6}, \quad (7.225)$$

$$C = \frac{(\mu\lambda^2(2 + \cos \lambda) + 2\hat{\mu})}{2\lambda^8} \cot(\lambda^2 \tilde{L}) - \frac{\hat{\mu}}{\lambda^8} \csc(\lambda^2 \tilde{L}), \quad (7.226)$$

$$D = \frac{1}{2\lambda^8} (\mu\lambda^2(2 + \cos \lambda) + 2\hat{\mu}), \quad (7.227)$$

and

$$\tilde{H}_p = A - B\tilde{L} + \frac{\mu\tilde{L}^2}{2\lambda^4} - C \sin(\lambda^2 \tilde{L}) + D \cos(\lambda^2 \tilde{L}). \quad (7.228)$$

This equation, in addition to (7.214), allows us to solve for μ and λ and hence obtain the unknown U and ξ_* (note that $\hat{\mu}$ can be rewritten in terms of λ and μ only). This remains to be done numerically.

7.4 A filling-flow impact model with general constitutive law $p = p(H)$

In §7.2, we considered a filling flow impacting a membrane under applied pressure P . In this section, we pose a more general model in which the pressure on the cavity boundary is a prescribed function of H ,

$$p = p(H). \quad (7.229)$$

We will, at first, only state that $p(H)$ is a monotonically increasing function, so that a higher fluid pressure p corresponds to the height of the free boundary being greater.

7.4.0.1 Outer region

The bulk of the outer analysis is the same as in §7.2.1, the only difference being the replacement of the membrane equation (7.96) with the general constitutive law (7.229). To recapitulate, we write the equations for conservation of momentum and mass in matrix form as:

$$\begin{pmatrix} 1 & 0 \\ 0 & 1 \end{pmatrix} \begin{pmatrix} \hat{u} \\ H \end{pmatrix}_t + \begin{pmatrix} \hat{u} & \frac{p'(H)}{\rho} \\ H & \hat{u} \end{pmatrix} \begin{pmatrix} \hat{u} \\ H \end{pmatrix}_\xi = \begin{pmatrix} -\ddot{X}_0 \\ 0 \end{pmatrix}, \quad (7.230)$$

where \hat{u} is the velocity in the frame moving with the inner turnaround point. The eigenvalues λ_\pm are given by

$$\lambda_\pm = \hat{u} \pm \sqrt{\frac{Hp'(H)}{\rho}}. \quad (7.231)$$

Owing to the assumption of $p(H)$ being monotonically increasing, the eigenvalues are real and distinct. Hence the system is *hyperbolic*, with characteristic equations

$$\frac{d\xi}{dt} = \hat{u} \pm \sqrt{\frac{Hp'(H)}{\rho}}. \quad (7.232)$$

We now solve for the left eigenvectors, \mathbf{l}_\pm , which correspond to the eigenvalues λ_\pm , yielding

$$\mathbf{l}_\pm = \left(1, \mp \sqrt{\frac{p'(H)}{\rho H}} \right), \quad (7.233)$$

and so separately multiplying the system (7.230) by \mathbf{l}_\pm leads to

$$d\hat{u} \pm d\left(\int \sqrt{\frac{p'(H)}{\rho H}} dH\right) + \ddot{X}_0 dt = 0. \quad (7.234)$$

Integrating this gives us the *Riemann invariants* for the system as

$$\hat{u} \pm \int \sqrt{\frac{p'(H)}{\rho H}} dH + \dot{X}_0, \quad (7.235)$$

which are constant on the characteristics (7.232).

The boundary conditions are

$$\hat{u}(b(t) - X_0(t)) = \dot{b} - \dot{X}_0, \quad (7.236)$$

and

$$H(b(t) - X_0(t)) = 0, \quad (7.237)$$

with matching conditions being continuity of H into the inner region and equations (7.123)-(7.124). We also suppose that, without loss of generality, $X_0(0) = 0$ and $b(0) = b_0$.

A sensible first choice of $p(H)$ is to pick a linear relationship between p and H , so we write

$$p = \rho g H, \quad (7.238)$$

where g is a constant. Substituting this relationship into the system (7.230), we recover the shallow water equations in a moving frame with gravitational acceleration g .

There are numerous examples in the literature of the shallow water equations where the gravity term is important. One relevant example is in the consideration of ‘gravity currents’. These consist of two fluids of differing constant densities, one of which flows into the other under the effect of gravity. Typically, such currents arise in oceanography, fluid-spreading problems (such as oil slicks) and in many other industrial examples. The significant feature of these flows is that the lengthscales involved naturally lead to a small parameter, and hence to the shallow-water equations (with nonzero gravity) as in the version of (7.230) in a non-accelerating frame.

Using high-speed photography, gravity-currents can be investigated experimentally. Thomas *et al.* [88] examine the region local to the advancing head of the denser fluid in a large Reynolds number regime. Looking at a flow in which the front is moving with near-constant velocity (“slumping phase”), they track individual fluid particles and discover a locally-turbulent flow that is in agreement with numerical models.

Analytically, it is important to track the position of the interface between the two fluids and the shape of the free boundary in these systems, especially for large time. Grundy *et al.* [27], [29] do so by looking at a classical travelling-wave solution to the problem. The

important boundary condition they use is to balance the buoyancy term with inertia at the ‘tip’, assuming that the height does not go down to zero there. They then obtain a large-timescale linearly stable solution, valid up to a cut-off time where the viscous forces become important (and so inertia must balance viscosity after this point). Sadly, the buoyancy boundary condition is only valid for a nonzero tip-height, which is incompatible with our boundary condition at the tip⁷. However, their analysis does suggest that we might try a similarity solution.

7.4.1 Similarity solution

If we were to follow in the footsteps of previous sections, we would continue by attempting a global travelling-wave solution. For such a solution to exist, the length of the outer region must remain constant by virtue of mass conservation. This corresponds to the $k = \frac{1}{2}$ regime, and so the constant outer pressure is given by (7.164), as in §7.2.2. However, if the pressure is constant, then the height of the boundary H must also be constant in the outer region via (7.229). We conclude that a global travelling wave solution is not possible. Thus, in this section, we adopt the linear law (7.238) and attempt to find a similarity solution. We start by looking for such solutions with inner solution $X_0 = U_0 t$, say, for constant U_0 .

With the previous hypothesis, consider the outer system (7.230), with boundary conditions (7.237)-(7.236) and initial conditions $X_0(0) = 0$ and $b(0) = b_0$. We suppose that the variables scale $x \sim \alpha$, $t \sim \beta$, $\hat{u} \sim \gamma$ and $H \sim \lambda$. For the equations to remain scale-invariant under these scalings, we must have

$$\frac{\lambda}{\beta} = \frac{\lambda\gamma}{\alpha} \text{ and } \frac{\gamma}{\beta} = \frac{\gamma^2}{\alpha} = \frac{\lambda}{\alpha}. \quad (7.239)$$

The matching conditions must also scale correctly. Using the linear pressure law, (7.123) becomes

$$gH_0 = 2\sqrt{\frac{h_j}{H_0}} \left(1 - \sqrt{\frac{h_j}{H_0}} \right) (V - U_0)^2. \quad (7.240)$$

This gives a quartic for the matching height H_0 in terms of the velocity U_0 and, in conjunction with (7.124), shows that $\gamma = \lambda = 1$ for the boundary conditions to remain invariant under the rescaling. Thus we introduce the similarity variable

$$\eta = \frac{\xi}{t - T}, \quad (7.241)$$

⁷A similar interface-problem in a shallow-water regime is considered in [28]. Here, the fluid is assumed to start from rest and the initial behaviour of the interface (tip) is considered. It is shown that the interface can remain stationary for finite time before moving, depending on the shape of the initial conditions local to the tip. These are called ‘waiting-time’ solutions. However, given the ferocity of the incoming shaped-charge jet, a small t expansion is likely to be practically irrelevant!

where introduction of an unknown T allows us to fit initial positions of $b(t)$ and $X_0(t)$. Writing the outer unknowns as $H = H(\eta)$ and $u = U(\eta)$, the outer equations become

$$-\eta U' + UU' + gH' = 0, \quad (7.242)$$

$$-\eta H' + (UH)' = 0. \quad (7.243)$$

Searching for polynomial solutions, we obtain

$$U(\eta) = \frac{2}{3}\eta + \frac{C}{3}, \quad (7.244)$$

$$H(\eta) = \frac{1}{9g}(C - \eta)^2, \quad (7.245)$$

for some constant C . The boundary condition (7.237) and the condition $b(0) = b_0$ lead to

$$b(t) - X_0(t) = C(t - T) = Ct + b_0, \quad (7.246)$$

and so the tip moves at constant velocity. This also determines $T = -b_0/C$. The second boundary condition (7.236) is automatically satisfied. Matching pressure into the inner region and writing $k_0 = \sqrt{\frac{h_j}{H_0}}$, we find

$$2k_0(1 - k_0)(V - U_0)^2 = \frac{C^2}{9}. \quad (7.247)$$

Matching the velocity yields

$$\frac{C}{3} = (2k_0 - 1)(V - U_0). \quad (7.248)$$

Eliminating $V - U_0$, we obtain the quadratic $(2k_0 - 1)^2 = 2k_0(1 - k_0)$, which has solution

$$k_0 = \frac{1}{2} + \frac{1}{\sqrt{12}}. \quad (7.249)$$

The positive square root has been taken to ensure $k_0 > \frac{1}{2}$.

Finally, matching the height into the inner region gives $H_0 = \frac{C^2}{9g}$, and thus we solve for C and reach

$$C = 3\sqrt{gh_j}(3 - \sqrt{3}) > 0. \quad (7.250)$$

Thus U_0 is determined via (7.248) and the boundaries $X_0(t)$ and $b(t)$ are given by

$$X_0(t) = U_0 t, \quad (7.251)$$

$$b(t) = U_0 t + Ct + b_0. \quad (7.252)$$

The outer solutions for H and u are

$$H(\xi, t) = \frac{1}{g} \left(\sqrt{gh_j}(3 - \sqrt{3}) - \frac{\xi}{3(t + \frac{b_0}{C})} \right)^2, \quad (7.253)$$

$$u(\xi, t) = \frac{2\xi}{3(t + \frac{b_0}{C})} + \sqrt{gh_j}(3 - \sqrt{3}). \quad (7.254)$$

The constant inner velocity is

$$U_0 = V_j - 3\sqrt{gh_j}(\sqrt{3} - 1). \quad (7.255)$$

Overall, we have some kind of stretching travelling wave solution; the solution to the inner is a travelling wave with known velocity U , whereas the profile of the outer region behaves like a stretching positively-oriented quadratic, whose minimum corresponds to the tip.

The solutions to the filling-flow models varying with height have resulted in some kind of travelling-wave solution (albeit just in the inner region). Although this will always predict an infinite penetration depth, it does demonstrate the possibility of similarity solutions in which the ratio between the inner height and incoming jet is fixed via (7.249).

7.5 Axisymmetric filling flows

Up until now, we have only considered two-dimensional filling flows, despite motivating an axisymmetric elastic/plastic model in Chapter 3. In this section, we remedy this and develop ideas generated from the two-dimensional models.

We consider the upper half of a general axisymmetric filling flow with velocity V and initial jet radius r_j , returning jet radius r_l , as shown in Fig. 7.17. For simplicity and in

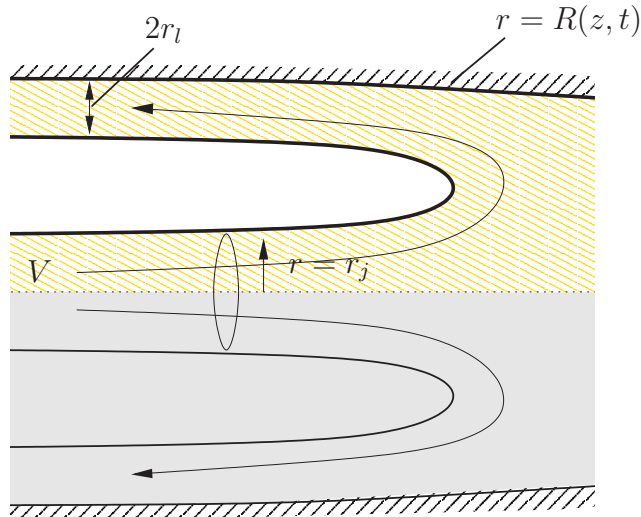


Figure 7.17: An axisymmetric filling flow.

a manner consistent with the two-dimensional model, we initially suppose that the filling flow is occurring in a cylinder with radius R . Initially, we say nothing about the nature of the free boundary $r = R(z, t)$.

7.5.0.1 Inner region

With little thought, it is clear that we can proceed in a manner almost identical to the two-dimensional derivation, but replacing lengths in the two-dimensional models with areas for the axisymmetric model⁸. Hence, using the same notation as in the previous section and in direct correspondence with (7.13)-(7.15), we can once more write down equations describing conservation of mass, force and a Bernoulli balance in a frame moving with the turnaround point $X_0(\tau)$:

$$\pi R^2(u_0(\tau) - \dot{X}_0(\tau)) + \pi r_l^2(V - \dot{X}_0(\tau)) = \pi r_j^2(V - \dot{X}_0(\tau)), \quad (7.256)$$

$$(P + \rho(u_0(\tau) - \dot{X}_0(\tau))^2)\pi R^2 = \rho(V - \dot{X}_0(\tau))^2(\pi(R^2 + r_l^2)), \quad (7.257)$$

$$\frac{P}{\rho} + \frac{1}{2}(u_0(\tau) - \dot{X}_0(\tau))^2 = \frac{1}{2}(V - \dot{X}_0(\tau))^2. \quad (7.258)$$

Introducing the dimensionless constant $k = \frac{r_j}{R}$, we can manipulate the three equations and arrive at the familiar results of

$$P = 2\rho k(1 - k)(V - \dot{X}_0)^2, \quad (7.259)$$

and

$$u_0 - \dot{X}_0 = (2k - 1)(V - \dot{X}_0). \quad (7.260)$$

We observe that the main difference between this model and the two-dimensional model is that k is proportional to the reciprocal of the square root of the height in the latter, whereas it is proportional to the reciprocal of the radius in the former.

7.5.0.2 Outer region

Much of the work for writing down the equations for this outer region has already been done in §4.1.1. Consequently, we quickly recall the salient equations, making the appropriate modifications as necessary.

Analogous to the two-dimensional solution, we assume that the flow in the outer region is both incompressible and irrotational so that there exists a velocity potential that satisfies Laplace's equation. Changing to outer coordinates,

$$r = \varepsilon r', \quad (7.261)$$

$$\xi = z - X_0(t), \quad (7.262)$$

$$\tau = t, \quad (7.263)$$

⁸Had we derived the conditions (7.13)-(7.15) using complex variable methods, this direct analogy would not have been possible. Lamentably, this method does not give the equation of the inner free boundary.

and writing a new potential $\hat{\phi} = \phi - \dot{X}_0 \xi$ so that the new fluid velocity is given by $\mathbf{u} = (\hat{u}, 0, \hat{w}) = \left(\frac{\partial \hat{\phi}}{\partial \xi}, 0, \frac{1}{\varepsilon} \frac{\partial \hat{\phi}}{\partial r} \right)$, we arrive at (4.5). The boundary conditions for the fluid are now zero radial flow on the base $r' = 0$ (as a result of symmetry) and a kinematic condition on the free boundary $r' = R(\xi, t)$. Thus, in the same vein as (4.16) and writing t for the inner temporal variable,

$$\frac{\partial \hat{\phi}}{\partial r'} - \varepsilon^2 \frac{\partial R}{\partial \xi} \frac{\partial \hat{\phi}}{\partial \xi} = \varepsilon^2 \frac{\partial R}{\partial t} \quad \text{on } r' = R(\xi, t), \quad (7.264)$$

and

$$\frac{\partial \hat{\phi}}{\partial r'} = 0 \quad \text{on } r' = 0. \quad (7.265)$$

Expanding $\hat{\phi}$ in powers of ε^2 and substituting into Laplace's equation and the boundary conditions, we discover at leading order that $\hat{\phi}_0 = \hat{\phi}_0(\xi, t)$. At $\mathcal{O}(\varepsilon^2)$, we again discover that $\hat{\phi}_2$ satisfies (4.26). This is where the analysis differs slightly from §4.1.1; we now apply the zero flow boundary condition on $r' = 0$ and reach mass conservation:

$$\frac{\partial}{\partial t} (R(\xi, t)^2) + \frac{\partial}{\partial \xi} \left(\frac{\partial \hat{\phi}_0}{\partial \xi} R(\xi, t)^2 \right) = 0. \quad (7.266)$$

We could also have derived this by balancing flux through a slender cylinder.

The z -component of the momentum equation has also been derived (and integrated) in (4.9), which we write as

$$\frac{\partial \hat{w}}{\partial t} + \hat{w} \frac{\partial \hat{w}}{\partial \xi} + \frac{1}{\rho} \frac{\partial p}{\partial \xi} = -\ddot{X}_0. \quad (7.267)$$

Irrespective of the nature of the free boundary $r = R(\xi, t)$, the boundary conditions for the system are zero radius at the tip,

$$R(b(t) - X_0(t)) = 0, \quad (7.268)$$

the usual condition on the fluid velocity at the tip,

$$\hat{u}(b(t) - X_0(t)) = \dot{b}(t) - \dot{X}_0. \quad (7.269)$$

and the matching conditions motivated by the inner equations (7.259)-(7.260):

$$R(0, t) = R_0(t), \quad (7.270)$$

$$p(0, t) = 2\rho k_0(1 - k_0)(V - \dot{X}_0)^2, \quad (7.271)$$

$$\hat{u}(0, t) = (2k_0 - 1)(V - \dot{X}_0). \quad (7.272)$$

Here, R_0 is the inner radius obtained from matching and $k_0 = \frac{r_j}{R_0}$.

7.5.0.3 Comments

At first sight, the obvious progression of this model seems to be to develop a model for a jet impacting a membrane (or beam-equivalent). The problem with such a model is the boundary condition for the membrane at the tip. In the two-dimensional model for the membrane, say, it was trivial to write down that the height H and its derivative had to be continuous at the tip $\xi = b(\tau) - X_0(\tau)$, and penetration stemmed from a ‘peeling back’ action of the membrane at the tip. In axisymmetry, we still wish the membrane to come down to zero at the tip. However, the peeling-back mechanism is not possible and, more crucially, we will need to ‘create’ membrane at the tip for any penetration to transpire. It is not immediately obvious what the correct boundary condition should be at the tip, and so, as a consequence, we move to consider a general law for the pressure $p = p(R)$, as in §7.4. It is again sensible to assume that $p'(R) > 0$.

7.5.1 General constitutive law $p = p(R)$

Assuming a general law $p = p(R)$, we write down the axisymmetric equivalent of the two-dimensional system (7.230):

$$\begin{pmatrix} 1 & 0 \\ 0 & 1 \end{pmatrix} \begin{pmatrix} \hat{w} \\ R \end{pmatrix}_t + \begin{pmatrix} \hat{w} & \frac{p'(R)}{\rho} \\ \frac{1}{2}R & \hat{w} \end{pmatrix} \begin{pmatrix} \hat{w} \\ R \end{pmatrix}_\xi = \begin{pmatrix} -\ddot{X}_0 \\ 0 \end{pmatrix}. \quad (7.273)$$

The eigenvalues λ_\pm of this system are $\lambda_\pm = \hat{w} \pm \sqrt{\frac{Rp'(R)}{2\rho}}$, and so the characteristic equations are

$$\frac{d\xi}{dt} = \hat{w} \pm \sqrt{\frac{Rp'(R)}{2\rho}}. \quad (7.274)$$

Owing to the assumption that $p'(R) > 0$, we again have a hyperbolic system. This time, the left eigenvectors are

$$\left(1, \pm \sqrt{\frac{2p'(R)}{\rho R}} \right), \quad (7.275)$$

leading to Riemann invariants of

$$\hat{w} \pm 2 \int \sqrt{\frac{p'(R)}{2\rho R}} dR + \dot{X}_0. \quad (7.276)$$

These are constant on the characteristics (7.274).

To close the model, we need to use a suitable constitutive law relating the pressure to the radius. The simplest law such that $p'(R) > 0$ is a linear one,

$$p(R) = \rho g R, \quad (7.277)$$

where g is again constant. Substitution of this law into the system (7.273) yields the axisymmetric shallow water equations in an accelerating frame. Similar systems have been briefly discussed in §7.4 and so we again consider the possibility of a similarity solution.

7.5.2 Similarity solution

In this section, we mirror the ideas from the two-dimensional similarity solution in §7.4.1. Thus, we assume that the inner solution is locally a travelling wave moving with constant velocity U_0 , and we adopt the linear law (7.277) for $p(R)$. This leads to the following outer system of equations:

$$\hat{w}_t + \hat{w}\hat{w}_\xi + gR_\xi = 0 \quad (7.278)$$

$$(R^2)_t + (\hat{w}R^2)_\xi = 0. \quad (7.279)$$

The boundary conditions are given by equations (7.268) and (7.269). The matching conditions are (7.268)-(7.269). We also suppose that $b(0) = b_0$ and, without loss of generality, that $X_0(0) = 0$.

After some algebra, we find that a suitable similarity variable is

$$\eta = \frac{z}{t - T}, \quad (7.280)$$

for some constant T . Writing $w = W(\eta)$ and $R = R(\eta)$, the momentum and mass conservation equations transform to

$$-\eta W' + WW' + gR' = 0, \quad (7.281)$$

$$-R'\eta + 2WR' + RW' = 0. \quad (7.282)$$

We look for polynomial solutions and discover the following solution analogous to (7.244)-(7.245):

$$R(\eta) = \frac{2}{25g}(\eta - D)^2, \quad (7.283)$$

$$W(\eta) = \frac{4}{5}\eta + \frac{D}{5}, \quad (7.284)$$

for some constant D . Use of the boundary conditions gives us the tip position as

$$b(t) = U_0t + D(t - T) = U_0t + b_0, \quad (7.285)$$

so that $T = -b_0/D$. Remembering the difference with the two-dimensional case, we recall $k_0 = r_j/R_0$, where R_0 is the matching radius from the inner region. Matching the pressure and velocity from (7.271)-(7.272), we see that

$$\frac{2}{25}D^2 = 2k_0(1 - k_0)(V - U_0)^2, \quad (7.286)$$

and

$$\frac{D}{5} = (2k_0 - 1)(V - U_0). \quad (7.287)$$

Solving for k_0 , we reach the quadratic $2(2k_0 - 1)^2 = 2k_0(1 - k_0)$, which has solutions

$$k_0 = \frac{1}{2} \left(1 \pm \frac{1}{\sqrt{5}} \right). \quad (7.288)$$

The positive root is taken to ensure $k_0 > \frac{1}{2}$. Continuing the analysis, we use continuity of R which yields

$$R_0 = \frac{2D^2}{25g}. \quad (7.289)$$

Along with (7.288), this equation pins down the unknown constant D as

$$D = \frac{5}{2} \sqrt{(5 - \sqrt{5})gr_j}. \quad (7.290)$$

The solutions are hence

$$X_0 = U_0 t, \quad (7.291)$$

$$b(t) = U_0 t + Dt + b_0, \quad (7.292)$$

$$R = \frac{2}{25g} \left(\frac{z}{t + \frac{b_0}{D}} - D \right)^2, \quad (7.293)$$

$$W = \frac{4z}{5(t + \frac{b_0}{D})} + \frac{D}{5}, \quad (7.294)$$

with constant tip velocity

$$U_0 = V - \frac{\sqrt{5(5 - \sqrt{5})gr_j}}{2}. \quad (7.295)$$

Despite changing from a two-dimensional to an axisymmetric geometry, we have an almost-identical solution in which the inner solution is locally a travelling wave, whilst the outer has a profile of a stretching quadratic, whose minimum is at the tip.

7.6 Remarks

In this chapter, we have used ideas from filling flows to model the jet region in the tip in an attempt to simplify the modelling. Some of the simpler models of §7.1.1 resulted in analytic solutions, yet other seemingly-facile models led to equations which could only be solved numerically. More representative two-dimensional models for jet-impact into a membrane and into a pre-stressed beam were then considered. Again, it was not possible to derive an analytic solution to the complete system, yet travelling-wave solutions and similarity solutions gave us insight into the local shape of the boundary of the jet with

the target. A similarity solution was possible with a linear law $p = \rho g H$, a result that also followed when modelling an axisymmetric jet.

The hyperbolic systems should be solved numerically and compared to known results for penetration and with the hydrocodes. This could motivate a more sensible choice of constitutive law $p = p(R)$. Apart from the linear law, a good possibility is to try a law that is based on the elasticity of the target. For example, recalling equations (5.4) and (5.20), we could try writing

$$R = \begin{cases} \frac{ap}{2\mu} & R \leq R_c \\ \frac{\sigma_Y a}{4\mu} \exp\left(\frac{2p}{\sigma_Y} - \frac{1}{2}\right) & R > R_c \end{cases}, \quad (7.296)$$

where μ is a Lamé constant, σ_Y is the yield stress, and R_c is some critical value of R derived from the yield condition. In order to model the residual displacement, a separate law for when the pressure on the free boundary is decreasing is required. Such a law would be trivially based on either (5.86) or on the nonlinear analysis of §5.2, and is shown graphically in Fig. 7.18. We would then have to solve hyperbolic systems in regions III and IV, with hysteretic boundary conditions. This model is a good way to unite the analysis of §5.3, in which the pressure-pulse was unknown, with the fluid-mechanics of the jet. This remains as further work.

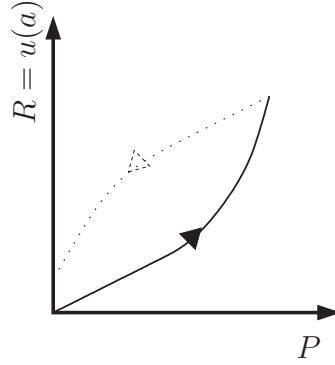


Figure 7.18: A schematic hysteresis diagram showing the displacement of the inner surface of a gun-barrel against applied cavity pressure, based on §5.1.6.

Chapter 8

Metallurgical and hydrocode analysis

Consideration of the microstructure of a penetrated target should help us to understand the mechanism of penetration more fully. In this chapter, we review the literature on how shaped-charge penetration affects the microstructure. We will then describe and appraise our own analysis on a block of hardened-steel that has been penetrated by a silver shaped charge jet. We conclude the chapter with a discussion of numerical results from the *QinetiQ* hydrocodes.

8.1 Shaped charge metallurgy literature

Firstly, we recall the observation of Walters [93] that there is no mass loss of the target material after penetration. Thus, we expect to see evidence of plastic flow as a method of excavating the target material.

Wells *et al* [98] analyse the microstructure of a titanium block penetrated by a low-impact ($\sim 700\text{ms}^{-1}$) hardened-steel projectile. Titanium is well-known to be very susceptible to adiabatic shear, with highly anisotropic mechanical properties. The authors initially use “X-ray computed tomography” (XCT) as a non-destructive method to look at the microstructure, before using the more destructive method of sectioning and etching the specimen. Their analysis is all done on plane-sections whose normals are parallel to the axis of penetration. The XCT shows orbital cracks, approximately 0.1mm long, within 6mm of the cavity. It also shows damage voids ($\sim 1\mu\text{m}$) in the same region. Sectioning and etching the specimen reveals a plastic zone extending about 6mm radially from the cavity, with the majority of the orbital cracks concentrated near the boundary of this zone with the bulk of the specimen. Shear bands and small cracks are also observed at an undisclosed higher magnification, with an increasing number of shear bands being present nearer the back of the penetrated target. The authors conclude that the orbital cracks are areas of shear-failure, connected by the shear bands.

An important investigation into the microstructure is given by Yin *et al* [104]. They consider penetration of four stacked ultra-high strength steel plates, each of thickness 20mm, by a copper jet with unknown impact velocity. The microstructure of the first and last plates are investigated. The first plate, after it has been etched with nital, exhibits a “white” etching layer. This layer is, on average, $75\mu\text{m}$ thick and many shear bands emanate from it. Conversely, the fourth plate has far fewer shear bands. Furthermore, if the specimen is instead etched with a super-saturated picric acid, the white etching layer is no longer seen. However, it is now easy to see that the shear bands include a central line following the band. This is thought to be where the majority of the shearing occurs (“local shear deformation zone”). The remainder of the shear band is described as “heat-affected zone”, a result of unloading from the extreme temperatures from the shearing in the central band (see §1.2.2.3). There is also evidence of recrystallization of austenite grains¹ in the white layer. This suggests a very localized temperature of 1000°C . This recrystallization is not evident in the heat-affected zones of the shear bands. Finally, a micro-hardness test is performed. It is found that the white-etched layer and shear bands have a higher hardness than the bulk material, whereas the region local to the white-etching layer has a slightly lower hardness than the bulk metal. This will be discussed later in the chapter.

Murr *et al* [53] discuss the microstructure of a copper target that has been impacted by a copper jet with impact velocity of 5.83km s^{-1} . They emphasise that there is no evidence for melt-related phenomena, and consistently find evidence of dynamic recrystallization, suggesting that it is of great importance for plastic flow.

The influence of shock-waves on the microstructure is also discussed by Murr *et al* [52]. They comment that, for an impact resulting in subsonic penetration, a shock-wave will move ahead of the elastic-plastic penetration at the bulk sound speed. This shock wave is likely to create lattice defects in the target, which may affect the ensuing penetration.

Other authors consider more specific target materials, such as aluminium and tantalum [26, 56], discussing the effects of shear localization, dynamic recrystallization and any localized temperature effects.

8.2 Metallurgical analysis

To assess the damage caused by penetration experimentally, a “firing” is done. In a typical firing, metal blocks of target material are stacked up, and the charge is fired vertically

¹Austenite is a high-temperature phase of steel alloys, occurring in simple steels at temperatures above 723°C . The structure of an austenite consists of a face-centred cubic structure of iron with carbon in solid solution. This is a very closely-packed structure. It is often used in stainless steel cutlery.

into the target at known stand-off (Fig. 8.1). We have analysed blocks from *QinetiQ*

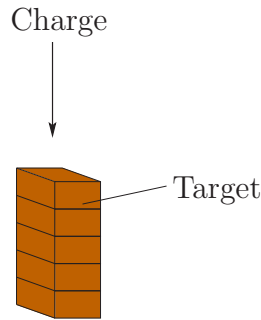
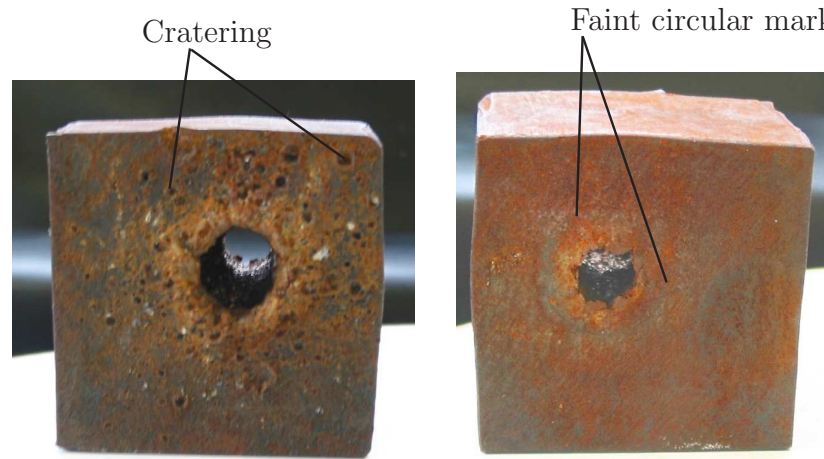


Figure 8.1: The set-up for a typical firing. The charge is fired down into stacked blocks of the target metal. The blocks are analysed afterwards.

into which a silver jet was fired with impact velocity 7.43km s^{-1} . Each of the blocks was originally $100\text{mm} \times 100\text{mm} \times 80\text{mm}$, with the shorter side being vertical.

Before any microstructure analysis, we can comment on the macrostructure of the target blocks. Firstly, we consider the block that was uppermost on the stack (Fig. 8.2). The upper side has a large hole where the charge entered. It is also dimpled throughout



(a) The entry wound of the uppermost block of the penetrated target.

(b) The exit wound of the uppermost block of the penetrated target.

Figure 8.2: The entry and exit points of a shaped charge after penetrating a hardened-steel block.

the upper surface, evidence of spall and of a sufficiently high impact velocity [73]. The exit wound of the block is a lot cleaner. Observe the almost-circular marking on the block, with centre along the axis of penetration. These markings occur consistently on all of the other blocks. The radius of this marking is roughly twice the radius of the cavity. It is possible that this could represent the boundary of the plastic region, in agreement with

$\varepsilon - \varepsilon$ scaling of Chapter 4 for jet and plastic region. Indeed, writing the cavity radius as a and radius of the elastic-plastic boundary as b , we can perform a rough back-of-envelope calculation, arguing that the volume of material displaced must approximately equal the volume of the plastic annulus, so that

$$\pi(b^2 - a^2) = \pi a^2, \quad (8.1)$$

and hence $b \approx \sqrt{2}a$, roughly agreeing with the observation. This will hopefully be clarified by a microscopic analysis.

The next block down and subsequent blocks have much more regular cavities. Recall Fig. 3.1, which motivated axisymmetric modelling. The cavities are rough in nature, lined with a thin layer of silver.

A key observation is that all the blocks have bowed. The importance of this observation on the modelling of the elasticity of the target has already been discussed in §4.5. We can corroborate the observation of zero-mass loss during penetration up to an order of magnitude by estimating the volume of the hole and the total volume of bowed material. These values are in remarkable agreement.

We present two more macroscopic images in Figs 8.3 and 8.4. These are *QinetiQ* cross-sections depicting penetration of a copper jet into a thicker piece of metal (at unknown velocity). The first figure shows the scale of the penetration and cavity size. More interestingly, the second figure shows a scalloped cavity, with similarly-shaped structures following the cavity shape at several different distances away. It is possible that this is the same kind of phenomena responsible as for the faint circle in Fig. 8.2, although it is equally probable that it is an artefact of the sawing. Diagonal lines in this picture are likely to be a result of the machining.

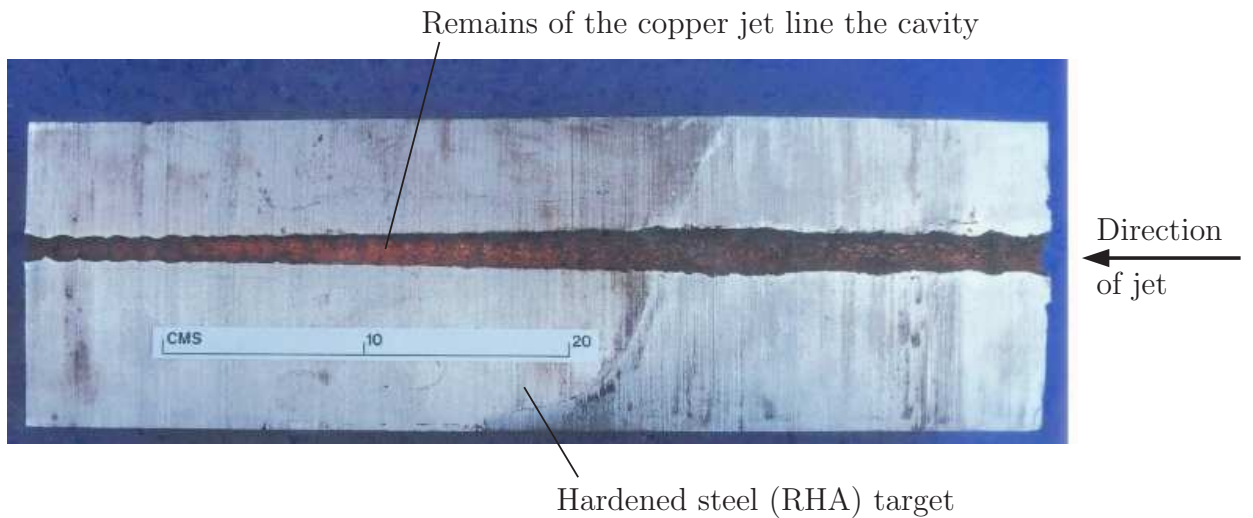


Figure 8.3: A cross-section of a target material showing penetration of a copper jet.

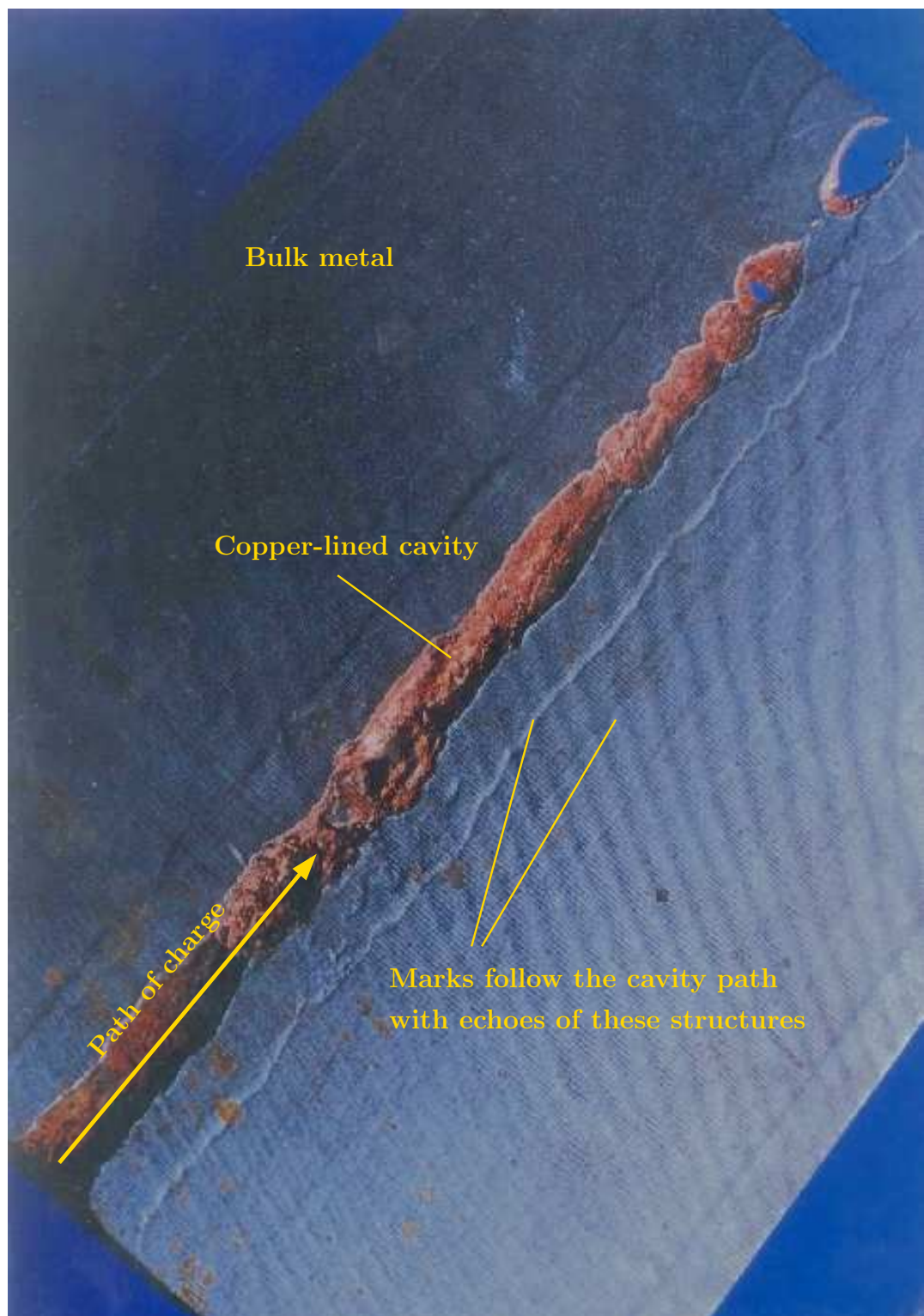


Figure 8.4: Another cross-section of a target showing a copper-lined cavity.

8.2.1 Microscopic analysis

The cavity is very regular in the second and third blocks. Consequently, these blocks are less likely to exhibit unique effects resulting from the initial stages of penetration. This motivated us to perform metallurgical tests on the third block.

Three slices were made into the block using a very hard and powerful circular saw: two in planes parallel to two sides passing through the centre of the cavity (*i.e.* $\theta = 0$ and $\theta = \frac{\pi}{2}$ in cylindrical polar coordinates), and a third to cut the block into two equal pieces, in a plane perpendicular to direction of penetration (Fig. 8.5).

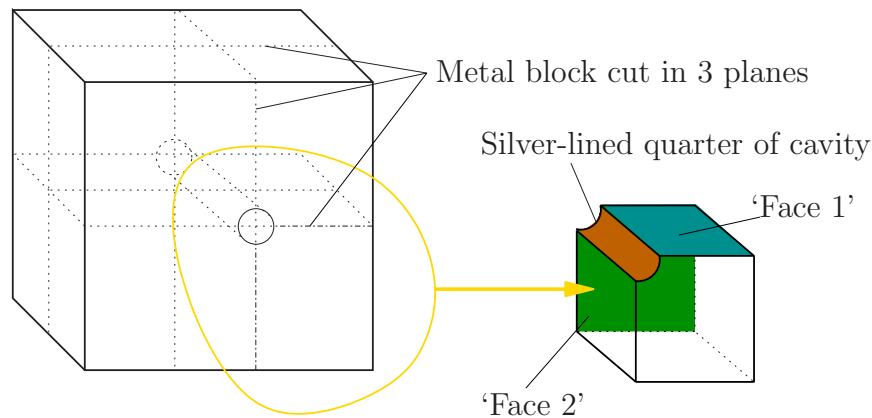


Figure 8.5: The large block is cut into a smaller, more manageable piece. The two marked faces will be polished.

A quick look at the microstructure at this preliminary stage reveals that the cut block is still not ready for analysis, as the machining of the saw is far too coarse (Fig. 8.6). Indeed, by looking at the block one merely sees a dull hue. Hence, we polished the two marked

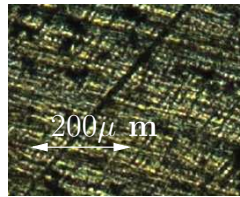


Figure 8.6: Microstructure of an unpolished, sawn face.

faces on a rotating wheel using silicon carbide paper of different (decreasing) thicknesses. The final polishing was done with a damp soft rotating pad, on which a polycrystalline diamond paste was lightly spread. The particles in the paste were 1-micron in dimension. Finally, the surface, now with the finish of a very good mirror, was etched with 2% nital solution for a few seconds at a time and examined between the successive etches. This process enables the features of the microstructure to be examined under a microscope.

8.3 Pictures of the microstructure

Numerous pictures were taken of the microstructure at various resolutions for two of the faces, described in Fig. 8.5. In this section, we simply include the pictures, before commenting on them *en bloc*.

8.3.1 Images from ‘Face 1’

The following images are taken from ‘Face 1’, in which the penetration has taken place from the top to the bottom of the images. We will present pictures for increasing amounts of etching, starting with images with a light 3 second etch.

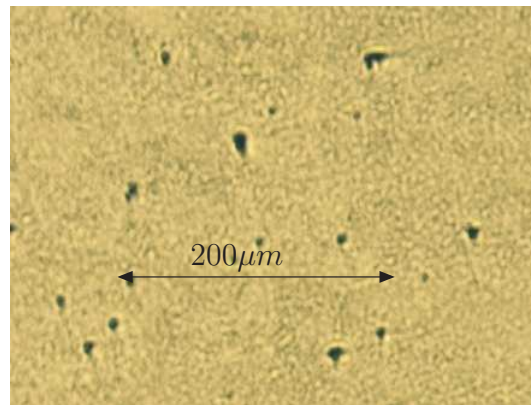


Figure 8.7: A photo of the bulk microstructure of the target sufficiently far away (at least 1mm) from the edge of the cavity. Note that there is no evidence of cracking, shear bands or the silver jet.

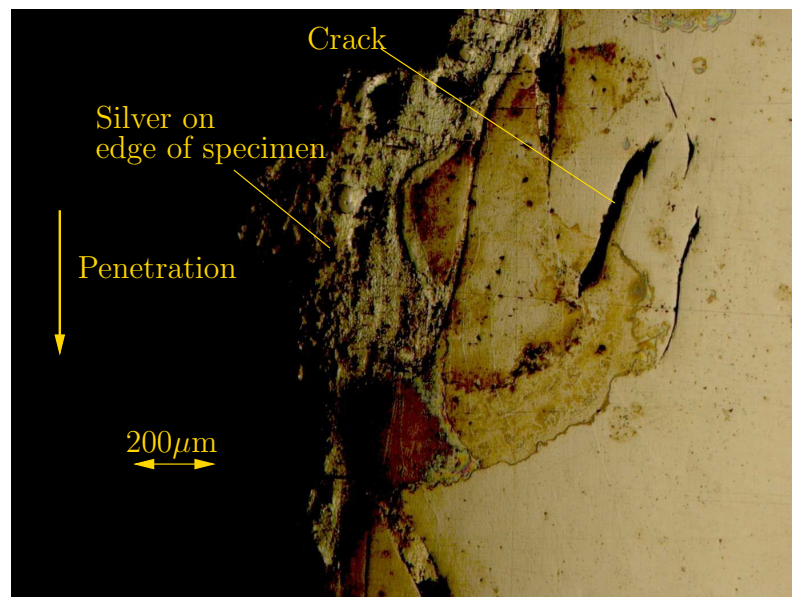


Figure 8.8: A typical view of the microstructure within 1mm of the cavity edge after a very light etch. We consistently see that a band of width $\sim 0.8\text{mm}$ from the edge of the cavity has etched significantly more than the bulk.

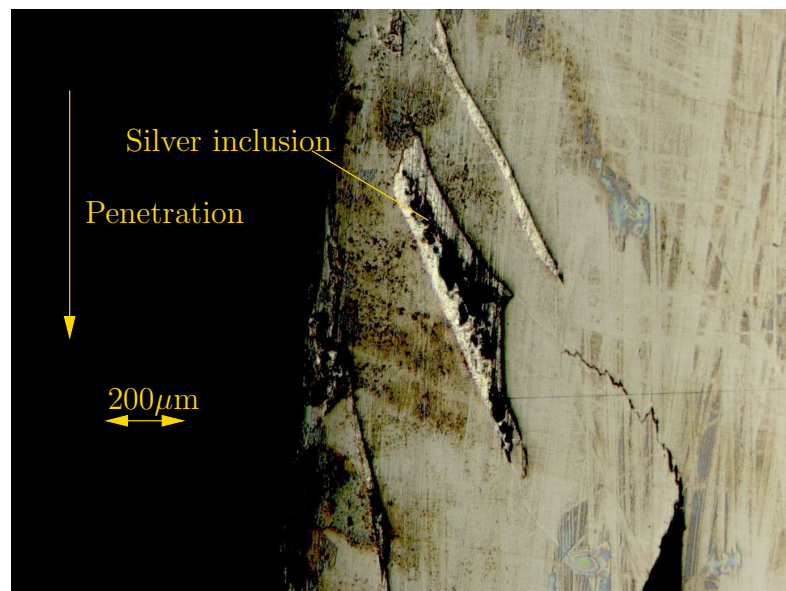


Figure 8.9: Another view of the thin band local to the cavity after a light etch. We can see thin inclusions of silver. We also note from the brown markings that the thin band has etched significantly more than the outer bulk.



Figure 8.10: A view of the inner band after more etching. Note the darker colouring in the band and the silver inclusions.

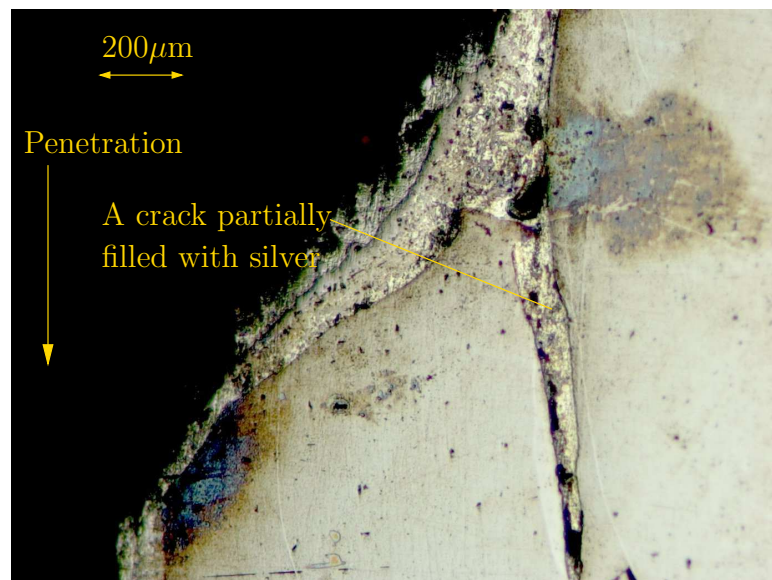


Figure 8.11: A second view of the inner band after more etching. We observe silver tracking down the edge of the cavity and a crack partially-filled with silver in this particular image.

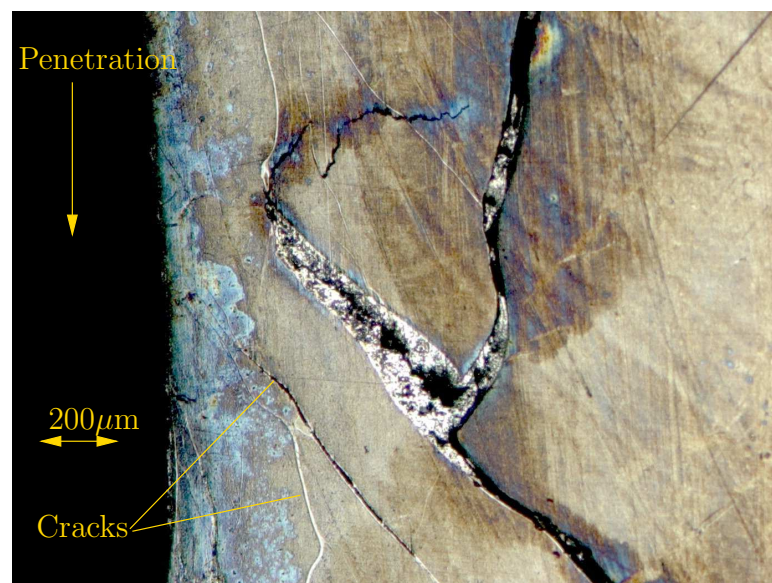


Figure 8.12: A clearer view of a silver inclusion after a total of 10 seconds of etching. The inner band now clearly shows cracks.

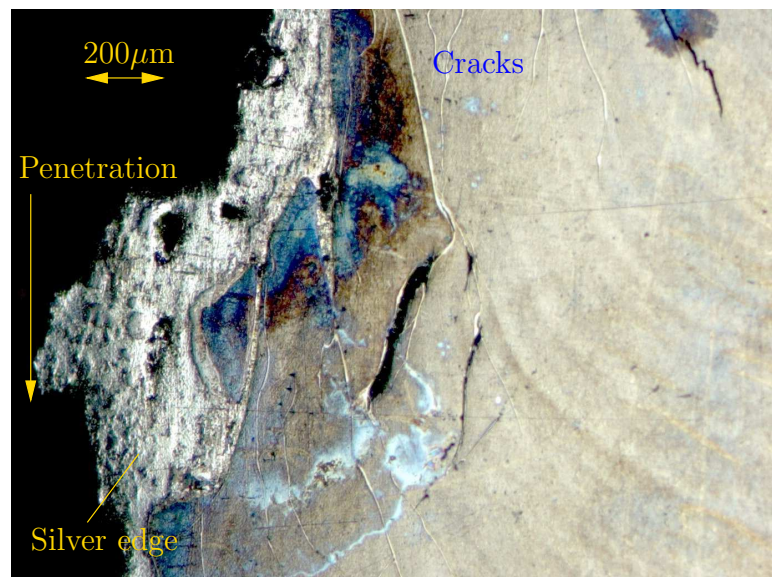


Figure 8.13: A picture showing cracks, silver inclusions, and a silver-lined cavity (with 10 seconds of etching).

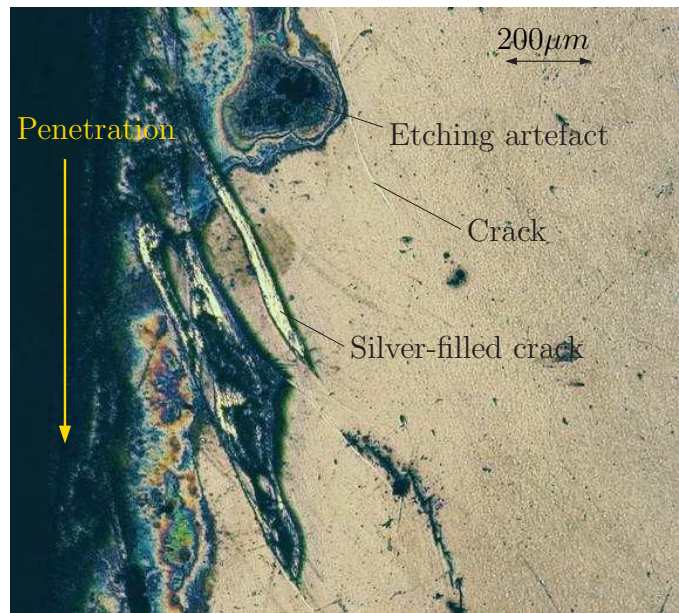


Figure 8.14: This is another typical view of the microstructure local to the cavity after a 10 second etch. We can consistently observe that cracks and silver inclusions appear in the band $\sim 0.8\text{mm}$ from the cavity. The blue colouring shows where the specimen has been significantly etched.

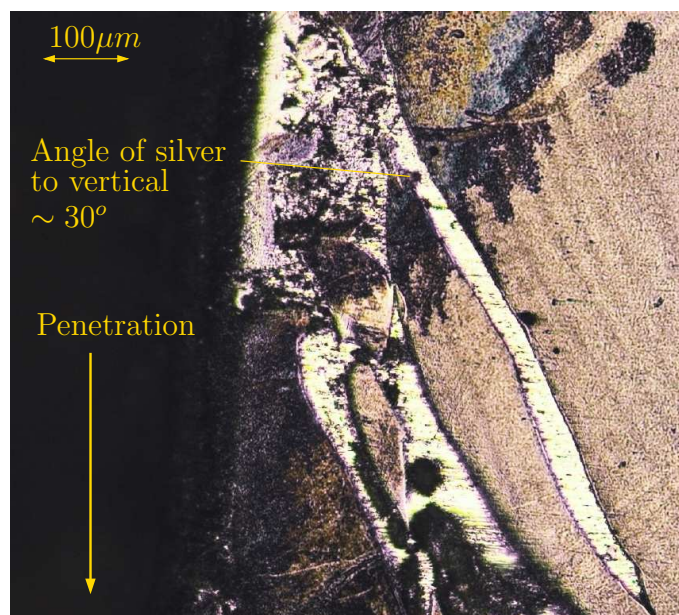


Figure 8.15: A photo showing a closer view of one of the silver inclusions. Typically, they are at an angle of 30° to the direction of penetration, with a length of the order of 0.6mm .

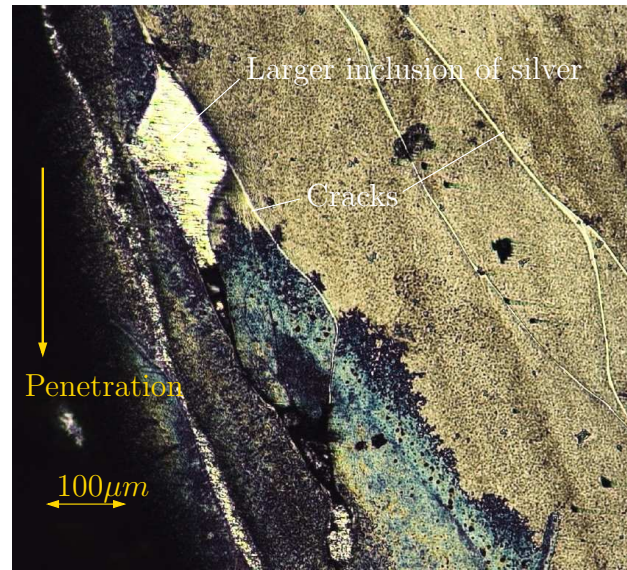


Figure 8.16: A picture showing an inclusion of silver, larger than in Fig. 8.15. We can also see a network of cracks, mainly at an angle of between 20° and 40° to the direction of penetration. Note that the silver inclusion doesn't start from the edge of the cavity and that there is a crack at the bottom of the inclusion.

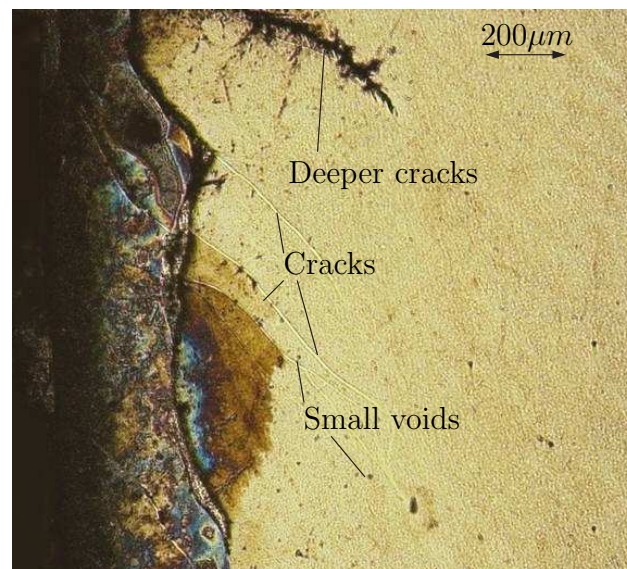


Figure 8.17: Another picture showing cracked regions. The wider black regions are also cracks, at a different altitude to the thinner cracks (and hence not in focus). There are also small damage voids, evident by altering the focus on the microscope.



Figure 8.18: A photograph within 0.8mm of the edge of the cavity, showing a silver inclusion and a network of cracks. Note, again, that the silver inclusion leads into several cracks.

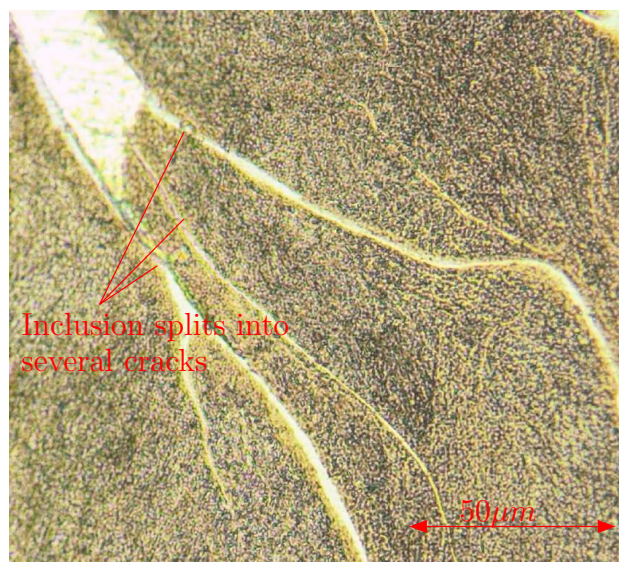


Figure 8.19: A close-up of Fig. 8.18. From this, we observe that the width of a typical inclusion is 25 μm. We can see that several cracks emanate from the end of the inclusion.

8.3.2 Images from ‘Face 2’, with penetration occurring ‘into’ the paper

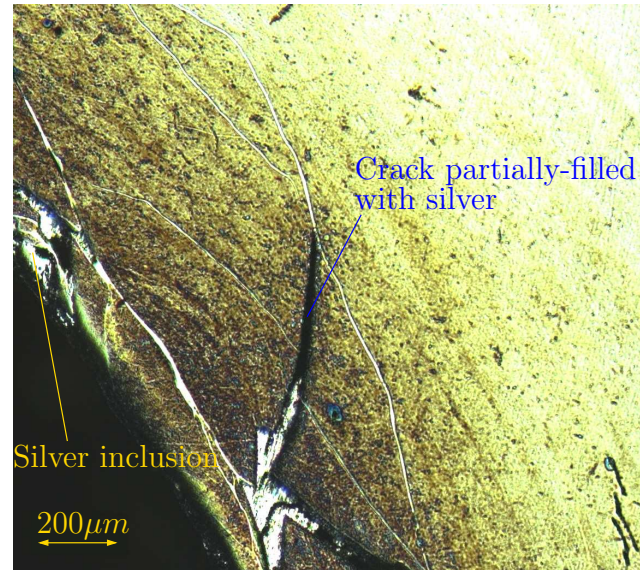


Figure 8.20: A cross-sectional view of the target reveals cracking and silver inclusions around the cavity after a 10 second etch. This is seen consistently on other parts of the block, and the bulk is indistinguishable from Fig. 8.7.

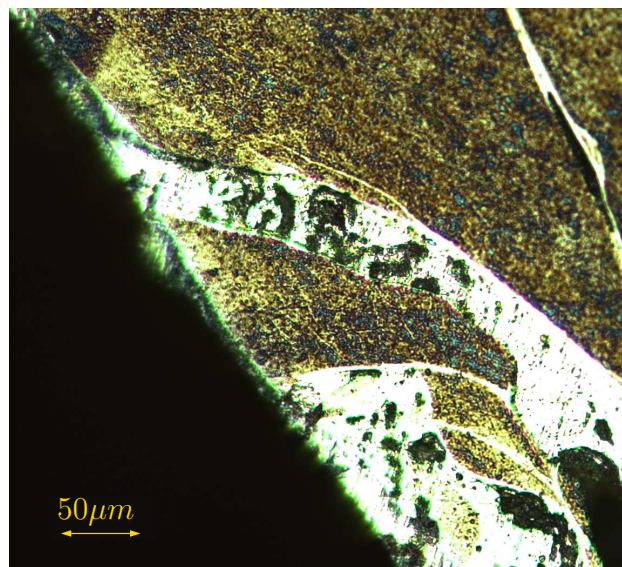


Figure 8.21: A close-up of the silver inclusion uppermost in Fig. 8.20. The width is about 50 μm. This inclusion emanates from the edge of the cavity.

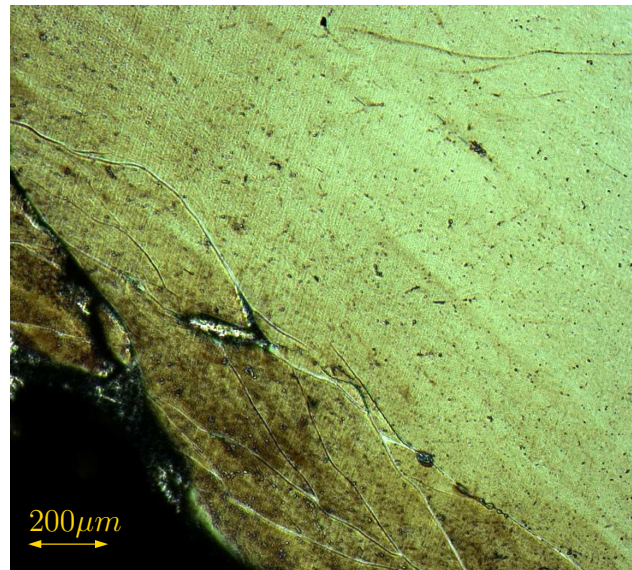


Figure 8.22: A picture showing a network of cracks around the cavity. Observe a silver inclusion amidst the cracks, which doesn't emanate from the edge.

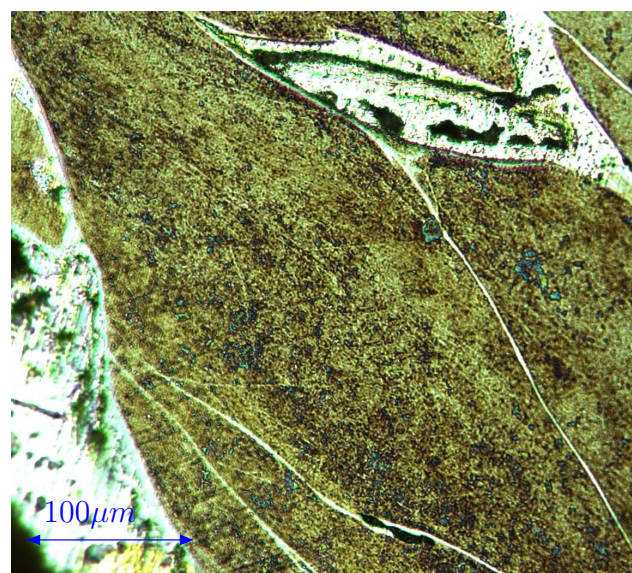


Figure 8.23: A close-up of the inner silver inclusion from Fig. 8.22.

8.3.3 Observations

The microstructure can be divided up into the bulk region (Fig. 8.7) and a thin band local to the cavity that extends out 1mm. Apart from a few material defects, the material outside this thin band is uniform. Conversely, the microstructure of the thin band is fascinating. We now describe and explain its salient features:

- **Dark etching**

Even when lightly etching the specimen for three seconds, the thin band is a lot darker than the bulk material. This is apparent to the naked eye, and is clearly shown in Figs. 8.8, 8.9, 8.20. This is a result of severe deformation, corresponding to nuclei of strain. Apart from the obvious permanent deformation of the target, this high concentration of dislocations is the first clear sign of plastic flow. Even when the specimen is etched for significantly longer, the bulk metal never shows anywhere near a comparable amount of deformation. This indicates that the extent of the plastic region is not as suggested by the faint marking in Fig. 8.2(b). Indeed, there is no noticeable change in the microstructure corresponding to the faint marking on the exterior of the block.

- **Silver-lined cavity**

From Figs. 8.11 and 8.13, we can clearly see that the cavity is lined with a very thin layer of silver, as seen on the macroscale.

- **Silver inclusions and cracks**

Silver-inclusions, fully or partially silver-filled cracks and smaller cracks without silver are a major feature of the microstructure in the band, shown in Figs. 8.8-8.23. To our knowledge (and somewhat strangely), silver-filled cracks are not mentioned in the literature. All of these features are confined to the thin band.

Typically, the larger silver-filled cracks are oriented at an angle near 30° to the direction of penetration, and have a length of the order of 0.6mm (Fig. 8.15). These filled-cracks may not be observed with other liners owing to the high ductility of silver [9]. Images from ‘face 2’ show that the cracks are radial in nature, in agreement with the observations of [98]. It is clear that many of these cracks are not fully filled with silver (Fig. 8.20, Fig. 8.22). The thickness of the inclusions varies between $20\mu\text{m}$ and $50\mu\text{m}$ (Fig. 8.19, 8.21).

Fig. 8.18 and Fig. 8.19 demonstrate the contrast in thickness between the silver-filled cracks and the smaller, empty cracks. The latter tend to have a thickness of the order of $2\mu\text{m}$ and often emanate from the thicker cracks with a similar orientation

to the direction of penetration (Fig. 8.16). Furthermore, there are more of these smaller cracks, and they tend to extend out a little further into the thin band (Fig. 8.20)

The final position and orientation of the cracks is likely to be the result of different processes occurring in several stages. Firstly, a compressive shock-wave will propagate ahead of the jet tip, creating lattice defects. The direction of propagation will be mainly along the z -axis, corresponding to the normal impact of the target. As the jet penetrates, the extreme stress causes severe deformation locally to the jet, thus creating cracks at lattice defects and as a result of the plasticity. The axial penetration and radial expansion determine the orientation of the cracks, which we observe to be between 20° and 40° to the axis of penetration, shown in Figs. 8.12-8.17. The silver, flowing plastically, fills and significantly expands the larger cracks as the jet passes. The stresses decrease as the jet tip passes and so the silver behaves elastically as the target relaxes. More cracks will open in this relaxation phase. The cracks that were fully filled with silver open further. As the silver in these cracks is no longer flowing, voids will be created, thus accounting for the partially-filled cracks observed in Fig. 8.11.

- **Shear bands and grain boundaries**

We cannot see any evidence of shear bands or of grain boundaries in any of the figures. The former is not surprising, since steel's propensity to form shear bands is very dependent on the particular nature of the steel and whether it has gone through any heat or chemical treatment processes. We are slightly surprised not to see any grain boundaries or individual grains, which we would expect to be on a scale somewhere between $1\mu\text{m}$ and $100\mu\text{m}$, depending on the steel. This may be a consequence of the particular type of etchant used and, again, the exact metallurgy of the type of steel, which is, alas, unknown.

- **Damage voids**

When slightly perturbing the focus of the microscope, very small holes come in and out of focus. These holes are damage voids, likely to be a result of shock waves from the impact [52]. Fig. 8.11 and Fig. 8.17 show some of these voids, which are the same order of magnitude as observed by [98]. The voids are also apparent in the bulk metal.

8.3.4 Remarks

Our microscopic analysis is illuminating in many respects, yet leaves some questions unanswered. The analysis suggests that the likely width of the plastic zone is small compared to the cavity radius, although more accurate tests should be done to confirm this. This is likely to be a combination of two major factors: firstly, the block that was dissected was the third block in the original stack, so near the termination of penetration; secondly, the material properties of the steel are likely to dominate its response, potentially having large effects on the position of the elastic-plastic boundary. Consideration of different blocks in the original stack and a more detailed analysis into different target materials would go a long way to clarify these observations.

The presence of both the smaller cracks and the larger filled cracks is unlikely to affect the large-scale modelling of penetration, although a complete model should really include fracture.

Further analysis should be done using a more powerful microscope, such as a scanning electron microscope. We would then, hopefully, be able to see grains and grain boundaries clearly, and we may even observe signs of dynamic recrystallization. Sadly, this is not available to us. More-detailed microscopy may also be able to explain the near-circular markings on Fig. 8.2(b). However, although there is no noticeable difference in the microstructure at this radius, it is possible that there is a significant change in the hardness of the block. This motivates performing a hardness test on the polished specimen.

8.4 Hardness

The *hardness* of a material is a measure of its resistance to abrasion or scratching. However, when considering metallurgical properties of a material, the hardness usually refers to a measure of the material's resistance to plastic deformation. Thus, the hardness of a metal is affected by, for example, any thermal changes, work-hardening and plasticity that may have occurred in the metal.

The simplest form of hardness test is to scratch one material with another material and assess the relative hardness using the Moh's scale of hardness. Clearly, this only gives a qualitative measure. A quantitative measure is obtained by indenting the surface of the metal with a small *indenter*. The size of the indentation is then measured and so, knowing the force on the indenter and the time over which indentation took place, a quantitative measure of hardness can be obtained. Various different measures can be obtained, depending predominantly on the geometry of the indenter. The main three measures are the *Brinell* hardness test (using a spherical indenter), *Rockwell* hardness test (typically indenting with a diamond cone under a preliminary load and then measuring

permanent deformation after application of a large load) and the *Vickers* hardness test. We shall use the latter. This test involves indenting the test metal with a right-pyramidal diamond indenter, which has a square base and an angle of 136° between opposite faces². Typically, a force of between 10N and 1000N is applied, for a duration of between 10s and 15s. A schematic of this set-up is shown in Fig. 8.24. The result is an indentation, whose

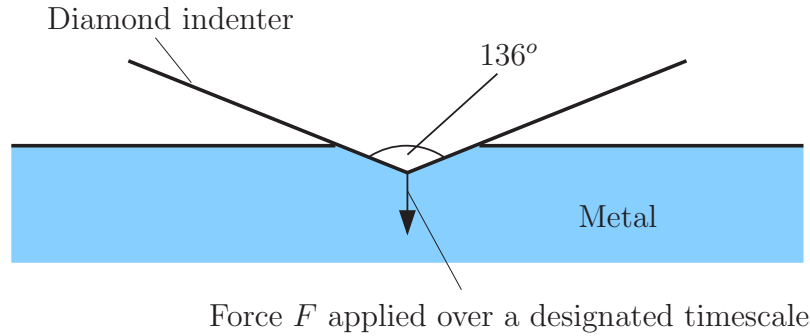


Figure 8.24: A schematic of a diamond indenter which is indenting a metal.

projection on the horizontal plane is a nearly-square rectangle (Fig. (8.25)). The lengths

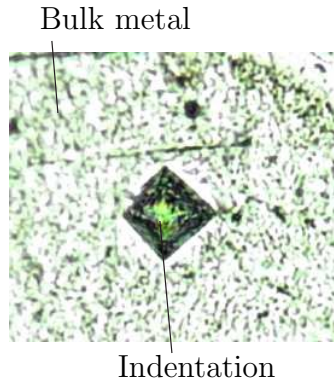


Figure 8.25: A typical indentation by a diamond indenter made into rolled hardened steel. The dimension of the indentation is of the order 1.6×10^{-2} mm.

of the diagonals can be measured accurately through a microscope, and so an estimate for the total surface area can be obtained using the arithmetic mean of these two lengths. The Vickers hardness (HV) is thus defined by the ratio of the force³ F applied to the total surface area of the indentation,

$$HV = \frac{2F \sin 68^\circ}{d^2}. \quad (8.2)$$

²The angle is chosen to mimic the most desirable ratio of indentation radius to ball radius in the Brinell test.

³Usually, the formula is quoted by engineers in terms of the “kilogram force”.

8.4.1 Hardness testing of the steel specimen

Two rows of indentations were made across the specimen. Initially, the separation between each indentation on one row was 0.1mm. This distance was relaxed sufficiently far from the cavity (Fig. 8.26). A 50g load was applied for 10 seconds during each indentation.

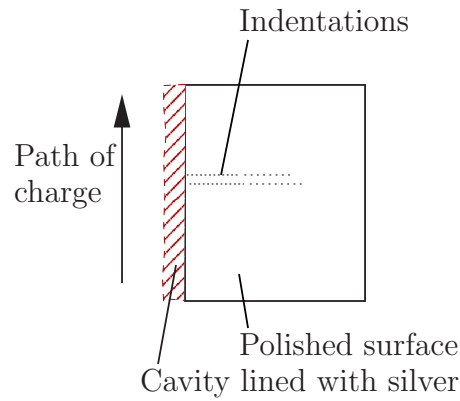


Figure 8.26: A plan-view diagram showing indentations in the polished surface of our specimen.

The Vickers hardness was then calculated using (8.2). The individual numerical values are tabulated in Table E.1, and plotted in Fig. 8.27.

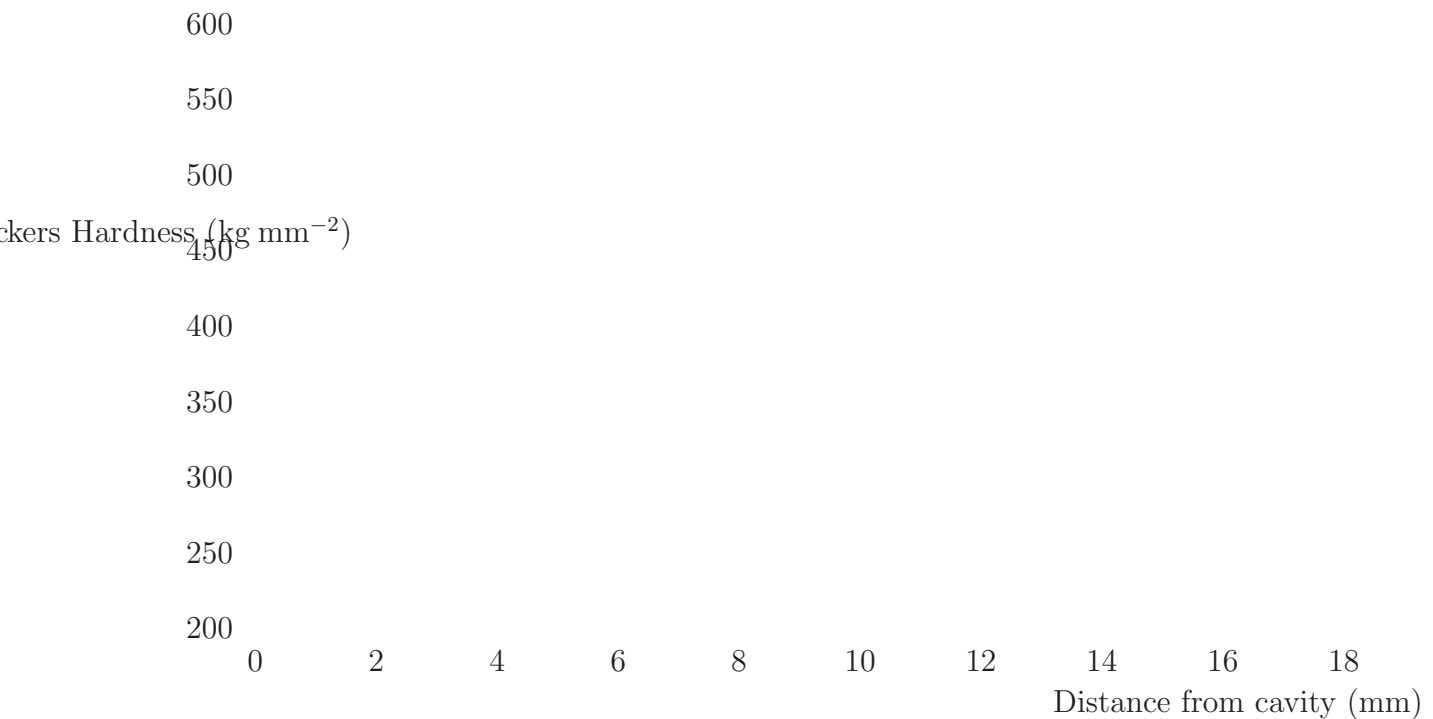


Figure 8.27: Plots from Vickers Hardness tests.

8.4.2 Remarks on hardness test results

In general, the hardness of the specimen is up to 60% higher within a 1mm band of the cavity than in the bulk, agreeing qualitatively with the work of Yin *et al* [104]. This band is in direct correspondence with the darker band described in the previous section. Outside this band, the hardness quickly reduces to relatively small oscillations about some mean value, with a few outlying points. Furthermore, there is no noticeable change in hardness at the distance of the faint almost-circular marking in Fig. 8.2(b), which occurs roughly 10mm out from the cavity.

These observations add weight to our supposition that the thin band parallel to the cavity is where plastic flow occurred. They do not, however, shed any light on the faint ring about 10mm from the edge of the cavity on the exterior of the block. The steel could have gone through many unknown different thermal and mechanical treatments beforehand, and so it is likely to be very anisotropic. Thus, the texture of the steel will dominate its response. This is probably the chief contributory factor in the outliers and any anomalies in the ‘bulk’ and inner band. It would be useful to compare and contrast the analysis with metallurgical studies for penetration with different liner and target materials, and to perform analysis at an earlier point in the penetration to see the size of the plastic region. This is a significant amount of work.

8.5 Hydrocode analysis

In this section, we present results from the Eulerian *QinetiQ* hydrocode, GRIM, as described in §2.2.3. Given the choice of geometry, choice of constitutive law and the large number of material parameters involved, the number of possible hydrocode runs is extremely large. Hence, we elect to use simple parameter regimes, and will consider a sufficiently large target, thus neglecting the effects of waves from the side and back walls on the penetration local to the jet.

We consider axisymmetric shaped-charge penetration occurring in a large domain given by $0 \leq r \leq 35\text{cm}$ and $-16\text{cm} \leq z \leq 39\text{cm}$. Initially, the target material, chosen to be rolled-homogenous armour (RHA) with a yield stress of $\sigma_Y = 6.4 \times 10^{10}\text{kg m}^{-1}\text{s}^{-2}$, occupies $0 \leq r \leq 30\text{cm}$ and $0 \leq z \leq 38\text{cm}$. The small air gaps between the target and the edge of the domain are deliberately present to allow for expansion of the target and to prevent any numerical edge effects. The lower boundary is modelled as rigid, whereas the other three boundaries use transmissive boundary conditions (*i.e.* no reflection of waves). The jet initially occupies $0 \leq r \leq 0.4\text{cm}$ and $-15\text{cm} \leq z \leq 0\text{cm}$, and is modelled using a Mie-Gruneisen equation of state. The remainder of the domain is air. We also add ‘stations’ to the target. These are points at which physical quantities can be measured

as the penetration occurs. We use nine stations, equally spaced on the line between $(r, z) = (1.5, 2.0)$ and $(r, z) = (5.0, 20.0)$, labelled from 1 up 9, respectively. This initial set-up is shown in Fig. 8.28.

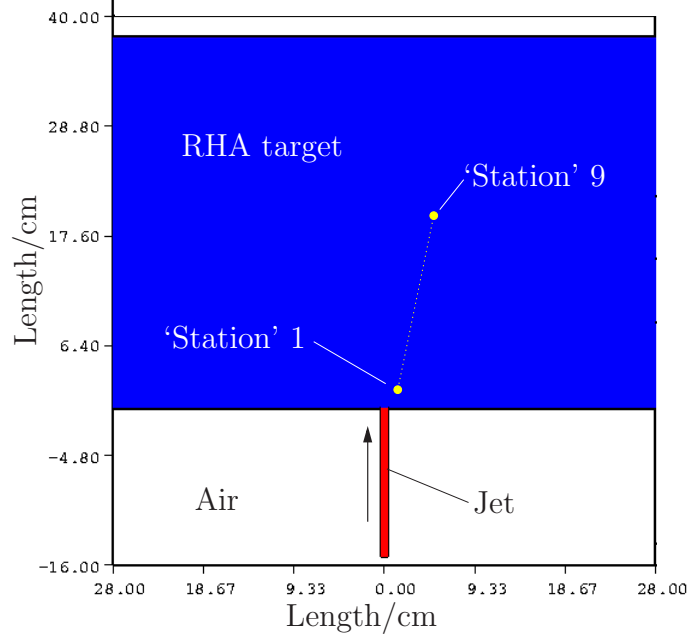


Figure 8.28: A schematic of the initial conditions and the positions of the stations for the hydrocode runs. The edge of the domain $r = 35\text{cm}$ is not shown.

The jet is given an initial vertical velocity between 2.5km s^{-1} and 10.0km s^{-1} . The time-step is taken to be 10^{-8} seconds, and a perfect-plastic constitutive model is used for the penetration. A small artificial viscosity is also added to the model for the jet and the target in order to smooth out the numerical solutions. Finally, two fine grids were chosen, one with 350 radial grid points and 500 axial grid points, and a finer one with 750 radial grid points and 750 axial grid points. The latter grid was chosen to look at the earlier stages of penetration. Plots of stress, strain and velocities were then output at different time intervals.

8.5.1 Hydrocode plots

In the same manner as the metallurgical analysis, we present images *en bloc* before commenting on them individually. We begin with a ‘station’ plot for σ_{rr} , before presenting rasters showing stress, strain, and velocity distributions. We omit any plots of σ_{rz} , as the hydrocode gives that it is zero everywhere in the target.

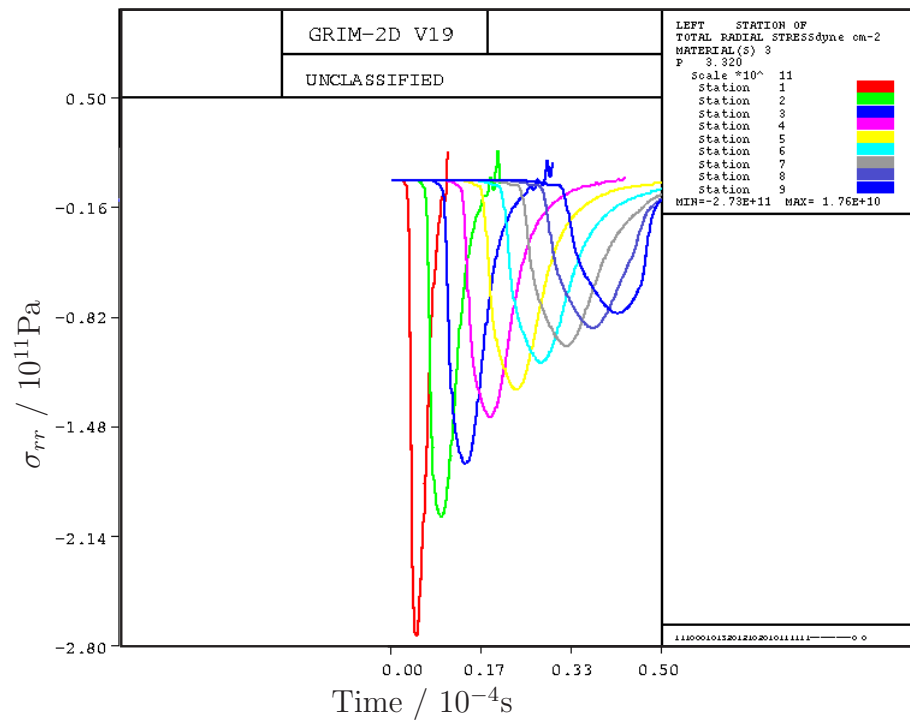
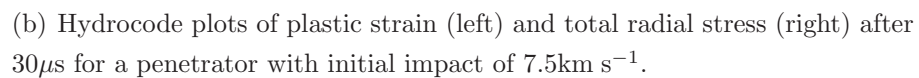
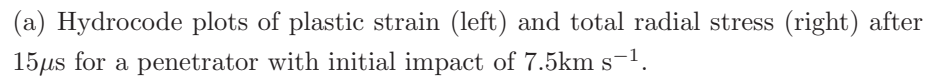
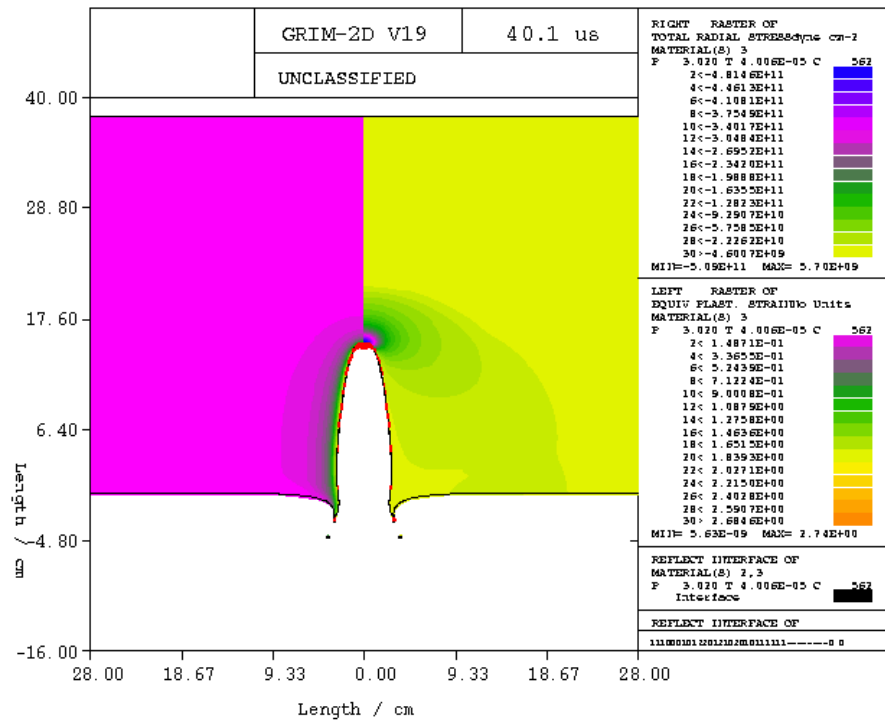
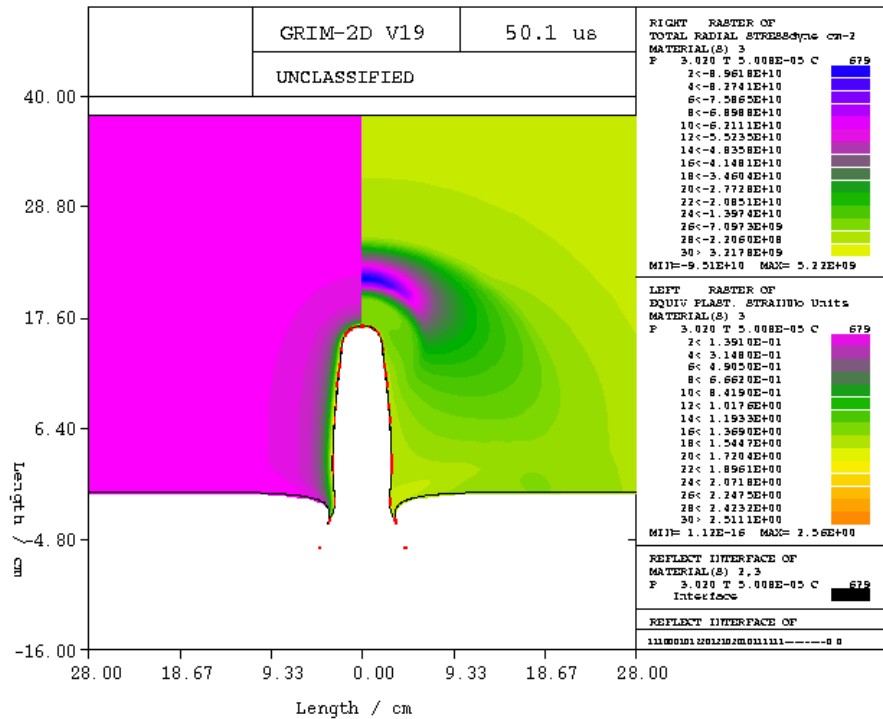


Figure 8.29: A plot showing the distribution of σ_{rr} as a function of time for stations 1 to 10 in the target. The initial velocity of the jet is 7.5 km s^{-1} , and its position can be tracked via Fig. 8.30.





(c) Hydrocode plots of plastic strain (left) and total radial stress (right) after $40.1\mu\text{s}$ for a penetrator with initial impact of 7.5km s^{-1} .



(d) Hydrocode plots of plastic strain (left) and total radial stress (right) after $50.1\mu\text{s}$ for a penetrator with initial impact of 7.5km s^{-1} .

Figure 8.30: Four plots showing the time-evolution plastic strain and total radial stress for transonic penetration. Observe the compressive stress-wave moving ahead of the penetration.

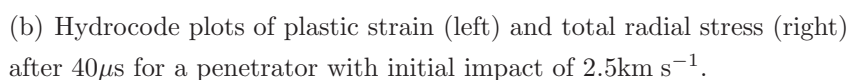
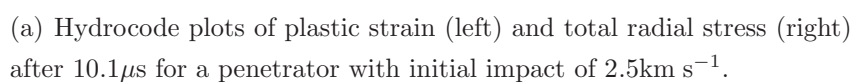
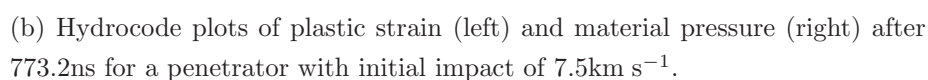
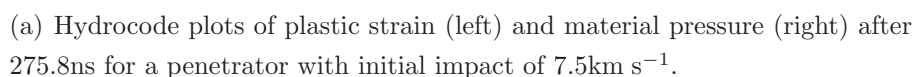


Figure 8.31: Two plots of plastic strain and total radial stress for a lower impact velocity. The white regions in the pressure plots represent negative pressure (compressive waves). Note that these waves propagate ahead of the tip even at the early stages of penetration.



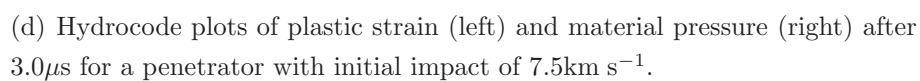
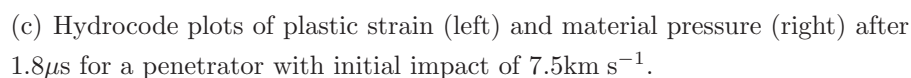
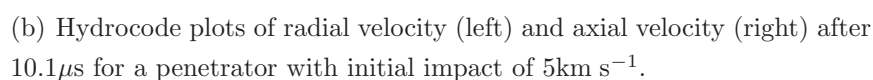
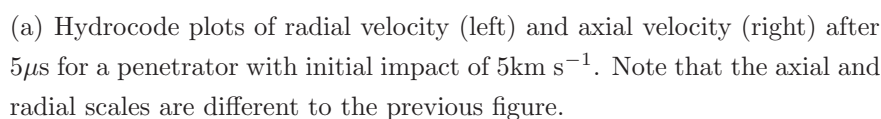


Figure 8.32: Four plots showing plastic strain and material pressure during the early stages of penetration. These results were run on the finer grid.



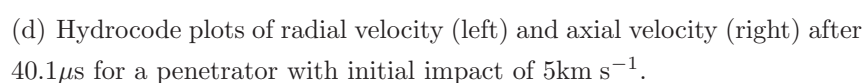
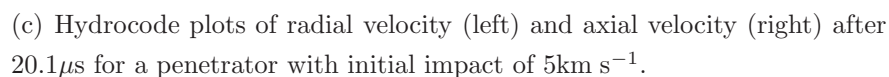


Figure 8.33: Four plots showing the evolution of radial and axial velocity components.

8.5.2 Analysis of hydrocode results

We start by comparing Fig. 8.29 and Fig. 8.30. The former shows values of σ_{rr} taken at the fixed stations⁴ near the edge of the cavity, as described in Fig. 8.28, whereas the latter figure depicts the progress of penetration and the effect of the jet on the distribution of σ_{rr} in the bulk. After approximately $40\mu\text{s}$, we observe that all of the jet is used up and so the penetration has significantly slowed down. It is at this point when a compressive stress-wave propagates into the bulk of the target. Recalling parameter values from Table 3.1 and the (good) Birkhoff estimate from §2.1.1, it is not surprising that there is no wave propagation ahead of the tip until it slows significantly, as the penetration speed is greater than the shear wave speed. Similar behaviour is exhibited by a jet with impact velocity of 10km s^{-1} (supersonic penetration).

The behaviour of σ_{rr} at the individual stations in Fig. 8.29 is also as one might expect: each station exhibits a large peak in stress as the jet nears it, with the amplitude of the peaks decreasing monotonically the deeper the penetration. Note that the jet has just run out at $40\mu\text{s}$. Hence, the amplitude of σ_{rr} at station 9 is a result of the compressive stress wave emanated from the tip.

The right-hand plots in the sequence of figures in Fig. 8.30 show a measure of the plastic strain as the penetration progresses. Clearly, the plastic strain is up to an order of magnitude greater in a region local to the cavity. The width of this region is comparable to the width of the jet. Further, there is nonzero plastic strain extending out a few cavity radii from the cavity. This strain is significantly smaller. We must remember that, even if there is a nonzero plastic strain in a region, it does not mean that there is plastic flow (see Chapter 5), and so we could interpret this some of this region as plasticised material with residual stresses (*c.f.* §6.1). Again, very similar behaviour is demonstrated by a jet with impact velocity of 10km s^{-1} .

The final observation from Fig. 8.30 is concerning the shape of the cavity. As well as seeing evidence of spall from the rear of the cavity, we observe that the hydrocodes predict a travelling-wave profile of the crater, where the radius of the cavity is at a minimum at the tip, increasing to a slight bulge as z decreases, then decreasing again as we approach the rear of the cavity. When the jet has been used up, the cavity becomes more cylindrical.

In contrast to the transonic penetration, Fig. 8.31 shows two plots of plastic strain and material pressure for a jet with impact velocity of 2.5km s^{-1} . The Birkhoff estimate for penetration velocity is thus approximately 1.25km s^{-1} . This is below the sound speed. Hence, there is a marked difference in the wave propagation, namely that waves propagate ahead of the tip before the jet is used up. Again, the negative material pressure tells us

⁴Lagrangian stations can also be used in the hydrocodes.

that the waves are compressive in nature. The left-hand plot of plastic strain has a very similar geometry to the transonic case, though has a smaller region of nonzero plastic strain, the natural result of a lower velocity impact.

The early stages of how the hydrocode interprets the penetration is visualised in Fig. 8.32. This is the precursor to Fig. 8.30. We observe the evolution of the plastic region, the initial stages of the copper jet turning around, and backflow of the target material at the rear of the hole. The white region ahead of the tip corresponds to negative material pressure (a region of compression). This region will stay near the tip until the penetration slows significantly, at which point the compression wave propagates further into the bulk of the target.

Finally, plots of the radial and axial velocity are presented in Fig. 8.33. It is clear that the radial velocity is consistently greater throughout the penetration near the tip of the jet, where the jet has just turned around. Even after this part of the jet has passed, the target still experiences a significant radial component of velocity local to the cavity. The axial component of velocity is more interesting. Firstly, there is a region just in front of the tip, near the z -axis, that has negligible radial velocity and a large positive axial component of velocity. This region moves with the tip, almost like a snow-plough (shown in yellow and green). There is a region of backflow ahead of the ‘green’ region. From plots of plastic strain, which we omit for the 5.0km s^{-1} impact, we see that the upper boundary of this region of backflow corresponds to the boundary of zero and nonzero plastic strain (elastic-plastic boundary), as expected.

8.5.3 Comments

The plots from the previous section gave a very general overview of hydrocode runs. Even with the simplest of geometries and constitutive laws, marked differences between subsonic, transonic and supersonic penetration were apparent, thus indicating the varying importance of inertia in the problem. Furthermore, the stress and velocity profiles near the tip of the jet are non-trivial. In conjunction with the model of Chapter 6, this indicates that it will be hard to develop any analytical formulation that fully represents the underlying physics in the tip region and that a numerical solution based on a good mathematical understanding of the problem is the best way forward for the tip.

Of course, we could present many more results showing the effects of different parameters on penetration. For example, the effects of large standoff, radial drift and particulation of the jet can be modelled by the hydrocode in countless geometries. By doing these tests, comparisons can be made with experimental results to ascertain where the hydrocode performs best and where further analytical work is needed to improve the hydrocode. This work is nontrivial.

Chapter 9

Conclusions

9.1 Summary of thesis

We opened Chapter 1 with a brief historical account of shaped charges, before outlining the mechanics of the formation of a stretching axisymmetric jet. Various applications of this remarkable technology were given, ranging from boring for oil to tree-felling. We then set the stage for the following chapters by detailing equations for elasticity and plasticity, in addition to presenting a paradigm of slender-body theory.

In Chapter 2, we outlined the classic two-dimensional Birkhoff hydrodynamic jet-fluid impact model, before considering hydrodynamic models with finite confinement for both continuous and particulated jets. We noted that these models were a good first approximation, but did not fully represent the true physical processes involved. We moved on to consider rock mining via a high-velocity water jet as an analogy, before discussing more realistic models from solid mechanics. Initially, we illustrated some basic crater-expansion models and then gave a précis of the literature on plastic instability and jet particulation. We closed the chapter by setting out our thesis objectives.

Chapter 3 was concerned with laying the foundations of elastic-plastic equivalent to the hydrodynamic Birkhoff impact model. We motivated an axisymmetric model via experimental results and wrote equations and boundary conditions for the jet, plastic and elastic regions. We then made the key assumption that the cavity is slender, again motivated by experimental evidence. This led us to divide the model into outer, slender and tip regions. Different possible tip scalings were discussed. These were based on both geometrical arguments and on the tip regions individually having a local aspect ratio of unity.

We developed the simplest slender scaling for plastic and jet regions in Chapter 4, namely the scaling in which the radial width of both regions is $\mathcal{O}(\varepsilon)$. We nondimensionalised the equations and expanded the variables in an asymptotic series. This reduced

the dimensionality of the system, eventually resulting in an ‘eikonal’ equation and a novel expression for the matching pressure into the plastic region. We used a Tresca yield condition and Lèvy-Mises flow law in the plastic region, and discussed two possible velocity scales.

The first velocity scale resulted in quasistatic equations of plasticity, enabling us to gain explicit expressions for the stresses and velocities in terms of the unknown free-boundaries. In the inner elastic region, we saw that the effects of inertia were not important, and obtained the classic Lamé solution for the radial displacement and stress, although the position of the elastic-plastic free-boundary was still unknown. The equations for the inner were then reformulated in terms of the Love stress function to facilitate matching with the outer elastic. We firstly considered an outer solution in which the effects of waves were negligible. In performing this matching, we saw that we only needed the stress decaying at infinity to determine enough unknowns in the inner. We then justified the arguments for the full outer problem via reciprocity in §4.2.2 and matched with the inner to obtain plastic stresses and velocities in terms of unknown free-boundaries and an unknown quasi-constant axial plastic velocity. The system would have to be closed via information from the tip. This methodology would have required nontrivial tip-analysis, and so we attempted a travelling-wave formulation. The analysis demonstrated that such a solution was not possible, suggesting that the plastic region must terminate.

We then considered a different plastic velocity scale, in which inertia became important in the plastic region. This resulted in an ill-posed equation, indicating either that the axial plastic velocity \dot{w} is constant or that this latter scaling is incorrect.

We concluded the chapter with the following question and observation:

- How could a linear-elastic-plastic model lead to a finite final cavity-radius, given that the applied pressure returns to zero after penetration?
- Experimental evidence shows that penetrated blocks have bowed after penetration, and that there is zero net weight loss after penetration.

This motivated looking more closely at a model which could ‘lock in’ plastic stresses and displacements, which would keep the cavity open after penetration had terminated. This provided the basis for Chapter 5.

We considered the paradigm two-dimensional, radially-symmetric cavity-expansion problem in some detail in §5.1. We found that if we decomposed the stress into parts for the expansion and contraction, we could derive expressions for residual plastic stresses and displacements, visualised in Fig. 5.4. The key concept was that, once the applied pressure had reached a peak (sufficient to induce plastic flow), decreasing the cavity pressure would cause the material to immediately become elastic again with a locked in (residual) stress,

although we showed that further plastic flow was possible if the initial pressure peak was great enough. Thus the plastic part from expansion was unrecoverable. We looked into the time history of the stresses when cyclically increasing and decreasing the cavity pressure, and found that the system can ‘forget’ elastic changes, as it is recoverable (recall Fig. 5.7). We then developed a hyperelastic equivalent to the modelling, again discovering important residual stresses and displacements. The relevance to shaped-charge penetration of these new ideas was discussed. To close the chapter, we considered a non-radially-symmetric boundary condition on the inner cavity of the gun-barrel, hoping to gain insight into how the plastic material was displaced in the tip. We found a solution for a small perturbation, but concluded that a numerical solution would be required if the θ -dependent part of the cavity boundary-condition was comparable in size to the radial part. We considered an asymmetric model permitting residual stresses in §5.4.4 and outlined a solution procedure. We illustrated interesting solutions to this problem using a finite element formulation. This gave us new insight into the shape of the plasticised-plastic free-boundary.

We posed a model for penetration including the plastic history of the solid in Chapter 6. This model incorporated a non-slender plastic region and extra free-boundaries for the ‘plasticised’ region. Sadly, this model was much more complicated than the slender model of Chapter 4, and would have to be solved numerically. We moved on to consider a mechanism to displace the plastic material in the tip via a squeeze film analogy. We found that a quasistatic plasticity solution was unstable when the squeeze film was under tension horizontally, leading to necking, but when under horizontal compression, we could solve the system. We went on to develop a two-dimensional plastic squeeze film model in intrinsic coordinates. We concluded the chapter by noting that these models only provided us with qualitative behaviour of the target under confinement, and by commenting on plastic mass conservation.

We considered the jet region in the tip in Chapter 7. With scaling ideas from Chapter 3, we modified Peregrine’s filling-flow analysis [67] to develop models for the fluid flow in the tip. Simple filling-flow models between two fixed plates and novel tip conditions showed interesting (albeit academic) solutions. More realistic models were considered in §7.2, where we considered a filling flow impacting a membrane, the latter representing the elasticity of the target. The model divided naturally into four different regions, one each for the incoming jet, outgoing jet, inner filling flow and the large outer region incorporating the tip. A travelling-wave solution was obtained for the system. We then replaced the membrane with a beam (so including stiffness into the model), and again reached a travelling-wave solution. A more general model for the elasticity of the target was considered in §7.4, in which we prescribed a general constitutive law $p = p(H)$ on the boundary between fluid and the solid body. A similarity solution for a particular $p(H)$

ensued. We were easily able to generalise the two-dimensional analysis to axisymmetric coordinates by using global balances rather than using conformal mapping techniques. Again, a similarity solution was derived for a particular constitutive law $p(R)$, and parallels were drawn with the classic equations of shallow-water theory. Finally, we proposed other possible constitutive laws in §7.6, based on the gun-barrel analysis of Chapter 5.

Chapter 8 began with a review of the metallurgical literature on shaped-charge targets. We then presented new results from a microscopic analysis of penetrated blocks provided by *QinetiQ*. We saw key features such as microcracks and damage voids. The former were within a very thin radius from the edge of the cavity, and were often filled with silver. The absence of shear bands was attributed to the specific nature of the steel target. In order to help determine the region of the target that had undergone plastic deformation, we conducted a hardness test on the specimen. This was inconclusive regarding the elastic-plastic boundary. We ended the chapter with a gallery of results from simple hydrocode runs. These illustrated the effects of waves, cavity size, stress state and target velocity for differing impact speeds. In particular, differences in supersonic and subsonic penetration were observed, an issue that is not fully-addressed by the shaped-charge theory.

9.2 Conclusions and discussion

The obvious elastic-plastic analogy to the Birkhoff hydrodynamic penetration model had some problems. We firstly found that the assumption of a slender plastic region was only feasible if the yield stress of the target was suitably low. Matching with the outer elastic problem and the argument of reciprocity told us that inertia is only important locally to the penetration if the axial component of the plastic velocity, \dot{w} is comparable to the axial component of the jet velocity, q_3 . However, analysis of such a regime led to an ill-posed problem, unless $\dot{w} = W$ for some constant W . We can speculate that $\dot{w} \ll q_3$ is realistic as the jet is unlikely to exert significant shear on the plastic region. The failure of a travelling-wave formulation for this parameter regime indicates that the plastic region should really terminate in the slender region or nearer the tip. Furthermore, this linear-elastic-plastic model can not predict the observed bowing in the blocks. We remedied this by considering loading-unloading phenomena in the classic gun-barrel problem. In doing so, we found that residual stresses and displacements were crucial, and so should be included in any elastic-plastic model. A relatively simple modification gave us the hyperelastic-plastic equivalent, exhibiting similar behaviour. Modelling the target as hyperelastic now furnishes us with a mechanism to generate finite residual displacements (rather than the infinitesimal displacements from linear elasticity), thus giving us two alternative methodologies to generate a cavity, namely a sufficiently large plastic region

(see §5.3), or finite displacement elasticity. Consideration of an asymmetric boundary condition to the gun-barrel inflation demonstrated exciting behaviour in the stress field, emphasising the importance of dividing the material into plastic, elastic, and plasticised regions. From the complicated stress field that follows, we can conclude that solving a full elastic-plastic model in this way must be done numerically.

A squeeze-film analogy will never be very accurate as the thin elastic-plastic layer is always confined by (and pinned to) a surrounding elastic medium. However, we can deduce that the confinement of the target acts against the pressure in the jet when creating a plastic region. The analogy also highlighted a problem with plastic mass conservation. The key observation is that, irrespective of the particular details of the model, if there is a finite plastic region and a hole is opened up, then either the plastic material has been compressed or there is a finite displacement in the elastic region.

Geometric ideas of slender *jet* scalings suggested tip scalings in the jet. Modelling the rapid turnaround of the jet as a filling flow gave us insight into the fluid flow, and toy models gave us ideas for the shape of the target-fluid boundary in both the two-dimensional and axisymmetric case.

Finally, analysis of the microstructure of a penetrated block was extremely revealing, yet perplexing. From the microscopic pictures, we can see numerous effects that aren't included in our modelling, such as microcracks filled with silver and the possibility of shear bands (in the literature). However, it is important to understand the key features, such as the cavity radius and bowing blocks, before incorporating the finer points. The novel model described in §6 is successful in incorporating many features that cannot be explained by existing models.

9.3 Future work

Throughout the thesis, we have illustrated various important, yet unresolved, issues. Firstly, the slender analysis should be redone with different constitutive laws. For example, the jet could be modelled as a shear-thinning fluid or as a plastic, and various plasticity models, such as the Zerilli-Armstrong model (1.41) should be investigated. Temperature effects should also be considered. Although it is likely that most of these will demand a numerical resolution, it is necessary to compare and contrast the different solutions in order to identify the important parameters and processes.

Inertia was of varying importance for the slender-body model and it is probable that it plays a significant role in the global response of the target. Its influence is likely to depend on whether the penetration is subsonic or supersonic. This is currently being investigated [57]. Compressibility of the jet should also be considered. This can lead to a complex

array of shock waves in the jet on impact. A relatively simple paradigm model for inertia and the ensuing elastic waves is to consider the gun-barrel problem with inertial terms in the force balance equations. This problem is outlined in Appendix F, and results in a novel free-boundary problem that remains to be solved numerically.

Another numerical solution is required for the full elastic-plastic model incorporating residual stresses and displacements in §6.1. This is a significant amount of work, although the FEMLAB calculations in §5.4.4 indicate that it is likely to be very illuminating. The simpler model mentioned in §5.3 also requires completion – this may represent the flow in a slender region far from the tip, but is unlikely to be realistic nearer the tip where there is a considerable axial component of the plastic velocity.

An exciting new avenue of research is to couple the filling-flow model for the jet (§7.5.1) with the elastic-plastic pressure-pulse model of §5.3. Like Barnea and Sela's model [4], it is an elastic-plastic model that divides the target up into two-dimensional slices. However, it has two main advantages: firstly, that it incorporates a more realistic three-dimensional model of the jet, thus replacing the *ad hoc* approach taken by Barnea and Sela; secondly, the all-important effects of residual stresses and displacements are included. This model will have to be solved numerically.

We considered the response of a two-dimensional target via a squeeze-film analogy. We could easily modify this analysis to consider an axisymmetric squeeze film. Again, we expect that this analysis would only give qualitative results, although could result in a novel flow-field.

The metallurgical analysis of §8.2 displayed a variety of microstructural phenomena. It demonstrated the prevalence of cracks, indicating that a model for fracture needs to be included for a complete model of penetration (although this is likely to be a less important mechanism, a result of shock waves). Repeating such metallurgical analysis for firings with different jet and target materials at various points throughout penetration for a range of impact velocities would be very beneficial. In particular, metallurgical tests highlighting differences between a supersonic and subsonic penetration velocity are crucial to enable a full understanding of the problem. Furthermore, our simple metallurgical tests should be refined – better tests more appropriate for a steel that has gone through several phase transitions are likely to yield superior results.

There are countless many other aspects of shaped-charge penetration that could be considered, such as particulation of the jet. One possible analogy can be drawn with the particulated water-jets (§2.1.2). Indeed, it may be possible to control the particulation via a corrugated liner; this remains to be investigated. Furthermore, the cyclic loading-unloading phenomena outlined in §5.1.7 could be of vital importance for such jets. We could also attempt to model new ideas such as lubricated penetration, or the effects of

various armours, such as reactive armour¹ or electric reactive armour², or the counter-measures taken against such armours, namely a tandem-warhead³. It is probable that any of these is possible to model in isolation, but that constructing an analytical model to cover all scenarios is unfeasible.

¹This consists of tiles of explosive sandwiched between two metal plates on, say, a tank. When a charge approaches, the explosive is detonated and one of the plates flies off into the path of the charge. Thus new material is continuously being fed into the path of the shaped charge, inhibiting penetration.

²This armour consists of two charged plates separated by an insulator. When the shaped charge penetrates, it ‘completes the circuit’ and so the tip ‘vaporises’.

³This warhead is made up of two shaped charges, fired in quick succession.

Appendix A

Stress and strain components in cylindrical polars for linear elasticity

Recall that the Cauchy strain tensor for linear elasticity is defined by

$$\varepsilon_{ij} = \frac{1}{2} \left(\frac{\partial u_i}{\partial x_j} + \frac{\partial u_j}{\partial x_i} \right). \quad (\text{A.1})$$

Writing the (r, θ, z) components of the displacement in cylindrical polars as (u, v, w) , respectively, the tensor becomes

$$\epsilon_{rr} = \frac{\partial u}{\partial r}, \quad (\text{A.2})$$

$$\epsilon_{\theta\theta} = \frac{1}{r} \frac{\partial v}{\partial \theta} + \frac{u}{r}, \quad (\text{A.3})$$

$$\epsilon_{zz} = \frac{\partial w}{\partial z}, \quad (\text{A.4})$$

$$\epsilon_{r\theta} = \frac{1}{2} \left(r \frac{\partial}{\partial r} \left(\frac{v}{r} \right) + \frac{1}{r} \frac{\partial u}{\partial \theta} \right), \quad (\text{A.5})$$

$$\epsilon_{z\theta} = \frac{1}{2} \left(\frac{1}{r} \frac{\partial w}{\partial \theta} + \frac{\partial v}{\partial z} \right), \quad (\text{A.6})$$

$$\epsilon_{rz} = \frac{1}{2} \left(\frac{\partial w}{\partial r} + \frac{\partial u}{\partial z} \right). \quad (\text{A.7})$$

For a homogenous, isotropic elastic material, the components of the stress tensor are

$$\sigma_{ij} = 2\mu\varepsilon_{ij} + \varepsilon_{kk}\lambda\delta_{ij}. \quad (\text{A.8})$$

Hence, the general components of stress in cylindrical polars are

$$\sigma_{rr} = (\lambda + 2\mu) \frac{\partial u}{\partial r} + \lambda \left(\frac{u}{r} + \frac{1}{r} \frac{\partial v}{\partial \theta} \right) + \lambda \frac{\partial w}{\partial z}, \quad (\text{A.9})$$

$$\sigma_{\theta\theta} = \lambda \frac{\partial u}{\partial r} + (\lambda + 2\mu) \left(\frac{u}{r} + \frac{1}{r} \frac{\partial v}{\partial \theta} \right) + \lambda \frac{\partial w}{\partial z}, \quad (\text{A.10})$$

$$\sigma_{zz} = \lambda \frac{\partial u}{\partial r} + \lambda \left(\frac{u}{r} + \frac{1}{r} \frac{\partial v}{\partial \theta} \right) + (\lambda + 2\mu) \frac{\partial w}{\partial z}, \quad (\text{A.11})$$

$$\sigma_{rz} = \mu \left(\frac{\partial u}{\partial z} + \frac{\partial w}{\partial r} \right), \quad (\text{A.12})$$

$$\sigma_{r\theta} = \mu \left(r \frac{\partial}{\partial r} \left(\frac{v}{r} \right) + \frac{1}{r} \frac{\partial u}{\partial \theta} \right), \quad (\text{A.13})$$

$$\sigma_{z\theta} = \mu \left(\frac{1}{r} \frac{\partial w}{\partial \theta} + \frac{\partial v}{\partial z} \right). \quad (\text{A.14})$$

With radial symmetry, these trivially simplify to

$$\sigma_{rr} = (\lambda + 2\mu) \frac{\partial u}{\partial r} + \lambda \frac{u}{r} + \lambda \frac{\partial w}{\partial z}, \quad (\text{A.15})$$

$$\sigma_{\theta\theta} = \lambda \frac{\partial u}{\partial r} + (\lambda + 2\mu) \frac{u}{r} + \lambda \frac{\partial w}{\partial z}, \quad (\text{A.16})$$

$$\sigma_{zz} = \lambda \frac{\partial u}{\partial r} + \lambda \frac{u}{r} + (\lambda + 2\mu) \frac{\partial w}{\partial z}, \quad (\text{A.17})$$

$$\sigma_{rz} = \mu \left(\frac{\partial u}{\partial z} + \frac{\partial w}{\partial r} \right), \quad (\text{A.18})$$

$$\sigma_{r\theta} = \sigma_{z\theta} = 0. \quad (\text{A.19})$$

Appendix B

Equations of small motion in cylindrical polars in an isotropic medium with no external body forces

The three components of Navier's equations in cylindrical polars that include inertial effects are

$$\frac{\partial \sigma_{rr}}{\partial r} + \frac{1}{r} \frac{\partial \sigma_{r\theta}}{\partial \theta} + \frac{\partial \sigma_{rz}}{\partial z} + \frac{\sigma_{rr} - \sigma_{\theta\theta}}{r} = \rho \frac{\partial^2 u}{\partial t^2}, \quad (\text{B.1})$$

$$\frac{\partial \sigma_{r\theta}}{\partial r} + \frac{1}{r} \frac{\partial \sigma_{\theta\theta}}{\partial \theta} + \frac{\partial \sigma_{z\theta}}{\partial z} + \frac{2\sigma_{r\theta}}{r} = \rho \frac{\partial^2 v}{\partial t^2}, \quad (\text{B.2})$$

$$\frac{\partial \sigma_{rz}}{\partial r} + \frac{1}{r} \frac{\partial \sigma_{\theta z}}{\partial \theta} + \frac{\partial \sigma_{zz}}{\partial z} + \frac{\sigma_{rz}}{r} = \rho \frac{\partial^2 w}{\partial t^2}. \quad (\text{B.3})$$

The equations in general curvilinear coordinates are given by Love [49].

Appendix C

Displacement and stress components in terms of the Love stress function $\chi(r, z, t)$ in cylindrical polars

The components of stress and displacement can be written in terms of the Love Stress function, χ , for a solid of revolution strained symmetrically by forces applied at its surface. The derivation of these components is non-trivial, though is performed by Love [49]. He finds that the stress function must satisfy

$$\nabla^4 \chi = 0, \quad (\text{C.1})$$

and that the components of stress and displacement are given in terms of χ as

$$u = -\frac{1}{2\mu} \frac{\partial^2 \chi}{\partial r \partial z} = -\frac{1+\nu}{E} \frac{\partial^2 \chi}{\partial r \partial z}, \quad (\text{C.2})$$

$$w = \frac{1}{2\mu} \left(\frac{\mu}{\lambda + \mu} \nabla^2 \chi + \frac{\partial^2 \chi}{\partial r^2} + \frac{1}{r} \frac{\partial \chi}{\partial r} \right) = \frac{1+\nu}{E} \left((1-2\nu) \nabla^2 \chi + \frac{\partial^2 \chi}{\partial r^2} + \frac{1}{r} \frac{\partial \chi}{\partial r} \right), \quad (\text{C.3})$$

$$\sigma_{rr} = \frac{\partial}{\partial z} \left(\frac{\lambda}{2(\lambda + \mu)} \nabla^2 \chi - \frac{\partial^2 \chi}{\partial r^2} \right) = \frac{\partial}{\partial z} \left(\nu \nabla^2 \chi - \frac{\partial^2 \chi}{\partial r^2} \right), \quad (\text{C.4})$$

$$\sigma_{\theta\theta} = \frac{\partial}{\partial z} \left(\frac{\lambda}{2(\lambda + \mu)} \nabla^2 \chi - \frac{1}{r} \frac{\partial \chi}{\partial r} \right) = \frac{\partial}{\partial z} \left(\nu \nabla^2 \chi - \frac{1}{r} \frac{\partial \chi}{\partial r} \right), \quad (\text{C.5})$$

$$\sigma_{zz} = \frac{\partial}{\partial z} \left(\frac{3\lambda + 4\mu}{2(\lambda + \mu)} \nabla^2 \chi - \frac{\partial^2 \chi}{\partial z^2} \right) = \frac{\partial}{\partial z} \left((2-\nu) \nabla^2 \chi - \frac{\partial^2 \chi}{\partial z^2} \right), \quad (\text{C.6})$$

$$\sigma_{rz} = \frac{\partial}{\partial r} \left(\frac{\lambda + 2\mu}{2(\lambda + \mu)} \nabla^2 \chi - \frac{\partial^2 \chi}{\partial z^2} \right) = \frac{\partial}{\partial r} \left((1-\nu) \nabla^2 \chi - \frac{\partial^2 \chi}{\partial z^2} \right). \quad (\text{C.7})$$

Appendix D

The Navier-Stokes Equations

The most famous equations to model the flow of a viscous fluid are the *Navier-Stokes* equations. Assuming incompressibility and constant kinematic viscosity μ , the (isothermal) equations for the flow of the fluid can be derived via conservation of momentum (see *e.g.* [59]), and are given by

$$\rho \left(\frac{\partial}{\partial t} + (\mathbf{q} \cdot \nabla) \right) \mathbf{q} = -\nabla p + \mu \nabla^2 \mathbf{q}, \quad (\text{D.1})$$

where \mathbf{q} is the fluid velocity. This can be easily nondimensionalised by scaling all lengths with some typical lengthscale L , components of velocity with a velocity scale U , and pressure with ρU^2 to reach

$$\left(\frac{\partial}{\partial t} + (\mathbf{q} \cdot \nabla) \right) \mathbf{q} = -\nabla p + \frac{1}{\mathcal{R}} \nabla^2 \mathbf{q}. \quad (\text{D.2})$$

The nondimensional parameter \mathcal{R} is the all-important *Reynold's number*, defined by

$$\mathcal{R} = \frac{\rho U L}{\mu}. \quad (\text{D.3})$$

Clearly, if this parameter is large, we can expect that inviscid fluid flow will generally be a good approximation to the flow.

Appendix E

Metallurgical data for hardness testing

Table E.1: Data showing distance from the cavity, x , dimensions of the indents (Δx and Δy) and the corresponding Vickers Hardness (HV). Some indents were unreadable owing to the local microstructure of the metal; this accounts for odd numbering in the table.

x /mm	Δx /mm	Δy /mm	HV /kg mm ⁻²	x /mm	Δx /mm	Δy /mm	HV /kg mm ⁻²
0.10	1.173×10^{-2}	1.403×10^{-2}	558.7	0.15	1.369×10^{-2}	1.438×10^{-2}	470.9
0.20	1.288×10^{-2}	1.564×10^{-2}	455.8	0.25	1.346×10^{-2}	1.369×10^{-2}	503.3
0.30	1.438×10^{-2}	1.633×10^{-2}	393.2	0.35	1.369×10^{-2}	1.415×10^{-2}	478.7
0.40	1.288×10^{-2}	1.311×10^{-2}	548.9	0.65	1.288×10^{-2}	1.484×10^{-2}	482.7
0.50	1.369×10^{-2}	1.323×10^{-2}	512.0	0.75	1.495×10^{-2}	1.461×10^{-2}	424.4
0.60	1.323×10^{-2}	1.231×10^{-2}	568.8	0.85	1.541×10^{-2}	1.656×10^{-2}	362.7
0.70	1.392×10^{-2}	1.334×10^{-2}	499.1	0.95	1.599×10^{-2}	1.507×10^{-2}	384.5
0.80	1.265×10^{-2}	1.300×10^{-2}	563.7	1.05	1.449×10^{-2}	1.622×10^{-2}	393.2
0.90	1.415×10^{-2}	1.461×10^{-2}	448.5	1.15	1.495×10^{-2}	1.449×10^{-2}	427.8
1.00	1.553×10^{-2}	1.622×10^{-2}	368.0	1.25	1.564×10^{-2}	1.541×10^{-2}	384.5
1.10	1.564×10^{-2}	1.668×10^{-2}	355.0	1.35	1.518×10^{-2}	1.518×10^{-2}	402.2
1.20	1.530×10^{-2}	1.622×10^{-2}	373.4	1.45	1.254×10^{-2}	1.587×10^{-2}	459.5
1.30	1.668×10^{-2}	1.748×10^{-2}	317.8	1.55	1.553×10^{-2}	1.587×10^{-2}	376.1
1.40	1.656×10^{-2}	1.576×10^{-2}	355.0	1.65	1.415×10^{-2}	1.622×10^{-2}	402.2
1.50	1.771×10^{-2}	1.645×10^{-2}	317.8	1.75	1.668×10^{-2}	1.610×10^{-2}	345.1
1.60	1.737×10^{-2}	1.760×10^{-2}	303.3	1.85	1.530×10^{-2}	1.564×10^{-2}	387.4
1.70	1.610×10^{-2}	1.668×10^{-2}	345.1	1.95	1.449×10^{-2}	1.357×10^{-2}	470.9
1.80	1.725×10^{-2}	1.679×10^{-2}	320.0	2.05	1.599×10^{-2}	1.553×10^{-2}	373.4
1.90	1.564×10^{-2}	1.691×10^{-2}	350.0	2.15	1.633×10^{-2}	1.691×10^{-2}	335.6
2.10	1.461×10^{-2}	1.622×10^{-2}	390.3	2.25	1.679×10^{-2}	1.760×10^{-2}	313.6
2.20	1.725×10^{-2}	1.691×10^{-2}	317.8	2.35	1.633×10^{-2}	1.564×10^{-2}	362.7
2.30	1.691×10^{-2}	1.668×10^{-2}	328.8	2.45	1.691×10^{-2}	1.610×10^{-2}	340.3
2.40	1.530×10^{-2}	1.518×10^{-2}	399.2	2.55	1.668×10^{-2}	1.702×10^{-2}	326.5
2.50	1.587×10^{-2}	1.553×10^{-2}	376.1	2.65	1.668×10^{-2}	1.645×10^{-2}	338.0
2.60	1.553×10^{-2}	1.587×10^{-2}	376.1	2.75	1.599×10^{-2}	1.702×10^{-2}	340.3

continued on next page

<i>continued from previous page</i>							
x /mm	Δx /mm	Δy /mm	HV /kg mm ⁻²	x /mm	Δx /mm	Δy /mm	HV /kg mm ⁻²
2.70	1.656×10^{-2}	1.645×10^{-2}	340.3	2.85	1.576×10^{-2}	1.702×10^{-2}	345.1
2.80	1.564×10^{-2}	1.576×10^{-2}	376.1	2.95	1.576×10^{-2}	1.656×10^{-2}	355.0
2.90	1.541×10^{-2}	1.599×10^{-2}	376.1	3.15	1.633×10^{-2}	1.771×10^{-2}	320.0
3.00	1.507×10^{-2}	1.610×10^{-2}	381.7	3.35	1.656×10^{-2}	1.633×10^{-2}	342.7
3.20	1.564×10^{-2}	1.714×10^{-2}	345.1	3.55	1.576×10^{-2}	1.645×10^{-2}	357.6
3.40	1.553×10^{-2}	1.794×10^{-2}	331.0	3.75	1.599×10^{-2}	1.530×10^{-2}	378.9
3.60	1.633×10^{-2}	1.668×10^{-2}	340.3	3.95	1.645×10^{-2}	1.576×10^{-2}	357.6
3.80	1.587×10^{-2}	1.702×10^{-2}	342.7	4.15	1.541×10^{-2}	1.472×10^{-2}	408.4
4.00	1.587×10^{-2}	1.783×10^{-2}	326.5	4.35	1.656×10^{-2}	1.771×10^{-2}	315.7
4.20	1.564×10^{-2}	1.495×10^{-2}	396.2	4.55	1.518×10^{-2}	1.507×10^{-2}	405.3
4.40	1.691×10^{-2}	1.714×10^{-2}	320.0	4.75	1.530×10^{-2}	1.564×10^{-2}	387.4
4.60	1.622×10^{-2}	1.645×10^{-2}	347.6	4.95	1.610×10^{-2}	1.725×10^{-2}	333.3
4.80	1.679×10^{-2}	1.610×10^{-2}	342.7	5.15	1.760×10^{-2}	1.702×10^{-2}	309.4
5.00	1.714×10^{-2}	1.645×10^{-2}	328.8	5.35	1.783×10^{-2}	1.656×10^{-2}	313.6
5.20	1.576×10^{-2}	1.576×10^{-2}	373.4	5.55	1.725×10^{-2}	1.679×10^{-2}	320.0
5.40	1.599×10^{-2}	1.564×10^{-2}	370.7	5.75	1.668×10^{-2}	1.806×10^{-2}	307.4
5.60	1.449×10^{-2}	1.392×10^{-2}	459.5	5.95	1.656×10^{-2}	1.691×10^{-2}	331.0
5.80	1.484×10^{-2}	1.507×10^{-2}	414.7	6.15	1.645×10^{-2}	1.714×10^{-2}	328.8
6.00	1.587×10^{-2}	1.541×10^{-2}	378.9	6.35	1.576×10^{-2}	1.679×10^{-2}	350.0
6.20	1.576×10^{-2}	1.576×10^{-2}	373.4	6.55	1.622×10^{-2}	1.576×10^{-2}	362.7
6.40	1.599×10^{-2}	1.633×10^{-2}	355.0	6.75	1.610×10^{-2}	1.691×10^{-2}	340.3
6.60	1.725×10^{-2}	1.737×10^{-2}	309.4	6.95	1.783×10^{-2}	1.714×10^{-2}	303.3
6.80	1.691×10^{-2}	1.679×10^{-2}	326.5	7.15	1.702×10^{-2}	1.702×10^{-2}	320.0
7.00	1.714×10^{-2}	1.633×10^{-2}	331.0	7.35	1.656×10^{-2}	1.610×10^{-2}	347.6
7.20	1.656×10^{-2}	1.760×10^{-2}	317.8	7.55	1.587×10^{-2}	1.668×10^{-2}	350.0
7.40	1.725×10^{-2}	1.679×10^{-2}	320.0	7.75	1.599×10^{-2}	1.599×10^{-2}	362.7
7.60	1.737×10^{-2}	1.679×10^{-2}	317.8	7.95	1.622×10^{-2}	1.610×10^{-2}	355.0
7.80	1.702×10^{-2}	1.679×10^{-2}	324.3	8.45	1.622×10^{-2}	1.668×10^{-2}	342.7
8.00	1.783×10^{-2}	1.748×10^{-2}	297.4	8.95	1.725×10^{-2}	1.760×10^{-2}	305.3
8.50	1.725×10^{-2}	1.679×10^{-2}	320.0	9.45	1.725×10^{-2}	1.702×10^{-2}	315.7
9.00	1.679×10^{-2}	1.599×10^{-2}	345.1	9.95	1.829×10^{-2}	1.771×10^{-2}	286.1
9.50	1.679×10^{-2}	1.714×10^{-2}	322.1	10.45	1.737×10^{-2}	1.760×10^{-2}	303.3
10.00	1.794×10^{-2}	1.748×10^{-2}	295.5	10.95	1.691×10^{-2}	1.633×10^{-2}	335.6
10.50	1.714×10^{-2}	1.645×10^{-2}	328.8	11.45	1.714×10^{-2}	1.656×10^{-2}	326.5
11.00	1.760×10^{-2}	1.702×10^{-2}	309.4	11.95	1.656×10^{-2}	1.668×10^{-2}	335.6
11.50	1.817×10^{-2}	1.748×10^{-2}	291.7	12.45	1.725×10^{-2}	1.748×10^{-2}	307.4
12.00	1.679×10^{-2}	1.668×10^{-2}	331.0	18.00	1.599×10^{-2}	1.737×10^{-2}	333.3
12.50	1.714×10^{-2}	1.748×10^{-2}	309.4				
13.00	1.771×10^{-2}	1.691×10^{-2}	309.4				
18.00	1.783×10^{-2}	1.714×10^{-2}	303.3				

Appendix F

Inertial elastic-plastic gun-barrel expansion

In this appendix, we again consider the elastic-plastic expansion of a gun-barrel. The key difference is that we now include inertial effects into the model, thus permitting waves. We start by increasing the cavity pressure inside the gun-barrel, assuming infinitesimal elastic displacement and a monotonically-increasing pressure profile $P(t)$.

F.1 Plastic region

The equations for the plastic region are the yield condition, a radial force balance (including inertia), and the associated flow law. These are written, respectively,

$$\sigma_{\theta\theta} - \sigma_{rr} = \sigma_Y, \quad (\text{F.1})$$

$$\frac{\partial \sigma_{rr}}{\partial r} + \frac{\sigma_{rr} - \sigma_{\theta\theta}}{r} = \rho \frac{\partial \dot{u}}{\partial t} \quad (\text{F.2})$$

$$\sigma'_{ij} = \Lambda \dot{\epsilon}_{ij}, \quad (\text{F.3})$$

where ρ is the density of the material and the sign of the yield condition is chosen with the benefit of hindsight. The inner boundary condition is unchanged, and is written

$$\sigma_{rr}(a) = -P. \quad (\text{F.4})$$

We now nondimensionalise the equations, scaling $\boldsymbol{\sigma} \sim \sigma_Y$, $P \sim \sigma_Y$, $r \sim a$, $\mathbf{u} \sim a$, $s(t) \sim a$ and $t \sim \frac{a}{c}$, where $s(t)$ is the position of the elastic-plastic boundary, and c is the longitudinal elastic wave-speed given by $c^2 = (\lambda + 2\mu)/\rho$. Equation (F.3) gives incompressibility, so that, now writing all variables nondimensionally,

$$\frac{\partial \dot{u}}{\partial r} + \frac{\dot{u}}{r} = 0. \quad (\text{F.5})$$

Hence,

$$\dot{u} = \frac{D(t)}{r}, \quad (\text{F.6})$$

for some unknown $D(t)$. The nondimensional stresses satisfy

$$\sigma_{rr} = -P(t) + \left(\frac{\lambda + 2\mu}{\sigma_Y} \dot{D}(t) + 1 \right) \log r, \quad (\text{F.7})$$

$$\sigma_{\theta\theta} = 1 - P(t) + \left(\frac{\lambda + 2\mu}{\sigma_Y} \dot{D}(t) + 1 \right) \log r. \quad (\text{F.8})$$

F.2 Elastic region

The nondimensional elastic-stresses are now given by

$$\sigma_{rr} = \left(\frac{\lambda + 2\mu}{\sigma_Y} \right) \frac{\partial u}{\partial r} + \left(\frac{\lambda}{\sigma_Y} \right) \frac{u}{r}, \quad (\text{F.9})$$

$$\sigma_{\theta\theta} = \left(\frac{\lambda}{\sigma_Y} \right) \frac{\partial u}{\partial r} + \left(\frac{\lambda + 2\mu}{\sigma_Y} \right) \frac{u}{r}. \quad (\text{F.10})$$

The force balance equation becomes

$$\frac{\partial^2 u}{\partial r^2} + \frac{\partial}{\partial r} \left(\frac{u}{r} \right) = \frac{\partial^2 u}{\partial t^2}. \quad (\text{F.11})$$

We now introduce the Lamé potential ϕ by writing $u = \frac{\partial \phi}{\partial r}$. Hence, (F.11) is transformed into the two-dimensional wave-equation with radial symmetry, namely

$$\frac{\partial^2 \phi}{\partial r^2} + \frac{1}{r} \frac{\partial \phi}{\partial r} = \frac{\partial^2 \phi}{\partial t^2}. \quad (\text{F.12})$$

As usual, a boundary condition on the stress is that $\sigma \rightarrow 0$ at infinity.

F.3 Matching conditions

As in the gun-barrel expansion without inertia, the (nondimensional) conditions on the elastic-plastic boundary $r = s(t)$ are continuity of σ_{rr} , continuity of \dot{u} , and the yield condition $\sigma_{\theta\theta} - \sigma_{rr} = 1$. Hence

$$\left(\left(\frac{\lambda + 2\mu}{\sigma_Y} \right) \frac{\partial u}{\partial r} + \frac{\lambda}{\sigma_Y} \frac{u}{s(t)} \right) \Big|_{r=s(t)} = -P(t) + \left(\frac{\lambda + 2\mu}{\sigma_Y} \dot{D}(t) + 1 \right) \log s(t), \quad (\text{F.13})$$

$$\frac{2\mu}{\sigma_Y} \left(\frac{u}{s(t)} - \frac{\partial u}{\partial r} \right) \Big|_{r=s(t)} = 1, \quad (\text{F.14})$$

$$\frac{\partial u}{\partial t} \Big|_{r=s(t)} = \frac{D(t)}{s(t)}. \quad (\text{F.15})$$

These conditions can easily be rewritten in terms of ϕ , and the resultant system remains to be solved numerically.

Bibliography

- [1] M. ABRAMOWITZ AND I. STEGUN. *Handbook of Mathematical Functions*. Dover Publications, 1965.
- [2] D.J. ACHESON. *Elementary Fluid Dynamics*. Clarendon Press, Oxford, 1990.
- [3] A.J. ARLOW AND J.P. CURTIS. Analytical computer models for the design and evaluation of shaped charges. In *Proc. 15th Int. Symp. Ballistics, Israel*, **2**, 1995.
- [4] N. BARNEA AND N. SELA. Why do shaped charges cease penetrating? *Proc. 16th Int. Symp. Ballistics, San Francisco*, pages 349–357, 1996.
- [5] M.L. BAUCCIO, editor. *ASM Metals Reference Book*. American Society of Metals, 3rd edition, 1993.
- [6] G. BIRKHOFF, D.P. MACDOUGALL, E.M. PUGH, AND G.I. TAYLOR. Explosives with lined cavities. *J. Appl. Phys.*, **19**(6), 1948.
- [7] G. BIRKHOFF AND E.H. ZARANTONELLO. *Jets, Wakes and Cavities*. New York: Academic Press, 1957.
- [8] J.G.A. BITTER. A study of erosion phenomena - Part I. *Wear*, **6**:5–21, 1963.
- [9] B. BOURNE, K.G. COWAN, AND J.P. CURTIS. Shaped charge warheads containing low melt energy metal liners. *Proc. 19th Int. Symp. Ballistics, Switzerland*, pages 583–589, 2001.
- [10] J.H. BRUNTON. High speed liquid impact. *Philos. Trans. R. Soc. London Ser. A*, **260**(1110):79–85, July 1966.
- [11] T.E. CAYWOOD AND G. BIRKHOFF. Fluid flow patterns. *J. Appl. Phys.*, 1949.
- [12] J. CHAKRABARTY. *Theory of Plasticity*. McGraw-Hill, 1987.
- [13] S.J. CHAPMAN, A.D. FITT, AND G. PULOS. Vacuum moulding of a superplastic in two dimensions. *IMA J. Appl. Math.*, **63**:217–246, 1999.

-
- [14] M.C. CHICK, R.B. FREY, AND A. BINES. Jet penetration in plexiglass. *Int. J. Impact Eng.*, **9**(4):433–439, 1990.
- [15] J.D. COLVIN, M. LEGRAND, B.A. REMINGTON, G. SCHURTZ, AND S.V. WEVER. A model for instability growth in accelerated solid metals. *J. Appl. Phys.*, **93**(9):5287–5292, 2003.
- [16] R. CORNISH. A 3D modelling study of the influence of side wall collision on long stand-off jet penetration. In *Proc. Int. Symp. Ballistics, Switzerland*.
- [17] R. CORNISH, J.T. MILLS, J.P. CURTIS, AND D. FINCH. Degradation mechanisms in shaped charge jet penetration. *Int. J. Impact Eng.*, **26**:105–114, 2001.
- [18] K.G. COWAN. Analytical modelling of stochastic jet break-up phenomena. *Proc. 20th Int. Symp. Ballistics, Florida*, pages 525–532, 2002.
- [19] K.G. COWAN AND B. BOURNE. Further analytical modelling of shaped charge jet break-up phenomena. *Proc. 19th Int. Symp. Ballistics, Switzerland*, pages 803–810, 2001.
- [20] J.P. CURTIS. Simulation of jet formation and target penetration with the jet suite. *Proc. 6th European Mobile Anti-Armour Symp.*, 1997.
- [21] J.P. CURTIS AND R.J. KELLY. Circular streamline model of shaped-charge jet and slug formation with asymmetry. *J. Appl. Phys.*, **75**(12):7700–7709, 1994.
- [22] A. DOIG. Some metallurgical aspects of shaped charge liners. *J. Battlefield Technology*, **1**:1–3, 1998.
- [23] D. EDDINGFIELD, J.L. EVERS, AND A. SETORK. Mathematical modeling of high velocity water jets. In *Proc. 1st US Water Jet Conference*, pages 25–39, 1981.
- [24] C.M. ELLIOTT AND J.R. OCKENDON. *Weak and Variational Methods for Moving Boundary Problems*. Pitman Advanced Publishing Program, 1982.
- [25] GALILEO GALILEI. *Discorsi e dimstrazioni matematiche*. Appresso gli Elsevirii, MDCXXXVIII.
- [26] D.E. GRADY AND J.R. ASAY. Calculation of thermal trapping in shock deformation of aluminium. *J. Appl. Phys.*, **53**(11):7350–7354, 1982.
- [27] R.E. GRUNDY. Local similarity solutions for the initial-value problem in non-linear diffusion. *IMA J. Appl. Math.*, **30**:209–214, 1983.

-
- [28] R.E. GRUNDY AND V.A. BELL. Waiting time solutions of the shallow water equations. *Proc. R. Soc. London, Ser. A*, **441**:641–648, 1993.
- [29] R.E. GRUNDY AND J.W. ROTTMAN. The approach to self-similarity of the solutions of the shallow-water equations representing gravity-current releases. *J. Fluid Mech.*, **156**:39–53, 1985.
- [30] P. GUMBSCH AND H. GAO. Dislocations faster than the speed of sound. *Science*, **283**:965–968, 1999.
- [31] M. HASHISH. A modeling study of metal cutting with abrasive waterjets. *J. Eng. Mater. Technol. (Trans. ASME)*, **106**:88–100, 1984.
- [32] R. HEBDON. *Penetration Mechanics of a Shaped Charge*. Master’s thesis, Oxford University, 1999.
- [33] L.G. HECTOR ET AL. Thermomechanical models of air gap nucleation during pure metal solidification on moving molds with periodic surface topographies. In *Proc. 14th Ann. Workshop Math. Problems in Industry*, June 1998.
- [34] M. HELD. Liners for shaped charges. *J. Battlefield Technology*, **4**(3):1–7, 2001.
- [35] R. HILL. General features of plastic-elastic problems as exemplified by some particular solutions. *J. Appl. Mech.*, **16**:295–300, September 1949.
- [36] R. HILL. *The Mathematical Theory of Plasticity*. Oxford University Press, 1950.
- [37] R. HILL, E.H. LEE, AND S.J. TUPPER. The theory of combined plastic and elastic deformation with particular reference to a thick tube under internal pressure. *Proc. R. Soc. London Ser. A*, **191**(1026):278–303, 1947.
- [38] E.J. HINCH. *Perturbation Methods*. Cambridge University Press, 1991.
- [39] G.A. HOLZAPFEL. *Nonlinear Solid Mechanics*. John Wiley & Sons, 2004.
- [40] D.F. HOPKINS AND J.M. ROBERTSON. Two-dimensional incompressible fluid jet penetration. *J. Fluid Mech.*, **29**:273–287, 1967.
- [41] W.K.E HUNTINGTON-THRESHER, J.P. CURTIS, P.R. GREENWOOD, P. MOSS, AND J. SMETHURST. Assessment of shaped charge jet mitigation, and the development of a hydrocode, analytical model link. *Proc. 19th Int. Symp. Ballistics, Switzerland*, pages 897–904, 2001.

-
- [42] V. JEANCLAUDE AND C. FRESSENGEAS. Dynamic necking of rods at high strain rates. *J. Phys. IV*, **C3**:699–704, 1997.
- [43] R.J. KELLY, J.P. CURTIS, AND K.G. COWAN. An analytical model for the prediction of incoherent shaped charge jets. *J. Appl. Phys.*, **86**(3):1255–1265, 1999.
- [44] H. KOLSKY. *Stress Waves in Solids*. Dover Publications, 2nd edition, 1963.
- [45] A. KOROBKIN. Impact of two bodies one of which is covered by a thin layer of liquid. *J. Fluid Mech.*, **300**:43–58, 1995.
- [46] S.J. LEACH AND G.L. WALKER. Some aspects of rock cutting by high speed water jets. *Philos. Trans. R. Soc. London Ser. A*, **260**(1110):295–308, 1966.
- [47] H.W. LIEPMANN AND A. ROSHKO. *Elements of Gasdynamics*. John Wiley & Sons, 1956.
- [48] P. LIVIERI AND P. LAZZARIN. Autofrettaged cylindrical vessels and Bauschinger effect: an analytical frame for evaluating residual stress distributions. *J. Press. Vess. (Trans. ASME)*, **124**:38–46, 2002.
- [49] A.E.H. LOVE. *A Treatise on the Mathematical Theory of Elasticity*. Dover Publications, 1926.
- [50] L.M. MILNE-THOMSON. *Plane Elastic Systems*. Springer-Verlag, 1960.
- [51] L.M. MILNE-THOMSON. *Theoretical Hydrodynamics*. Dover Publications, 5th edition, 1968.
- [52] L.E. MURR, E. FERREYRA, S. PAPPU, E.P. GARCIA, J.C. SANCHEZ, W. HUANG, J.M. RIVAS, C. KENNEDY, A. AYALA, AND C.-S. NIOU. Novel deformation processes and microstructures involving ballistic penetrator formation and hypervelocity impact and penetration phenomena. *Mater. Charact.*, **37**(5):245–276, 1996.
- [53] L.E. MURR, C.-S. NIOU, E.P. GARCIA, T. FERREYRA, J.M. RIVAS, AND J.C. SANCHEZ. Comparison of jetting-related microstructures associated with hypervelocity impact crater formation in copper targets and copper shaped charges. *Mater. Sci. Eng.*, **A**(222):118–132, 1997.
- [54] T. MYERS. Modelling of the oil film in the cold mill roll gap. In *Proc. 2nd South Africa MISG*, 2005.

- [55] E.B. NEBEKER. Development of large-diameter percussive jets. In *Proc. 1st US Water Jet Conference*, pages 207–220, 1981.
- [56] V.F. NESTERENKO, M.A. MEYERS, J.C. LASALVIA, M.P. BONDAR, Y.J. CHEN, AND Y.L. LUKYANOV. Shear localization and recrystallization in high-strain, high-strain-rate deformation of tantalum. *Mater. Sci. Eng.*, **A(229)**:23–41, 1997.
- [57] R.S. NOVOKSHANOV AND J.R. OCKENDON. A mathematical model of high-rate penetration. In preparation.
- [58] R.S. NOVOKSHANOV AND N. PETRINIC. Numerical modelling of shaped charge penetration. In preparation.
- [59] H. OCKENDON AND J.R. OCKENDON. *Viscous Flow*. Cambridge University Press, 1995.
- [60] H. OCKENDON AND J.R. OCKENDON. *Waves and Compressible Flow*. Springer, 2004.
- [61] H. OCKENDON AND A.B. TAYLOR. *Inviscid Fluid Flows*. Springer-Verlag, 1983.
- [62] R.W. OGDEN. *Non-linear Elastic Deformations*. Dover, 1997.
- [63] J.M. OLIVER. *Water Entry and Related Problems*. PhD thesis, Oxford University, 2002.
- [64] D.C. PACK AND J.P. CURTIS. On the effect of asymmetries on the jet from a linear shaped charge. *J. Appl. Phys.*, **67**(11):6701–6704, 1990.
- [65] D.C. PACK AND W.M. EVANS. Penetration by high-velocity (‘munroe’) jets: I. *Proc. Phys. Soc.*, **64**:298–302, 1951.
- [66] A.P. PARKER. Autofrettage of open-end tubes - pressures, stresses, strains, and code comparisons. *J. Press. Vess. (Trans. ASME)*, **123**:271–281, 2001.
- [67] D.H. PEREGRINE AND S. KALLIADASIS. Filling flows, cliff erosion and cleaning flows. *J. Fluid Mech.*, **310**:365–374, 1996.
- [68] D.H. PEREGRINE AND L. THAIS. The effect of entrained air in violent water wave impacts. *J. Fluid Mech.*, **325**:377–397, 1996.
- [69] C.J. POOLE, J.R. OCKENDON, AND J.P. CURTIS. Gas leakage from fragmentation warheads. *Proc. 20th Int. Symp. Ballistics, Florida*, pages 113–117, 2002.

-
- [70] K.M. POWELL. Precision blasting techniques for avalanche control. *EGS XXVII General Assembly, Nice*, **27**:1720–+, 2002.
- [71] W. PRAGER AND P.G. HODGE. *Theory of Perfectly Plastic Solids*. John Wiley & Sons, 1951.
- [72] LORD RAYLEIGH. On the instability of jets. *Proc. London Math. Soc.*, **10**:4–13, 1878-1879.
- [73] J.M. RIVAS, S.A. QUINONES, AND L.E. MURR. Hypervelocity impact cratering: microstructural characterization. *Scripta metallurgica et materialia*, **33**(1):101–107, 1995.
- [74] L.A. ROMERO. The stability of stretching and accelerating plastic sheets I. *J. Appl. Phys.*, **69**(11):7474–7486, 1991.
- [75] L.A. ROMERO. The stability of stretching and accelerating plastic sheets II. *J. Appl. Phys.*, **69**(11):7487–7499, 1991.
- [76] P. ROSAKIS. Supersonic dislocation kinetics from an augmented Peierls model. *Phys. Rev. Lett.*, **86**(1):95–98, 2001.
- [77] S SAMI AND H. ANSARI. Governing equations in a modulated liquid jet. In *Proc. 1st US Water Jet Conference*, pages 14–24, 1981.
- [78] W.S. SLAUGHTER. *The Linearized Theory of Elasticity*. Birkhäuser, 2002.
- [79] I.S. SOKOLNIKOFF. *Mathematical Theory of Elasticity*. McGraw-Hill, 2nd edition, 1956.
- [80] A. STACEY AND G.A. WEBSTER. Determination of residual stress distributions in autofrettaged tubing. *Int. J. Pres. Ves. Pip.*, **31**:205–220, 1988.
- [81] R.K. SWANSON, M. KILMAN, S. CERWIN, AND W. TARVER. Study of particle velocities in water driven abrasive jet cutting. In *Proc. 4th US Water Jet Conference*, pages 163–171, 1987.
- [82] J.W. SWEGLE AND A.C. ROBINSON. Acceleration instability in elastic-plastic solids. I. Numerical simulations of plate acceleration. *J. Appl. Phys.*, **66**(7):2838–2858, 1989.
- [83] J.W. SWEGLE AND A.C. ROBINSON. Acceleration instability in elastic-plastic solids. II. Analytical techniques. *J. Appl. Phys.*, **66**(7):2859–2872, 1989.

- [84] T. SZENDREI. Analytical model for high-velocity impact cratering with material strengths: extensions and validation. *Proc. 15th Int. Symp. Ballistics, Israel*, pages 123–131, 1995.
- [85] T. SZENDREI. Link between axial penetration and radial crater expansion in hypervelocity impact. *Proc. 17th Int. Symp. Ballistics, South Africa*, pages 25–32, 1998.
- [86] A. TATE. Long rod penetration models - part I. A flow field model for high speed long rod penetration. *Int. J. Mech. Sci.*, **28**:535–548, 1986.
- [87] A. TATE. Long rod penetration models - part II. Extensions to the hydrodynamic theory of penetration. *Int. J. Mech. Sci.*, **28**:599–612, 1986.
- [88] L.P. THOMAS, S.B. DALZIEL, AND B.M. MARINO. The structure of the head of an inertial gravity current determined by particle-tracking velocimetry. *Exp. Fluids*, **34**:708–716, 2003.
- [89] T.Y. THOMAS. *Plastic Flow and Fracture in Solids*, **2**. Academic Press, 1961.
- [90] R. THUMSER, J.W. BERGMANN, AND M. VORMWALD. Residual stress fields and fatigue analysis of autofrettaged parts. *Int. J. Pres. Ves. Pip.*, **79**:113–117, 2002.
- [91] E.O. TUCK AND A. DIXON. Surf-skimmer planing hydrodynamics. *J. Fluid Mech.*, **205**:581–692, 1989.
- [92] M. VAN DYKE. *Perturbation Methods in Fluid Mechanics*. Parabolic Press, 1975.
- [93] W.P. WALTERS. An overview of the shaped charge concept. *11th Ann. ARL/USMA Technical Symp.*, 2003.
- [94] W.P. WALTERS AND D.R. SCHEFFLER. A technique for inhibiting the collapse of a shaped charge liner. In *Structures under extreme loading conditions*, 361, pages 257–263, 1998.
- [95] W.P. WALTERS AND J.A. ZUKAS. *Fundamentals of Shaped Charges*. John Wiley and Sons, 1989.
- [96] R. WATKINS. *Asymptotics of Shaped Charge Jet Penetration*. Master’s thesis, Oxford University, 2000.
- [97] A.J. WATSON AND C.J. MOXON. Ultra high velocity water jets. In *Proc. 3rd US Water Jet Conference*, pages 117–131, 1985.

-
- [98] J.M. WELLS, W.H. GREEN, N.L. RUPERT, A. COLE, S.J. ALKEMADE, S.J. CIMPOERU, AND M. SZYMCZAK. Ballistic damage visualization in monolithic Ti-6Al-4V with X-ray computed tomography. *Proc. 20th Int. Symp. Ballistics, Florida*, pages 1112–1119, 2002.
- [99] S.K. WILSON. *The Mathematics of Ship Slamming*. PhD thesis, Oxford University, 1989.
- [100] T.W. WRIGHT. *The Physics and Mathematics of Adiabatic Shear Bands*. Cambridge University Press, 2002.
- [101] GAO XIN-LIN. An exact elasto-plastic solution for an open-ended thick-walled cylinder of a strain-hardening material. *Int. J. Pres. Ves. Pip.*, **52**:129–144, 1992.
- [102] Q. XUE, M.A. MEYERS, AND V.F. NESTERENKO. Self organization of shear bands in stainless steel. *Mater. Sci. Eng.*, **A(384)**:35–46, 2004.
- [103] A.L. YARIN. On instability of rapidly stretching metal jets produced by shaped charges. *Int. J. Eng. Sci.*, **32**(5):847–862, 1994.
- [104] Z.X. YIN, C.M. MA, S.X. LI, AND G.Q. CHENG. Perforation of an ultra-high strength steel penetrated by shaped charge jet. *Mater. Sci. Eng.*, **A(379)**:443–447, 2004.
- [105] F.J. ZERILLI AND R.W. ARMSTRONG. Dislocation-mechanics-based constitutive relations for material dynamics calculations. *J. Appl. Phys.*, **61**(5):1816–1825, 1987.